STANFORD EXPLORATION PROJECT

Ali Almomin, Ohad Barak, Biondo Biondi, Jason Chang, Jon Claerbout, Robert Clapp, Noha Farghal, Antoine Guitton, Stewart Levin, Musa Maharramov, Sjoerd de Ridder, and Shuki Ronen

Report Number 148, Oct 2012

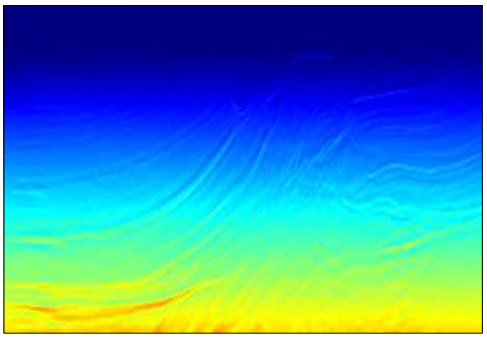

Extended FWI inversion

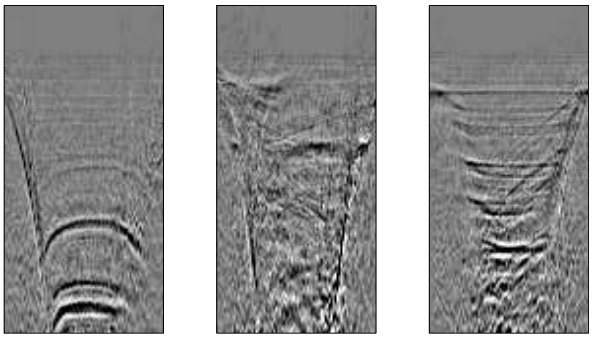

Extended FWI velocity gathers

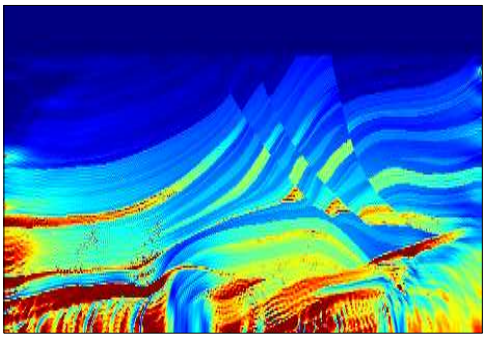

Tomographic FWI inversion

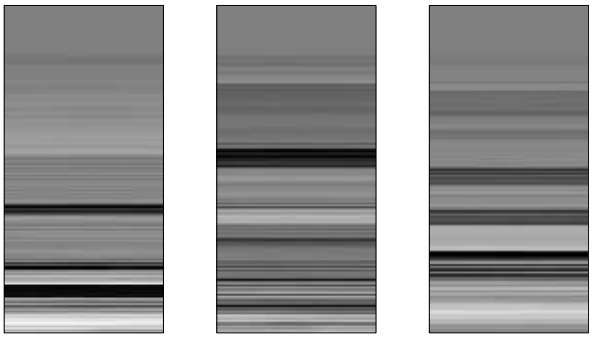

Tomographic FWI velocity gathers

Preface

The electronic version of this report[1] makes the included programs and applications available to the reader. The markings [ER], [CR], and [NR] are promises by the author about the reproducibility of each figure result. Reproducibility is a way of organizing computational research that allows both the author and the reader of a publication to verify the reported results. Reproducibility facilitates the transfer of knowledge within SEP and between SEP and its sponsors.

ER denotes Easily Reproducible and are the results of processing described in the paper. The author claims that you can reproduce such a figure from the programs, parameters, and makefiles included in the electronic document. The data must either be included in the electronic distribution, be easily available to all researchers (e.g., SEG-EAGE data sets), or be available in the SEP data library[2]. We assume you have a UNIX workstation with Fortran, Fortran90, C, C++, X-Windows system and the software downloadable from our website (SEP makerules, SEPlib, and the SEP latex package), or other free software such as SU. Before the publication of the electronic document, someone other than the author tests the author's claim by destroying and rebuilding all ER figures. Some ER figures may not be reproducible by outsiders because they depend on data sets that are too large to distribute, or data that we do not have permission to redistribute but are in the SEP data library.

CR denotes Conditional Reproducibility. The author certifies that the commands are in place to reproduce the figure if certain resources are available. The primary reasons for the CR designation is that the processing requires 20 minutes or more, MPI or CUDA based code, or commercial packages such as Matlab or Mathematica.

NR denotes Non-Reproducible figures. SEP discourages authors from flagging their figures as NR except for figures that are used solely for motivation, comparison, or illustration of the theory, such as: artist drawings, scannings, or figures taken from SEP reports not by the authors or from non-SEP publications.

Our testing is currently limited to LINUX 2.6 (using the Intel compiler), but the code should be portable to other architectures. Reader's suggestions are welcome. More information on reproducing SEP's electronic documents is available online[3].

[1] http://sepwww.stanford.edu/private/docs/sep148
[2] http://sepwww.stanford.edu/public/docs/sepdatalib/toc_html
[3] http://sepwww.stanford.edu/research/redoc/

SEP148 — TABLE OF CONTENTS

Deconvolution

FWI and Velocity Estimation

Modeling and Processing

Passive Seismic Monitoring

Fast log-decon with a quasi-Newton solver

Antoine Guitton

ABSTRACT

I speed up the log-decon method by replacing the slow steepest-descent method with a faster quasi-Newton technique known as the limited-memory BFGS.

INTRODUCTION

The log-decon method of Claerbout et al. (2011) estimates a filter that can both handle non-minimum phase wavelets (e.g., Ricker) and produce sparse seismic reflections where the polarity is easily identifiable. This method is extended in Claerbout et al. (2012) to include variable gain. Claerbout proposes to compute the filter coefficients with a steepest-descent approach, where the step length can be estimated very accurately with a Newton-search technique. Steepest descent is notoriously slow: its convergence rate depends on the conditioning of the problem producing a well-known zig-zagging effect close to the solution. Here, I propose to employ the L-BFGS method, a quasi-Newton technique that improves the convergence and decreases the number of iterations.

TWO SOLVERS

In this section, I follow Claerbout's notations for all the variables: lower case letters are for variables in time and space, while upper case letters are for variables in frequency and space.

The slow steepest-descent method

The steepest descent method requires the computation of the gradient. The model space is a vector of filter coefficients $u(t)$. Claerbout shows that the gradient $du(t)$ of the sparse log-decon method corresponds to the crosscorrelation of the residual (the reflectivity series) with the soft-clipped residual (see Claerbout et al. (2012) for a generalization with a variable gain). The pseudo-code below shows the steepest descent algorithm.

Once $u(t)$ is estimated, we obtain the wavelet $w(t) = FT^{-1}\left(e^{-U(\omega)}\right)$ and the sparse decon output $r(t) = FT^{-1}\left(D(\omega)e^{U(\omega)}\right)$, where $D(\omega)$ is the Fourier transformed input data.

The fast L-BFGS method

The L-BFGS method is a member of the quasi-Newton family: it updates at each iteration an approximation of the inverse Hessian $\mathbf{Q}$. This technique is very cost effective: given

the most recent history of gradient and model vectors (usually around 5) kept in memory, the quasi-Newton search direction **Qdu** (inverse Hessian times the gradient) is computed directly with simple vector multiplications. Therefore, the L-BFGS solver can be used for large non-linear problems (Nocedal, 1980).

Contrary to steepest descent where the step length is estimated with a Newton-search technique, the step length in L-BFGS is computed such that sufficient decrease of the error and of the local curvature is attained (so called "Wolfe conditions"). The appendix shows the L-BFGS solver in more details. The L-BFGS code can be downloaded at http://users.eecs.northwestern.edu/~nocedal/lbfgs.html The pseudo-code below shows both the steepest-descent and L-BFGS algorithms.

```
U = 0.        # or other initializations
Remove the mean from U(omega).

Iteration {
     dU = 0
     Compute dU
     Remove mean from dU
     du = FT(dU)
     if (steepest descent)
       {
       Compute alfa with Newton iterations
       u  = u + alfa*du
       }
     else if (L-BFGS)
       {
       Compute alfa with More and Thuente method
       u  = u + alfa*Qdu # Q = inverse approximate Hessian
       }
          }
```

A fair warning

Comparing the convergence of optimization techniques can be quite difficult to do in a fair manner. My steepest descent algorithm includes a termination criterion based on the Armijo rule only, namely, a sufficient decrease condition of the objective function (whereas L-BFGS use the Wolfe conditions). In addition, both the steepest descent and L-BFGS algorithms have different line-searches, which will affect convergence and computational performances. The L-BFGS line-search is based on the More and Thuente method, which uses bracketing and quadratic/cubic interpolation. The steepest-descent algorithm uses a very simple scheme where the step length is divided by two until the sufficient decrease condition is respected. Therefore, some of the computational differences come from the line-search algorithm and stopping criteria in addition to the inherent convergence properties of the two methods.

A COMPARISON ON A FIELD-DATA EXAMPLE

Figure 1 shows a near-offset section of a 2-D line from the Gulf of California used in Claerbout et al. (2012). The left side displays the input data and the right side the deconed data when the L-BFGS solver is used. I do not show the result of the steepest-descent because both methods estimate very similar wavelets, as shown in Figure 2. As expected, the reflectivity of the deconed data in Figure 1 is revealed quite well: the polarity of large reflectors is enhanced. Also, a non-minimum phase wavelet is obtained, regardless of the method (Figure 2).

In terms of convergence speed, it takes 35 iterations and 1.7 seconds for the L-BFGS technique to reach a minimum, and 123 iterations and 24 seconds for the steepest-descent algorithm (Figure 3). Ignoring the time it takes to read and write data on disk, each iteration of the L-BFGS algorithm is about five times faster, with almost four times less iterations. Clearly, this difference is not solely due to the better convergence properties of the quasi-Newton algorithm over the steepest-descent method. As mentioned before, different line-search strategies and stopping criteria matter as well.

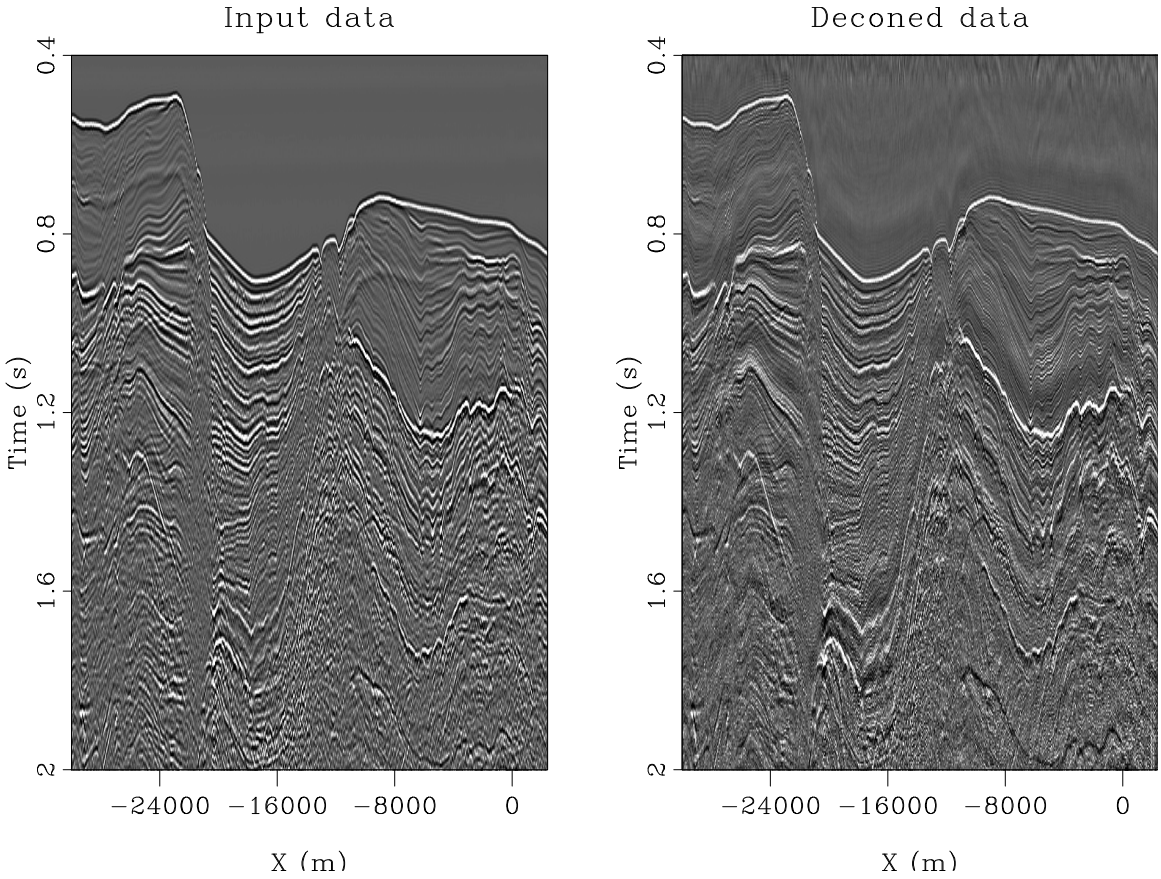

Figure 1: Left: input data. Right: deconed data with the L-BFGS solver antoine1/. Comp-cabo

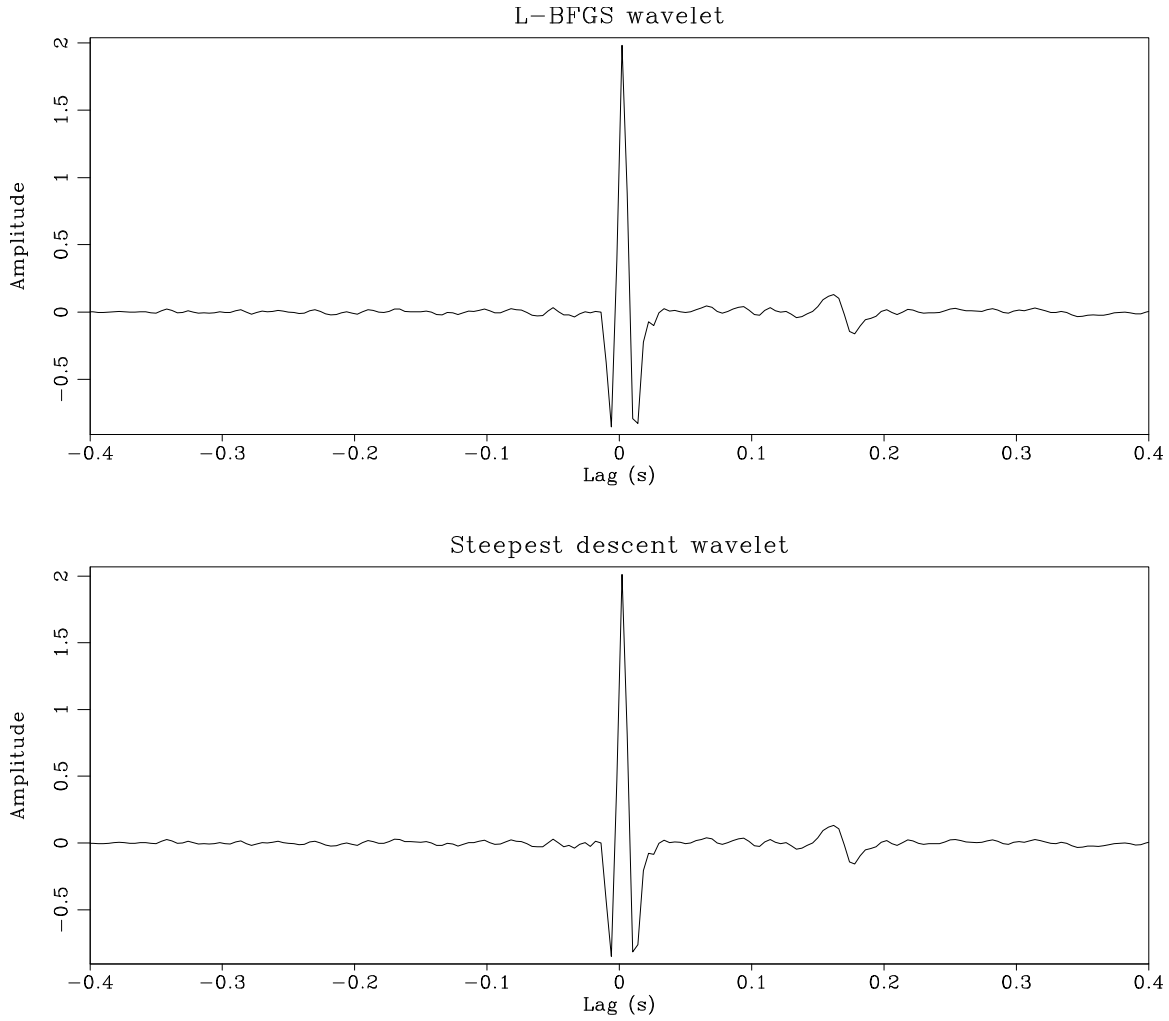

Figure 2: Top: wavelet estimated with the L-BFGS method. Bottom: wavelet estimated with the steepest-descent method. antoine1/. Comp-wvlt

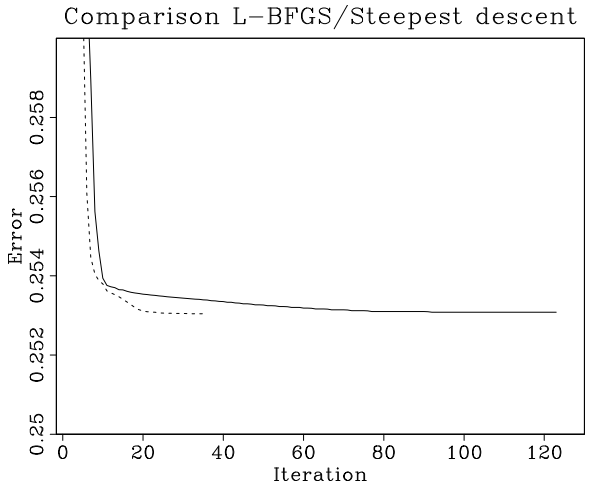

Figure 3: Convergence comparison between the steepest descent (solid) and L-BFGS (dash) methods. Note the narrow horizontal scale to highlight small differences close to the convergence point. antoine1/. Comp-fct

CONCLUSION

The log-decon method is sped up by using the L-BFGS method compared to the steepest-descent solver. A factor 20 is observed in this paper but results will vary depending on the experimental setup.

APPENDIX

The L-BFGS method is suitable for smooth functions where local minima exist. It is not a method for global optimization where the global minimum is sought. L-BFGS is presented here in general terms using global definitions for the different variables: it does not follow the notations of the log-decon method.

We define $\mathbf{m}^*$ a local minimizer for $f(\mathbf{m})$ and we assume that $f(\mathbf{m})$ and $\mathbf{m}^*$ satisfy the "standard requirements":

1. f is twice differentiable,
2. $\nabla f(\mathbf{m}^*) = 0$,
3. $\nabla^2 f(\mathbf{m}^*)$ is positive definite , i.e., $\mathbf{m}'\nabla^2 f(\mathbf{m}^*)\mathbf{m} > 0$ for all $\mathbf{m} \in \Re^N$ ($'$ denotes the adjoint).

where N is the dimension of the model vector $\mathbf{m}$ and $\Re^N$ the real space for the model vector $\mathbf{m}$. Any vector $\mathbf{m}^*$ that satisfies the standard requirements is a local minimizer of $f(\mathbf{m})$.

Newton's method is an iterative process where the solution to the problem is updated as follows:

$$\mathbf{m}_{k+1} = \mathbf{m}_k - \lambda_k \mathbf{H}_k^{-1} \nabla f(\mathbf{m}_k), \tag{1}$$

where $\mathbf{m}_{k+1}$ is the updated solution at iteration $k+1$, λ_k the step length computed by a line search that ensures a sufficient decrease of $f(\mathbf{m})$ and $\mathbf{H}_k = \nabla^2 f(\mathbf{m}_k)$ the Hessian (or second derivative). In many circumstances the inverse of the Hessian can't be computed directly. It happens for example when the matrix $\mathbf{H}$ is too big or when operators are used rather than matrices. Fortunately we might be able to compute an approximation of the Hessian of $f(\mathbf{m})$. This strategy gives birth to quasi-Newton methods where the way in which the Hessian is computed determines the method (Kelley, 1999).

A possible update of the Hessian is given by the BFGS technique Broyden (1969); Fletcher (1970); Goldfarb (1970); Shanno (1970). The BFGS update is given by

$$\mathbf{H}_{k+1} = \mathbf{H}_k + \frac{\mathbf{y}\mathbf{y}'}{\mathbf{y}'\mathbf{s}} - \frac{(\mathbf{H}_k\mathbf{s})(\mathbf{H}_k\mathbf{s})'}{\mathbf{s}'\mathbf{H}_k\mathbf{s}}, \tag{2}$$

where $\mathbf{s} = \mathbf{m}_{k+1} - \mathbf{m}_k$ and $\mathbf{y} = \nabla f(\mathbf{m}_{k+1}) - \nabla f(\mathbf{m}_k)$. In practice, however, we rather write the previous equation in terms of the inverse matrices. We have then

$$\mathbf{H}_{k+1}^{-1} = \left(\mathbf{I} - \frac{\mathbf{s}\mathbf{y}'}{\mathbf{y}'\mathbf{s}}\right) \mathbf{H}_k^{-1} \left(\mathbf{I} - \frac{\mathbf{y}\mathbf{s}'}{\mathbf{y}'\mathbf{s}}\right) + \frac{\mathbf{s}\mathbf{s}'}{\mathbf{y}'\mathbf{s}}. \tag{3}$$

In addition, we use the history of the iterations to compute the new Hessian rather than a full storage of the matrix $\mathbf{H}_k^{-1}$. This requires that a gradient step vector $\mathbf{y}$ and a solution

step vector $\mathbf{s}$ are kept in memory after each iteration. Consequently this method might not been affordable with large data and model space. In the next section a modified version of the BFGS method that limits the storage needed to compute the update of the Hessian is proposed.

The limited-memory BFGS method

Nocedal (1980) derives a technique that partially solves the storage problem caused by the BFGS update. Instead of keeping all the $\mathbf{s}$ and $\mathbf{y}$ from the past iterations, we update the Hessian using the information from the l previous iterations, where l is given by the end-user. This implies that when the number of iterations is smaller than l, we have the usual BFGS update, and when it is larger than l, we have a limited-memory BFGS (L-BFGS) update.

I give the updating formulas of the Hessian as presented by Nocedal (1980). First, we define

$$\rho_i = 1/\mathbf{y}_i'\mathbf{s}_i,\ \mathbf{v}_i = (I - \rho_i \mathbf{y}_i \mathbf{s}_i') \text{ and } \mathbf{H}^{-1} = \mathbf{B}.$$

As described above, when k, the iteration number, obeys $k+1 \leq l$, where l is the storage limit, we have the BFGS update

$$\begin{aligned} \mathbf{B}_{k+1} &= \mathbf{v}_k'\mathbf{v}_{k-1}' \cdots \mathbf{v}_0'\mathbf{B}_0\mathbf{v}_0 \cdots \mathbf{v}_{k-1}\mathbf{v}_k \\ &\quad + \mathbf{v}_k' \cdots \mathbf{v}_1'\rho_0\mathbf{s}_0\mathbf{s}_0'\mathbf{v}_1 \cdots \mathbf{v}_k \\ &\quad \vdots \\ &\quad + \mathbf{v}_k'\rho_{k-1}\mathbf{s}_{k-1}\mathbf{s}_{k-1}'\mathbf{v}_k \\ &\quad + \rho_k\mathbf{s}_k\mathbf{s}_k'. \end{aligned} \tag{4}$$

For $k+1 > l$ we have the limited-memory update

$$\begin{aligned} \mathbf{B}_{k+1} &= \mathbf{v}_k'\mathbf{v}_{k-1}' \cdots \mathbf{v}_{k-l+1}'\mathbf{B}_0\mathbf{v}_{k-l+1} \cdots \mathbf{v}_{k-1}\mathbf{v}_k \\ &\quad + \mathbf{v}_k' \cdots \mathbf{v}_{k-l+2}'\rho_{k-l+1}\mathbf{s}_{k-l+1}\mathbf{s}_{k-l+1}'\mathbf{v}_{k-l+2} \cdots \mathbf{v}_k \\ &\quad \vdots \\ &\quad + \mathbf{v}_k'\rho_{k-1}\mathbf{s}_{k-1}\mathbf{s}_{k-1}'\mathbf{v}_k \\ &\quad + \rho_k\mathbf{s}_k\mathbf{s}_k'. \end{aligned} \tag{5}$$

These equations show how the update of the Hessian is calculated.

Usually the L-BFGS method is implemented with a line search for the step length λ_k to ensure a sufficient decrease of the misfit function. Convergence properties of the L-BFGS method are guaranteed if λ_k in equation (2) satisfies the *Wolfe conditions* (Kelley, 1999):

$$f(\mathbf{x}_k + \lambda_k\mathbf{d}_k) \leq f(\mathbf{x}_k) + \mu\lambda_k\nabla f(\mathbf{x}_k)'\mathbf{d}_k, \tag{6}$$

$$|\nabla f(\mathbf{x}_k + \lambda_k\mathbf{d}_k)'\mathbf{d}_k| \geq \nu|\nabla f(\mathbf{x}_k)'\mathbf{d}_k|. \tag{7}$$

ν and μ are constants to be chosen a priori and $\mathbf{d}_k = -\mathbf{B}_k\nabla f(\mathbf{m}_k)$. For ν and μ we set $\nu = 0.9$ and $\mu = 10^{-4}$ as proposed by Liu and Nocedal (1989). Equation (6) is a sufficient decrease condition that all line search algorithms must satisfy. Equation (7) is a curvature

condition. The line search algorithm has to be carefully designed since it absorbs most of the computing time. I programmed a line search based on the More and Thuente (1994) method. Because the line search is time consuming, the step length $\lambda_k = 1$ is always tested first. This procedure saves a lot of computing time and is also recommended by Liu and Nocedal (1989). I now give the algorithm used to minimize any objective function involving nonlinear problems.

An efficient algorithm for solving nonlinear problems

The solver works as follows:

1. Choose $\mathbf{m}_0$, l, $\mathbf{B}_0$. Set $k = 0$.
2. Compute

$$\mathbf{d}_k = -\mathbf{B}_k \nabla f(\mathbf{m}_k), \tag{8}$$
$$\mathbf{m}_{k+1} = \mathbf{m}_k + \lambda_k \mathbf{d}_k, \tag{9}$$

   where λ_k meets the Wolfe conditions.

3. Let $\hat{l}$=min$\{k, l-1\}$. Update $\mathbf{B}_0$ $\hat{l}+1$ times using the pairs $\{\mathbf{y}_i, \mathbf{s}_i\}_{j=k-\hat{l}}^{k}$, i.e., let

$$\begin{aligned} \mathbf{B}_{k+1} = {} & \mathbf{v}_k' \mathbf{v}_{k-1}' \cdots \mathbf{v}_{k-\hat{l}}' \mathbf{B}_0 \mathbf{v}_{k-\hat{l}} \cdots \mathbf{v}_{k-1} \mathbf{v}_k \\ & + \mathbf{v}_k' \cdots \mathbf{v}_{k-\hat{l}+1}' \rho_{k-\hat{l}} \mathbf{s}_{k-\hat{l}} \mathbf{s}_{k-\hat{l}}' \mathbf{v}_{k-\hat{l}+1} \cdots \mathbf{v}_k \\ & \vdots \qquad (10) \\ & + \mathbf{v}_k' \rho_{k-1} \mathbf{s}_{k-1} \mathbf{s}_{k-1}' \mathbf{v}_k \\ & + \rho_k \mathbf{s}_k \mathbf{s}_k'. \qquad (11) \end{aligned}$$

4. Set $k = k + 1$ and go to 2 if the residual power is not small enough.

The update $\mathbf{B}_{k+1}$ is not formed explicitly; instead we compute $\mathbf{d}_k = -\mathbf{B}_k \nabla f(\mathbf{x}_k)$ with an iterative formula Nocedal (1980). Liu and Nocedal (1989) propose scaling the initial symmetric positive definite $\mathbf{B}_0$ at each iteration as follows:

$$\mathbf{B}_k^0 = \frac{\mathbf{y}_k' \mathbf{s}_k}{\| \mathbf{y}_k \|_2^2} \mathbf{B}_0. \tag{12}$$

This scaling greatly improves the performances of the method. Liu and Nocedal (1989) show that the storage limit for large-scale problems has little effects. A common choice for l is $l = 5$. In practice, the initial guess $\mathbf{B}_0$ for the Hessian is the identity matrix $\mathbf{I}$; then it might be scaled as proposed in equation (12). The nonlinear solver as detailed in the previous algorithm converges to a local minimizer $\mathbf{m}^*$ of $f(\mathbf{m})$.

REFERENCES

Broyden, C. G., 1969, A new double-rank minimization algorithm: AMS Notices, **16**, 670.

Claerbout, J., Q. Fu, and Y. Shen, 2011, A log spectral approach to bidirectional deconvolution: SEP-Report, **143**, 297–300.

Claerbout, J., A. Guitton, and Q. Fu, 2012, Decon in the log domain with variable gain: SEP-Report, **147**, 313–322.

Fletcher, R., 1970, A new approach to variable metric methods: Comput. J., **13**, 317–322.

Goldfarb, D., 1970, A family of variable metric methods derived by variational means: Math. Comp., **24**, 23–26.

Kelley, C. T., 1999, Iterative methods for optimization: SIAM in applied mathematics.

Liu, D. C. and J. Nocedal, 1989, On the limited memory BFGS method for large scale optimization: Mathematical Programming, **45**, 503–528.

More, J. J. and J. Thuente, 1994, Line search algorithms with guaranteed sufficient decrease: ACM Transactions on Mathematical Software, **20**, 286–307.

Nocedal, J., 1980, Updating quasi-Newton matrices with limited storage: Mathematics of Computation, **95**, 339–353.

Shanno, D. F., 1970, Conditioning of quasi-Newton methods for function minimization: Math. Comp., **24**, 647–657.

Modeling data error during deconvolution

Jon Claerbout and Antoine Guitton

ABSTRACT

Our current decons take the data sacrosanct and find the best noncausal wavelet to deconvolve it with. We propose allowing the data to include an explicit noise that does not fit the convolutional model. We write regressions to define this noise, and develop an expression for the gradient needed to fit the regressions.

INTRODUCTION

Data fitting with the ℓ_1 norm has well-known remarkable qualities. Even more suitable to seismic problems is the hyperbolic penalty function $h(r) = \sqrt{1+r^2} - 1$ (Li et al. (2010)). Applying it to deconvolution of 2-D synthetic data easily solved a complicated case not solveable by ℓ_2 decons (Zhang and Claerbout (2010a)). Unfortunately, application to field data was not successful. Returning to synthetic data, the culprit turned out to be the minimum-phase assumption. This can be understood by examining the Ricker (non-minimum phase) wavelet, a long-standing example of a wavelet hard to spike.

Solving for a product of forward and backward PEFs achieved an excellent result on synthetic data and a spectacular result on a Gulf of Mexico data set (Zhang and Claerbout (2010b)). By deconvolving properly we were delighted to find we had made reflection coefficient polarity much more clear. We were highly motivated to improve on this and integrate it with impedance estimation. Not well documented were difficulties connected with polarity reversal and apparent time shifts. They were attributed to the non-linearity of the method.

Claerbout et al. (2011) reformulated the problem in the frequency domain with the unknown parameters being the values at lags defining the log spectrum. This avoided many problems, but extensive testing by Qiang Fu and Yi Shen revealed reliability issues much like those identified by Zhang. For a long while we understood our difficulty to be a need for preconditioning to guide the non-linear problem closer to the desired solution. Suddenly we came to realize the problem is more like a null space, though not exactly that because of the nonlinearity. The apparent polarity reversals and time shifts resulted from spiking the first or the third lobe of the Ricker wavelet instead of consistently spiking the middle lobe. Claerbout (2012) resolved these problems by means of a regularization (called the Ricker regularization) that ensures Ricker-like wavelets. Unfortunately, like all regularizations, you can never be sure how much to add, leading to degraded results when you add too much.

Then the non commutivity of gain with filtering was theoretically resolved leading to small but noticable improvements (Claerbout et al. (2012)). Guitton and Claerbout (2012) also added a regularization term that penalizes long positive or negative lags of the filter. This penalty ensures that the estimated wavelet does not shift in masking areas that can be present in the gain function (i.e., preventing local minima).

With stability now under much better control (we still need to experiment with strength of the regularizations) we set out to demonstrate that sparse decon principles could find natural cutoffs for high and low frequencies in data. We seemed to be seeing frequencies dangerously close to the 125Hz Nyquist on our available 4ms data so we ordered and waited to obtain 2ms data to boost the Nyquist to 250 Hz. Much to our horror (Guitton and Claerbout (2012)), sparseness decon, like old fashioned l_2 decon, boosts energy up to near the new much higher Nyquist. Also discovered in that paper is that our shot wavelets are picking up sea swell noise. We do not wish to filter out sea swell as a preprocess because we do not wish to lose low frequency information that could be essential to impedance estimation. Swell noise modeling has been done by Parrish (2005). Subtracting such models should work better than filtering.

The formulation of this paper integrates sea swell modeling with our non minimum-phase, sparseness goaled, shot waveform estimation and data deconvolution. The experimental results mentioned above led to the theory you find here. What else might we find? We expect the noise to contain any bits of the data with non-typical spectra, both amplitude and phase. Besides the low-frequency sea swell, we might find the water bottom itself and its multiples contain the very high frequencies that we do not expect in waves that penetrate the earth.

INTRODUCING NOISE AS ITSELF A MODEL

The idea of this paper is that we should not try push all our data into the convolutional model. We should explicitly solve for an unknown part of the data that poorly fits this model. I call this part noise and define it negatively $-N$ (so the minus sign is missing from all the analysis and code).

The decon filter $C = e^U$, parameterized by U, we take as noncausal. The constraint is no longer a spike at zero lag, but a filter whose log spectrum vanishes at zero lag, $0 = u_0 = \int \ln C(\omega)\ d\omega$, so we are now constraining the mean of the log spectrum. This is a fundamental change which we confess to being somewhat mysterious.

The single regression for U including noise N now becomes two.

$$0 \quad \approx_h \quad (D+N)e^U = (D+N)C \tag{1}$$

$$0 \quad \approx_2 \quad N \tag{2}$$

The notation $\approx_h$ means the data fitting is done under a hyperbolic penalty function. The regularization need not be ℓ_2. To save clutter I leave it as ℓ_2 until the last step when I remind how it can easily be made hyperbolic.

Under the constraint of a causal filter with $c_0 = 1$, traditional auto regression for $c_t = \mathrm{FT}^{-1}C$ with its regularization looks more like

$$0 \quad \approx \quad N \;=\; Dc \tag{3}$$

$$0 \quad \approx \quad c \tag{4}$$

Comparing equations 1-2 with 3-4 you see we are not simply rehashing traditional methodology but seem to be off in a wholly new direction! We are here because $C = e^U$ solved our

non-minimum phase problem, and seeing sea swell in our estimated shot wavelets told us we need to replace D by $D+N$.

Antoine noticed the quasi-Newton method of data fitting requires gradients but not knowledge of how to update residuals $\Delta\mathbf{r}$ so the only thing we really need to think about is getting the gradient. The gradient wrt U is the same as before (Claerbout et al. (2011)) except that $D+N$ replaces D. The gradient wrt N is the new element here.

Let d, n, and c be time functions (data, noise, and filter). Let $r=(d-n)*c$ be the residual. Let $h_t=h(r_t)=$ hyperbolic stretch of r. Expressing our two regressions in the time domain we minimize

$$\min_n \quad \sum_t n^2/2 \;+\; h((d+n)*c) \tag{5}$$

A scaling factor is required between the terms. We expect to learn it by experimentation.

Now we go after the gradient, the derivative of the penalty function wrt each component of noise n_s. Let the derivative of the penalty function $h(r_t)$ wrt its argument r_t be called the softclip and be denoted $h'_t=h'(r_t)$. Let H' denote the FT of h'. Let $c'(t)$ be the time reverse of $c(t)$ while in Fourier space C' is the conjugate of C.

$$\begin{aligned}
\Delta n_s &= n_s \;+\; \frac{\partial}{\partial n_s} \sum_t h(r_t) && (6)\\
&= n_s \;+\; \sum_t h'(r_t)\; \frac{\partial}{\partial n_s}\; (d+n)*c && (7)\\
&= n_s \;+\; \sum_t h'_t\; \frac{\partial}{\partial n_s} \sum_\tau n_{t-\tau} c_\tau && (8)\\
&= n_s \;+\; \sum_t h'_t\; \frac{\partial}{\partial n_s} \sum_j n_j c_{t-j} && (9)\\
&= n_s \;+\; \sum_t h'_t\; c_{t-s} && (10)\\
&= n_s \;+\; \sum_t h'_t\; c'_{s-t} && (11)\\
\Delta N &= N \;+\; C'H' && (12)
\end{aligned}$$

For simplicity I set out with a quadratic penalty function on the noise, but it is easy to make it hyperbolic. Simply use softclip on n. Change $\Delta n = n + \cdots$ to $\Delta n = h'(n) + \cdots$.

Now having the gradient we should be ready to code.

ALGORITHM

Before altering the old algorithm we need to be careful about a couple things. We may need different gain functions for $(d+n)*c$ and for n. Sea swell is quite stationary in its physics, but the hyperbolic penalty function applies to the statistical perspective which is one where images are boosted in time from their physical form. We also need to be careful not to mix up $h(n)$ with $h(r=(d+n)*c)$. We will need to scale the regularization with the fitting by experimentation.

We could update the old algorithm (Claerbout et al. (2011)) with the new noise parts. Alternately, we could follow the suggestion of Antoine and switch to the quasi Newton method. In either case we'll need to introduce a scale factor (learned from practice) to choose how much of D ends out in N.

INTERNET HUMOR

Theory is when you know everything but nothing works.

Practice is when everything works, but you don't know why.

In our lab, theory and practice are combined. Nothing works and nobody knows why.

REFERENCES

Claerbout, J., 2012, Polarity preserving decon in "N log N" time: SEP-Report, **147**, 305–312.

Claerbout, J., Q. Fu, and Y. Shen, 2011, A log spectral approach to bidirectional deconvolution: SEP-Report, **143**, 297–300.

Claerbout, J., A. Guitton, and Q. Fu, 2012, Decon in the log domain with variable gain: SEP-Report, **147**, 313–322.

Guitton, A. and J. Claerbout, 2012, Six tests of sparse log decon: SEP-Report, **148**, 35–48.

Li, Y., Y. Zhang, and J. Claerbout, 2010, Geophysical applications of a novel and robust l1 solver: SEP-Report, **140**, 155–164.

Parrish, J. F., 2005, Streamer string waves and swell noise: SEG Technical Program Expanded Abstracts, **24**, 72–75.

Zhang, Y. and J. Claerbout, 2010a, Least-squares imaging and deconvolution using the hybrid norm conjugate-direction solver: SEP-Report, **140**, 129–142.

———, 2010b, A new bidirectional deconvolution method that overcomes the minimum phase assumption: SEP-Report, **142**, 93–104.

Decon comparisons between Burg and conjugate-gradient methods

Antoine Guitton and Jon Claerbout

ABSTRACT

In testing on several nearby data sets, three shown here, the Burg method of deconvolution exhibited no issues of numerical round-off. In every case it did exhibit whiteness, an aspect of the theory normally considered desirable. Prediction-error code based on conjugate gradients (actually conjugate directions) showed some minor issues. Output comparisons of the two were never perceptibly different on paper documents such as this. When those same PDF documents are viewed on a screen, differences might be noticeable with "blink" screen presentation. Doing no more than the number of iterations theoretically predicted (equal to the number of filter coefficients) gave differences generally noticeable with blink presentation. Tripling the number of iterations made the differences much smaller, sometimes differing at a mere handful of pixels. Although discrepancies were minuscule on the filtered data, the differences are quite clear in a spectral comparison. Differences tend to occur at the very high and very low frequencies that are weak in the field data.

INTRODUCTION

The classical stationary linear least-squares deconvolution problem may be solved in a variety of ways. While testing our new sparseness deconvolution method (non-causal, nonlinear, hyperbolic penalty) we had occasion to use some classic methods for comparisons. In particular, we used the Burg decon code (Claerbout, 1976) and the conjugate direction (CD) code (`Pef` in Claerbout and Fomel (2012)). In the absence of precision issues, the CD code is theoretically equivalent to the conjugate gradient method. Unexpectedly, during our early studies some astonishing differences appeared. Were these differences due to coding bugs, improper comparisons, or precision issues not previously recognized by us? Perhaps all. These two methods do differ in some fundamental aspects, principally but not entirely related to end effects. Another difference is that the Burg method assures a minimum-phase filter but that is not true of the regression methods in GEE, namely `Pef`.

PRECISION AND ACCURACY

Focusing on precision we arrange our study so end effects are minimal and the stationarity assumption is not stressed. We are not attempting an exhibition of known theoretical differences, but we do intend to obtain for practical work, guidelines for dealing with poorly understood numerical-analysis issues.

Reflection data is not stationary; and it comes exhibiting diverse aspects [reference Yilmaz and Cumro shot profiles]. We chose simply to test with several of our current data

sets of interest. Results with three of them are included here. To simulate stationarity, Kjartansson t-squared gain is applied. We also taper the ends of the trace to avoid any transients there. Additionally, we average spectra of hundreds to thousands of traces in each data set. This average spectrum is used to devise a single decon filter applied to every trace in the data set.

We were not aware of precision issues with the Burg method, neither were we aware that it has been tested under modern environments where high order filters are easily computed.

The conjugate-direction method in GEE has some issues likewise never investigated. Theoretically it converges in a number of steps equal the filter length, but this says nothing about precision. It is easy enough to do more iterations than required. Thus we have compared the theoretical number of iterations with triple that number. Accuracy greater still should be obtainable by an additional measure that we did not try. The algorithm proceeds by updating a residual. These updates might accumulate errors. Thus, the residual could be recomputed from time-to-time during iteration. The textbook program `Pef` in GEE is not doing that. We could have tested that additional grasp for precision, but we did not.

More fundamentally, the Burg method builds in the stationarity assumption and minimum phase (by assuring a sequence of reflection coefficients is bounded between ± 1). The `Pef` code (concerned with multidimensional data containing gaps) makes no such effort. It could predict a growing function which is obviously non-stationary. Does that mean the output of `Pef` could be non-white? Likely so, but we don't know if that is a practical issue.

RESULTS

We began by using the usual Kjartansson t^2 gain correction. One power of t is a geometrical divergence correction. The other power of t is the expected loss of bandwidth propagating through a constant-Q medium. Not wanting to study the end-effect differences between the two methods (as they are already well defined by theory) we taper both ends of each seismogram to zero.

We compute the spectrum of each data set in the usual way. We average the energy spectrum of each trace, then take the logarithm of the average, and finally shift the logarithm as a function of frequency to be zero at 40Hz.

REFERENCES

Claerbout, J., 1976, Fundamentals of Geophysical Data Processing: Blackwell Scientific Publications.

Claerbout, J. and S. Fomel, 2012, Image Estimation by Example: Geophysical Soundings Image Construction: Class notes, http://sepwww.stanford.edu/sep/prof/index.html.

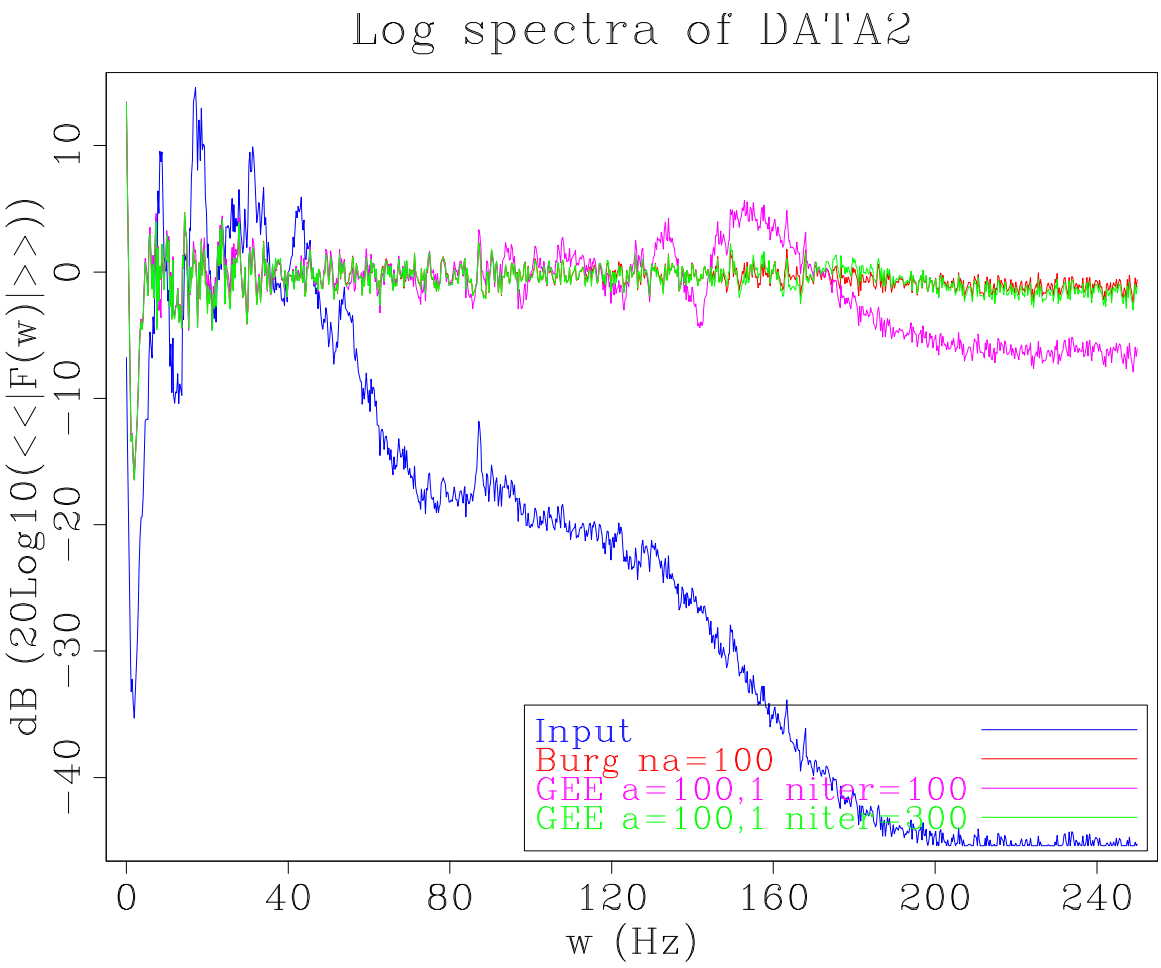

Figure 1: The log spectrum of the the Kjartansson data set and decon outputs by the three different methods. The wide ranging spectrum is that of the input data. The two near constant spectra are the Burg and the "triply iterated" CG decon outputs. By triply iterated we mean 3× the number of iterations theoretically required. The "not-so-near-constant" curve arises from CD with the theoretically needed iterations, namely, as many as the filter coefficients. This curve seems to resist the theoretical requirement to boost very low and very high frequencies (which in practice might not be a bad idea!). [**ER**]

antoine2/. DeconLogFourier-DATA2

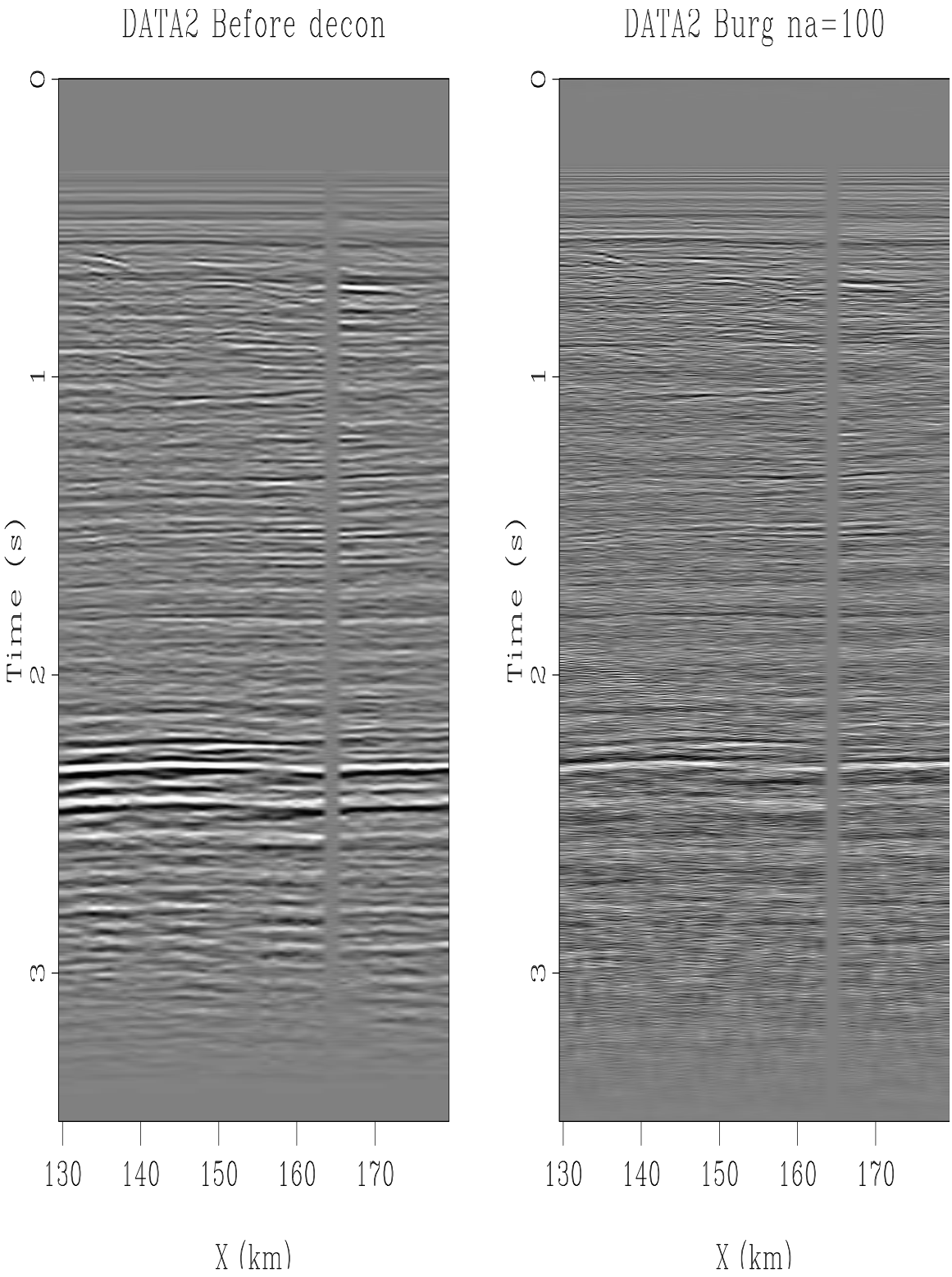

Figure 2: Left is a portion of the Kjartansson data set. Right is its Burg decon. Outputs of the CG Pef were on paper indistinguishable from Burg decon, but slightly distinguishable when alternately blinking on a screen. [**ER**] antoine2/. Decon-DATA2

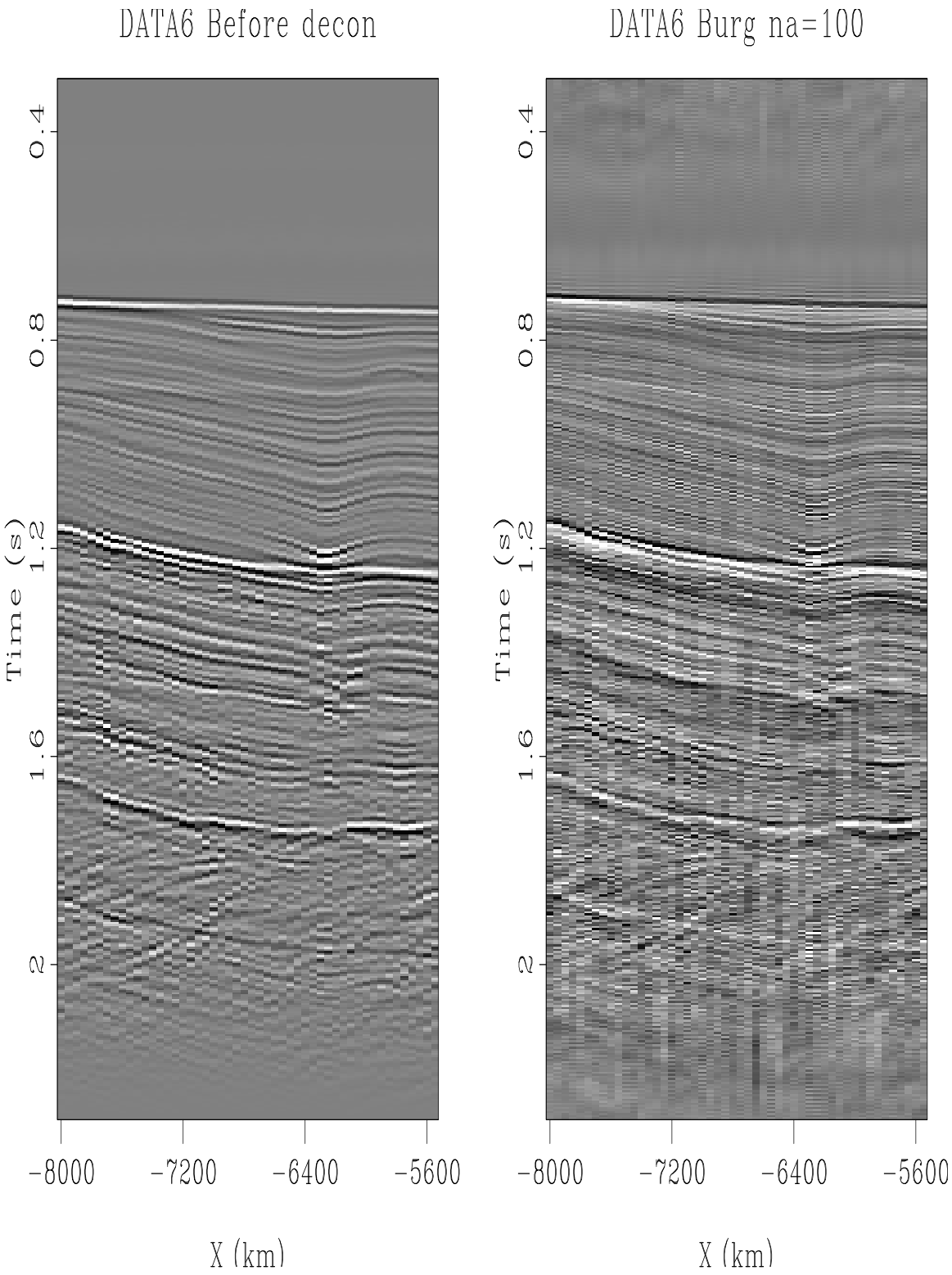

Figure 3: The Gulf of California data set. Unwelcome near-zero frequencies appear from trace to trace. These appeared with all decon methods. Apparent precursors to the water bottom are PDF document artifacts. [**ER**] antoine2/. Decon-DATA6

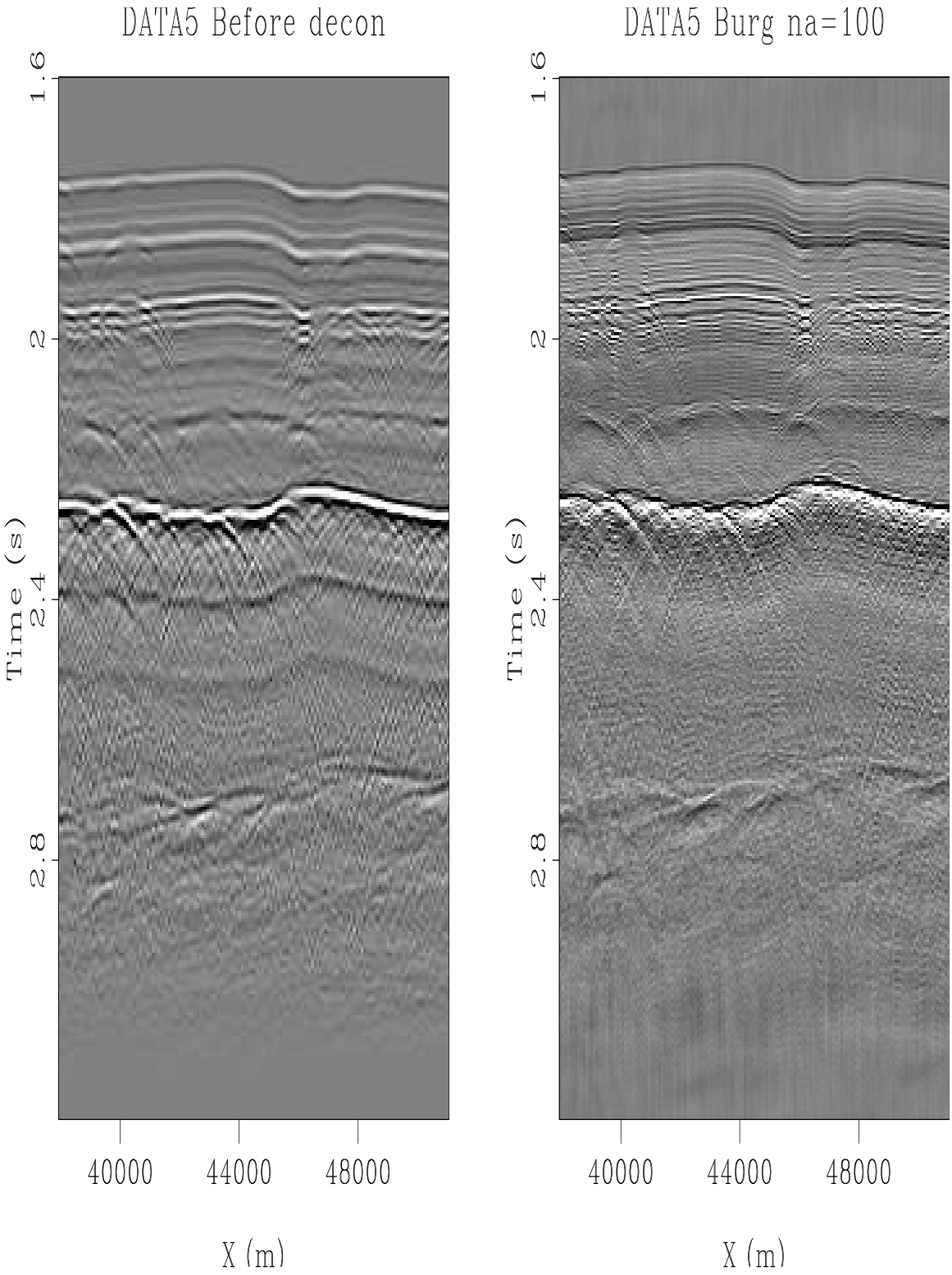

Figure 4: Gulf of Mexico data set. Suspicious low frequencies are strongest following the top of salt reflector at 2.3s but visible throughout the data. Seems likely someone filtered this data before it came to us. [**ER**] antoine2/. Decon-DATA5

Decon in the log domain - practical considerations

Ohad Barak, Antoine Guitton and Shuki Ronen

ABSTRACT

We apply deconvolution in the log domain to marine seismic data. The inversion promotes sparsity. We compare the deconvolution results of using two types of regularizations: filter symmetry and filter length. We show that the regularizations aid in acquiring the correct shot waveform, and in sparsifying the data. An consideration that we can add to the inversion is the elimination of the marine acquisition notch frequency.

INTRODUCTION

In marine streamer acquisition, both the source and the receivers are at some depth. As a result, their reflection from the water surface generates "ghost" arrivals. These ghosts are recorded in addition to the primary path of energy propagation from source to reflector to receiver. This causes the recordings of the specular reflections to be in practice non-minimum phase wavelets, and more similar to Ricker wavelets, as most of the energy does not arrive at the onset of the wavelet. Since Ricker is a delayed zero-phase wavelet, predictive decon will have limited success on marine streamer data, as the inverse filter will have coefficients that increase with time. Additionally, the airgun typically employed as a source in marine surveys generates a low-frequency bubble, whose reverberations contaminate the recorded data.

Zhang et al. (2011) extended traditional deconvolution to non-minimum phase wavelets. Claerbout et al. (2011) replaced the unknown filter coefficients by lag coefficients in the log spectrum of the deconvolution filter. Given data $D(\omega)$, the deconvolved output r_t is:

$$r_t \;=\; \mathrm{FT}^{-1} \;\left[D(\omega) \;\exp\left(\sum_t u_t Z^t \right) \right] \tag{1}$$

where FT^{-1} is the inverse Fourier transform, and $Z = e^{i\omega}$. u_t are the log spectrum variables of the deconvolution filter. The source wavelet is the inverse of the exponent of these log variables. The positive lag coefficients correspond to the causal part of the wavelet, and the negative ones to the anticausal part.

Claerbout et al. (2012) introduced the concept of inverting for sparsity, with the added complication that seismic data is non-stationary but decreases in amplitude over time. A gained residual $q_t = g_t r_t$ is sparsified using a hyperbolic penalty function $H(q_t)$, where g_t is a known gain function. The inversion finds the model parameters u_t which cause the gained residual q_t to be as sparse as possible. The purpose is to enhance frequencies where they promote sparsity, which is our assumption about the underlying geology. In addition they proposed two regularizations:

Symmetry regularization
The expected shot waveform is a zero-phase Ricker wavelet, ignoring the bubble which arrives later. Therefore, in the log spectral domain it is desirable to have only even parts of the filter coefficients u_t around the zero-lag. The symmetry regularization does this by incorporating the odd parts near zero-lag into the residual:

$$0 \approx \epsilon_1 \sum_\tau w_\tau (u_\tau - u_{-\tau}), \tag{2}$$

where u_τ are the coefficients at positive lags and $u_{-\tau}$ the coefficients at negative lags. w_τ is a weighting function that decreases from one to zero with increasing lag. Conceptually, the width of the weighting function should be just large enough to contain the Ricker wavelet of the data. ϵ_1 controls the degree to which this regularization affects the objective function.

Filter length regularization
The deconvolution filter's positive lags should include both the zero-phase Ricker wavelet of the reflections, and the wavelet of the bubble with its reverberations (which are caused by the implosion of water into the cavity generated by the airgun). The filter should not have large negative lags, beyond those needed for the anti-causal part of the Ricker wavelet. Therefore a filter length lag regularization is added to the residual

$$0 \approx \epsilon_2 \sum_\tau \left(c_\tau u_\tau + a_{-\tau} u_{-\tau} \right), \tag{3}$$

where c_τ is the weighting function for the positive lags. This function starts at zero for small positive lags, until the lag deemed to be sufficient to contain the bubble. $a_{-\tau}$ is the weighting function for the negative lags. This function is zero for small negative lags, and it ramps up from zero to one within a small time lag, since we do not expect anything before zero time other than the first lobe of the Ricker.

Additional considerations

Another consequence of the source and receiver ghost signals is the presence of notch frequencies. The particular frequency value in which a notch will occur depends on the time difference between the positive and negative lobes of the Ricker, and therefore on the depths of the source and receiver, and their offset:

$$f_n = \frac{V_w}{2d\cos(\theta)}, \tag{4}$$

where V_w is the water velocity, d is the depth and θ is the reflection angle. Since the sources and receivers are usually towed at a depth of only a few meters, the notch frequency is quite high (above 100Hz), and increases with offset. In order to see it in the spectrum of the data we would usually require a time sampling of 2ms.

The purpose of deconvolution is to separate out the parts of the data that are a result of acquisition from the parts that are a result of geology. Therefore, if the notch is visible in the spectrum of the data, we expect that after a successful deconvolution the notch will have been filled in.

In this paper, we show the results of applying this deconvolution method to various offsets of a marine streamer dataset, with and without regularizations. The code used is the same as in Claerbout et al. (2012), and was written by Antoine Guitton.

DECON RESULTS

Near offset

The dataset we used is a single 2D line from a marine streamer survey in the Gulf of Baja California (Lizzaralde et al., 2002). This line consists of 2298 shots. There were 480 receivers along the cable, and the group spacing was 12.5m. The nearest offset was 180m, and the farthest was 6180m.

Figure 1 is the near-offset section of the data. A gain of t^2 has been applied. Note the Ricker-like appearance of the reflections. Note also the bubble visible 200ms below the sea-bottom reflection. Other weaker bubble reverberations are within the section. A weak direct arrival of one of the bubble reverberations appears faintly at 500ms.

We ran two types of inversions:

1. Gained input deconvolution: Inversion is applied to data which was gained by t^2, and there is no gain applied to the residual ($g_t = t^0$).
2. Gained output deconvolution: Input data was not gained, but the residual was gained at each iteration of the inversion ($g_t = t^2$).

Additionally, for each gain type, we ran the inversion with and without regularizations, by setting the values of ϵ_1 and ϵ_2 in equations (2) and (3) accordingly.

Figure 2(a) shows the gained input deconvolution run without regularizations. Note that while the deconvolution has indeed spiked the reflections on the central lobe of the Ricker wavelet, the bubble is still visible, and the precursors are strong. Figure 2(b) is the gained output deconvolution run without regularizations. While the bubble seems to have been dealt with better in this section, the precursors above the sea-bottom reflection are stronger, and the entire section appears noisier. Figure 4(a) shows the shot-waveform estimated by the gained input deconvolution, and 4(b) is the one estimated by the gained output deconvolution. In each plot, the upper trace is the same as the lower trace, except that it has been clipped in order to enhance the smaller coefficients in the display. The smaller coefficients are important, since deconvolution is a division operation. Note how much more energy is in the anti-causal part of the shot-waveform in Figure 4(b) as compared to Figure 4(a). Both of them however show the main shot-waveform as a Ricker centered at zero-lag, and a bubble with its associated reverberations. This means that the inversion has indeed arrived at what we assumed to be the correct objective: in order to sparsify the data, the Ricker wavelet and the bubble must be removed.

Figure 3(a) is the gained input deconvolution run with the symmetry and filter length regularizations. Compared to Figure 2(a), the bubble is weaker, and so are the precursors. This can be further validated by comparing the precursors of the shot waveform in Figure 4(a) vs. Figure 4(c). Figure 3(b) is the gained output deconvolution run with the regularizations. Compared to Figure 3(a), the bubble is better eliminated. There is a slight

difference in the estimated bubble in the shot-waveforms of Figures 4(c) and 4(d), and this is enough to cause the difference in bubble elimination. The precursors for the gained output deconvolution with regularization are the weakest, which is a direct result of forcing the filter length to be short.

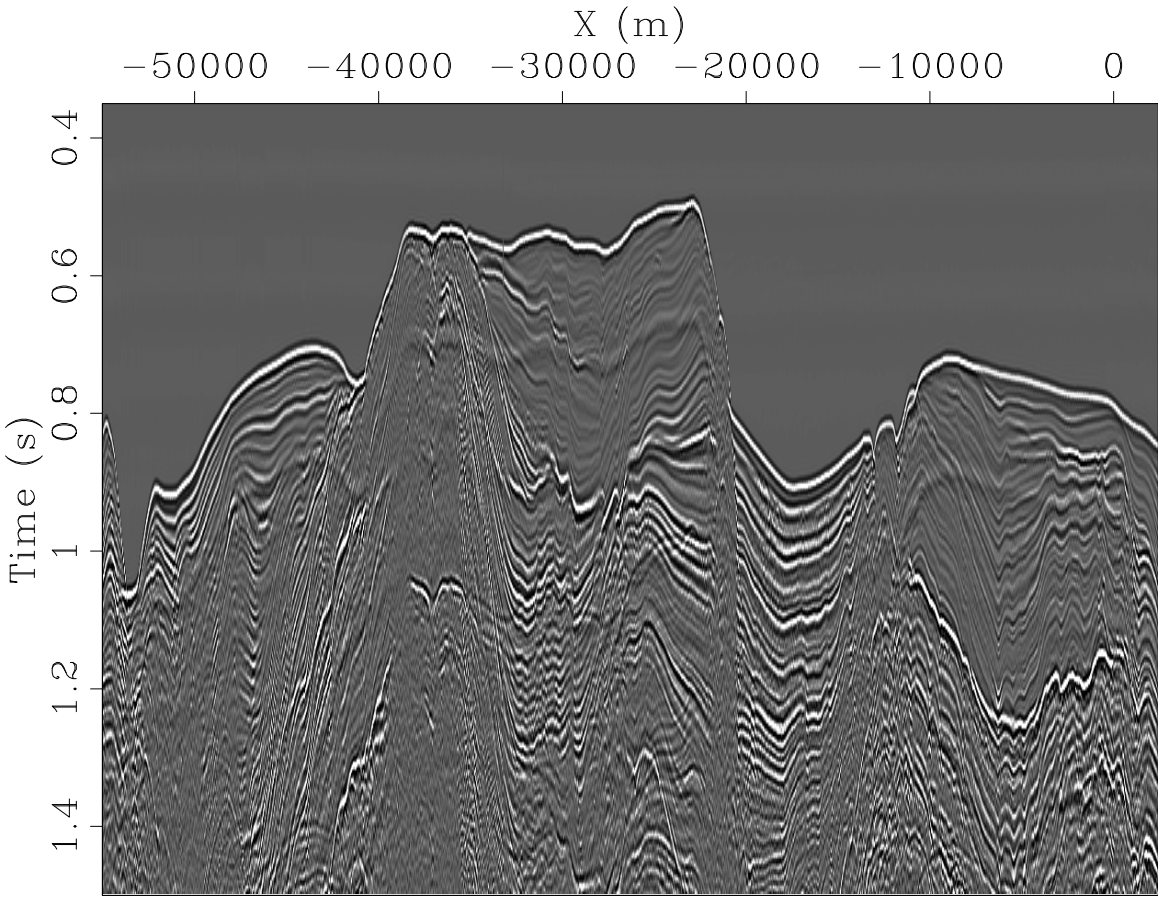

Figure 1: Gained near-offset section of Baja data. Offset is 180m. Note the Ricker-like appearance of the reflections, and the bubble around 200ms below the sea-bottom reflection. [**ER**] ohad1/. EW05s

Offset group

In this section, the purpose was to test whether utilizing more of the data will aid the inversion in acquiring the effective shot waveform, and therefore produce the sparsest result. We have seen that for the near offset section, even without regularization the estimated waveform was a Ricker wavelet. We now apply the inversion to a near-offset range, from 180m to 1180m.

Figure 5(a) is the result of applying the gained input deconvolution to the offset group without regularization, and then windowing out the near offset only for display. Compared to the same process applied to the near offset only (Figure 2(a)), the polarity of the reflections is incorrect, and the precursor is stronger. We can also see a low frequency precursors in the water. The deconvolution has spiked the Ricker on its second negative lobe.

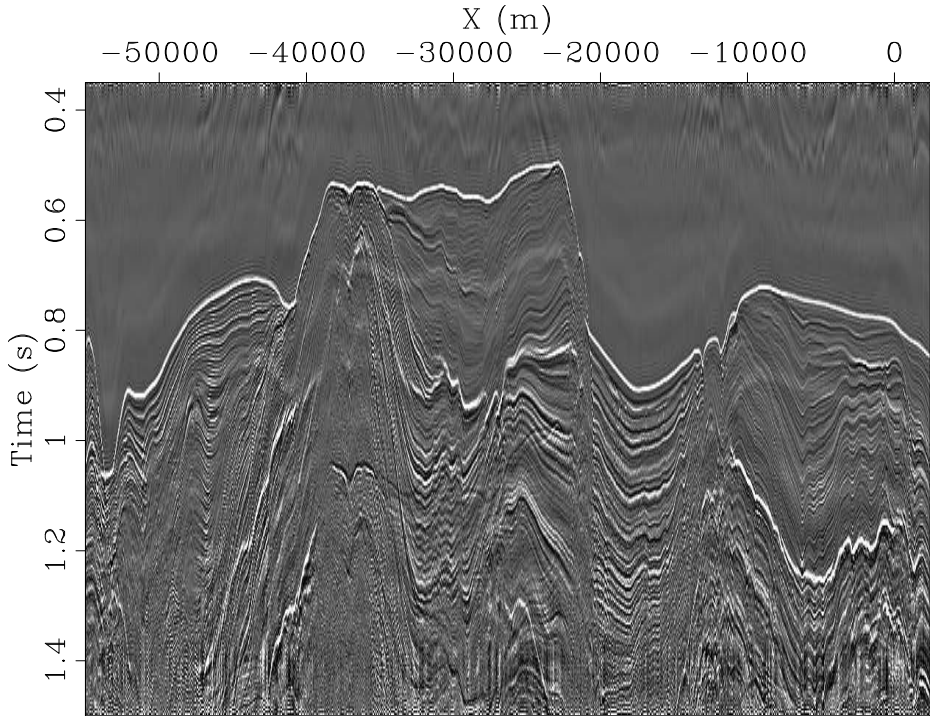

(a)

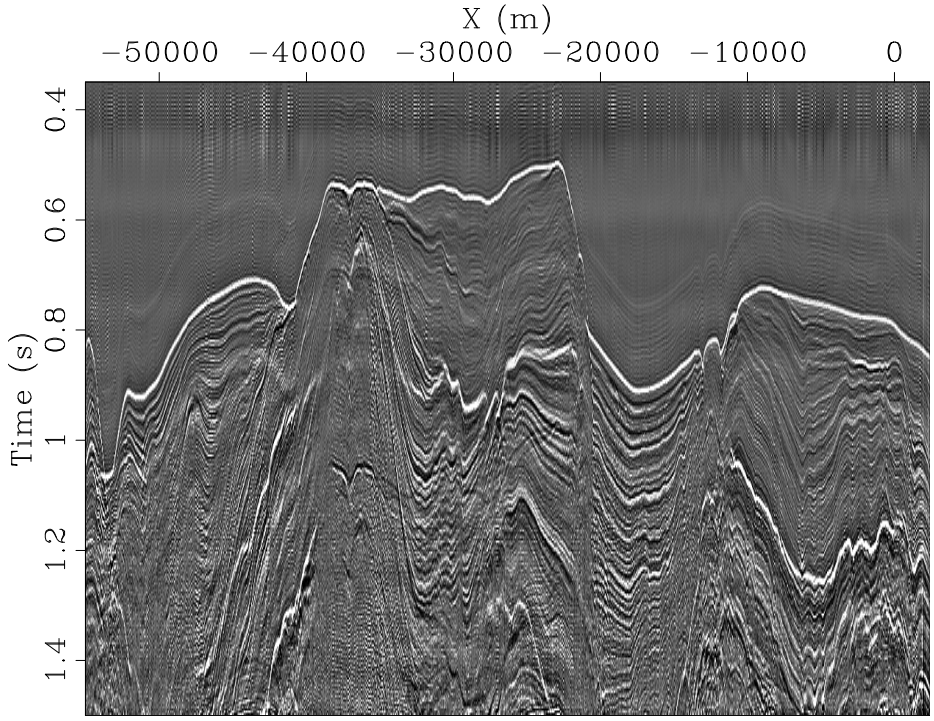

(b)

Figure 2: Deconvolution of the 180m offset only. (a) Gained input deconvolution without regularization. (b) Gained output deconvolution without regularization. Note how the Ricker wavelet has been spiked, and the strong precursors. [**ER**] ohad1/. deconEW05s-t0-6,deconEW05s-t2-6

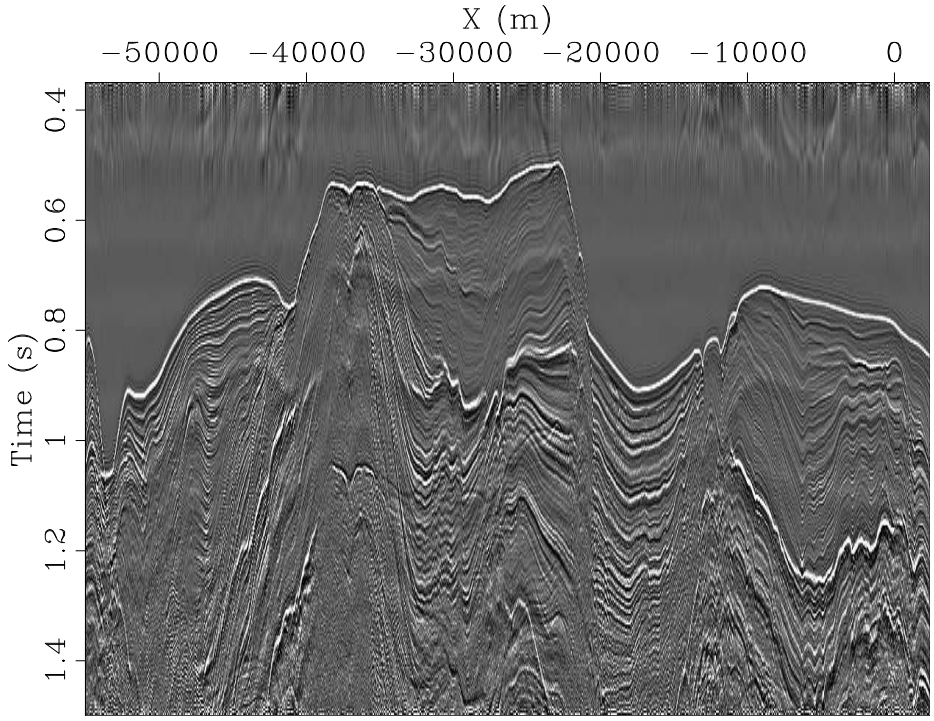

(a)

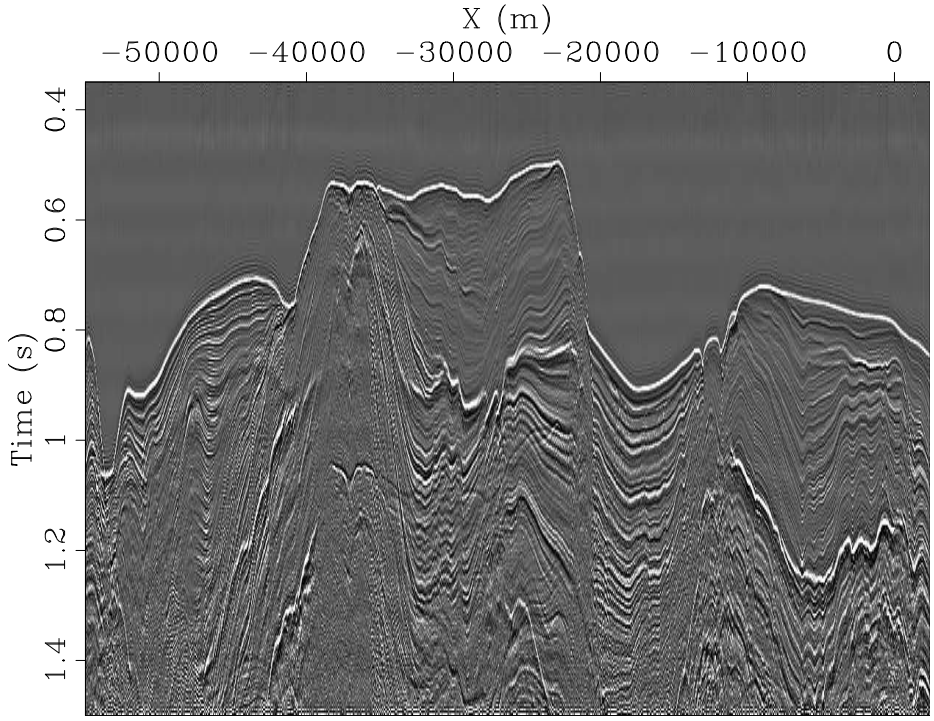

(b)

Figure 3: Deconvolution of the 180m offset only. (a) gained input deconvolution with regularization. (b) gained output deconvolution with regularization. Compared to Figures 2(a) and 2(b), the precursors are weaker and the bubble is better handled. In (b) there is less noise than in (a). [**ER**] ohad1/. deconEW05s-t0-reg-6,deconEW05s-t2-reg-6

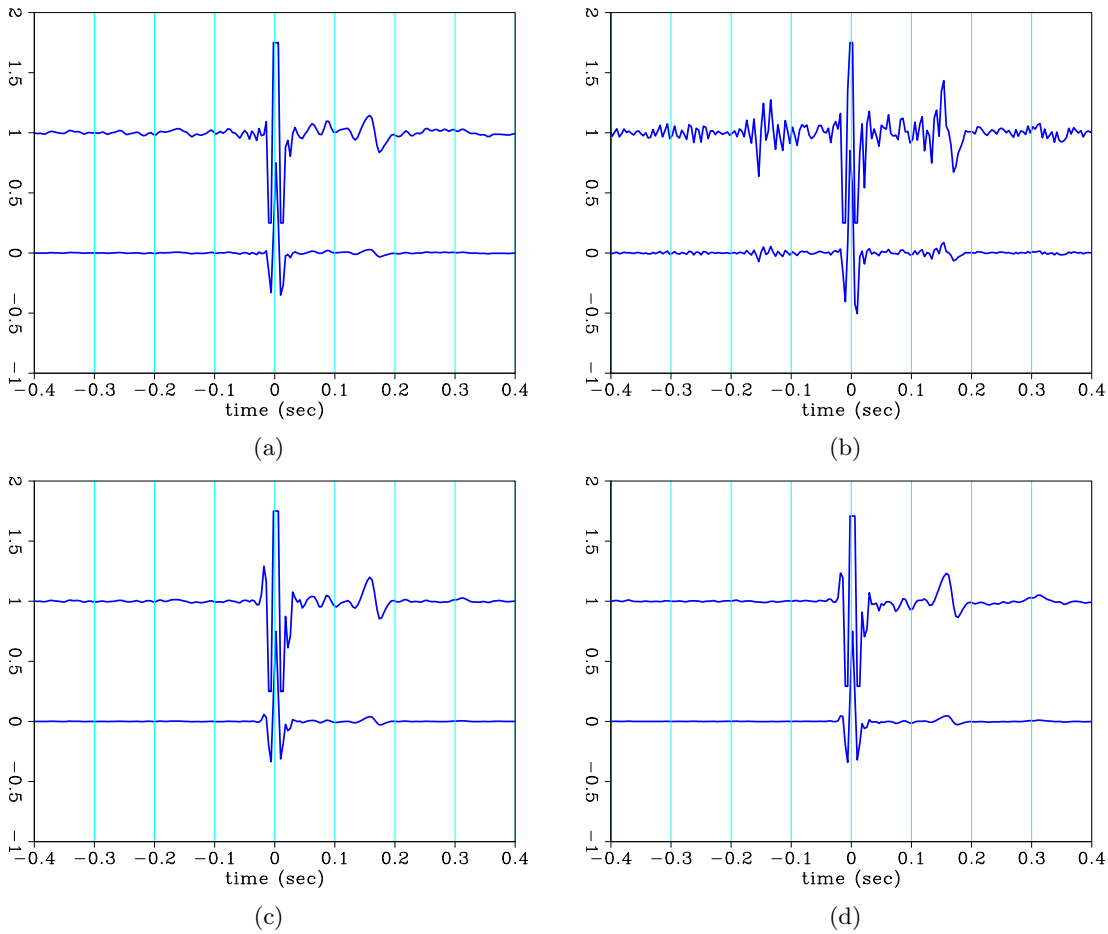

Figure 4: Estimated shot waveforms resulting from inversion using near offset data only. In each graph, the lower trace is unclipped, and the upper trace is clipped to enhance the small coefficients. (a) Gained input decon without regularization (link to figure 2). (b) Gained output decon without regularization. (a) and (b) are the shot waveforms, and their inverses are those that generated Figures 2(a) and 2(b) after deconvolution. Note how much more energy is in the anti-causal part of the shot waveform in (b) compared to (a). (c) Gained input decon with regularization. (d) Gained output decon with regularization. (c) and (d) are shot waveforms, the inverses of which generated Figures 3(a) and 3(b) after deconvolution. [**ER**] ohad1/. EW05s-t0-6,EW05s-t2-6,EW05s-t0-reg-6,EW05s-t2-reg-6

Figure 5(b) is the result of applying the gained output deconvolution to the offset group without regularization. When compared with Figure 2(b), the polarity of the reflections is again wrong, but the precursor is weaker. The low-frequency precursor is visible here too. In this case, the deconvolution has spiked the Ricker on its first negative lobe.

The respective estimated shot waveforms are shown in Figures 7(a) and 7(b). Note the shift of the negative spike about the zero-lag in these two figures. Note also the low frequency (visible in the clipped traces) in the anti-causal part of the shot waveforms. These results show that for the range of offsets chosen here, requiring the inversion to produce the sparsest output does not result in the correct shot waveform. The interpretation of these results is that the shot waveform varies over this offset range. This change is sufficient to have the inversion produce a shot waveform that *on average* creates the sparsest output when it is deconvolved with the data.

Figure 6(a) is the result of gained input deconvolution with regularizations on the offset group. Compared to Figure 5(a), we can see how the polarity of the reflections is now correct, and also that the precursor is weaker. The bubble however, has not been eliminated.

Figure 6(b) is the gained output deconvolution with regularizations. For this figure, we see spiking with the correct polarity. The precursors are much weaker than the gained input result in Figure 6(a). The bubble has been strongly attenuated, though not as well as in Figure 4(d).

Figures 7(c) and 7(d) are the estimated shot waveforms of the regularized gained input and gained output deconvolutions, respectively. The central Ricker wavelet is almost identical between them, but there are slight differences in the estimated bubble. There is just a hint of stronger anti-causal coefficients in Figure 7(c). Observing the obvious differences in the decon results, we can see why these slight differences are important.

EFFECTS OF DECON ON SPECTRUM

Synthetic test notch elimination

The frequency notch of marine data is an attribute of the acquisition system. We wish to test whether this deconvolution removes the frequency notch under "perfect" conditions. For this purpose, a synthetic wavelet was constructed of three spikes, so as to resemble a Ricker wavelet. The time difference between the lobes are such that they simulate a situation where the source and receivers were at a depth of 9m. The wavelet itself is nearly zero-phase, the spikes having the values $[-1, 2, -0.99]$.

Figure 8(a) is the wavelet, and Figure 8(b) is its amplitude spectrum. The notch is at 83Hz. The regularized deconvolution was applied to this trace. In Figure 8(c) is the estimated shot waveform, and Figure 8(d) is its spectrum. The waveform resembles the synthetic trace, but its first negative lobe is slightly smaller than the second negative lobe, and it has small anti-causal and causal coefficients. Its spectrum is similar in shape, with the notch at the correct frequency. However it does not go to zero at the zero frequency, or at the notch frequency, as in the synthetic trace spectrum.

Figure 8(e) is the deconvolution result. Though the correct lobe has been spiked, there are strong precursors. It appears that the deconvolution has constructed some low frequen-

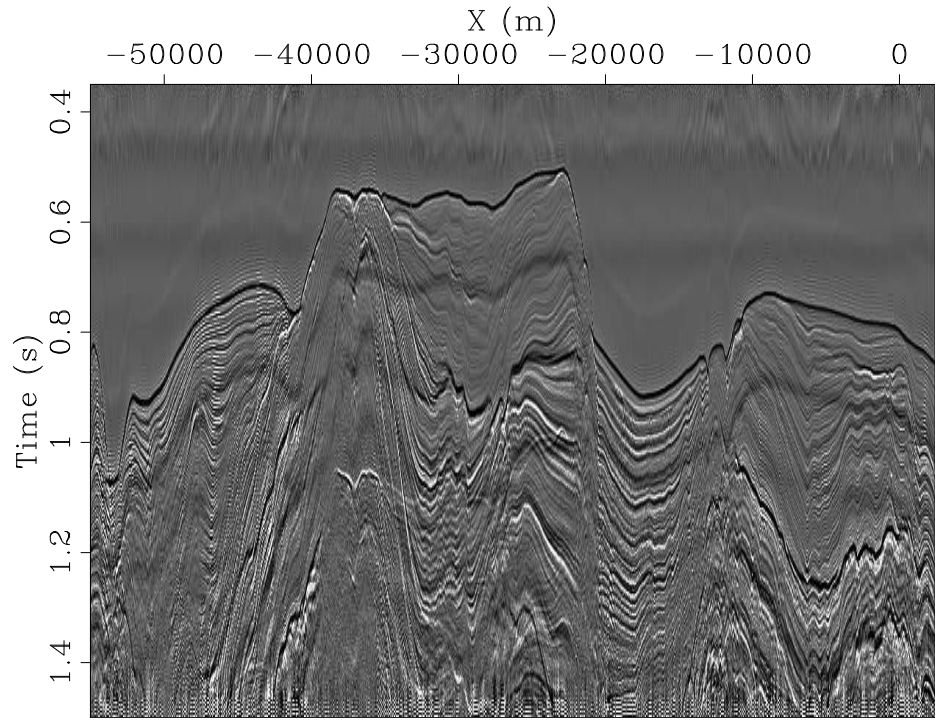

(a)

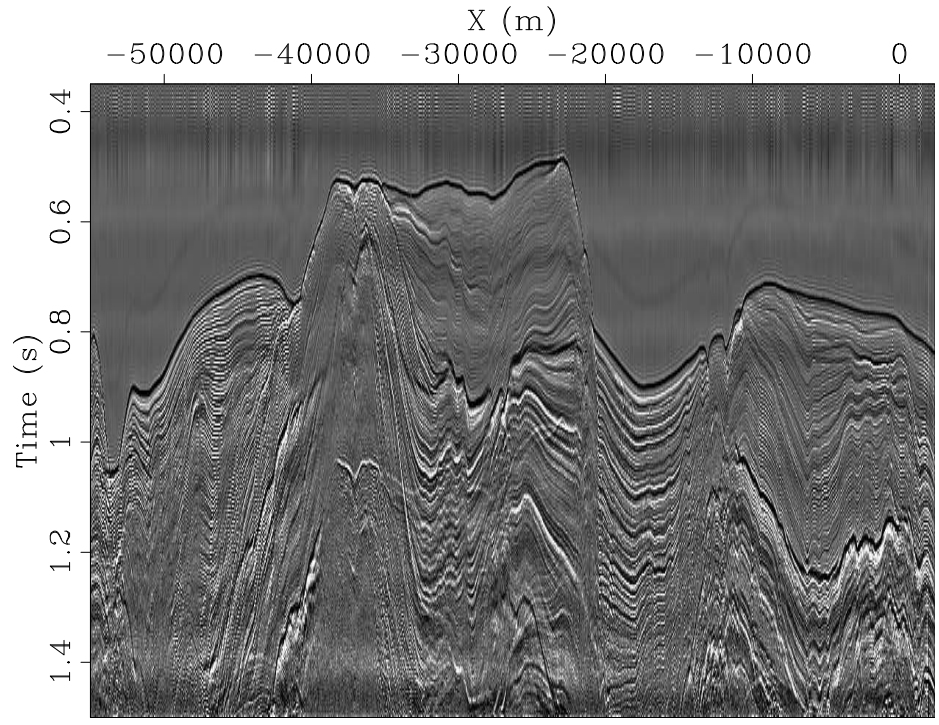

(b)

Figure 5: Deconvolution of offset group (180m - 1180m). (a) Gained input deconvolution without regularization. (b) Gained output deconvolution without regularization. The deconvolution was applied to all offsets in the range, but only the 180m offset deconvolution result is displayed. Note that the wavelet was spiked on a negative lobe. The bubble is still prominent, and there are strong low-frequency precursors in the water. [**ER**] ohad1/. deconEW05g-t0-6,deconEW05g-t2-6

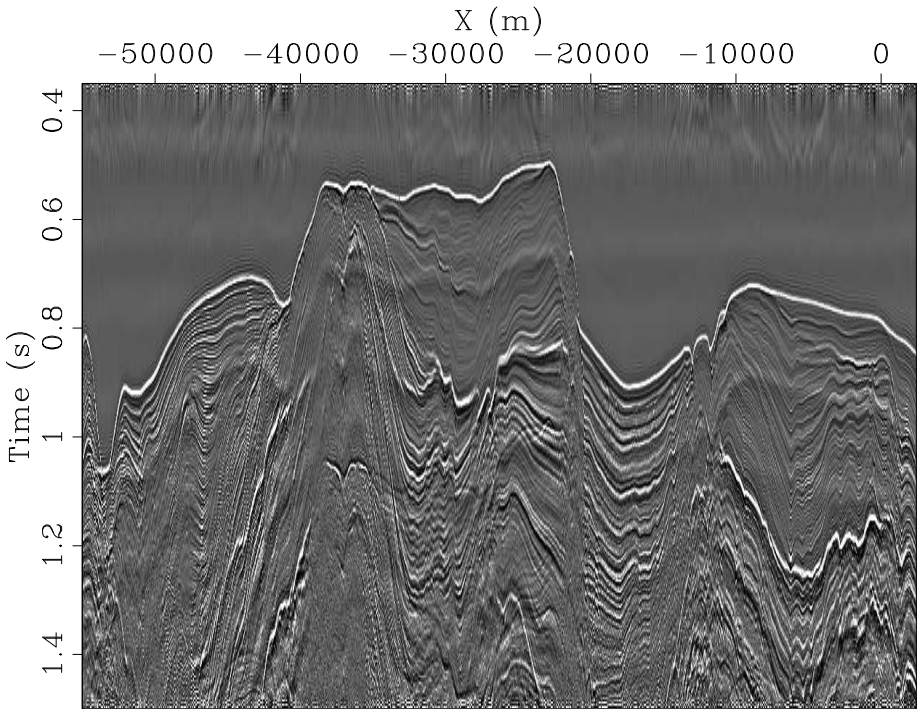

(a)

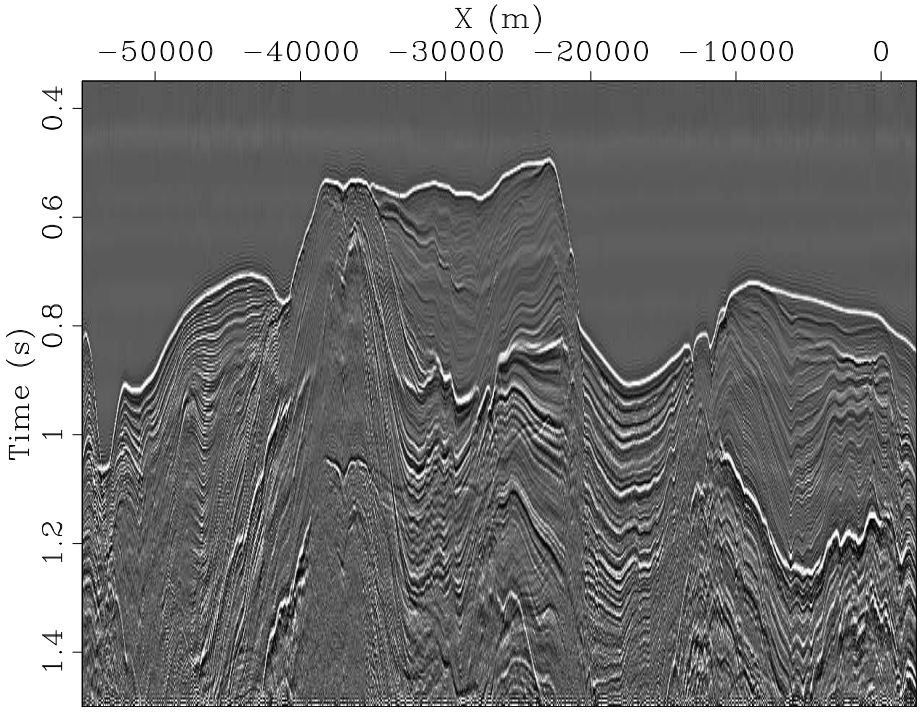

(b)

Figure 6: Deconvolution of offset group (180m - 1180m). (a) gained input deconvolution with regularization. (b) gained output deconvolution with regularization. The deconvolution was applied to all offsets in the range, but only the 180m offset deconvolution result is displayed. Note how with regularization, both have been spiked on the central positive lobe of the Ricker wavelet. The precursors have been removed. The bubble is better removed in (b). [**ER**] ohad1/. deconEW05g-t0-reg-6,deconEW05g-t2-reg-6

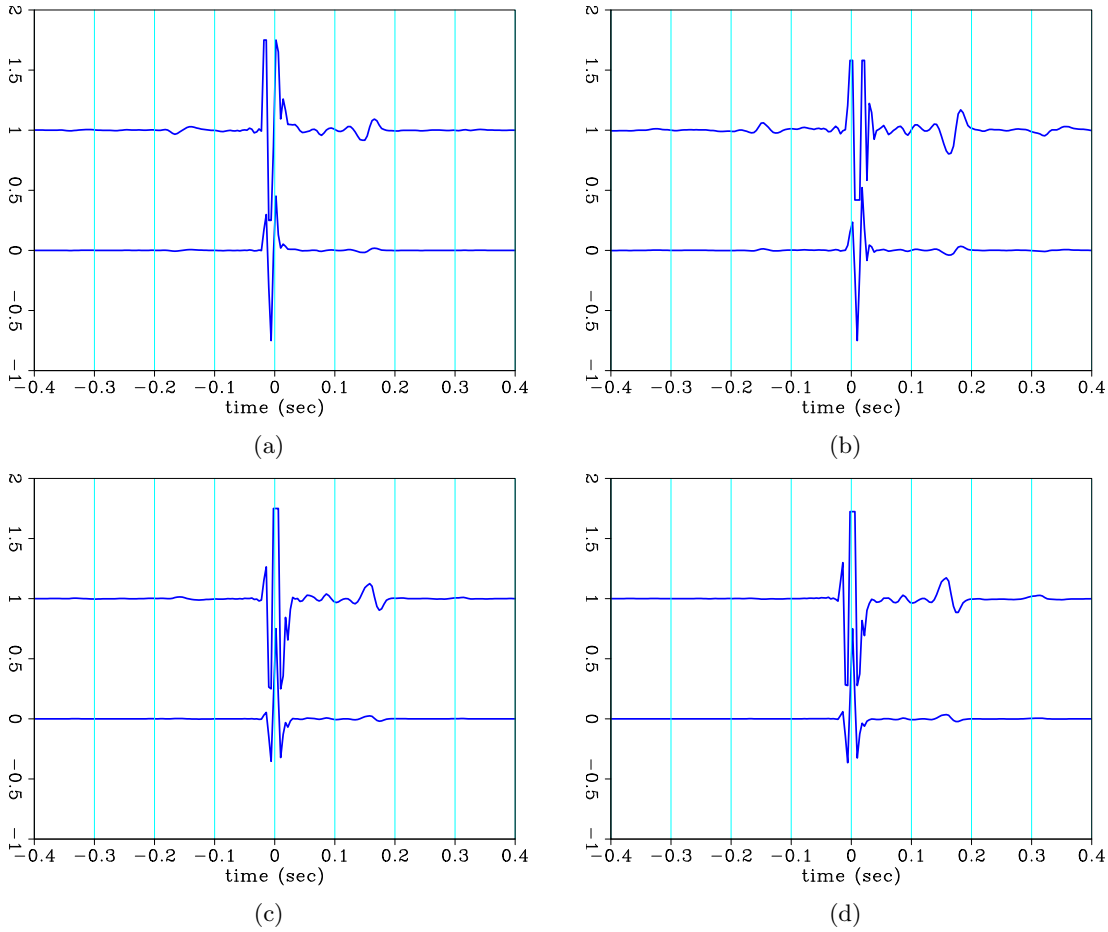

Figure 7: Estimated shot waveforms resulting from inversion using offset group. In each graph, the lower trace is unclipped, and the upper trace is clipped to enhance the small coefficients. (a) Gained input decon without regularization. (b) Gained output decon without regularization. (a) and (b) are shot waveforms, the inverses of which generated Figures 5(a) and 5(b) after deconvolution. In both cases, the main lobe has the wrong polarity. In (a) it is before zero-lag, and in (b) it is after zero-lag. (c) Gained input decon with regularization. (d) Gained output decon with regularization. (c) and (d) are shot waveforms, the inverses of which generated Figures 6(a) and 6(b) after deconvolution. Note how regularization helped to generate a more correct shot waveform, with much weaker precursors. [**ER**] ohad1/. EW05g-t0-6,EW05g-t2-6,EW05g-t0-reg-6,EW05g-t2-reg-6

cies that were absent from the data. In Figure 8(f) we can see that the notch frequency has not been filled as such, but rather that the other frequencies have been decreased so as to equalize the spectrum. The notch frequency of this waveform does not have zero energy, however.

Field data notch elimination

Before applying deconvolution, it is useful to check which frequencies are in the data, as some frequencies may have been filtered out in preprocessing, or were simply not acquired. We also need to test if the notch is apparent in the data, as we expect the deconvolution to remove it. If the source and receivers are deep enough, we will be able to see the notch with the 4ms data we usually have. For the Baja dataset, the source and receivers were at a depth of about 9m, putting the theoretical notch frequency for zero offset at 83Hz, and therefore visible at the data's sampling rate of 4ms.

Figure 9(a) is part of a single near-offset trace, which contains the direct arrival and some of the bubble reverberations. There is no "geology" in the part of the recording, only the effective source signature. Figure 9(b) is the log of the frequency spectrum of this time series. We can see that the very low frequencies have either not been acquired or have been filtered. The bubble harmonics are apparent starting from 6.5Hz at intervals of about 6-7Hz. The source notch is apparent around 113Hz.

Figure 10(a) is the same near-offset trace with the addition of some reflection data. Figure 10(b) is the log spectrum of the entire trace. The notch now appears at around 103Hz. This notch is the result of the combined source and receiver ghosts, which have time delays pertaining to the receivers' and sources' depths in the water, and their offsets. Figures 11(a) and 11(b) are a single shot gather and its log spectrum. The notch starts from around 90Hz in the near offset, and increases in frequency with increasing offset, as illustrated by equation 4.

Figure 12(a) shows the log spectrum of the near-offset section shown in Figure 1. Especially apparent is how the frequency notch moves about the spectrum, from 90Hz to 110Hz. We interpret this as the result of the changing depths of the airgun and the receivers, as they are towed behind the acquisition vessel in the sea. Figure 12(b) is the log spectrum of the regularized gained input deconvolution result, and Figure 12(c) is that of the gained output deconvolution result.

These figures show some additional considerations which are useful for understanding the data, and can aid in evaluating the deconvolution results. In this case, we know that the inversion cannot work perfectly, since the lowest frequencies are not present. We also know that the notch is not at a constant frequency, and therefore the shot waveform is necessarily not constant along the entire near-offset section. We can also see that the deconvolution with the current regularizations is only mildly successful in removing the acquisition frequency notch.

DISCUSSION AND CONCLUSION

The inversion optimizes for sparsity, since we assume that geology is sparse, but that requirement alone is not enough. We assume that in a particular marine survey, a single

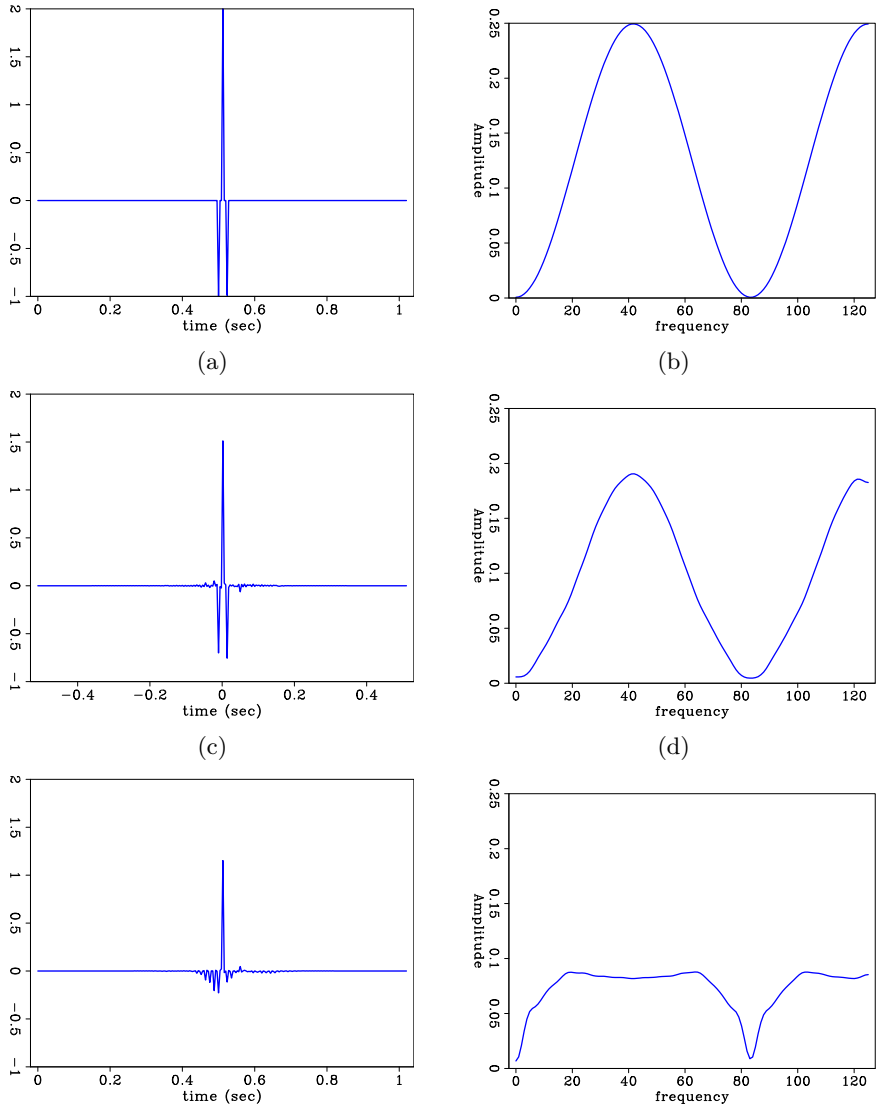

Figure 8: (a) Input trace. (b) Spectrum of input trace. Note the notch at zero and 83Hz (c) Estimated shot waveform from deconvolution. (d) Spectrum of estimated shot waveform. Note how the notch frequencies have some energy. (e) Deconvolved trace. The deconvolution has added some low frequency noise. (f) Spectrum of deconvolved trace. [**ER**]

ohad1/. synth-trace,spec-synth-trace,synth-t0,spec-synth-t0,deconsynth-t0,spec-deconsynth-t0

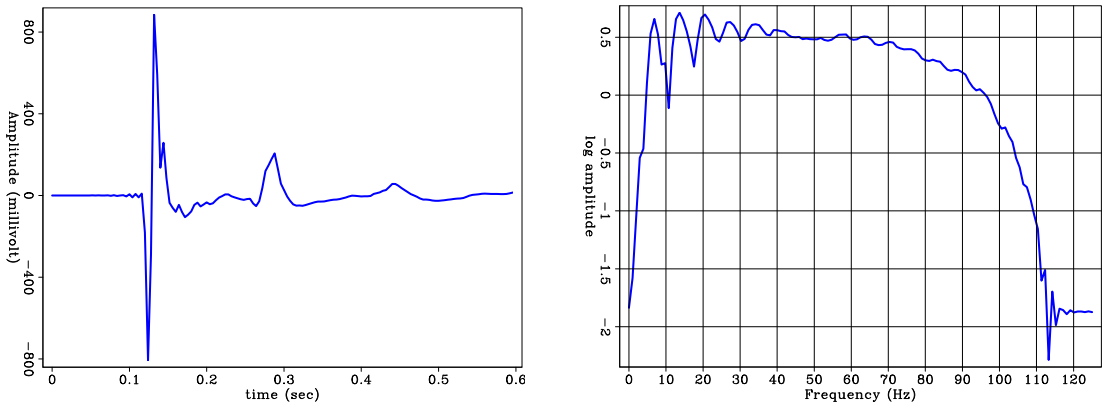

(a) (b)

Figure 9: One near offset trace. (a) Direct arrival and bubble. (b) Log of spectrum of direct arrival and bubble. [**ER**] ohad1/. EW05-bubble,EW05-bubblespec

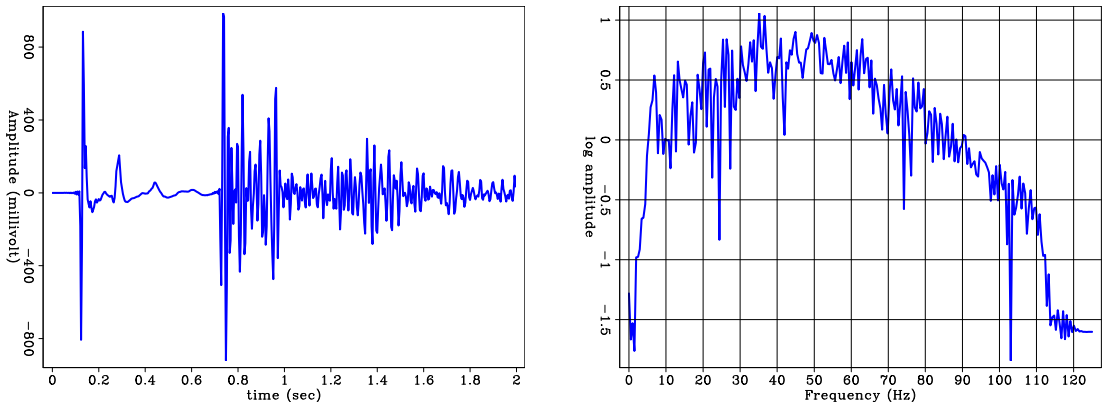

(a) (b)

Figure 10: One near offset trace. (a) Direct arrival, bubble and reflections. (b) Log of spectrum of direct arrival, bubble and reflections. [**ER**] ohad1/. EW05-notch,EW05-notchspec

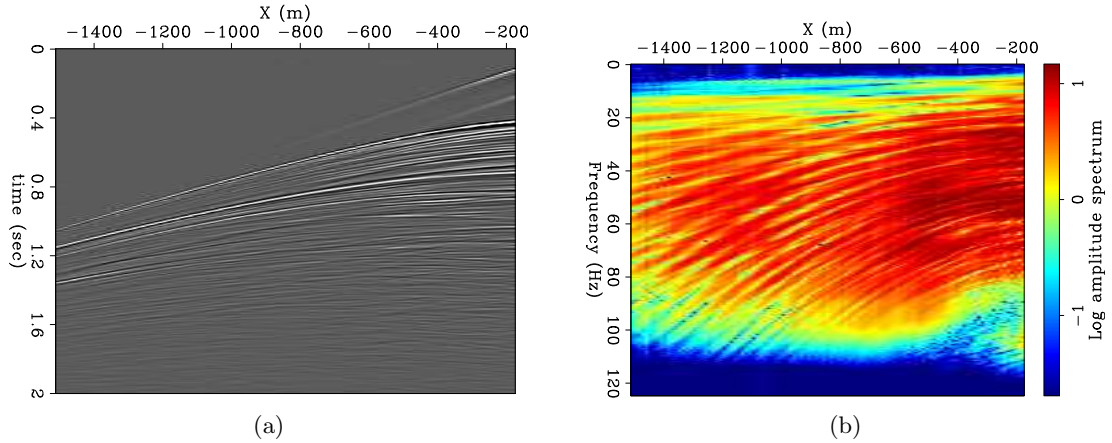

Figure 11: (a) Shot gather for shot at x=-62850 (b) Log of spectrum of shot gather, showing the notch frequency at around 90Hz at near offsets. [**ER**] ohad1/. EW05-shot992,EW05-ft

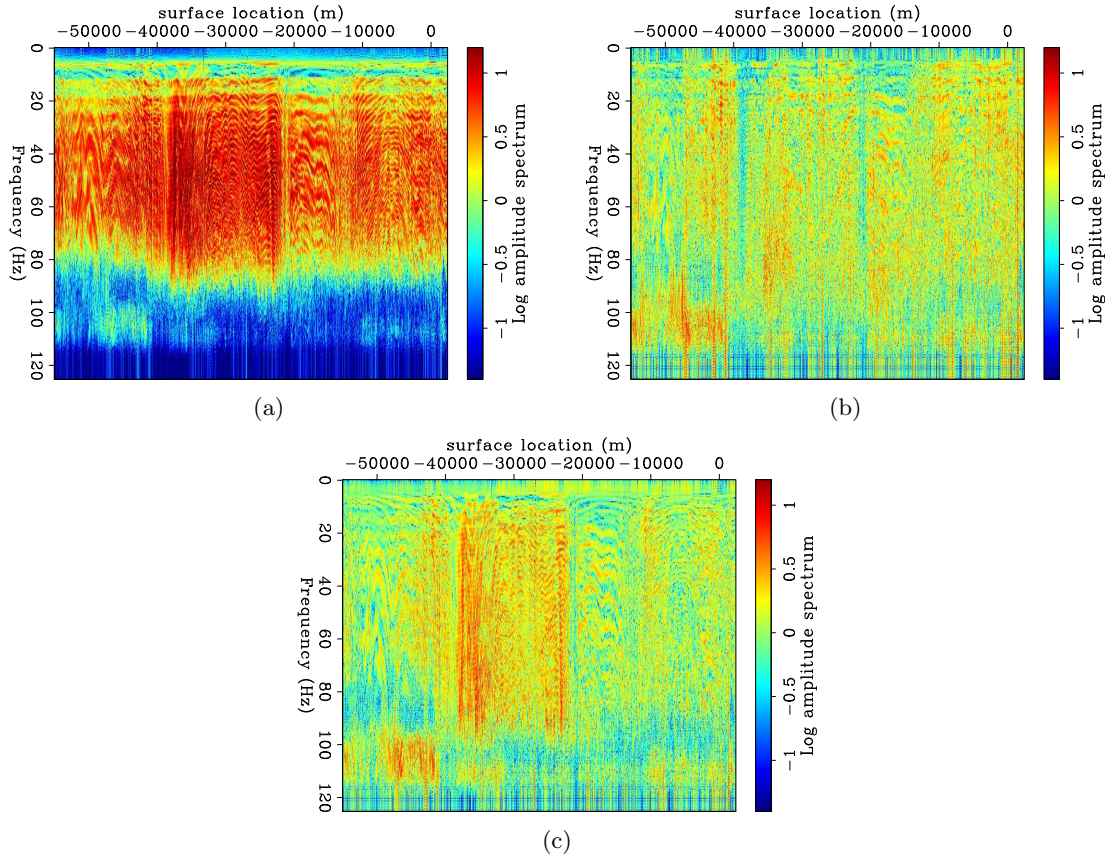

Figure 12: (a) Log spectra of near offset section. (b) Log spectra of gained input decon. (c) Log spectra of gained output decon. Note the notch in (a) and how it changes frequency with surface location, which is a result of perturbations in the source and receiver depths as they are towed behind the vessel. The notch is better filled in (b), but it appears to be filled by some noise generated by the deconvolution itself, just as in Figure 8(e). [**ER**] ohad1/. spec-EW05s,spec-EW05s-t0-reg-6,spec-EW05s-t2-reg-6

effective shot waveform was used to record all data, and therefore a single filter should be sufficient to deconvolve the entire dataset. The question is how much does that assumption stand up to reality. When considering increasing offsets the recorded waveform may change, and the data is likely to contain not just specular reflections but refractions as well. If there is a significant difference between effective shot waveforms within a survey, the inversion may estimate a shot waveform that produces the best average result for the input data it was given. However, this result may not be very useful for any particular trace in the data. This indicates that we should estimate the shot-waveform only from near-offset data.

The symmetry and filter length regularizations enable us to shape the desired shot waveform to our expectation: a Ricker wavelet, with some bubble reverberations trailing after it. These regularizations help in arriving at a useful result even when the shot waveform varies, such as when we use many offsets. They are easy to implement in the lag-log domain.

Instead of applying the deconvolution to a constant offset or to a multiple offset section, within which the shot waveform can change as a result of different angles of incidence, it may be preferable to apply it to data sorted by angles of incidence. For specular reflections of the same incidence angle, we can assume that the waveform is constant. Therefore, one possibility is to transform the data to the $\tau - p$ domain, and run the deconvolution on constant ray-parameter slices.

The source and receiver depths can change over the acquisition line, and therefore the effective shot waveform and its associated frequency notch may change at each shot. One way of evaluating the success of the deconvolution is in testing how it deals with the frequency notch. We would like to see the notch removed from the data, but we do not want the inversion to fill it with noise. A further avenue of research is to add the notch elimination as a parameter into the inversion.

It is important to check whether the low frequencies were filtered out in preprocessing. This will affect the result since the inversion may compensate by generating low frequencies that have nothing to do with the geology. Also, the filtering may affect the source wavelet, meaning that the Ricker we see is as much a result of preprocessing as it is of the acquisition.

Another conclusion is that success of this deconvolution method is on a dataset by dataset basis. How it functions depends on the data characteristics, and the variability of the shot waveform over traces. Considering the regularization parameters, we cannot conclude from one dataset what set of parameters will work on another.

REFERENCES

Claerbout, J., Q. Fu, and Y. Shen, 2011, A log spectral approach to bidirectional deconvolution: SEP-Report, **143**, 297–300.

Claerbout, J., A. Guitton, and Q. Fu, 2012, Decon in the log domain with variable gain: SEP-Report, **147**, 313–322.

Lizzaralde, D., G. Axen, G. Kent, J. Fletcher, A. Gonzalez, A. Harding, S. Holbrook, and P. Umhoefer, 2002, PESCADOR seismic experiment. funding agency: NSF. data set accessed 20 July 2012 at http://www.ig.utexas.edu/sdc/.

Zhang, Y., J. Claerbout, and A. Guitton, 2011, A new bi-directional sparse/spike deconvolution method that overcomes the minimum phase assumption: 73th EAGE Conference and Exhibition Extended Abstract, F001.

Six tests of sparse log decon

Antoine Guitton and Jon Claerbout

ABSTRACT

Previously, we developed a sparseness-goaled decon method. Here we test it on six data sets. None showed the unfortunate phase-shift we always see with minimum-phase decon. None showed the polarity reversals or time shifts that perplexed our earlier work. Results on all six data sets enhance polarity visibility. We had expected to see sparseness decon limit the bandwidth in some natural way unlike prediction-error decon with its white output. Instead, in all the cases our sparseness decon boosted frequencies much the way predictive decon does. We had not expected to see an estimated shot waveform containing a lot of low-frequency sea surface waves. One such result provoked a new theoretical development not yet tested (Claerbout and Guitton, 2012).

INTRODUCTION

We have tested our basic sparse deconvolution method on six data sets. Results are generally positive, but not totally as expected. We are pleased to report none of the results here showed the kind of phase-shift issues we always see with minimum-phase decon. For the most part, the decons enhance the appearance of polarity. One of the data sets (DATA4) had a clearly defective gun array with an extremely non-minimum phase wavelet and our deconvolution worked wonders on it (see Figure 5).

One problem persisted until about six months ago: we could not be sure which of the three lobes of the Ricker wavelet would be enhanced. Then a new regularization, proposed theoretically, ensured spiking on the central Ricker lobe, meaning we shall no longer see apparent polarity reversals or time shifts.

We had expected to see that sparseness would limit the bandwidth in some natural way. Instead, in all the cases the sparseness decon boosted frequencies much the same way predictive decon does. Worse yet, one of the shot waveforms contained a lot of low-frequency sea surface waves. Serendipitously this bad result provoked Jon Claerbout to introduce theory augmentations (Claerbout and Guitton, 2012) that have not yet been coded or tested.

REGULARIZATIONS

Because predictive decon fails on the Ricker wavelet, Zhang and Claerbout (2010) devised an extension to non-minimum phase wavelets. Then Claerbout et al. (2011) replaced the traditional unknown filter coefficients by lag coefficients u_t in the log spectrum of the de-

convolution filter. Given data $D(\omega)$, the deconvolved output is

$$r_t \;=\; \mathrm{FT}^{-1}\;\left[D(\omega)\;\exp\left(\sum_t u_t Z^t\right)\right] \tag{1}$$

where $Z = e^{i\omega}$. The log variables u_t transform the linear least squares (ℓ_2) problem to a non-linear one that requires iteration. The gained residual $q_t = g_t r_t$ is "sparsified" by minimizing $\sum_t H(q_t)$ where

$$q_t \;=\; g_t\; r_t \tag{2}$$

$$H(q_t) \;=\; \sqrt{q_t^2+1}-1 \tag{3}$$

$$\frac{dH}{dq} \;=\; H'(q) \;=\; \frac{q}{\sqrt{q^2+1}} \;=\; \mathrm{softclip}(q) \tag{4}$$

Traditional decon approaches are equivalent to choosing a white spectral output. Here we opt for a sparse output.

Earlier frustrations led to various regularizations. We minimize the following functional:

$$J(\mathbf{u}) = |\mathbf{q}|_{hyp} + \frac{\epsilon_1}{2}\|\mathbf{W}_1\mathbf{u}\|_2 + \frac{\epsilon_2}{2}\|\mathbf{W}_2\mathbf{J}\mathbf{u}\|_2 \tag{5}$$

where bold faces are for either vectors or matrices. The first regularization term tends to limit the range of filter lags (Figure 1). The second term, introduced by Claerbout et al. (2012) encourages symmetry ($u_{-\tau} = u_\tau$) around the central Ricker lobe. It does this by a matrix $\mathbf{J}$ that senses asymmetry $u_\tau - u_{-\tau}$ at small lags τ and suppressing it.

The gradient search direction becomes

$$\Delta\mathbf{u} = \sum_t (r_{t+\tau})\,\big(g_t H'(q_t)\big) + \epsilon_1\mathbf{W}_\mathbf{1}'\mathbf{r}_{u1} + \epsilon_2\mathbf{J}'\mathbf{W}\mathbf{r}_{u2} \tag{6}$$

It happened in all the examples in this paper (except the one with a defective airgun array) the ϵ_2 "Ricker regularization" was not needed because no polarity reversals or apparent time shifts were noted so $\epsilon_2 = 0$ in all cases. The value of ϵ_1 was selected by trial and error.

Data plots

Data panels have gained raw data on the left and the results of sparseness decon on the right. Observe how they almost invariably show the sparseness panel preserving signal polarity.

Sparse decon is applied on six different data sets referred as DATA4, DATA5, DATA6, DATA8, DATA11 and DATA12.

DATA4 was dug out from our SEP data server (Δt=2 ms). Its origins are unknown.

DATA5 is a common-offset section from the Gulf of Mexico (Δt=4 ms). It was Yang's "discovery" data set, in many ways still the most interesting data set, but with some problems noted.

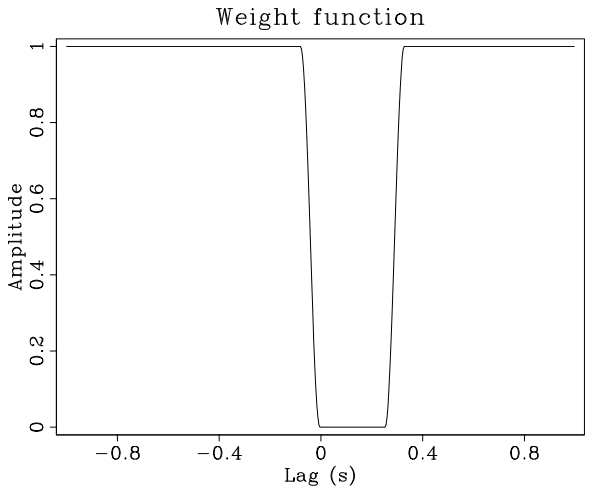

Figure 1: Weighting function used in the regularization to force long lags to be zero. The positive lags allow more non-zero coefficients to include the bubble. These limits apply in the lag-log space of u_τ and so apply only approximately to the shot waveform and the decon filter. [**ER**] antoine3/. Weight

DATA6 is a common-channel section from a 2-D line shot in Baja California (Lizzaralde et al., 2002) during the PESCADOR experiment (Δt=4 ms). It was downloaded from the academic seismic portal at the University of Texas, Austin (http://www.ig.utexas.edu/sdc/)

DATA8, 11 and 12 are unprocessed, raw common-channel sections coming from 2-D lines shot offshore Washington state as part of the COAST project (Δt=2 ms).

Spectral plots

The spectrum calculation in all the cases (except for DATA4) is based on gaining the output by t^{tpow}. The value of *tpow* was chosen to balance amplitudes throughout the section. With the sparse decon, that gain is done after filtering. We have since decided a more appropriate gain function is $t^2/t_0(x)$ where $t_0(x)$ is water depth, but our software to do it requires completion and more testing.

Unexpectedly, we found that sparse decon yields nearly white output for all six datasets. Its whiteness is comparable to that of the Burg decon. We had hoped it would drop off naturally at high and low frequencies as those frequencies should contribute little to sparseness. This observation was another prod to Jon Claerbout to revise the current sparseness theory to an augmented theory found elsewhere in this report. This augmented theory provides those "bad frequencies" another place to go besides the decon output.

Shot waveforms

The shot waveforms turned out to be Ricker like in all cases except DATA4 which clearly has misfiring guns.

ACKNOWLEDGMENTS

We thank workers here at SEP that worked earlier in this area. Yang Zhang's classic result charged up our initial enthusiasm. Yi Shen and Qiang Fu coded up the logarithmic

parametrization and found it generally superior to the earlier product parametrization. Qiang Fu's last work (unpublished) eventually led Jon to the long needed "Ricker regularization".

We thank Bob Clapp for extracting for us 2-D constant-line data sets from a 3-D data set here at SEP. Unfortunately that data turned out to be uninteresting.

We gratefully acknowledge Steve Holbrook for sending us DATA8, 11 and 12. We feel more confidence than usual that his data was unprocessed before we received it. We also gratefully thank Stew Levin for importing Holbrook's SEG-D data into the SEP system. We thank him also for reading and struggling to convert other data offered freely on the internet but which contained many glitches and ultimately turned out to be too noisy to be of interest.

REFERENCES

Claerbout, J., Q. Fu, and Y. Shen, 2011, A log spectral approach to bidirectional deconvolution: SEP-Report, **143**, 297–300.

Claerbout, J. and A. Guitton, 2012, Modeling data error during deconvolution: SEP-Report, **148**, 9–12.

Claerbout, J., A. Guitton, and Q. Fu, 2012, Decon in the log domain with variable gain: SEP-Report, **147**, 313–322.

Lizzaralde, D., G. Axen, G. Kent, J. Fletcher, A. Gonzalez, A. Harding, S. Holbrook, and P. Umhoefer, 2002, PESCADOR seismic experiment. funding agency: NSF. data set accessed 20 july 2012 at http://www.ig.utexas.edu/sdc/.

Zhang, Y. and J. Claerbout, 2010, A new bidirectional deconvolution method that overcomes the minimum phase assumption: SEP-Report, **142**, 93–104.

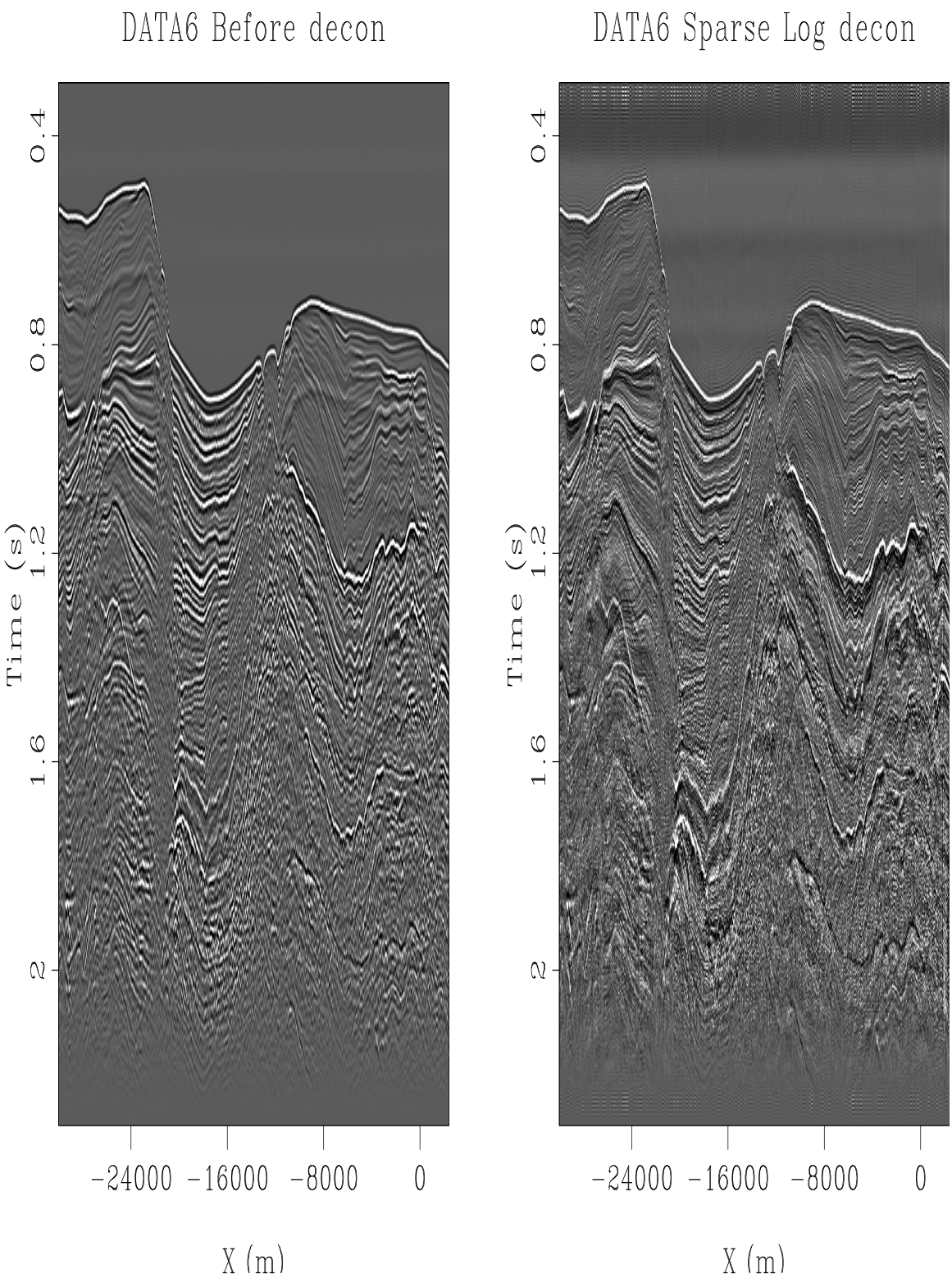

Figure 2: Data set from Baja California. The decon is bringing up some low frequencies after strong events in the water, but not after the water bottom. We observed that the Burg predictive decon does the same (not shown here). We feel this is wrong, most likely a result of this data having an unknown preprocessing history, likely a low-cut filtering of the sea swell. [**ER**] antoine3/. DeconShort-DATA6

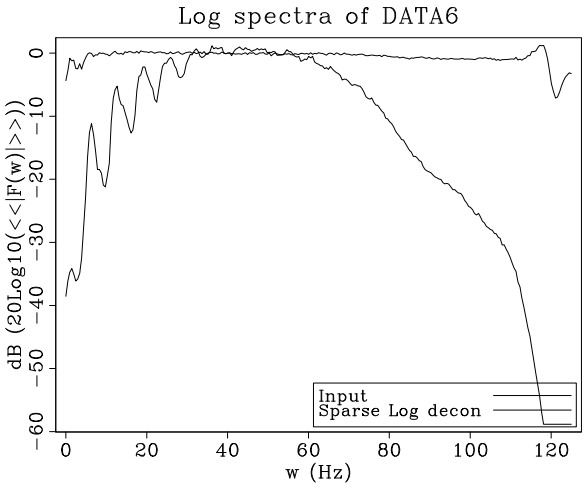

Figure 3: The data spectrum shows we have 4ms sampling. Sparse decon is almost as white as an industry PEF. [**ER**] antoine3/. DeconLogFourierShort-DATA6

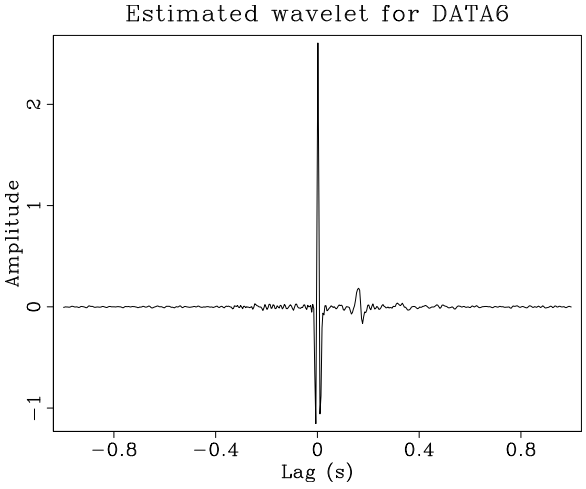

Figure 4: A shot waveform beautifully consistent with our preconceived ideas about causality, Ricker wavelets, and bubbles. [**ER**] antoine3/. Wavelet-DATA6

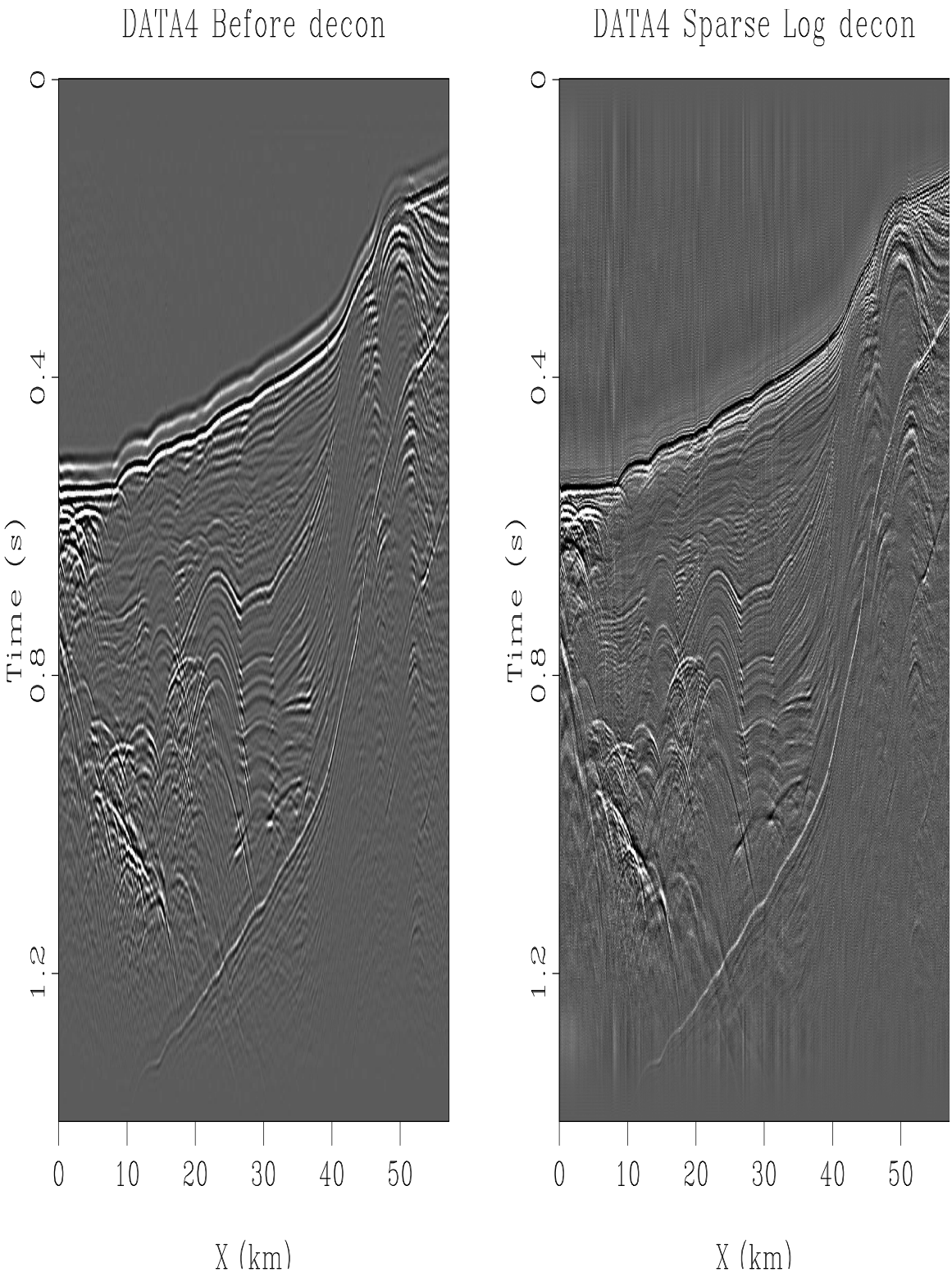

Figure 5: This data was very badly recorded (precursor to main pop) and would have been tossed out except that it very nicely demonstrates sparse decon's ability to handle a drastically non-minimum phase source. [**ER**] antoine3/. DeconShort-DATA4

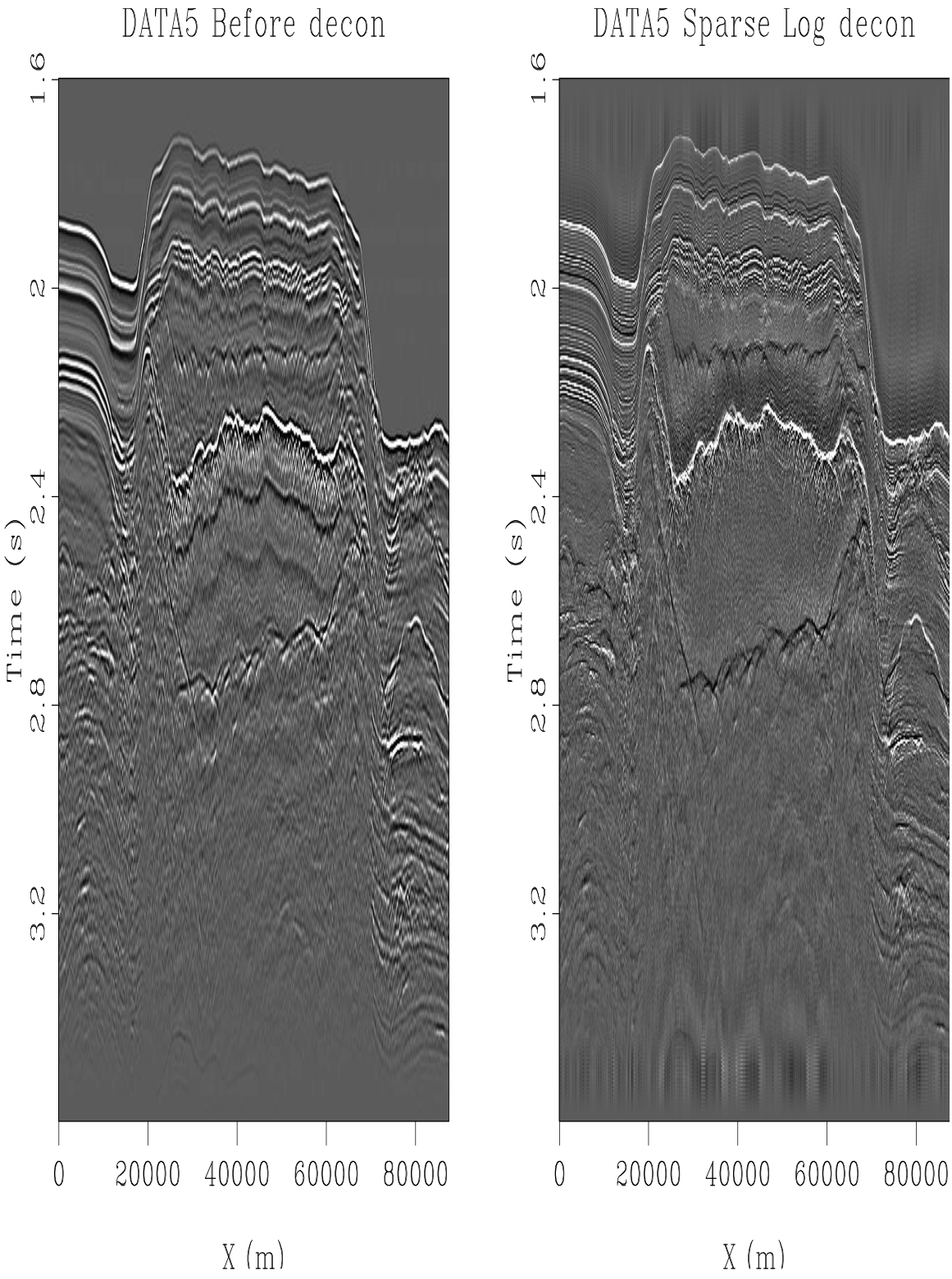

Figure 6: Yang's discovery data set from the Gulf of Mexico. We love this one because it shows so clearly the opposite wave polarity (black) on the bottom of the salt (2.7 sec). It also shows another delightful soft layer (black), a rugose layer above the top of salt (2.1 sec). [**ER**] antoine3/. DeconShort-DATA5

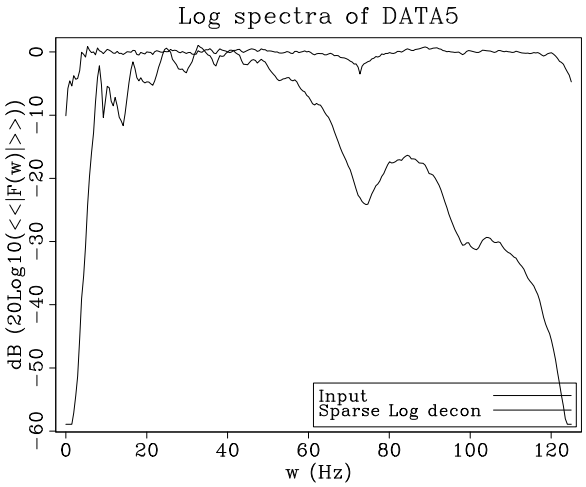

Figure 7: The data spectrum shows we have 4ms sampling. Sparse decon output is almost as white as an industry PEF decon (not shown). Again it's annoying that the sparse decon so strongly boosts very high and very low frequencies. [**ER**] antoine3/. DeconLogFourierShort-DATA5

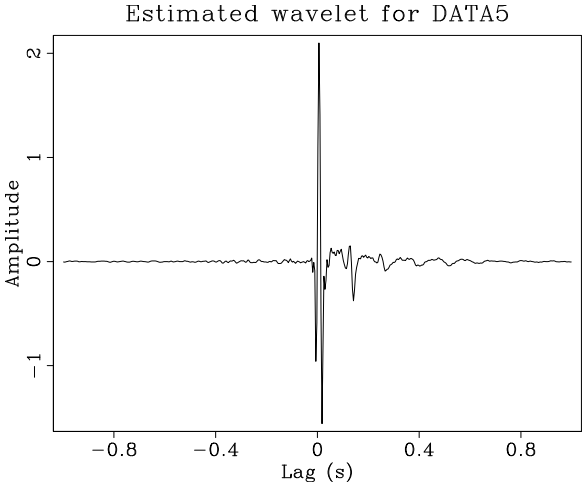

Figure 8: A shot waveform with good causality and bubble, but would be improved if we were to use some of the "Rickerness" regularization. [**ER**] antoine3/. Wavelet-DATA5

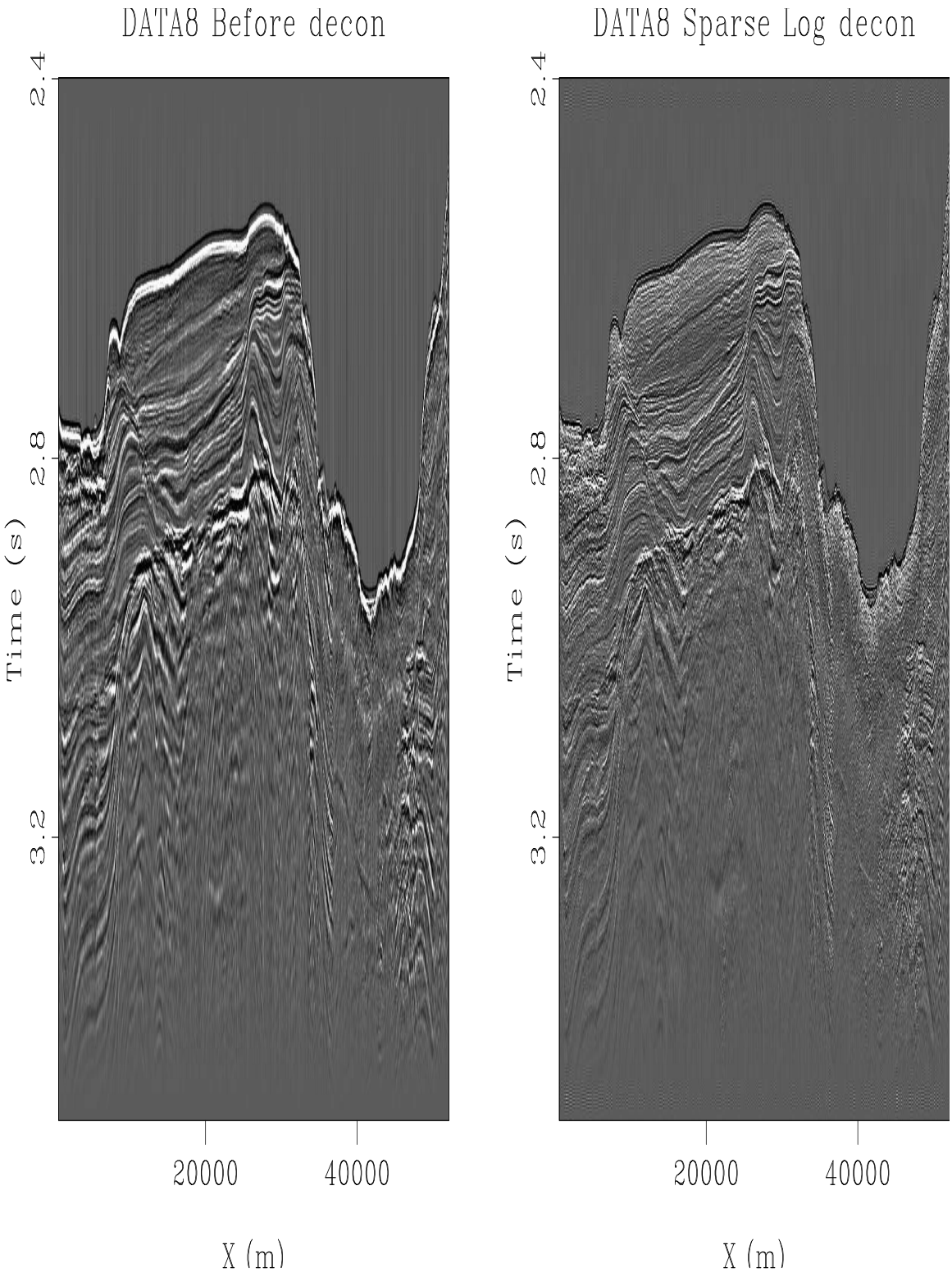

Figure 9: The data set from offshore Washington. This data set misbehaves. The water bottom does not look as Ricker-like as we usually see and the sparseness decon happens to have spiked the first lobe instead of the middle lobe. So this is a case for which we might like to introduce some "Ricker regularization". [**ER**] antoine3/. DeconShort-DATA8

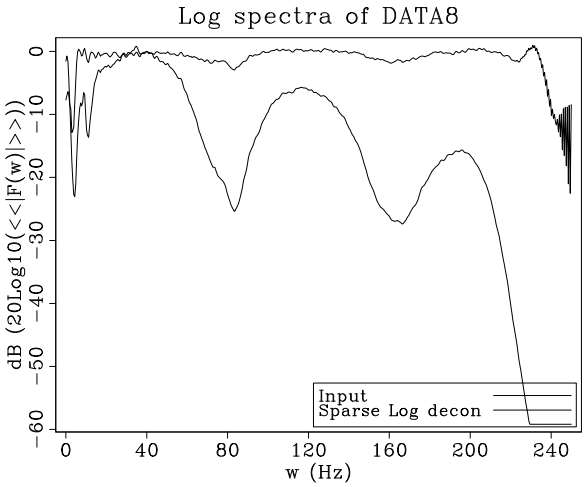

Figure 10: The spectrum shows sparse decon pulling up frequencies all the way to 240Hz. This is very suspicious! Essentially, the same result (not shown) was seen with DATA11 and DATA12. This result is unexpected to us. We suspect it means we will find such a result with almost any 2ms data set. [**ER**]

antoine3/. DeconLogFourierShort-DATA8

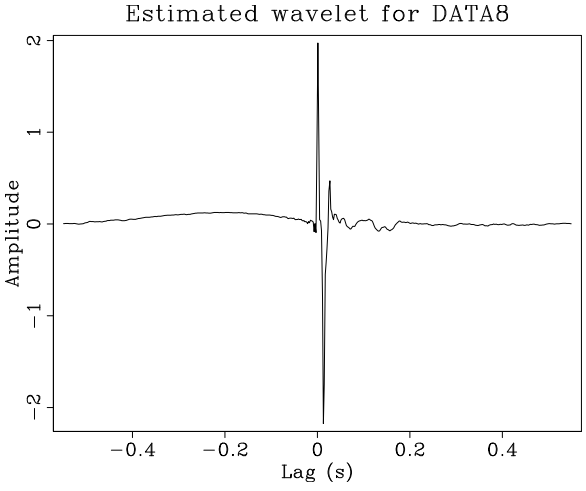

Figure 11: This shot waveform is obviously wrong. Understanding why was a great boon to Jon Claerbout who has an augmented theory paper in this report. The shot waveform here appears to have a low frequency that has soaked up a lot of the ocean surface-wave frequency, a fraction of a Hertz. [**ER**]

antoine3/. Wavelet-DATA8

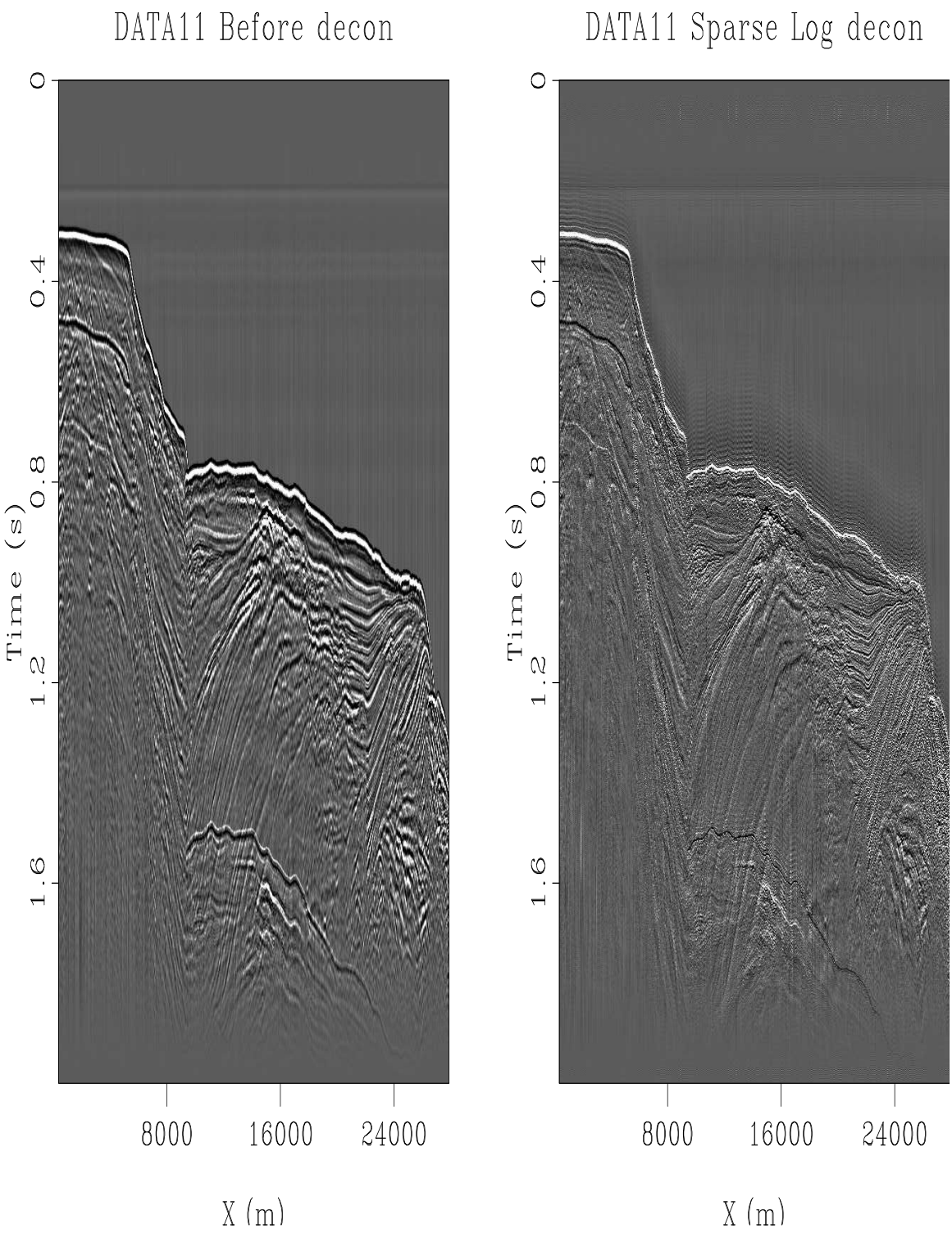

Figure 12: Data set from offshore Washington. On multiples where we obviously expect to be able to recognize polarities we find them nicely enhanced by the deconvolution. Unfortunately, we don't pick up such sharp events in the sedimentary section. The sparseness decon is very high frequency, as any decon. Again, we feel the "bad frequencies" are coming through much more strongly than the sparseness goals suggests. [**ER**] antoine3/. DeconShort-DATA11

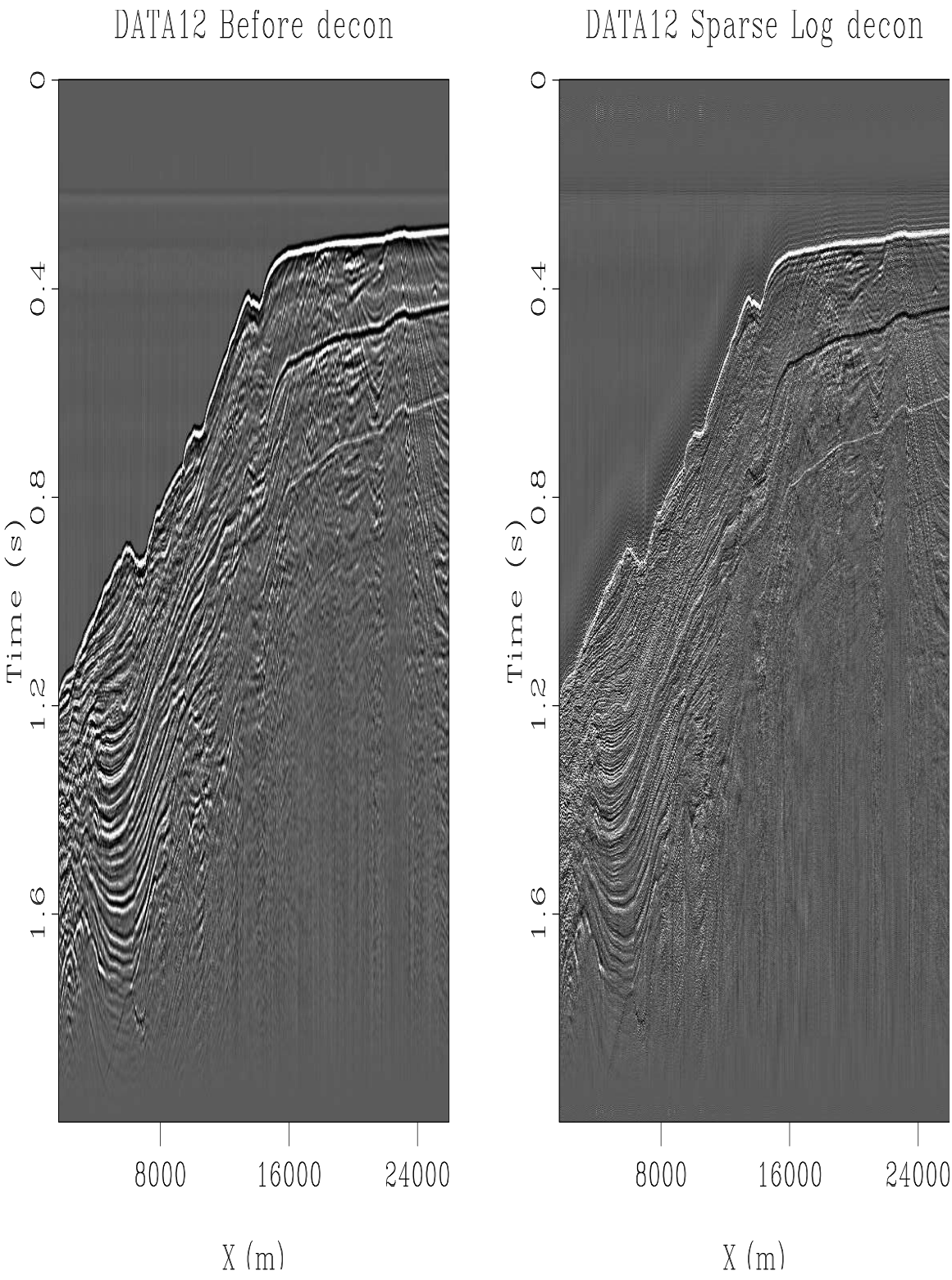

Figure 13: Another data set from offshore Washington. Conclusions similar to DATA11. [**ER**] antoine3/. DeconShort-DATA12

SEP reports.....

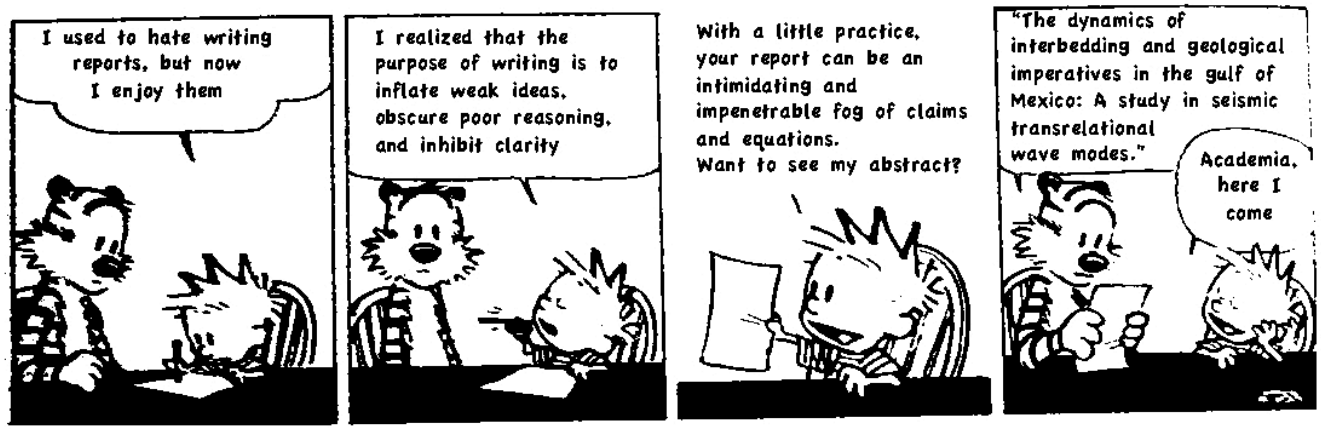

Adapted from Bill Waterson's "Calvin and Hobbes" comic strip

Tomographic full waveform inversion and linear modeling of multiple scattering

Biondo Biondi

ABSTRACT

I present a tomographic full waveform inversion method that is based to an extension of the velocity model in time. The resulting wavefield modeling operator is linear with respect to the non-zero time lags of the extended velocity, but can effectively model multiple scattering caused by velocity perturbations. This property is attractive to achieve robust global convergence in a waveform inversion algorithm. A simple 1D numerical example illustrates the properties of the new modeling operator and its promises for robust waveform inversion.

INTRODUCTION

In a recent report Biondi and Almomin (2012) and Almomin and Biondi (2012) presented waveform-inversion methods with robust convergence characteristics even when the initial velocity model is far away from the correct one. These methods are based on an extension of velocity and reflectivity along the subsurface offset axes. This extension enables the kinematics of reflected to be correctly modeled by a linear operator even when the velocity errors are large. However, the extension also explodes the null space of the inverse problem. To ensure convergence towards desirable models a tomographic term is added to the inversion objective function that penalizes velocity models with energy at non-zero subsurface offsets.

In this paper I introduce a tomographic full waveform inversion (TFWI) that is based on an extension of the velocity model along the time axis instead of the subsurface offset axes. This time extension has the theoretical advantage that it can be directly linked to the modeling of multiple scattering phenomena; therefore, overcoming the limitations of conventional full waveform inversion (FWI), whose gradient is based on a first-order scattering approximation. Furthermore, the velocity extension along the time axis should enable robust convergence from transmitted, or refracted events, in addition to reflected events. This versatility can be beneficial when inverting long offset data that contain overturned and refracted events as well conventional reflections. A one-dimensional extension along time is also computationally more efficient than a two-dimensional extension along subsurface offsets. This is an important practical advantage since the computational cost of modeling wave propagation in extended velocity models is substantially larger than in conventional velocity models (Almomin, 2012).

Throughout this paper I illustrate the theory with simple 1D examples. Waves are propagated in 1D, and model parameter, both background and perturbations, are averaged over the whole propagation interval. In addition to be fast to compute by using Matlab, the 1D examples have the advantage of reducing the dimensionality of the model space and

thus making the analysis of behavior of objective functions and gradients illustrative of the more general conceptual contributions of the paper. The numerical examples describes a transmission tomography problem to illustrate the capability of the proposed method to effectively use transmitted events, in addition to reflected ones.

CONVENTIONAL FULL WAVEFORM INVERSION (FWI)

Conventional full waveform inversion is performed by solving the following optimization problem

$$\min_{\mathbf{v}^2} J_{\mathrm{FWI}}\left(\mathbf{v}^2\right) \tag{1}$$

where:

$$J_{\mathrm{FWI}}\left(\mathbf{v}^2\right) = \frac{1}{2}\left\|\mathcal{L}\left(\mathbf{v}^2\right) - \mathbf{d}\right\|_2^2, \tag{2}$$

$\mathbf{v} = v\left(\vec{x}\right)$ is the velocity vector, $\mathcal{L}$ is a wave-equation operator non linear with respect to velocity perturbations and the data vector $\mathbf{d}$ is the pressure field $\mathbf{P} = P\left(t, \vec{x}\right)$ measured at the surface.

The wave-equation operator is evaluated by recursively solving the following finite difference equation

$$\left[\mathbf{D_2} - \mathbf{v}^2\nabla^2\right]\mathbf{P} = \mathbf{f}, \tag{3}$$

where $\mathbf{D_2}$ is a finite-difference representation of the second derivative in time, ∇^2 is a finite-difference representation of the Laplacian, and $\mathbf{f}$ is the source function.

Gradient computation with FWI

The efficient solution of the optimization problem expressed in equation 1 is performed by gradient based methods, and thus requires the evaluation of the linear operator $\mathbf{L}$, which is the linearization of $\mathcal{L}$ with respect to velocity perturbations $\delta\mathbf{v}^2$. This linear operator can be derived by perturbing equation 3 as follows

$$\left[\mathbf{D_2} - \left(\mathbf{v_o}^2 + \delta\mathbf{v}^2\right)\nabla^2\right]\left(\mathbf{P_o} + \delta\mathbf{P_o}\right) = \mathbf{f}, \tag{4}$$

where $\mathbf{P_o}$ and $\mathbf{v_o}$ are the background wavefield and velocity, respectively, and $\delta\mathbf{P_o}$ is the scattered wavefield.

Equation 4 can be rewritten as the following two equations:

$$\begin{aligned}\left[\mathbf{D_2} - \mathbf{v_o}^2\nabla^2\right]\mathbf{P_o} &= \mathbf{f}, &(5)\\ \left[\mathbf{D_2} - \mathbf{v_o}^2\nabla^2\right]\delta\mathbf{P_o} &= \delta\mathbf{v}^2\nabla^2\left(\mathbf{P_o} + \delta\mathbf{P_o}\right), &(6)\end{aligned}$$

which represents a nonlinear relationship between velocity perturbations and scattered wavefield. To linearize this relationship we drop the term multiplying the perturbations with each other; that is, we drop the scattered wavefield from the right hand side of equation 6 and obtain the following coupled equations:

$$\begin{aligned}\left[\mathbf{D_2} - \mathbf{v_o}^2\nabla^2\right]\mathbf{P_o} &= \mathbf{f}, &(7)\\ \left[\mathbf{D_2} - \mathbf{v_o}^2\nabla^2\right]\delta\mathbf{P_o} &= \delta\mathbf{v}^2\nabla^2\mathbf{P_o}. &(8)\end{aligned}$$

The linear operator $\mathbf{L}$ used to compute the gradient of the FWI objective function 2 is evaluated by recursively propagating the background wavefield $\mathbf{P_o}$ and the scattered wavefield $\delta\mathbf{P_o}$ by solving equations 7–8.

The scattered wavefield $\delta\mathbf{P_o}$ is a linear function of the velocity perturbations $\delta\mathbf{v}^2$ because equation 8 takes into account only fist order scattering. Notice that the linear operator $\mathbf{L}\left(\mathbf{v_o}^2\right)$ is itself a non linear function of the background velocity, both directly by determining the propagation speed of the scattered wavefield (left hand side in equation 8), and indirectly through the background wavefield (right hand side in equation 8).

Problems with FWI

Unfortunately, high-order scattering must be taken into account to model accurately wavefield perturbations when the velocity perturbations have wide spatial extent and/or large amplitude. Such velocity perturbations cause significant (larger than one fourth of wave cycle) time shifts in the propagating wavefield. The linear operator $\mathbf{L}$ cannot model large time shifts because the source function on the right-hand side of equation 8 is triggered by the background wavefield reaching a velocity perturbation, and consequently it has the timing as the background wavefield. Furthermore, the perturbed wavefield is propagated with the background velocity $\mathbf{v_o}$. In mathematical terms

$$\mathcal{L}\left(\mathbf{v_o}^2+\delta\mathbf{v}^2\right) \neq \mathcal{L}\left(\mathbf{v_o}^2\right)+\mathbf{L}\left(\mathbf{v_o}^2\right)\delta\mathbf{v}^2. \tag{9}$$

The problem is even deeper. When $\delta\mathbf{v}^2$ causes large time shifts by multiple scattering, there is no perturbation $\widehat{\delta\mathbf{v}^2}$ that can model those time shifts by single scattering; that is,

$$\mathcal{L}\left(\mathbf{v_o}^2+\delta\mathbf{v}^2\right) \neq \mathcal{L}\left(\mathbf{v_o}^2\right)+\mathbf{L}\left(\mathbf{v_o}^2\right)\widehat{\delta\mathbf{v}^2} \text{ for any } \widehat{\delta\mathbf{v}^2}. \tag{10}$$

The non linearity of the modeling operator makes the objective function equation 2 to be non convex when the velocity perturbations are sufficiently large. Figure 1 shows an example of non-convexity of the objective function. The result correspond to several 1D transmission problems sharing the same starting velocity (1.2 km/s) and with different true velocities. For all these experiments the source-receiver offset is 4 km and the source function is a zero-phase wavelet bandlimited between 5 and 20 Hz. The FWI norm is plotted as a function of the true velocity. If the true velocity is lower than $\approx$ 1.18 km/s or larger than $\approx$ 1.22 km/s a gradient based method will not converge to the right solution, even in this simple and low-dimensionality example.

The challenges of solving the optimization problem in equation 1 by gradient based optimization can be alternatively represented by graphing, as a function of the initial velocity error, the search direction (opposite sign of the gradient direction) of the objective function with respect to velocity square. Figure 2 display this function computed by applying the adjoint of the linear operator $\mathbf{L}$ to the data residuals; that is

$$\nabla J_{\text{FWI}} = \mathbf{L}'\left[\mathcal{L}\left(\mathbf{v_o}^2\right)-\mathbf{d}\right]. \tag{11}$$

For a gradient based method to converge, the search direction should be always negative when the true velocity is lower than 1.2 km/s, and positive when the true velocity is higher.

Multiple-scattering modeling

We can achieve accurate modeling of perturbed wavefield by solving equations 5–6 instead of equations 7–8. Equations 5–6 can be solved numerically with a simple explicit method; that is, one that adds the scattered wavefield up to time t to the right-hand side of equation 6 to compute the scattered wavefield at $t+\Delta t$. Even in presence of large velocity variations, the scattered wavefield has now the correct time shift. Numerical solutions produce accurate results, although the scattered wavefield is still propagated with the background velocity, because multiple scattering is taken into account of.

The challenge with using these equations in a gradient-based inversion algorithm is that the relation between the scattered wavefield $\delta\mathbf{P_o}$ and the velocity perturbations $\delta\mathbf{v}^2$ is now nonlinear. In the next section, I present a method for linearizing this relation that is alternative to the conventional one represented by equations 7–8, and is based on an extension of the velocity model in time.

TOMOGRAPHIC FULL WAVEFORM INVERSION (TFWI)

We can rewrite equations 5–6 by performing the following substitution

$$\delta\mathbf{P_o} = \mathbf{P_o} \overset{t'}{*} (\mathbf{T}-\mathbf{I}), \tag{12}$$

and consequently

$$\mathbf{P_o} + \delta\mathbf{P_o} = \mathbf{P_o} \overset{t'}{*} \mathbf{T}, \tag{13}$$

where $\mathbf{T}$ is a convolutional operator in time that may vary both in space and time; $\mathbf{I}$ is the identity operator. For example, when the perturbed wavefield is a time-shifted version of the background wavefield, the operator $\mathbf{T}$ is a shifted delta function. With this substitution equation 6 can be rewritten as

$$\left[\mathbf{D_2} - \mathbf{v_o}^2\nabla^2\right]\delta\mathbf{P_o} = \delta\mathbf{v}^2\left(\widetilde{\mathbf{T}} \overset{t'}{*} \nabla^2\mathbf{P_o}\right), \tag{14}$$

where the substitution of $\mathbf{T}$ with $\widetilde{\mathbf{T}}$ takes into account of the Laplacian.

If we define an velocity model *extended* in time $\delta\tilde{\mathbf{v}}^2(t,t') = \delta\mathbf{v}^2 \overset{t'}{*} \widetilde{\mathbf{T}}$, we can rewrite equation 14 as

$$\left[\mathbf{D_2} - \mathbf{v_o}^2\nabla^2\right]\delta\mathbf{P_o} = \delta\tilde{\mathbf{v}}^2\left(t,t'\right) \overset{t'}{*} \nabla^2\mathbf{P_o}. \tag{15}$$

The estimation of an extended velocity as a function of both t and t', and for each seismic experiment (e.g. shot), can be unpractical. We can approximate equation 15 by making the velocity dependent only from the convolutional time lag; that is, $\tau = t - t'$ and the same for each seismic experiment. The approximation of equation 15 can be written as

$$\left[\mathbf{D_2} - \tilde{\mathbf{v}}^2(\tau=0)\nabla^2\right]\mathbf{\Delta P} = \delta\tilde{\mathbf{v}}^2(\tau) \overset{\tau}{*} \nabla^2\mathbf{P_o}, \tag{16}$$

where the change of notation from $\delta\mathbf{P_o}$ to $\mathbf{\Delta P}$ indicates that the scattered wavefield $\mathbf{\Delta P}$ is now an approximation of the true multiple-scattered wavefield $\delta\mathbf{P_o}$.

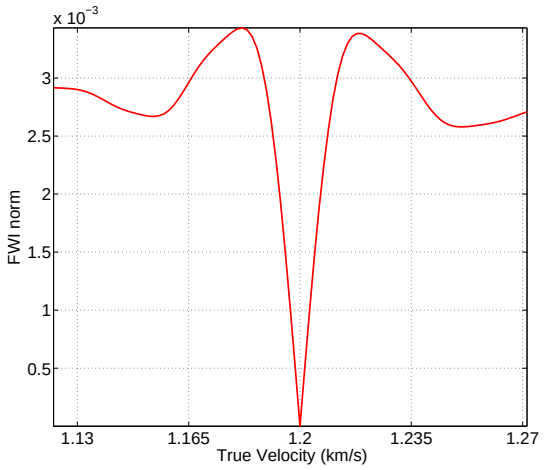

Figure 1: FWI norm as a function of the true velocity, when the starting velocity is equal to 1.2 km/s. biondo1/. FWI-Norm-new

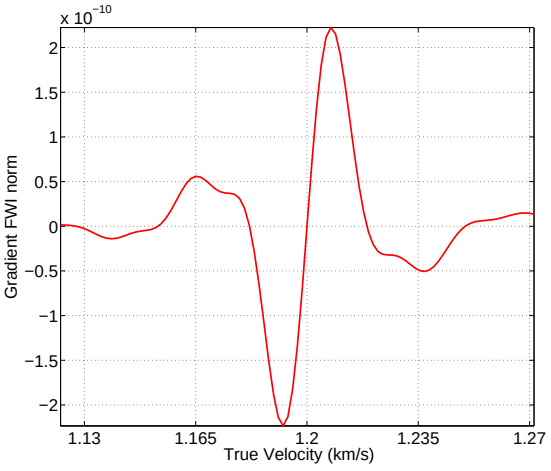

Figure 2: FWI search direction as a function of the true velocity, when the starting velocity is equal to 1.2 km/s. biondo1/. FWI-Grad-new

Formally solving equation 16 we obtain

$$\mathbf{\Delta P} = \left[\mathbf{D_2} - \tilde{\mathbf{v}}^2\left(\tau=0\right)\nabla^2\right]^{-1}\left[\delta\tilde{\mathbf{v}}^2\left(\tau\right) \overset{\tau}{*} \nabla^2\mathbf{P_o}\right] \tag{17}$$

that is a linear relationship between $\delta\tilde{\mathbf{v}}^2$ and $\mathbf{\Delta P}$ defined by the linear operator $\widehat{\mathbf{L}}$ such as $\mathbf{\Delta P} = \widehat{\mathbf{L}}\delta\tilde{\mathbf{v}}^2$.

If we define the total wavefield to be

$$\mathbf{P} = \mathbf{P_o} + \mathbf{\Delta P}, \tag{18}$$

and the extended non-linear modeling operator as

$$\tilde{\mathcal{L}}\left(\tilde{\mathbf{v}}\right) = \mathcal{L}\left(\tilde{\mathbf{v}}\left(\tau=0\right)\right) + \widehat{\mathbf{L}}\left(\tilde{\mathbf{v}}\right)\delta\tilde{\mathbf{v}}^2, \tag{19}$$

the objective function

$$J_{\mathrm{EFWI}}\left(\tilde{\mathbf{v}}\right) = \frac{1}{2}\left\|\tilde{\mathcal{L}}\left(\tilde{\mathbf{v}}\right) - \mathbf{d}\right\|_2^2 \tag{20}$$

has the same local minima of the original FWI objective function, but it also provides smooth descending paths to the global minimum in the additional dimensions. The problem is now under constrained because many solutions fit the data equally well. Among all these possible solutions we are interested in the solutions for which the extended velocity model is as focused as possible around the zero time lag of the model.

To converge towards a desirable solution we can add an additional term to the objective function that penalizes extended velocity model with significant energy at non-zero time lag; that is,

$$\min_{\tilde{\mathbf{v}}} J_{\mathrm{TFWI}}\left(\tilde{\mathbf{v}}\right), \tag{21}$$

with

$$J_{\mathrm{TFWI}}\left(\tilde{\mathbf{v}}\right) = \frac{1}{2}\left\|\tilde{\mathcal{L}}\left(\tilde{\mathbf{v}}\right) - \mathbf{d}\right\|_2^2 - \epsilon\mathcal{F}\left(\tilde{\mathbf{v}}\right), \tag{22}$$

where $\mathcal{F}$ is an operator that measure the focusing of the model at zero time lag. A straightforward example of such operator is

$$\mathcal{F}\left(\tilde{\mathbf{v}}\right) = -\left\||\tau|\,\tilde{\mathbf{v}}\right\|_2^2. \tag{23}$$

Gradient computation with TFWI

The gradient computation of the TFWI objective function has three components. The first component takes into account the dependency of the background wavefield from velocity; it is the same as for the FWI case. The second component is related to the dependency of the approximation of the scattered wavefield $\mathbf{\Delta P}$ from the extended velocity. It is performed by applying the adjoint of the linear operator $\widehat{\mathbf{L}}$. The application of $\widehat{\mathbf{L}}'$ to the data residual is accomplished similarly to the FWI gradient by injecting the residual at the receiver location and running backward in time the propagation expressed in equation 17.

The third component takes into account the dependency of $\mathbf{\Delta P}$ from the velocity at zero time lag; its evaluation is more involved than for the previous two terms but is crucial to the convergence of the inversion towards a velocity model that explain the kinematics in

the data. The forward operator can be evaluated as a chain of two operators. The first one relates perturbations in velocity to perturbations in the background wavefield, as expressed by equations 7–8. The second one is computed by forward solving in time equation 17, where the source term is given by the perturbations in the background wavefield, and not by the perturbations in the extended velocity. Consequently this term is zero when the extended velocity perturbations $\delta\tilde{\mathbf{v}}^2$ are zero, independently from the perturbations in the background wavefield. The adjoint is computed by applying the adjoint of these two operators in reverse order.

Finally, the gradient of the regularization terms depends on the expression of the specific focusing operator $\mathcal{F}$. For the choice expressed in equation 23, the computation of the gradient is trivial.

NUMERICAL 1D EXAMPLE

I will use a simple 1D numerical example to analyze some of the characteristics of the TFWI method I presented in the previous sections. Figure 3 shows the difference between the background wavefield propagated with $\mathbf{v}$=1.2 km/s and the wavefield propagated with the true velocity of $\mathbf{v}$=1.13 km/s. The difference wavefield is displayed as a function of propagation distance and traveltime. The data are recorded with a receiver located at 7 km for a total of 4 km offset from the source. The velocity error is sufficiently high that the wavefields are completely out of phase at the receiver location. We are therefore in the situation described by equation 10. Because the events are out of phase at the receiver, the backprojection of the data residual into the velocity model yields a gradient (equation 11) that is substantially zero, as it can be verified in Figure 2. Conventional FWI would have troubles to converge even for this simple problem.

On the contrary, the linearized modeling equation defined in equation 17 would have no troubles to model the data residual. For example, we can easily reproduce the wavefield difference shown in Figure 3 by setting the extended-velocity perturbation to be a delta function along the τ axis, where the shift of the delta function linearly increases with the distance from the origin. This linear shift is computed by integrating the difference in slowness between the background model and the true model. The extended-velocity perturbation is shown in Figure 4. Figure 5 shows the result of solving equation 17 with the model shown in Figure 4. The approximation of the scattered wavefield $\mathbf{\Delta P}$ is almost identical to the wavefield difference shown in Figure 3.

Next step is the backprojection of the data residual recorded by extracting the wavefields at the receiver position into the extended velocity model. In the previous section, I explained that there are three terms in this backprojection. In this case, the first and the third are zero. As discussed previously, the first component is zero because the events in the data residual are out of phase. The third term is zero because the starting extended model is zero at non-zero time lags. Figure 6 shows the contribution of the second component of the gradient. It is zero on the right of the receiver location, and it is basically constant as function of the propagation distance on the left of the receiver location.

Forward modeling solving equation 17 with the model shown in Figure 6 yields a scattered wavefield that at the receiver location is extremely close to the original residual shown in Figure 3. Therefore, the first term of the objective function 22 has a well-behaved

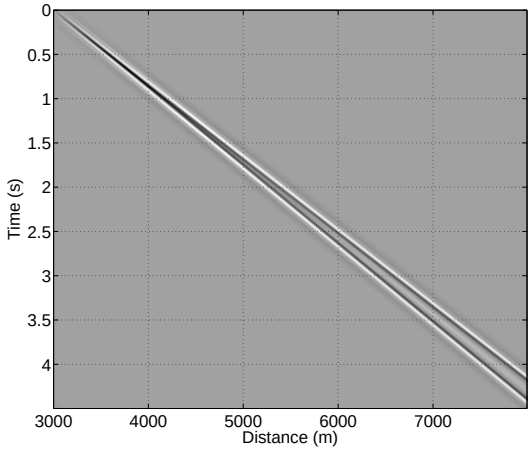

Figure 3: Difference between background wavefield computed with the starting velocity (1.2 km/s) and the wavefield propagated with the true velocity (1.13 km/s). biondo1/. Init-Residual

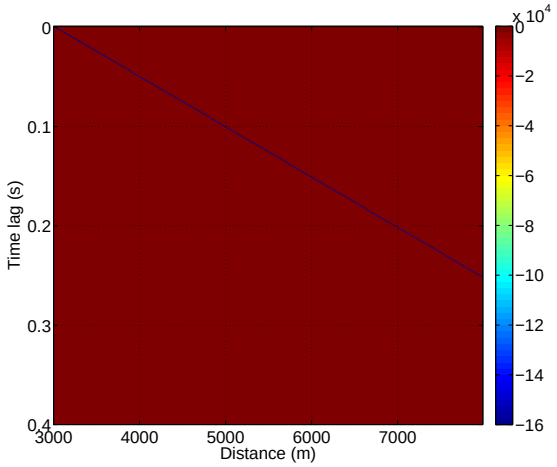

Figure 4: Extended velocity perturbation chosen to approximately model the wavefield difference shown in Figure 3 by applying equation 17. biondo1/. Delta-Vel-Extend

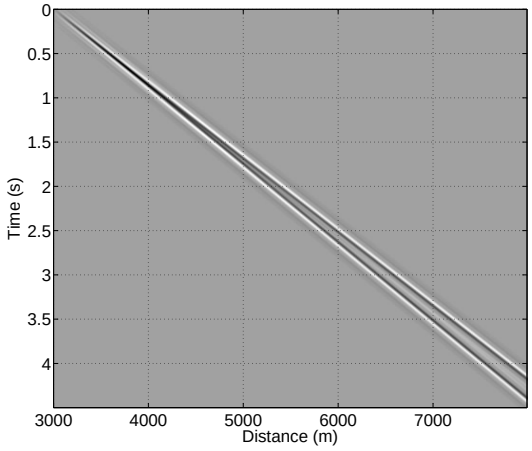

Figure 5: Perturbed wavefield computed by solving equation 17 with the model shown in Figure 4. biondo1/. Lin-Forw-Ext-new

parabolic shape as a function of the step size applied to the search direction, with well-defined minimum that determines the extended model after a first iteration of an iterative inversion algorithm.

The extended model obtained at the first iteration can then be used to compute the data residuals and gradient at the second iteration. Since the data residual are small, the main contribution to the gradient comes from the second term of the objective function; that is, the focusing operator. It is straightforward to verify that for the choice of focusing operator in 23, the most significant component of this gradient is away from the zero time lag. The projection of this gradient in the data space has a non-zero component and will create a data residual, which can in turn be backprojected into the velocity model. The most interesting component of this backprojection is at zero-time lag since it is the one that will effect the propagation velocity of the background wavefield at the next iteration.

Among the three gradient components discussed in the previous section, only the third one effects the extended velocity at zero-time lag. Figure 7 shows the search direction obtained by averaging this gradient component along the whole propagation interval as a function of the true velocity. As before the the starting velocity is 1.2 km/s. In contrast with the conventional FWI search direction shown in Figure 2, the search directions shown in Figure 7 is always negative for a true velocity lower than 1.2 km/s, and always positive for a true velocity larger than 1.2 km/s. This indicates that no matter how large the initial velocity error, the TFWI method will start moving the zero-lag component of the extended model in the correct direction. This result is far from being a proof of global convergence, but is definitely encouraging.

CONCLUSIONS

Perturbations in the propagating wavefield caused by multiple scattering can be approximately modeled by a linear operator when the velocity function is extended in time. A tomographic full waveform method based on a time extension of the velocity model is likely to have attractive global-convergence characteristics, and thus to overcome one of the main challenges of conventional full waveform inversion.

REFERENCES

Almomin, A., 2012, Computational analysis of extended full waveform inversion: SEP-Report, **148**, 59–70.

Almomin, A. and B. Biondi, 2012, Tomographic full waveform inversion: Practical and computationally feasible approach: SEP-Report, **147**, 13–26.

Biondi, B. and A. Almomin, 2012, Tomographic full waveform inversion (TFWI) by combining full waveform inversion with wave-equation migration velocity analysis: SEP-Report, **147**, 1–12.

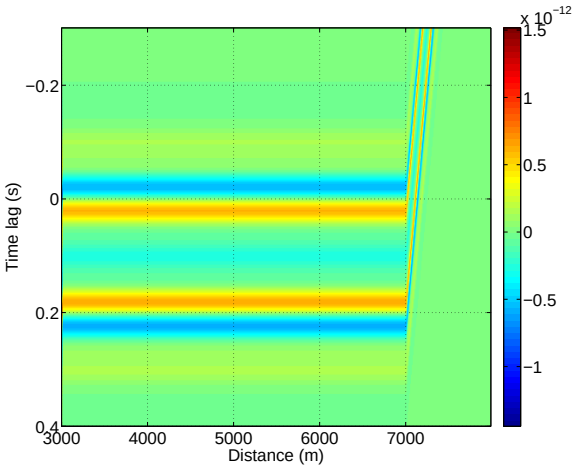

Figure 6: Extended-velocity gradient computed by applying the adjoint of the linear operator $\widehat{\mathbf{L}}$ to the data residuals measured at the receiver located at a distance of 7 km. biondo1/. Back-Vel-Extend

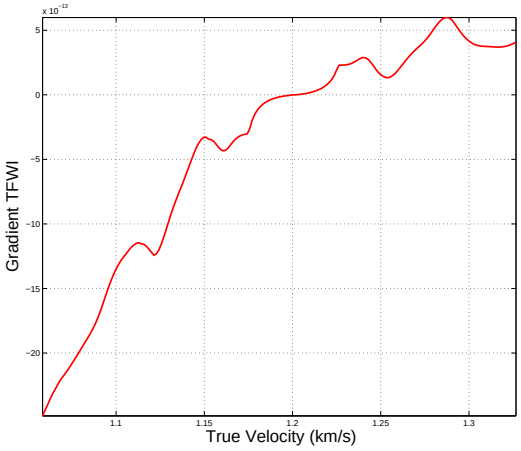

Figure 7: Search directions obtained at the second iteration of the inversion process and caused by the focusing term of the TFWI objective function. These search directions are obtained by averaging the gradient along the whole propagation interval. Notice that the search directions are always negative for a true velocity lower than 1.2 km/s, and always positive for a true velocity larger than 1.2 km/s. biondo1/. Grad-Phys

Computational analysis of extended full waveform inversion

Ali Almomin

ABSTRACT

I compare the computational cost of conventional full-waveform inversion to the extended full-waveform inversion in both space and time. These model space extensions provide accurate results but increase the cost drastically. I also compare the cost of the nonlinear inversion to linearized inversion by scale-separation. I then propose extending the inversion in data space where there are more underlying assumptions but whose cost competes with the conventional inversion. I test extending the inversion by source ray parameter on the Marmousi model. The results of the synthetic tests show that convergence is possible even with large errors in the initial model which would have prevented convergence of conventional full-waveform inversion.

INTRODUCTION

Seismic velocity analysis methods can be divided into two major groups. First, there are techniques that aim to minimize the misfit in the data domain, e.g., full waveform inversion (FWI) (Tarantola, 1984; Pratt, 1999; Luo and Schuster, 1991). Second, there are other techniques (Symes and Carazzone, 1991; Biondi and Sava, 1999; Shen, 2004; Zhang et al., 2012), that aim to improve the quality in the image domain, such as migration velocity analysis (MVA). These approaches try to measure some quality of the image and then invert for the estimated image perturbation using a linearized wave-equation operator.

There are significant advantages to minimizing the residual in the image space: global convergence, increased signal-to-noise ratio, and decreased complexity of the data (Tang et al., 2008). However, a common drawback to doing velocity analysis in the image domain is that only the transmission effects of the velocity are used. This results in incomplete vertical resolution in the estimated model updates. On the other hand, FWI does not have that problem, since it utilizes the information from both the forward-scattered and back-scattered wavefields. This results in higher resolution model estimates. Moreover, the data misfit is computed in the data space directly without the need to go to another domain or to separate the data into several components. This direct computation results in a relatively simple relationship between the data residuals and the model updates. However, FWI has the disadvantage that its objective function is far from being smooth and convex; it requires the starting model to be very close to the true model to avoid convergence to local minima.

Biondi (2012) presents a generalized framework for full waveform inversion that avoids the cycle-skipping problem while utilizing all the components of seismic data to invert for the medium parameters. This is achieved in two steps: first by extending the velocity model through an additional degree of freedom, and second by imposing a regularization to constrain this added degree of freedom.

In this paper, I compare the cost of conventional full waveform inversion to extended inversion in model space that uses subsurface offset and time lags. I also compare the cost of the extended inversion to linearized inversion by scale separation (Almomin and Biondi, 2012). Next, I propose extending full waveform inversion through a data space axis, such as source location or source ray parameter, instead of model space axes. Finally, I test the source ray parameter extension on the Marmousi model.

COMPUTATIONAL COST

Nonlinear wave equation inversions are commonly performed using gradient-based iterative optimization. Each iteration typically consists of three steps. First, calculate the residuals, which requires one nonlinear forward operation. Second, calculate the gradient, which requires one linearized adjoint operation. Finally, determine the step size by a line search, which requires few nonlinear forward operations. For our calculations, we will assume the line search requires three forward operations results in a total per iteration effort of four forward and one adjoint operations.

Conventional FWI

For conventional full waveform inversion, the modeled data is computed using the nonlinear forward operator as:

$$d(\omega, \mathbf{x}_r, \mathbf{x}_s; v(\mathbf{x})) = \sum_{\mathbf{x}} f(\omega, \mathbf{x}_s) G(\omega, \mathbf{x}, \mathbf{x}_s; v(\mathbf{x})) \delta(\mathbf{x}_r - \mathbf{x}), \tag{1}$$

where $d(\omega, \mathbf{x}_r, \mathbf{x}_s; v(\mathbf{x}))$ is the modeled data, $v(\mathbf{x})$ is the velocity model, $f(\omega, \mathbf{x}_s)$ is the source function, ω is frequency, $\mathbf{x}_s$ and $\mathbf{x}_r$ are the source and receiver coordinates, and $\mathbf{x}$ is the model coordinate. In the acoustic, constant-density case, the Green's function $G(\omega, \mathbf{x}, \mathbf{x}_s; v(\mathbf{x}))$ satisfies:

$$\left(\frac{\omega^2}{v^2(\mathbf{x})} + \nabla^2 \right) G(\omega, \mathbf{x}, \mathbf{x}_s; v(\mathbf{x})) = \delta(\mathbf{x}_s - \mathbf{x}). \tag{2}$$

The propagation can be done in the time domain by convolving each model point with a finite-difference stencil. However, the time marching requires the time axis sampling to satisfy dispersion and stability conditions (Marfurt, 1984), generally much finer than the data sampling. Moreover, each time step requires multiplying the time slice by the velocity squared. Therefore, the cost of forward modeling can be written as:

$$C_{\text{FWI-F}} = N_x N_y N_z N_{\text{source}} (N_{tp} C_{\text{FDTD}} + N_{tp}), \tag{3}$$

where N_x, N_y and N_z, are the number of points along the three spatial axes, N_{source} is the number of sources, C_{FDTD} is the cost of convolving one model location by the time-domain finite-difference stencil and N_{tp} is the number of time samples for propagation. By linearizing equation 1 over the squared slowness, we can compute the adjoint as:

$$\Delta s^2(\mathbf{x}) = \sum_{\omega, \mathbf{x}_r, \mathbf{x}_s} \omega^2 f(\omega, \mathbf{x}_s) G(\omega, \mathbf{x}, \mathbf{x}_s; v(\mathbf{x})) G(\omega, \mathbf{x}, \mathbf{x}_r; v(\mathbf{x})) \Delta d^*(\omega, \mathbf{x}_r, \mathbf{x}_s; v(\mathbf{x})), \tag{4}$$

where $\Delta s^2(\mathbf{x})$ is the perturbation in squared slowness and * denotes the complex conjugate. For the adjoint, the imaging time sampling can be much larger than that of propagation since it does not need to satisfy the dispersion and stability conditions. Hence, the cost of computing the adjoint of FWI can be written as:

$$C_{\text{FWI}-\text{A}} = N_x N_y N_z N_{\text{source}}(2 \times N_{tp} C_{\text{FDTD}} + 2 \times N_{tp} + N_{ti}), \tag{5}$$

where N_{ti} is the number of time samples for imaging. The total cost of one iteration of FWI becomes

$$C_{\text{FWI}} = N_x N_y N_z N_{\text{source}}(6 \times N_{tp} C_{\text{FDTD}} + 6 \times N_{tp} + N_{ti}). \tag{6}$$

Model-Space Extensions

Biondi and Almomin (2012) introduced an extension to full waveform inversion that can mitigate the cycle-skipping problem and allow for a larger error in the initial model. This is achieved by extending the velocity model along the subsurface offset and then solving the corresponding extended wave equation. The modeled data becomes:

$$d(\omega, \mathbf{x}_r, \mathbf{x}_s; v(\mathbf{x}, \mathbf{x}_h)) = \sum_{\mathbf{x}} f(\omega, \mathbf{x}_s) G(\omega, \mathbf{x}, \mathbf{x}_s; v(\mathbf{x}, \mathbf{x}_h)) \delta(\mathbf{x}_r - \mathbf{x}), \tag{7}$$

and the extended Green's function satisfies:

$$\left(v^2(\mathbf{x}, \mathbf{x}_h) *^{-1} \omega^2 + \nabla^2\right) G(\omega, \mathbf{x}, \mathbf{x}_s; v(\mathbf{x}, \mathbf{x}_h)) = \delta(\mathbf{x}_s - \mathbf{x}), \tag{8}$$

where $\mathbf{x}_h$ is subsurface offset and $*^{-1}$ denotes a deconvolution operator over subsurface offset. This extended wave equation convolves each time slice by all subsurface offsets of velocity. The cost of extended forward modeling becomes:

$$C_{\text{EFWI}-\text{F}} = N_x N_y N_z N_{\text{source}}(N_{tp} C_{\text{FDTD}} + N_{tp} N_{hx} N_{hy}), \tag{9}$$

where N_{hx} and N_{hy} are number of subsurface offsets along the x and y axes, respectively. By linearizing equation 7 over the velocity squared, we can compute the adjoint as:

$$\begin{aligned} \Delta v^2(\mathbf{x}, \mathbf{x}_h) = \sum_{\omega, \mathbf{x}_r, \mathbf{x}_s} & \nabla^2 f(\omega, \mathbf{x}_s) G(\omega, \mathbf{x} - \mathbf{h}, \mathbf{x}_s; v(\mathbf{x}, \mathbf{x}_h)) \\ & G(\omega, \mathbf{x} + \mathbf{h}, \mathbf{x}_r; v(\mathbf{x}, \mathbf{x}_h)) \Delta d^*(\omega, \mathbf{x}_r, \mathbf{x}_s; v(\mathbf{x}, \mathbf{x}_h)). \end{aligned} \tag{10}$$

Therefore, the cost of computing the adjoint of EFWI can be written as

$$C_{\text{EFWI}-\text{A}} = N_x N_y N_z N_{\text{source}}(2 \times N_{tp} C_{\text{FDTD}} + 2 \times N_{tp} N_{hx} N_{hy} + N_{ti} N_{hx} N_{hy}) \tag{11}$$

and the total cost of one iteration of EFWI becomes

$$C_{\text{EFWI}} = N_x N_y N_z N_{\text{source}}(6 \times N_{tp} C_{\text{FDTD}} + 6 \times N_{tp} N_{hx} N_{hy} + N_{ti} N_{hx} N_{hy}). \tag{12}$$

We can see that the computational cost becomes extremely high when we include the subsurface offsets in the velocity model. One way to reduce the cost is presented in Biondi (2012) where the velocity model is extended over time instead of horizontal offset. In that case, the cost becomes a function of one time-lag parameter instead of two horizontal lags in 3D:

$$C_{\text{TimeEFWI}} = N_x N_y N_z N_{\text{source}}(6 \times N_{tp} C_{\text{FDTD}} + 6 \times N_{tp} N_\tau + N_{ti} N_\tau), \tag{13}$$

where N_τ is the number of time lags. The computational disadvantage is that several time slices need to be held in memory for each time instead of the conventional two slices.

Linearized Model-Space Extensions

Any of the previously mentioned inversions can be linearized by scale separation as shown in Almomin and Biondi (2012). To linearize the conventional FWI, the velocity model is separated as:

$$s^2(\mathbf{x}) = b(\mathbf{x}) + r(\mathbf{x}), \tag{14}$$

where $b(\mathbf{x})$ is the background component and $r(\mathbf{x})$ is the perturbation component. The linearized FWI forward operator can be written as follows:

$$d(\omega, \mathbf{x}_r, \mathbf{x}_s; b(\mathbf{x}), r(\mathbf{x})) = \sum_{\mathbf{x}} \omega^2 f(\omega, \mathbf{x}_s) G(\omega, \mathbf{x}, \mathbf{x}_r; b(\mathbf{x})) r(\mathbf{x}) G(\omega, \mathbf{x}, \mathbf{x}_s; b(\mathbf{x})). \tag{15}$$

As shown in equation 15, the cost of the linearized forward operator is equal to the adjoint cost of conventional FWI. Also, the adjoint of the linearized operator with respect to the perturbation is the same as the conventional FWI adjoint and has the same cost as well. The adjoint with respect to the background is:

$$\begin{aligned}\Delta b(\mathbf{x}) = \sum_{\omega, \mathbf{x}_r, \mathbf{x}_s, \mathbf{y}} & \omega^4 f(\omega, \mathbf{x}_s) G(\omega, \mathbf{y}, \mathbf{x}_s; b(\mathbf{x})) r(\mathbf{y}) \\ & G(\omega, \mathbf{x}, \mathbf{y}; b(\mathbf{x})) G(\omega, \mathbf{x}, \mathbf{x}_r; b(\mathbf{x})) \Delta d^*(\omega, \mathbf{x}_r, \mathbf{x}_s; b(\mathbf{x}), r(\mathbf{x})) + \\ & \omega^4 f(\omega, \mathbf{x}_s) G(\omega, \mathbf{x}, \mathbf{x}_s; b(\mathbf{x})) G(\omega, \mathbf{x}, \mathbf{y}; b(\mathbf{x})) r(\mathbf{y}) \\ & G(\omega, \mathbf{y}, \mathbf{x}_r; b(\mathbf{x})) \Delta d^*(\omega, \mathbf{x}_r, \mathbf{x}_s; b(\mathbf{x}), r(\mathbf{x})).\end{aligned} \tag{16}$$

Although equation 16 has six Green's functions, only four propagations are required since each background wavefield is the same for two Green's functions. In addition, these background wavefields are the same for the adjoint of perturbation. Hence, the total cost of the linearized FWI per iteration, assuming complete reuse of background wavefields, is

$$C_{\text{LFWI}} = N_x N_y N_z N_{\text{source}} (12 \times N_{tp} C_{\text{FDTD}} + 12 \times N_{tp} + 9 \times N_{ti}). \tag{17}$$

This shows that scale separation by itself increases the cost of the original nonlinear operator since it adds several propagations, imaging and scattering steps. However, a significant cost cutting for extended inversions is possible by extending only the perturbation component without extending background component. By following the same derivation for linearized FWI, I find the cost of linearized extended FWI in subsurface offset when I extend perturbation only to be

$$C_{\text{LEFWI}} = N_x N_y N_z N_{\text{source}} (12 \times N_{tp} C_{\text{FDTD}} + 12 \times N_{tp} + 2 \times N_{ti} + 7 \times N_{ti} N_{hx} N_{hy}). \tag{18}$$

By extending only the perturbation, we remove the subsurface offset multiplication factor N_{tp}. This results in a large reduction in cost because the number of propagation time steps N_{tp} is much larger than the number of imaging time steps N_{ti}. Similarly, the cost of linearized extended FWI in time can be written as

$$C_{\text{TimeLEFWI}} = N_x N_y N_z N_{\text{source}} (12 \times N_{tp} C_{\text{FDTD}} + 12 \times N_{tp} + 2 \times N_{ti} + 7 \times N_{ti} N_{\tau}). \tag{19}$$

For the extended FWI in time, the cost reduction by linearization is less dramatic than the extended FWI in subsurface offset since there is only one additional convolution axis.

Data-Space Extensions

Model space extensions provide an accurate solution to the cycle skipping problem because they decompose the wavefields in the subsurface along the extended axes, either space or time. However, this is also reason for their high cost: each data point will interact with all points of the extended model. To avoid this problem, I propose extending full waveform inversion through a data space axis, such as source location, instead of model space axes. The reason for data space extension is that each extended model component operates on the corresponding component in data space and vice versa. In other words, each experiment can be computed similarly to the conventional way, but the model is changed between different experiments. However, extending the model through a data space axis has the underlying assumption that data components remain separated in the subsurface. This assumption depends on the complexity of the model. For instance, image space angle gathers and data space ray parameter gathers provide similar information in a fairly simple model (Sava and Fomel, 2003), but the latter breaks down in a very complicated model.

The extended inversion, whether in model space or data space, needs to satisfy two conditions. First, the observed data can always be explained by the extended model regardless of the selection of the initial model (Biondi, 2012). Second, the extended model should allow gradual change by regularization to produce a non-extended model. The data space extensions that can potentially satisfy these conditions are source location and source ray parameter. The source location extension has the advantage of using the exact same propagation engine as the conventional inversion, so its implementation requires minimal adjustment to existing applications. Moreover, the source location satisfies the extension conditions fairly well. Figure 1 shows source location image gathers for a two-layer model when using the correct velocity, a 10 percent lower velocity, and a 10 percent higher velocity. We see that regularizing the additional axis by a derivative can satisfy the second condition. The disadvantage of this extension is having a velocity model for each source location, which can require a very large memory size and burdensome I/O in 3D.

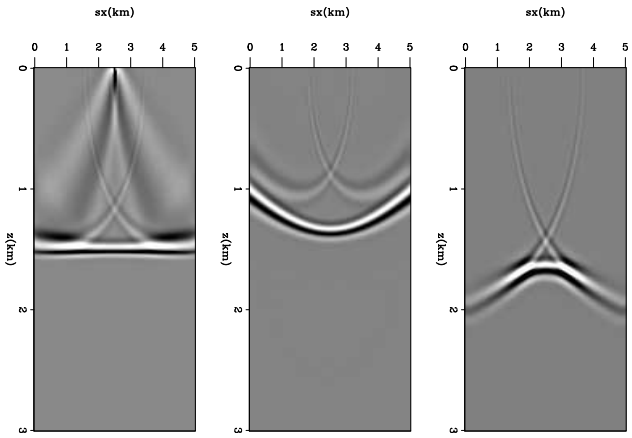

Figure 1: Source location image gather for a two-layer model when using the correct velocity (left), a 10 percent lower velocity (middle), and a 10 percent higher velocity (right). [**CR**] ali1/. image-s

Extending the model by source ray parameter requires plane-wave encoding of the data (Whitmore, 1995; Zhang et al., 2005; Liu et al., 2006). Figure 2 shows source ray parameter image gathers for a two-layer model when using the correct velocity, a 10 percent lower velocity, and a 10 percent higher velocity. Similar to source location, the source ray parameter seems to also satisfy the second condition of model extension. The first condition is tested in the Synthetic Examples section below. In addition, the number of planes is generally

much smaller than the number of source locations, so it both reduces the cost and makes the size of the extended model very manageable.

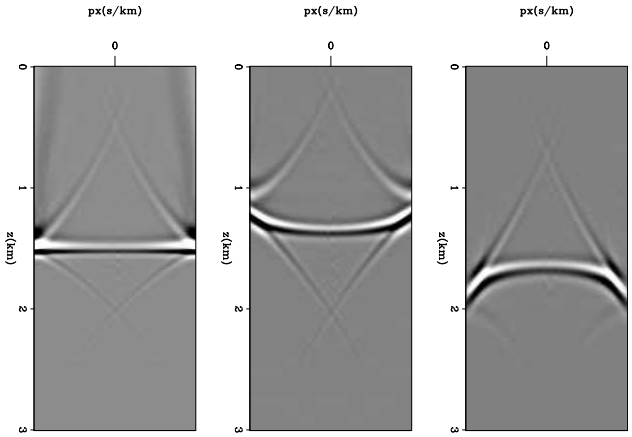

Figure 2: Source ray parameter image gather for a two-layer model when using the correct velocity (left), a 10 percent lower velocity (middle), and a 10 percent higher velocity (right). [**CR**] ali1/. image-p

The cost of source location encoding is the same as conventional FWI, whereas the cost of source ray parameter extension is

$$C_{\text{RayEFWI}} = N_x N_y N_z N_p (6 \times N_{tp} C_{\text{FDTD}} + 6 \times N_{tp} + N_{ti}), \tag{20}$$

where N_p is the number of planes. Figure 3 compares the costs of all mentioned inversions assuming $N_x = N_y = 1000$, $N_z = 100$, $N_{\text{source}} = 10000$, $C_{\text{FDTD}} = 16$, $N_{tp} = 1000$, $N_{ti} = 100$, $N_{hx} = N_{hy} = 100$, $N_\tau = 200$, and $N_p = 1000$, where the costs are normalized by the cost of conventional FWI. The log-scale highlights that the difference in cost between these inversions can be several orders of magnitude.

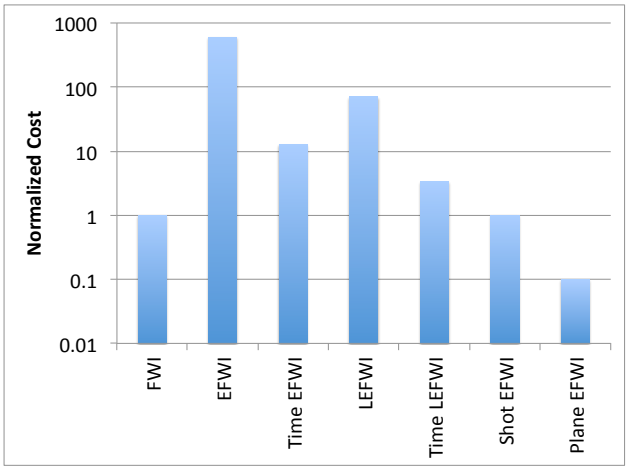

Figure 3: Cost comparison of conventional and extended full wavefrom inversions. [**NR**] ali1/. CostEFWI

SYNTHETIC EXAMPLES

A modified Marmousi model is used for the synthetic example where a 500m water layer is added to the top. Figure 4 shows the true velocity model. A Ricker wavelet with a fundamental frequency of 15 Hz and temporal sampling of 1.5 ms is used as a source function to model the data. There are 461 fixed receivers with a spacing of 20 m and 21 plane sources with ray parameter ranging from -1 s/km to 1 s/km. The initial model shown in Figure 5 is obtained by strongly smoothing the true model.

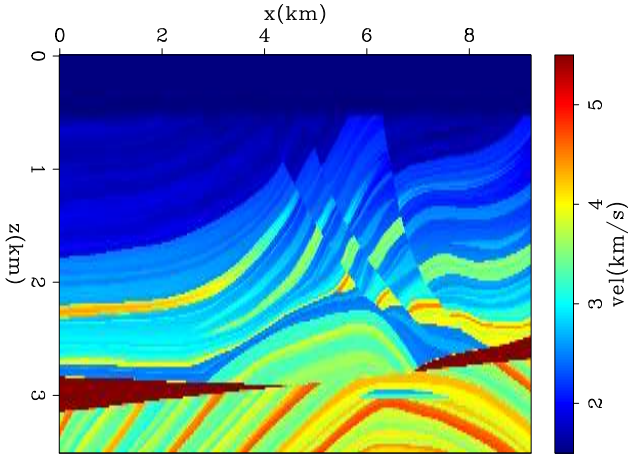

Figure 4: The true velocity of Marmousi model. [**ER**] ali1/. vtrue

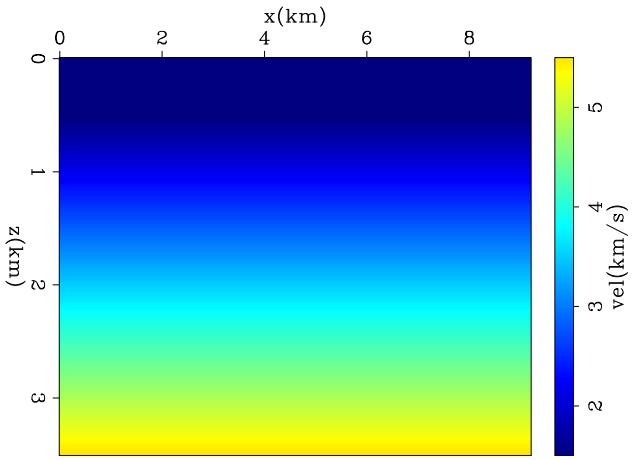

Figure 5: The initial velocity of Marmousi model. [**ER**] ali1/. init

I modeled the observed data with the conventional acoustic wave-equation nonlinear modeling operator. Then, I ran inversion without any tomographic regularization term. This inversion verified the first extension condition, that the modeled data can be explained using the initial model.

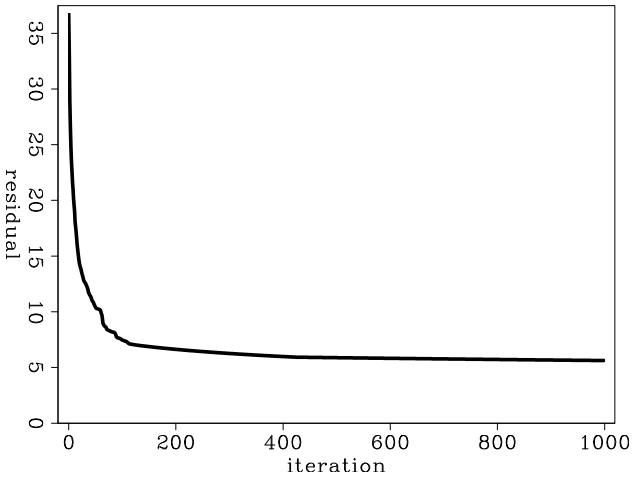

Figure 6: The data residual norm as a function of iterations of Marmousi model unregularized inversion. [**CR**] ali1/. res2

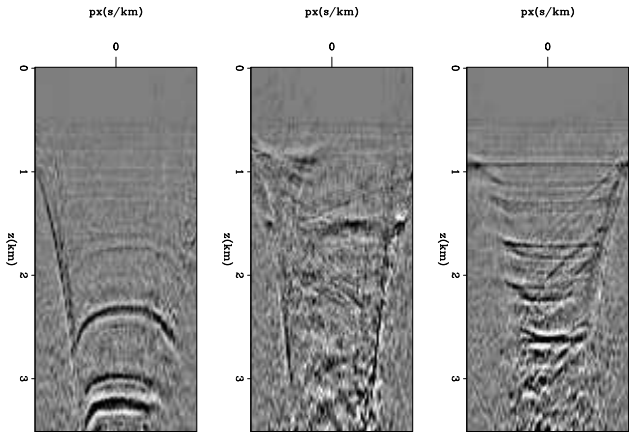

Figure 7: Three ray parameter gathers showing the difference between the initial model and the unregularized inverted model at x=2.5, 5, 7.5 km of Marmousi model. [**CR**] ali1/. inv2dv

I show the results of running 1000 iterations of the unregularized inversion. Figure 6 shows the residual of the data fitting as a function of iterations. The residual decreases monotonically without getting stuck in a local minima and is approaching zero. This means that the first condition is fairly satisfied for this example. Figure 7 shows the difference between the initial and final model at three locations as a function of depth and ray parameter. The three gathers show varying degrees of difference across the ray parameter axis, which indicates the inconsistency between these data components given the initial velocity model. Figure 8 shows the average of the final model across the ray parameter axis. Although the final model matches most of the observed data, no low wavenumber components are correctly estimated in this unregularized inversion since the kinematic errors are compensated for by the difference between ray parameter models.

Next, I show the results of running 10000 iterations of the inversion regularized by a derivative across the ray parameter axis. Figure 9 shows the residual of the data fitting and model regularization as a function of iterations. The data fitting residuals decrease slower than the data residuals in the unregularized inversion since two objective functions are competing to be minimized. Nonetheless, it is not getting stuck in a local minima and

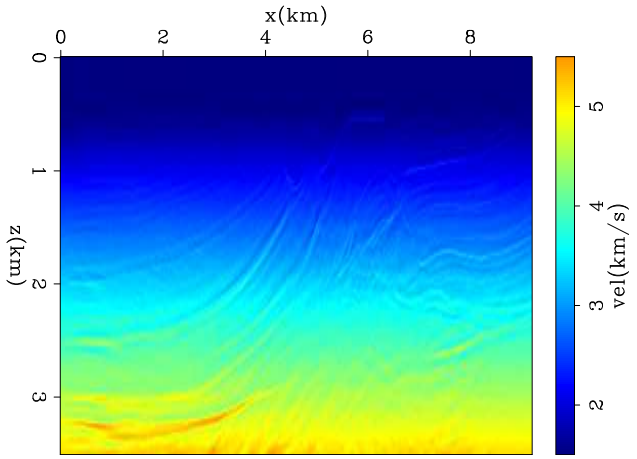

Figure 8: The unregularized inversion results of Marmousi model. [**CR**] ali1/. inv2

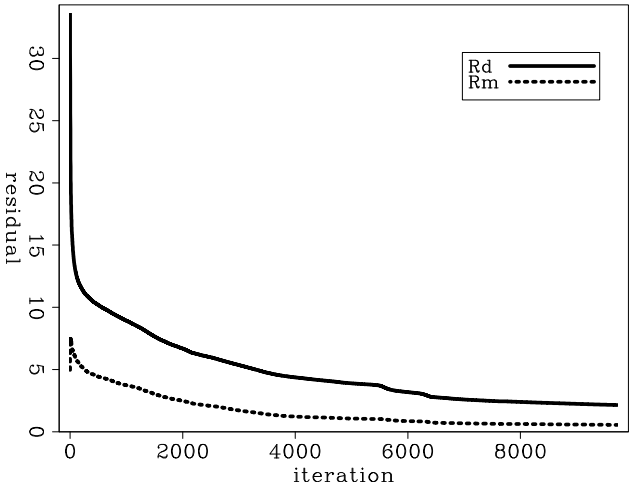

Figure 9: The data residual norm (solid line) and the model residual norm (dashed line) as a function of iterations of Marmousi model regularized inversion. [**CR**] ali1/. res

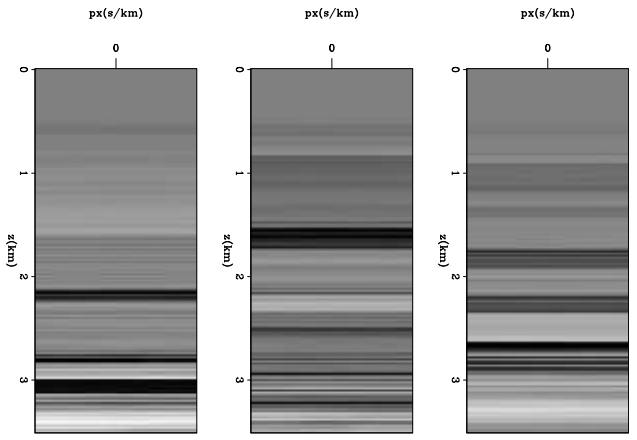

Figure 10: Three ray parameter gathers showing the difference between the initial model and the regularized inverted model at x=2.5, 5, 7.5 km of Marmousi model. [**CR**] ali1/. invdv

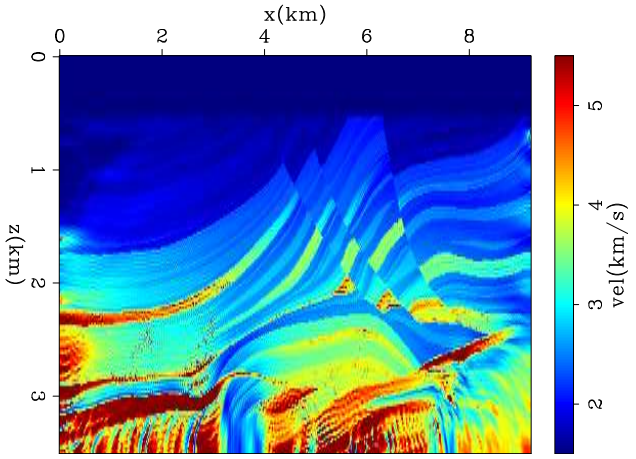

Figure 11: The regularized inversion results of Marmousi model. [**CR**] ali1/. inv

is approaching zero. Figure 10 shows the difference between the initial and final model at three locations as a function of depth and ray parameter. The three images show no variations across the ray parameter axis, which indicates that the inversion successfully converged the extended model to a physical model. Figure 11 shows the average of the final model across the ray parameter axis. Both low and high wavenumber components are correctly estimated and the inversion converged towards the true answer.

CONCLUSIONS

I have shown that extending the velocity in model axes increases the computational cost drastically. Scale separation can reduce the cost but remains much more expensive than conventional FWI. I presented an alternative approach to extended FWI by using data space axes. Although the underlying assumptions might make it less accurate than model space extensions in very complex models, the cost is greatly reduced and becomes similar to the cost of conventional FWI. The synthetic Marmousi example showed remarkable results even when the initial model had large errors. The results of this model are comparable to the results of model space extensions but are significantly cheaper in cost.

ACKNOWLEDGMENTS

I would like to thank the Stanford Exploration Project affiliate companies for financial support. I also thank Saudi Aramco for supporting my Ph.D. studies at Stanford University.

REFERENCES

Almomin, A. and B. Biondi, 2012, Tomographic full waveform inversion: Practical and computationally feasible approach: SEP-Report, **147**, 13–26.

Biondi, B., 2012, Tomographic full waveform inversion and linear modeling of multiple scattering: SEP-Report, **148**, 49–58.

Biondi, B. and A. Almomin, 2012, Tomographic full waveform inversion (TFWI) by combining full waveform inversion with wave-equation migration velocity analysis: SEP-Report, **147**, 1–12.

Biondi, B. and P. Sava, 1999, Wave-equation migration velocity analysis: SEG Technical Program Expanded Abstracts, **18**, 1723–1726.

Liu, F., D. W. Hanson, N. D. Whitmore, R. S. Day, and R. H. Stolt, 2006, Toward a unified analysis for source plane-wave migration: Geophysics, **71**, no. 4, S129–S139.

Luo, Y. and G. T. Schuster, 1991, Wave-equation traveltime inversion: Geophysics, **56**, 645–653.

Marfurt, K. J., 1984, Accuracy of finite-difference and finite-element modeling of the scalar and elastic wave equations: Geophysics, **49**, 533–549.

Pratt, R. G., 1999, Seismic waveform inversion in the frequency domain, Part 1: Theory and verification in a physical scale model: Geophysics, **64**, 888–901.

Sava, P. C. and S. Fomel, 2003, Angle-domain common-image gathers by wavefield continuation methods: Geophysics, **68**, 1065–1074.

Shen, P., 2004, Wave equation migration velocity analysis by differential semblance optimization: PhD thesis, Rice University.

Symes, W. W. and J. J. Carazzone, 1991, Velocity inversion by differential semblance optimization: Geophysics, **56**, 654–663.

Tang, Y., C. Guerra, and B. Biondi, 2008, Image-space wave-equation tomography in the generalized source domain: SEP-Report, **136**, 1–22.

Tarantola, A., 1984, Inversion of seismic reflection data in the acoustic approximation: Geophysics, **49**, 1259–1266.

Whitmore, N. D., 1995, An imaging hierarchy for common angle plane wave seismogram: PhD thesis, University of Tulsa.

Zhang, Y., B. Biondi, and Y. Tang, 2012, Residual moveout-based wave-equation migration velocity analysis: SEG Technical Program Expanded Abstracts, **31**, *submitted for publication.*

Zhang, Y., J. Sun, C. Notfors, S. H. Gray, L. Chernis, and J. Young, 2005, Delayed-shot 3D depth migration: Geophysics, **70**, E21–E28.

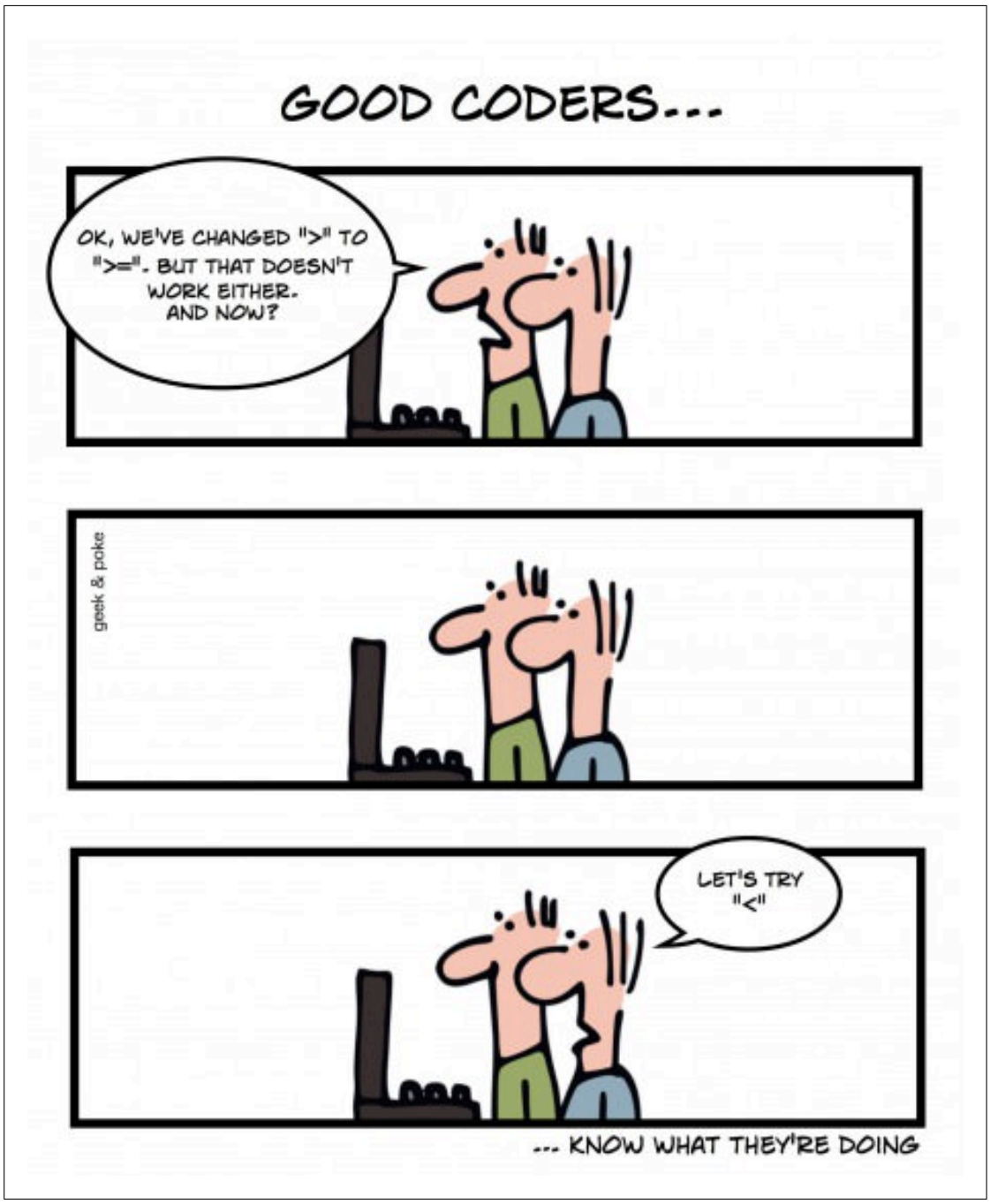
GOOD CODERS...
OK, WE'VE CHANGED ">" TO ">=". BUT THAT DOESN'T WORK EITHER. AND NOW?
geek & poke
LET'S TRY "<"
... KNOW WHAT THEY'RE DOING

Efficient depth extrapolation of waves in elastic isotropic media

Musa Maharramov

ABSTRACT

We propose a computationally efficient technique for extrapolating seismic waves in an arbitrary isotropic elastic medium. The method is based on factorizing the full elastic wave equation into a product of pseudo-differential operators. The method extrapolates displacement fields, hence can be used for modeling both pressure and shear waves. A significant reduction in the cost of elastic modeling can be achieved compared to the currently prevalent time- and frequency-domain numeric modeling methods and can contribute to making multicomponent elastic modeling part of the standard seismic processing work flow.

INTRODUCTION

Extrapolation of seismic wave fields in depth using one-way propagation operators is an efficient alternative to time- and frequency-domain modeling with the full wave equation, particularly in seismic migration applications (see (Claerbout, 1985), (Biondi, 2005)). While one-way extrapolators have long been established as key components of the seismic imaging toolbox for isotropic acoustic media, extrapolation of elastic wave fields is still carried out by solving the full elastodynamic system either in the time or frequency domain, either approach being computationally expensive. The high computational cost of wave extrapolation in elastic media is one of the barriers to a widespread adoption of multicomponent seismic processing in industrial applications. Some progress has been made recently in the development of efficient one-way methods for certain simplest *anisotropic* elastic models (e.g., vertically transversally isotropic or tilted transversally isotropic media – see (Shan, 2007), (Nolte, 2008), (Maharramov and Nolte, 2011)) However, these methods use the "pseudoacoustic" approximation (see (Grechka, 2009)) and are used for a kinematically accurate propagation of pressure waves only.

In this paper we present a method for one-way frequency-domain extrapolation of *displacement* fields in an elastic isotropic medium. The approach of this paper is based on factorizing the elastic wave equation using pseudo-differential operators without introducing stress-related unknown functions into the equations. Our approach is conceptually similar to the derivation of the acoustic single square-root equation (see (Claerbout, 1985)), except the resulting factorized propagation operators can not be obtained analytically, but are computed numerically.

THE METHOD

We start with the wave equation governing the displacement in an arbitrary heterogenous isotropic elastic medium in the *Navier form* (see (Segall, 2010)):

$$\rho\ddot{u^i} \;=\; \mu\Delta u^i + \frac{\mu}{1-2\nu}\frac{\partial}{\partial x_i}\frac{\partial u_k}{\partial x_k},\; i=1,2,3, \tag{1}$$

where u^i denote the components of a displacement field, μ is the shear modulus, ν is Poisson's ratio for the medium, and ρ is the density. In this paper we consider a heterogenous elastic medium under the assumption of *local homogeneity* – otherwise the elastic moduli would not be factored outside of the differentiation operators in equation 1. However, our method can be extended to cover the case when the local homogeneity assumption is dropped. "Freezing" the coefficients of equation 1 and applying the Fourier transform in time and horizontal variables $x_1 = x, x_2 = y$, and substituting

$$\frac{\mu}{1-2\nu} = \lambda + \mu, \tag{2}$$

where λ is the Lamé coefficient (see (Mavko et al., 2009),(Segall, 2010)), we get

$$\begin{aligned}
\rho\omega^2 u^1 + \mu\left[(-k_x^2-k_y^2)u^1 + \frac{\partial^2 u^1}{\partial z^2}\right] + (\lambda+\mu)\left[-k_x^2 u^1 - k_x k_y u^2 + ik_x\frac{\partial u^3}{\partial z}\right] &= 0,\\
\rho\omega^2 u^2 + \mu\left[(-k_x^2-k_y^2)u^2 + \frac{\partial^2 u^2}{\partial z^2}\right] + (\lambda+\mu)\left[-k_x k_y u^1 - k_y^2 u^2 + ik_y\frac{\partial u^3}{\partial z}\right] &= 0,\\
\rho\omega^2 u^3 + \mu\left[(-k_x^2-k_y^2)u^3 + \frac{\partial^2 u^3}{\partial z^2}\right] + (\lambda+\mu)\left[ik_x\frac{\partial u^1}{\partial z} + ik_y\frac{\partial u^2}{\partial z} + \frac{\partial^2 u^3}{\partial z^2}\right] &= 0,
\end{aligned} \tag{3}$$

where k_x, k_y are horizontal wave numbers and ω is the frequency. The left-hand side of system 3 is the result of an ordinary differential operator applied to a vector-function $\mathbf{u} = (u^1, u^2, u^3)$ and parameterized by horizontal wave numbers. In the present form equations 3 cannot be used for computationally efficient explicit depth extrapolation in a heterogeneous medium; however, these equations can be used for modeling displacements by solving a series of boundary-value problems (see (Maharramov, 2012)). In (Maharramov, 2012) it was suggested that equations 3 might be factorized in such a way as to allow solving them by alternating *one-way extrapolation* in opposite directions. More specifically, we seek a factorization of operator equation 3 of the form:

$$\left(E(\lambda,\mu)\frac{\partial}{\partial z} + A(k_x,k_y) + c_\omega I\right)\times\left(E(\lambda,\mu)\frac{\partial}{\partial z} + B(k_x,k_y) + c_\omega I\right)\mathbf{u} = 0, \tag{4}$$

where

$$\begin{aligned}
E(\lambda,\mu) \;&=\; \begin{bmatrix} \sqrt{\mu} & 0 & 0\\ 0 & \sqrt{\mu} & 0\\ 0 & 0 & \sqrt{\lambda+2\mu}\end{bmatrix},\\
c_\omega \;&=\; \sqrt{\rho}\omega,
\end{aligned} \tag{5}$$

and A, B are 3×3 matrices with components that are complex-valued functions of the horizontal wave numbers, I is the 3×3 identity matrix. Performing the multiplication in equation 4 and using equation 3, we obtain:

$$\begin{aligned}
A(k_x,k_y)B(k_x,k_y) + c_\omega[A(k_x,k_y) + B(k_x,k_y)] &= P(k_x,k_y),\\
A(k_x,k_y)E(\lambda,\mu) + E(\lambda,\mu)B(k_x,k_y) + 2c_\omega E(\lambda,\mu) &= S(k_x,k_y),
\end{aligned} \tag{6}$$

where

$$P = \begin{bmatrix} -(\lambda+2\mu)k_x^2 - \mu k_y^2 & -(\lambda+\mu)k_x k_y & 0 \\ -(\lambda+\mu)k_x k_y & -(\lambda+2\mu)k_y^2 - \mu k_x^2 & 0 \\ 0 & 0 & -\mu(k_x^2+k_y^2) \end{bmatrix},$$
$$S = \begin{bmatrix} 0 & 0 & i(\lambda+\mu)k_x \\ 0 & 0 & i(\lambda+\mu)k_y \\ i(\lambda+\mu)k_x & i(\lambda+\mu)k_y & 0 \end{bmatrix}. \tag{7}$$

Combining equations 6 and 7, we get the following equation for the operators A and B:

$$\begin{aligned} A(k_x,k_y)B(k_x,k_y) + c_\omega(A(k_x,k_y)+B(k_x,k_y)) &= P(k_x,k_y), \\ E(\lambda,\mu)B(k_x,k_y) + A(k_x,k_y)E(\lambda,\mu) &= \tilde{S}(k_x,k_y), \end{aligned} \tag{8}$$

where

$$\tilde{S}(k_x,k_y) = S(k_x,k_y) - 2c_\omega E(\lambda,\mu). \tag{9}$$

Equations 4, 8 in combination with equations 7 and 9 suggest the following procedure for extrapolating solutions to system 1 in depth:

1. Solve the system of matrix equations 8 for A, B, for each pair of horizontal wave numbers k_x, k_y and two reference values of each elastic parameter $\lambda_{\min}, \lambda_{\max}$ and $\mu_{\min}, \mu_{\max}$;

2. Evaluate
$$\left(E(\lambda,\mu)\frac{\partial}{\partial z} + B(-i\partial_x, -i\partial_y) + c_\omega I\right)\mathbf{u}(x,y,z=0)$$
from the initial conditions and assign the value to an auxiliary function $\tilde{\mathbf{u}}(x,y,z=0)$;

3. Solve
$$\left(E(\lambda,\mu)\frac{\partial}{\partial z} + A(-i\partial_x, -i\partial_y) + c_\omega I\right)\tilde{\mathbf{u}}(x,y,z) = 0 \tag{10}$$
by downward continuing in depth, using the formula
$$\tilde{u}(x,y,z+\Delta z) = \exp\left[-\Delta z E^{-1}(A(-i\partial_x,-i\partial_y)+c_\omega I)\right]\tilde{\mathbf{u}}(x,y,z). \tag{11}$$

4. Perform each step of the depth extrapolation for four combinations of the reference elastic parameters, then apply the inverse Fourier transform to the four fields and interpolate at each spatial point of the depth slice using true $\lambda(x,y), \mu(x,y)$ as e.g. in the PSPI method (see (Biondi, 2005)).

5. After reaching the desired maximum depth, find the solution $\mathbf{u}$ by *upward* extrapolation:
$$\left(E(\lambda,\mu)\frac{\partial}{\partial z} + B(-i\partial_x, -i\partial_y) + c_\omega I\right)\mathbf{u}(x,y,z) = \tilde{\mathbf{u}}(x,y,z). \tag{12}$$

6. Repeat the above steps for each frequency component $\mathbf{u}(\omega,x,y,z)$.

The above algorithm is stable if the spectrum of matrix

$$A(k_x, k_y) + c_\omega I \tag{13}$$

is not in the interior of the left half-plane, and the spectrum of

$$B(k_x, k_y) + c_\omega I \tag{14}$$

is not in the interior of the right half-plane. While the above algorithm tries to mimic two-way wave propagation, it is effectively just an approximation to the propagation process as it ignores the interaction between the up and down-going wave at intermediate depth steps. A less accurate alternative would be to downward-continue the wave field using equation 11 in a way similar to the one-way depth extrapolation using the scalar square-root equation (see (Claerbout, 1985),(Biondi, 2005)). The latter approach would be unable to image any dips beyond 90°, however, it would reduce the cost of extrapolation by a further factor of 2. Note the cost of solving equation 10 in depth is roughly three times that of solving the scalar square-root equation.

The above analysis may be extended to the case of an arbitrary anisotropic elastic medium. The fact that the components of the pseudo-differential operator matrices $A(-i\partial_x, -i\partial_y), B(-i\partial_x, -i\partial_y)$ are not given in an analytical form, but are only computed numerically, does not limit their applicability.

Factorization of system 3 in the elastostatic case was one of the approaches mentioned by the author in Maharramov (2012). However, the one-way extrapolation technique is mostly useful for elastodynamic problems as the passband of the factorized depth extrapolators (e.g., as in equation 11) narrows down to zero with the temporal frequency passing to the zero static limit.

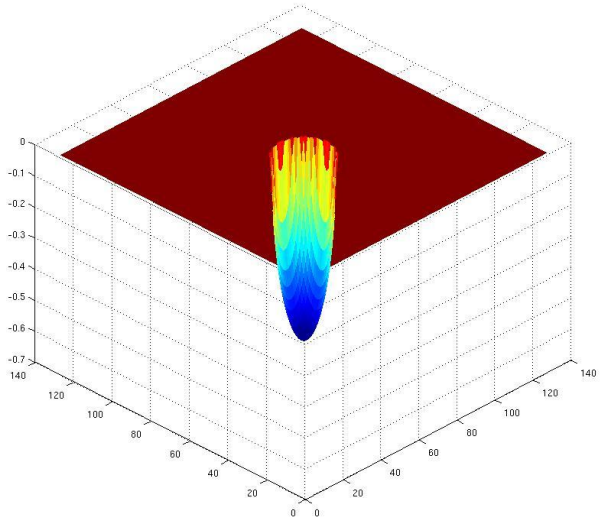

Figure 1: The phase of a phase-shift operator corresponding to the maximum imaginary part of the eigenvalues of operator 15. Multicomponent "phase-shift" is defined by three such scalar phase-shift operators and a 3×3 matrix Q of equation 16. [**ER**] musa/. maximageigenval

Note that equation 1 uses elastic parameterization that degenerates into a singularity if the shear modulus is equal to zero. This is not causing any problems with purely acoustic wave extrapolation as the singularity is effectively removed from equations 3 by the substitution in equation 2.

IMPLEMENTATION AND RESULTS

The system of matrix equations 8 is solved only once for each triple of temporal frequency and elastic moduli values, and for each pair of horizontal wave numbers. In our prototype implementation of the one-way extrapolator we compute the matrices A, B at the beginning of the frequency loop and subsequently use the tabulated matrices in the depth extrapolation loop (inside the frequency loop). A more efficient approach can be employed in a production implementation of the extrapolation method: system 8 can be solved using Newton's method (see e.g. (Higham, 2008)) in a one-off computation for each set of the temporal frequency, elastic moduli and horizontal wave numbers and stored in a look-up table. The symmetry of the extrapolation operators 11, that appear to be multi-component counterparts of the acoustic phase-shift operator (see Claerbout (1985)), can be exploited to achieve a substantial reduction in the size of the precomputed operator tables. Figure 1 is the plot of the maximum of the imaginary parts of the three eigenvalues of operator

$$K = -\Delta z E^{-1} \left[A(-i\partial_x, -i\partial_y) + c_\omega I \right], \tag{15}$$

within its passband. The operator is the one used later to produce images of Figures 2,3,4,5. The real parts of the eigenvalues of operator 15 are zero within the operator passband and negative outside. The imaginary parts of the other two eigenvalues exhibit similar behavior. Operator K, of equation 15, is the logarithm of the extrapolation operator 11, and the spectral plot of Figure 1 corresponds to the phase of the phase-shift extrapolator in the acoustic case (see (Biondi, 2005)). The crucial difference in the elastic multicomponent case is that the multicomponent "phase-shift" is defined by three such scalar phase-shift operators with phases ϕ_1, ϕ_2, ϕ_3, and a unitary operator Q, determined by the eigenvector expansion of K as follows:

$$K = Q \begin{bmatrix} i\phi_1 & 0 & 0 \\ 0 & i\phi_2 & 0 \\ 0 & 0 & i\phi_3 \end{bmatrix} Q^*. \tag{16}$$

The pass bands of the three phase shift operators are, generally, different, but the real parts of the eigenvalues of 15 are non-positive across all three pass bands.

Figures 2,3,4,5 demonstrate the result of applying our method to extrapolating displacement waves from a concentrated impulse at the surface. Medium parameters used in this test were 316 `m/s` shear-wave velocity

$$v_{\mathtt{S}} = \sqrt{\mu/\rho}$$

and 632 `m/s` pressure-wave velocity

$$v_{\mathtt{P}} = \sqrt{(\lambda + 2\mu)/\rho}.$$

The extrapolation grid was $128 \times 128 \times 128$ with a 5 `m` step, frequency range 2-12 `Hz` with 1 `Hz` step. The values of the elastic parameters used in this test are uncharacteristically low for seismic applications and were chosen solely for the purpose of fast small-scale simulation on a single-core PC using `Matlab`.

Since the impulse at the surface is an asymmetric horizontal displacement but can be assumed to be symmetric in the vertical direction, our waves are effectively a combination

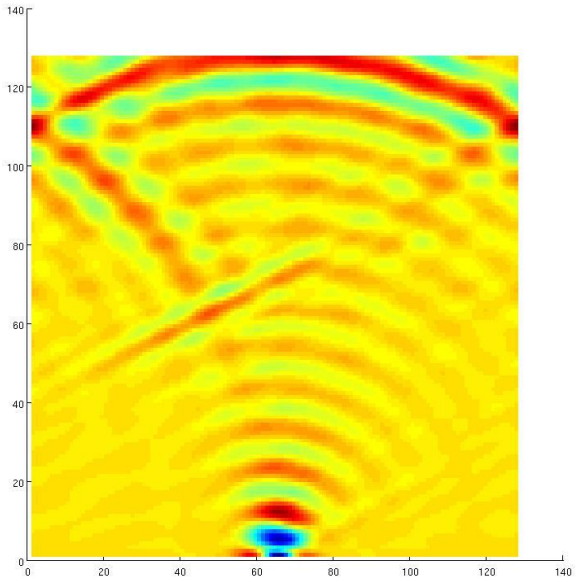

Figure 2: Pressure wave extrapolated from an impulse displacement, 2-12 `Hz`, $128 \times 128 \times 128$ grid, 5 `m` step, 316 `m/s` shear-wave and 632 `m/s` pressure-wave velocity. [**ER**] musa/. pressure

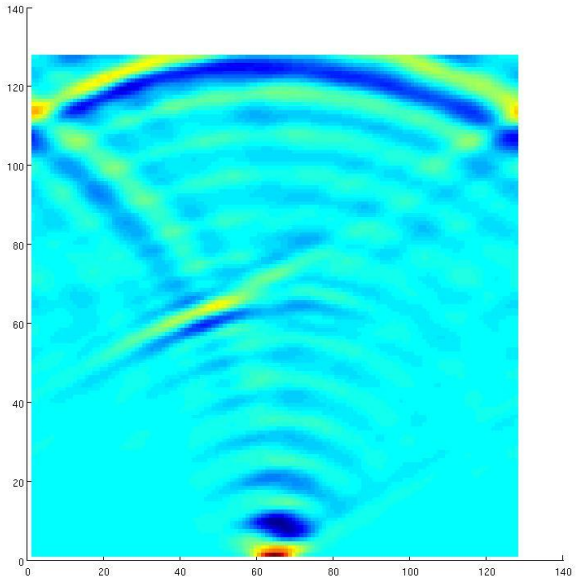

Figure 3: Vertical component of a wave extrapolated from an impulse displacement, inline section, 2-12 `Hz`, 128×128 grid, 5 `m` step, 316 `m/s` shear-wave and 632 `m/s` pressure-wave velocity. [**ER**] musa/. component3

pressure and shear waves for the horizontal components, while the vertical displacement wave should kinematically match the pressure wave. And indeed, the pressure wave plot 2 and vertical displacement plot 3 exhibit excellent kinematic agreement.

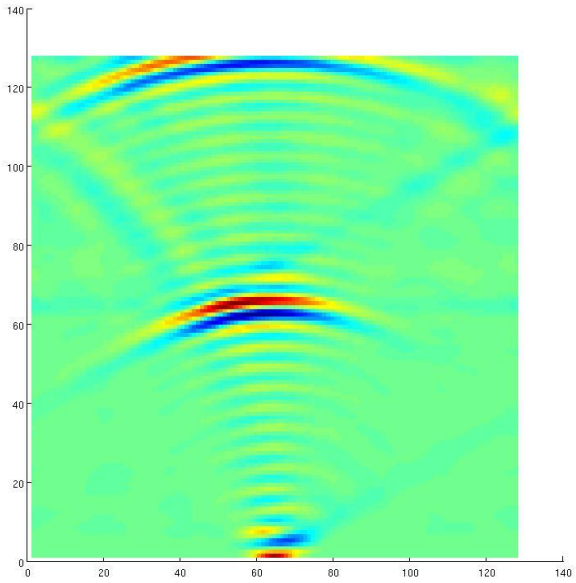

Figure 4: Inline component of a wave extrapolated from an impulse displacement, inline section, 2-12 `Hz`, $128 \times 128 \times 128$ grid, 5 `m` step, 316 `m/s` shear-wave and 632 `m/s` pressure-wave velocity. Note the slow shear wave. [**ER**] musa/. component1

The horizontal wave-component plots 4 and 5, on the other hand, show pressure- and shear-wave images, both correctly positioned in agreement with the velocity values used in the simulation. Boundary reflections and low frequency content cause some imaging artifacts that are not related to the method.

CONCLUSIONS AND DISCUSSION

The method presented in this paper can be used in seismic migration algorithms in order to achieve a substantial reduction of run time in comparison with reverse time migration. More specifically, stability of the time-domain modeling typically utilized in the reverse-time migration requires time steps significantly smaller than the time resolution of seismic data (see (Biondi, 2005)). Depth extrapolation of wave fields using one-way equations 10 and 12 can be performed for an arbitrary frequency range. Extrapolating wave fields in the frequency domain using two-way system 3 would require solving a large sparse system of equations using e.g. a finite element method, still posing significant computational challenges for inhomogeneous media. However, the one-way extrapolation method, while limited in dip and less accurate in terms of amplitudes, lends itself to efficient implementation using e.g. PSPI or finite differencing. Furthermore, the approach of this paper can be expected to apply to more complex elastic anisotropic models (see (Grechka, 2009)) and may be developed into a computationally efficient alternative to the existing pseudo-acoustic anisotropic modeling methods while allowing easy separation of pressure and shear waves.

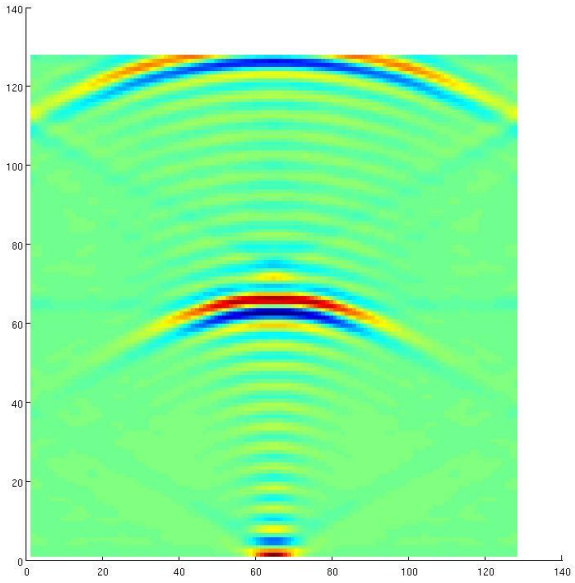

Figure 5: Crossline component of a wave extrapolated from an impulse displacement, inline section, 2-12 `Hz`, $128\times128\times128$ grid, 5 `m` step, 316 `m/s` shear-wave and 632 `m/s` pressure-wave velocity. Note the slow shear wave. [**ER**] musa/. component2

ACKNOWLEDGEMENTS

The author would like to thank the Stanford Exploration Project for supporting this work, and Jon Claerbout, Stewart Levin, Biondo Biondi and Paul Segall for a number of useful discussions.

REFERENCES

Biondi, B., 2005, 3D Seismic Imaging: Society of Exploration Geophysicists.

Claerbout, J., 1985, Imaging the earth's interior: Blackwell Scientific.

Grechka, V., 2009, Applications of seismic anisotropy in oil and gas industry: EAGE.

Higham, N., 2008, Functions of matrices: theory and computation: SIAM.

Maharramov, M., 2012, Identifying reservoir depletion patterns with applications to seismic imaging: SEP Report 147, 193–218.

Maharramov, M. and B. Nolte, 2011, Efficient one-way wave-equation migration in tilted transversally isotropic media: 73rd EAGE Conference and Exhibition, Extended Abstracts.

Mavko, G., T. Mukerji, and J. Dvorkin, 2009, The rock physics handbook: Cambridge University Press.

Nolte, B., 2008, Fourier finite-difference depth extrapolation for VTI media: 70th EAGE Conference and Exhibition, Extended Abstracts.

Segall, P., 2010, Earthquake and volcano deformation: Princeton University Press.

Shan, G., 2007, Optimized implicit finite-difference migration for TTI media: 77th SEG Conference and Exhibition, Extended Abstracts.

Modeling ocean-bottom seismic rotation rates

Ohad Barak and Shuki Ronen

ABSTRACT

Seismic systems today record up to four components which provide the particle displacement and the pressure. The pressure is proportional to the divergence of the displacement. We need the hydrophones because the divergence is useful and cannot be calculated in processing. The curl cannot be calculated from four component data just like the divergence cannot be directly calculated from the displacements. If the curl is useful, we can add rotation sensors to today's four component recorders and have seven component data.

To evaluate the added information that would come from rotation sensors we used elastic modeling. In our synthetic data experiment, we predicted the effect of a seabed scatterer on fully multi-component data. We used a pressure source that generates P waves. The P-waves are converted to S-waves and to surface waves propagating on the seabed. Our evaluation is that the added information from rotation sensors will be useful for identifying and separating surface waves from body waves.

INTRODUCTION

Four-component ocean-bottom seismic sensors (Figure 1) are a combination of a hydrophone and three-component geophones that measure linear particle velocity. The hydrophone records pressure changes in the water, and is ideally coupled to the water. It picks up mostly P-waves. The geophones are coupled to the sea-bed, and record particle velocities relating to all wave modes: P, S, and surface waves. The multiplicity of wave modes recorded by the geophones can be problematic for later sesimic processing stages, which assume a single wave mode recording (i.e., imaging with P-wave or S-wave data only). It is therefore desirable to be able to separate different wave modes within the data.

The divergence of particle motion is a spatial derivative. If we knew the displacement values everywhere within the seismic volume, then we could calculate the divergence. However, receiver stations are usually too sparse in relation to the acquired wavelengths to calculate the divergence, and in any case are always spread along a single surface (the sea bottom). The value of the divergence is not redundant even if we measure the three components of the displacement, since it can be used to detect the propagation direction of the waves incident on the sea bottom (upward or downward). The pressure that the hydrophone records is proportional to the divergence of the particle displacements, and is therefore used for upgoing/downgoing wavefield separation.

Similar to the divergence, we can measure the rotation of particle motion by calculating the curl of the displacements. As with the divergence, curl is a spatial derivative operator, and insufficient sampling of the waves in the field can inhibit its direct calculation. However, a recently-proposed rotation sensor can be used to measure the rotation "in place". A

rotation sensor measures the rotation rate (radians/unit time) of the ground at the receiver location. Similar to linear motion, the rotational motion has three components: roll, pitch and yaw. Figure 2 illustrates these motion components.

There are implementations of rotational seismic recording for earthquake seismology (Lee et al., 2009) employing ring lasers. However, these instruments are large and expensive, and are therefore not applicable to exploration acquisition. There have also been attempts to record rotational seismic data with a "Rotaphone": conventional geophones arranged along a circle (Brokesova and Malek, 2010). Newer technologies are currently under development to make rotational sensors a viable option for seismic acquisition systems. The interested reader can go to http://www.rotational-seismic.org for more information on this acquisition technology.

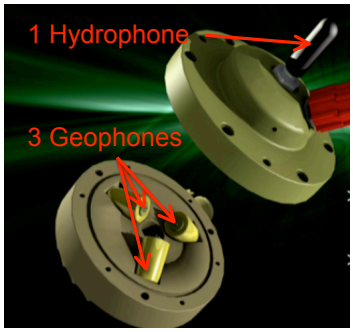

Figure 1: An example of a 4 component receiver package. One hydrophone and three geophones provide (after correction for the instrument response) the pressure of the water and the velocity of the sensor package, which is ideally coupled to the seabed. The particle velocity is the time derivative of the displacement vector, and the pressure is proportional to the divergence of the displacement, which is a spatial derivative. [**NR**] ohad2/. obnode

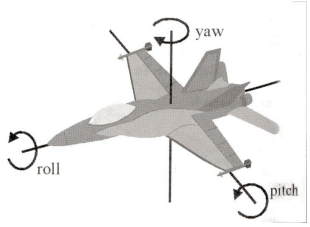

Figure 2: To know what an aircraft is doing, it is not sufficient to know its linear velocity but also the rotations. There are three components to the velocity, and in addition there are three components to the rotation: roll, pitch, and yaw. [**NR**] ohad2/. f18

The purpose of this paper is to estimate what kind of rotational motion we may expect in a simple model of ocean-bottom acquisition. We also want to show that additional information about the wave types can be acquired by having rotational motion data.

THEORY

The elastic isotropic wave equation has two state variables: the stress tensor and the particle velocity vector. The particle velocities are propagated by:

$$\partial_i \sigma_{ii} + \partial_j \sigma_{ij} + f_i(\mathbf{x}, t) = \rho \partial_t v_i, \tag{1}$$

where σ_{ii} are the normal stresses, σ_{ij} are the transverse stresses, f_i is a particle velocity force function in direction i, $\mathbf{x}$ is the spatial source location operating at time t, ρ is density and v_i is the particle velocity in direction i. The stresses are propagated using the stress-displacement relation:

$$\begin{aligned} \partial_t \sigma_{ii} &= (\lambda + 2\mu)\partial_i v_i + \lambda \partial_j v_j + f^P(\mathbf{x}, t), \\ \partial_t \sigma_{ij} &= \mu \left(\partial_j v_i + \partial_i v_j\right), \end{aligned} \tag{2}$$

where λ and μ are the Lamé elastic constants and f^P is a pressure force function. The pressure force is added equally to the normal stresses to generate a P-wave source.

We use the staggered time grid methodology for elastic propagation (Virieux, 1986), in which the stresses and particle velocities are half a time step apart. Therefore equations 1 and 2 are solved in alternation during the propagation.

The divergence of particle displacements is proportional to the pressure in the medium, the proportion being the medium parameters. It is equal to the average of the normal stresses in the stress tensor:

$$P = \overline{\boldsymbol{\sigma}} = (\lambda + \mu)\, \nabla \cdot \vec{\mathbf{u}}, \tag{3}$$

where P is the pressure value and $\vec{\mathbf{u}}$ are the displacements. Pressure waves cause a volumetric deformation in the medium, and their value can therefore be extracted by using equation 3 on forward modeled wavefields. However, other wave types can also generate a volumetric deformation at free surfaces, as a result of the discontinuity of the stresses.

We define rotation as the first time derivative of the curl of displacements:

$$\vec{\mathbf{R}} = \partial_t \nabla \times \vec{\mathbf{u}}. \tag{4}$$

The curl operation results in the non-volumetric part of the deformation, i.e. the "shear" deformation. At a free surface, this deformation will cause a rotation. In an isotropic medium, the curl is associated with S-waves. However, at a free surface, both P-waves and surface waves will also generate non-volumetric deformation. The units we use for rotations in this paper are milliradians/second.

MODELING RESULTS

The purpose of the modeling we ran was to synthesize ocean-bottom seismic acquisition, therefore we used a simple 2-layer model of water over solid. The source was at the water surface, and receivers were at the water bottom. We executed two runs: one with a near-seabed anomaly, and one without. The anomaly generated scattering of both P and S waves, which upon interacting with the seabed also gave rise to a seabed interface wave. The model without the anomaly enabled us to see which part of the wavefield was due to the scattering. The V_p velocity models used are shown in Figures 3(a) and 3(b). The parameters of the two layers were:

1. $V_{p1} = 1.5\,\mathrm{km/s}$, $V_{p2} = 1.6\,\mathrm{km/s}$.

2. $V_{s1} = 0\,\mathrm{km/s},\ V_{s2} = 0.6\,\mathrm{km/s}$.

3. $\rho_1 = 1.025\,\mathrm{gr/cm^3},\ \rho_2 = 1.7\,\mathrm{gr/cm^3}$.

The anomaly was a Gaussian, which extended outward to a radius of 10 meters, and was centered 10 meters below the seabed. The medium parameters at the center of the anomaly were: $V_p = 1.75\,\mathrm{km/s}$, $V_s = 0.9\,\mathrm{kms}$, and $\rho = 2.1\,\mathrm{gr/cm^3}$. We did not do any testing with the anomaly parameters, although presumably altering these parameters would result in greater or lesser scattering. At this point, all we required was a feasible source of surface waves. A near-seabed anomaly simulates a "rock" buried just below the seabed, or the leg of a platform, either of which could be sources for scattered surface waves. Our source was a pressure source simulating an airgun, located at the water surface. The wavelet was a Ricker with 25Hz central frequency. There is no source-side ghost from the water surface, since we used an absorbing upper boundary. However, this ghost is simulated by the second lobe of the injected Ricker wavelet.

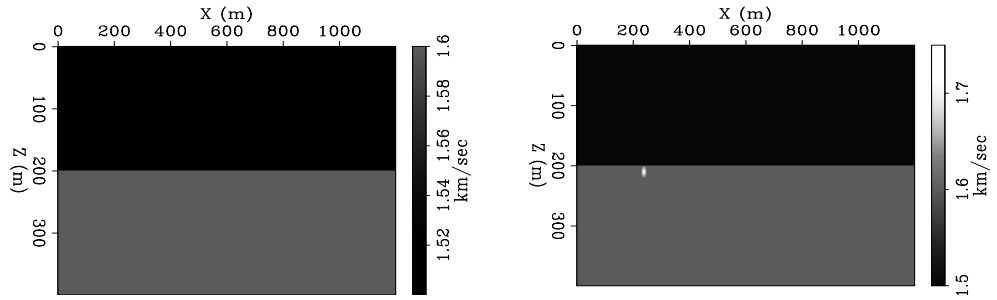

(a) (b)

Figure 3: P-wave velocity models. (a) velocity model without anomaly. (b) velocity model with anomaly. The anomaly is a Gaussian, with a diameter of 20 meters. [**ER**] ohad2/. vp2d,vp2d-anom

Figures 4(a) and 4(b) are snapshots of the vertical and horizontal P particle velocities of the entire wavefield at $t = 0.3$s. The incident, reflected and transmitted P-waves are prominent in these snapshots. Also visible is the transmitted S-wave, which is the conversion of the P-wave inciding on the seabed. The scattered S-wave and Scholte wave are visible as a semicircle, expanding from the anomaly location at $x = 100$m.

Figure 4(c) is the pressure as calculated by equation 3. We can see that the waves that generate most of the volumetric deformation are indeed the P-waves. However, the Scholte wave also generates some volumetric deformation at the seabed. Figure 4(d) is the rotation as calculated by equation 4. The waves that generate shear deformation (and thus rotational motion at the surface) are the transmitted S-wave, and the scattered S and Scholte waves. Notice that the transmitted S-wave is coming off the P head-wave, and is therefore propagating along the seabed at P-wave velocity.

Figures 5(a)-5(d) are snapshots of the same four fields, at $t = 0.8$s. The scattered S-wave and the scattered Scholte wave are separated at this point in the propagation, since the velocity of surface waves is slightly lower than that of S-waves. The imprint of the Scholte wave on both the pressure and the rotation sections is visible.

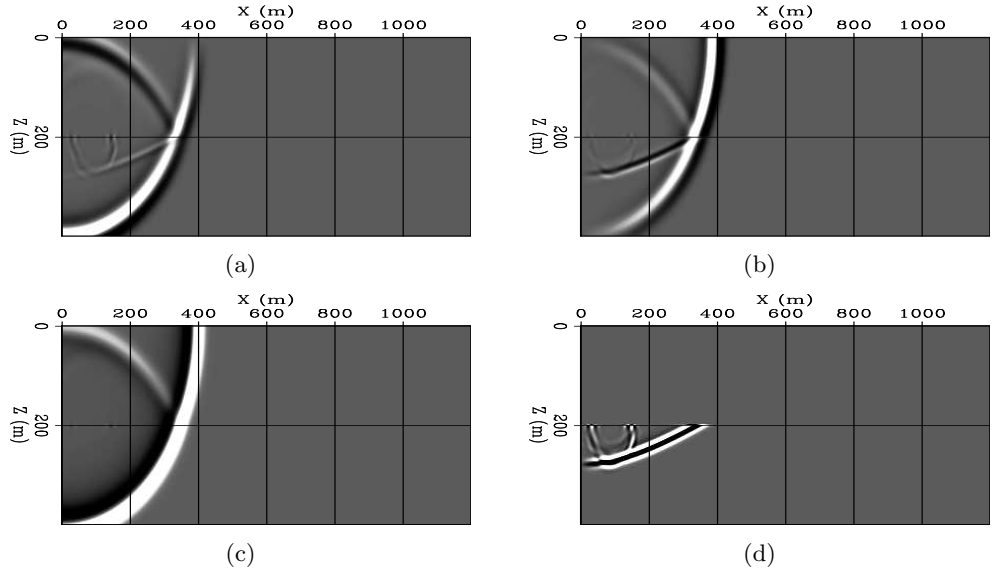

Figure 4: Wavefield snapshots at $t = 0.3$s seconds for the velocity model containing a near-surface anomaly. (a) Vertical particle velocity. (b) Horizontal particle velocity. (c) Pressure. (d) Rotation. The source is an airgun near the sea surface. In (a) and (b), all wave modes are present: direct P, reflected P, transmitted P and transmitted S. Also apparent are the S and Scholte waves which have scattered off the anomaly at $x = 100m$. In (c) and (d) there is separation: the S waves are not in (c) and P waves are not in (d). The surface waves are in both (c) and (d). [**ER**] ohad2/. 0vx2b,0vz2b,0P2b,0rot2b

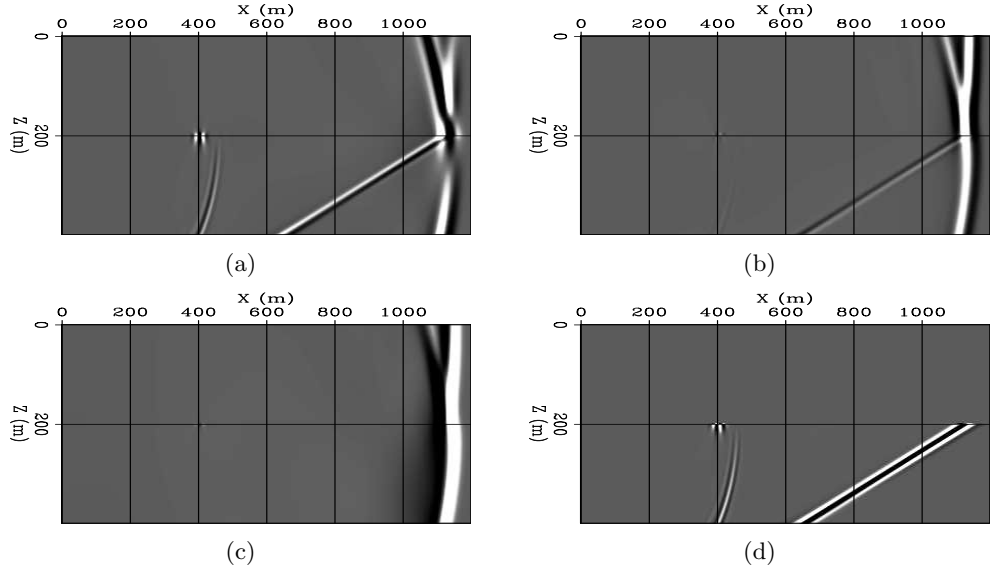

Figure 5: Wavefield snapshots at $t = 0.8$ seconds for the velocity model containing a near-surface anomaly. (a) Vertical particle velocity. (b) Horizontal particle velocity. (c) Pressure. (d) Rotation. Note how the scattered S body wave and the Scholte surface wave separate with travel time, as a result of their slightly differing velocities. Note that the Scholte wave generates both a rotational and a volumetric deformation. [**ER**] ohad2/. 0vx2,0vz2,0P2,0rot2

Figures 6(a) and 6(b) are the vertical and horizontal particle displacement recordings at the seabed for the velocity model without the anomaly. Figures 6(c) and 6(d) are the pressure and rotation, respectively. The incident P-wave causes both a pressure deformation and a shear deformation at the surface, and it therefore generates a transmitted S-wave. However the moveout of the S-wave is still that of the P-wave.

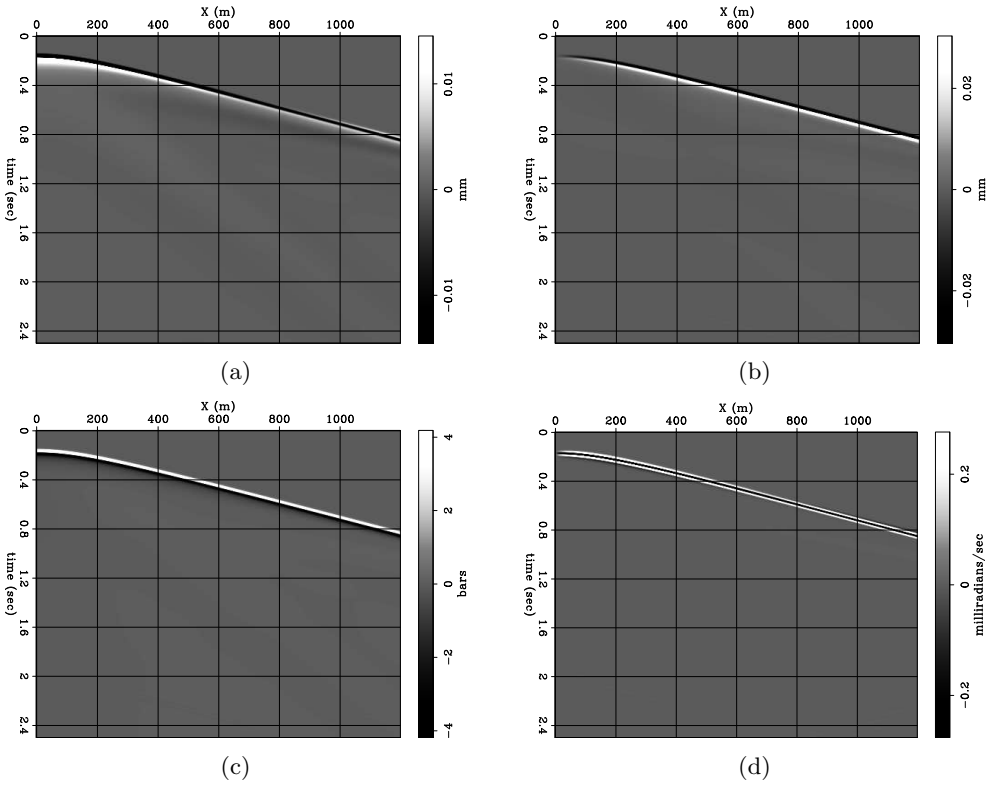

Figure 6: Synthetic data recording at sea-bottom without anomaly. (a) Vertical particle displacement. (b) Horizontal particle displacement. (c) Pressure. (d) Rotation. [**ER**] ohad2/. 0uxr1,0uzr1,0Pr1,0rotr1

Figures 7(a) and 7(b) are the vertical and horizontal particle displacement recordings at the seabed for the velocity model containing the anomaly. At $x = 1000$m, the arrivals of the direct P, scattered S and scattered Scholte wave are are marked. The S arrival is too weak compared to the P and Scholte waves to be observed in these sections. Figures 7(c) and 7(d) are the pressure and rotation recordings. We can think of these sections as the hydrophone and rotational sensor recordings. Comparing Figures 6(d) and 7(d), we can see that while most of the linear particle displacement is due to the P-wave, the Scholte wave is responsible for generating strong rotational motion.

Figures 8(a)-9(c) show the three separate arrival-time windows of each wave type. The arrival times and offset where they were extracted from are marked in Figure 7(a). Figure 8(a) is the volumetric pressure generated by the P-wave and Scholte wave arrivals, as calculated by equation 3. Figure 8(b) is the hodogram of particle displacements of those arrivals. Notice that the P hodogram is slightly elliptical, which means that the particle motion is not linear, as it is in a body wave. The reason for that is the mode conversion which takes place when the P-wave hits the seabed. What we are seeing is a combination

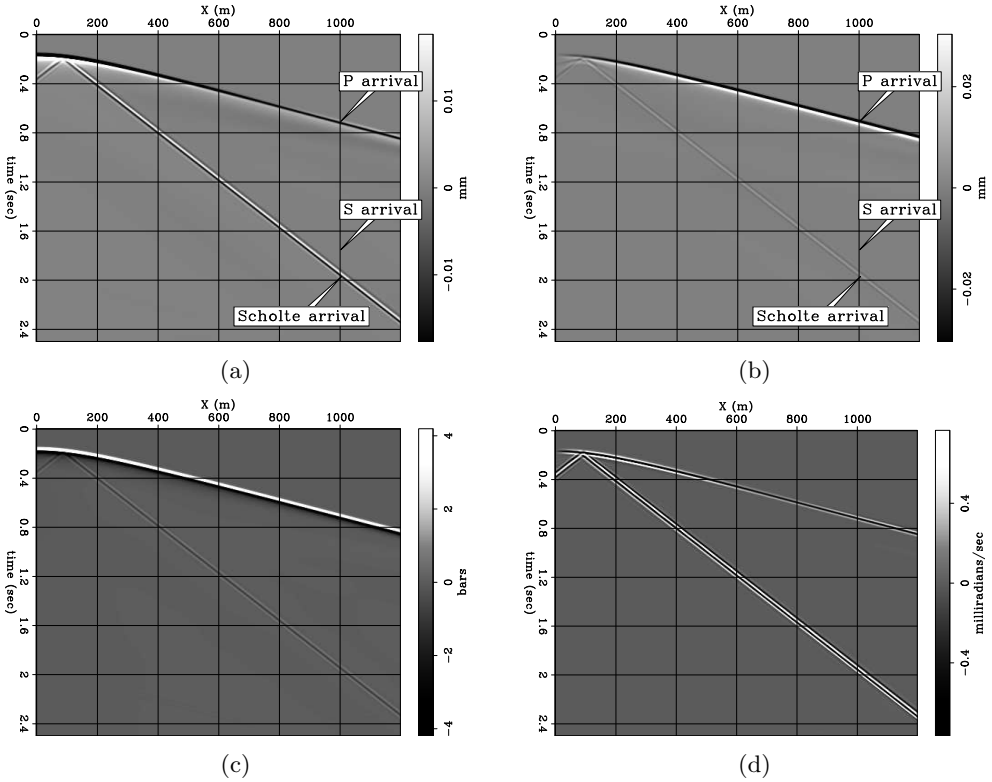

Figure 7: Synthetic data recording at sea-bottom with anomaly. The scattered Scholte wave is visible, but the scattered S-wave is relatively too weak to observe in these sections. The annotations indicate where time windows were taken for the plots in the next figure. (a) Vertical particle displacement. (b) Horizontal particle displacement. (c) Pressure. (d) Rotation. [**ER**] ohad2/. 0uxr2,0uzr2,0Pr2,0rotr2

of P and S displacements. We can see however that the Scholte displacement hodogram is very elliptical. Figure 8(c) is the rotation rate of the P and Scholte arrivals, as calculated by equation 4. The P-wave does generate some rotational motion, and this is again a result of the mode conversion at the seabed. However, the Scholte wave generates greater rotational motion, even though the linear displacements of this wave are much weaker than those of the P-wave.

Figures 9(a)-9(c) are the pressure, displacement hodogram and rotation rate of the scattered S-wave arrival. The volumetric pressure this arrival generates is very weak compared to the P-wave, but while its displacements are 3 orders of magnitude weaker than those of the P-wave, its rotational motion is only 2 orders of magnitude weaker. Note how the hodogram is nearly perpendicular to the P-wave displacement hodogram.

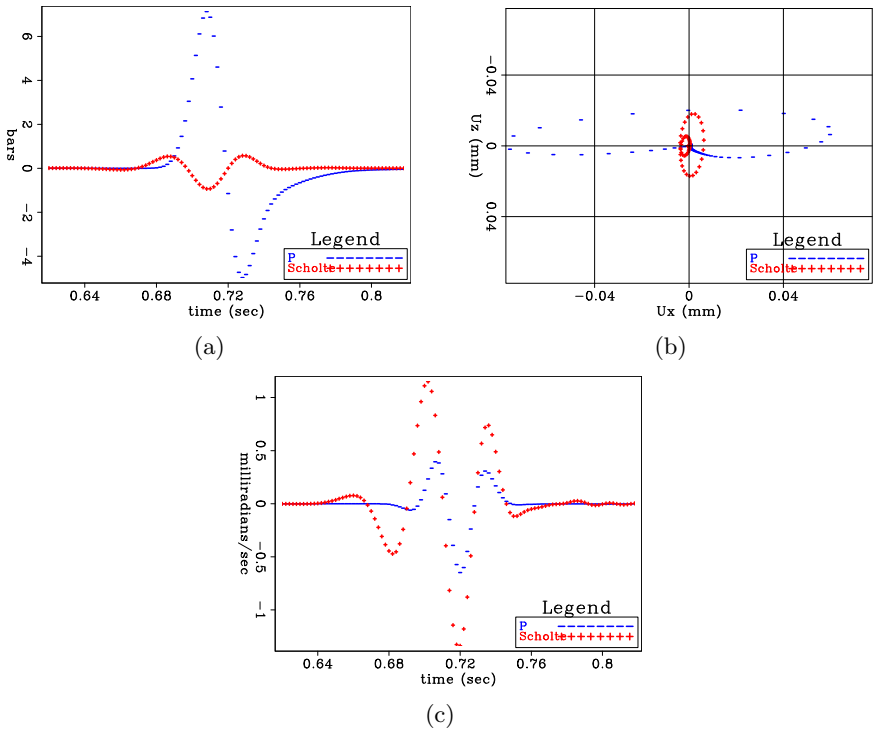

Figure 8: P and Scholte wave arrivals at the ocean-bottom receiver at $x = 1000m$, where the scattering was off the anomaly. (a) Pressure of arrivals. (b) Hodogram of displacements of arrivals. (c) Rotation rate of arrivals. Note how the P-wave has greater linear displacements compared to the Scholte wave, but a smaller rotation rate. [**ER**]

ohad2/. 0Pr2-p-gr,0uxzr2-p-gr-hodo,0rotr2-p-gr

Figures 10(a),10(b) and 10(c) are the ratios between the rotation rates and the absolute value of the displacement vectors of the P, S and Scholte wave arrivals. This ratio serves as a good indication as to which of the waves is a P-wave, and which are S or Scholte waves. The S and Scholte waves give rise to much more rotational motion in comparison to linear motion. P-waves, even when propagating along the seabed, generate mostly linear particle motion.

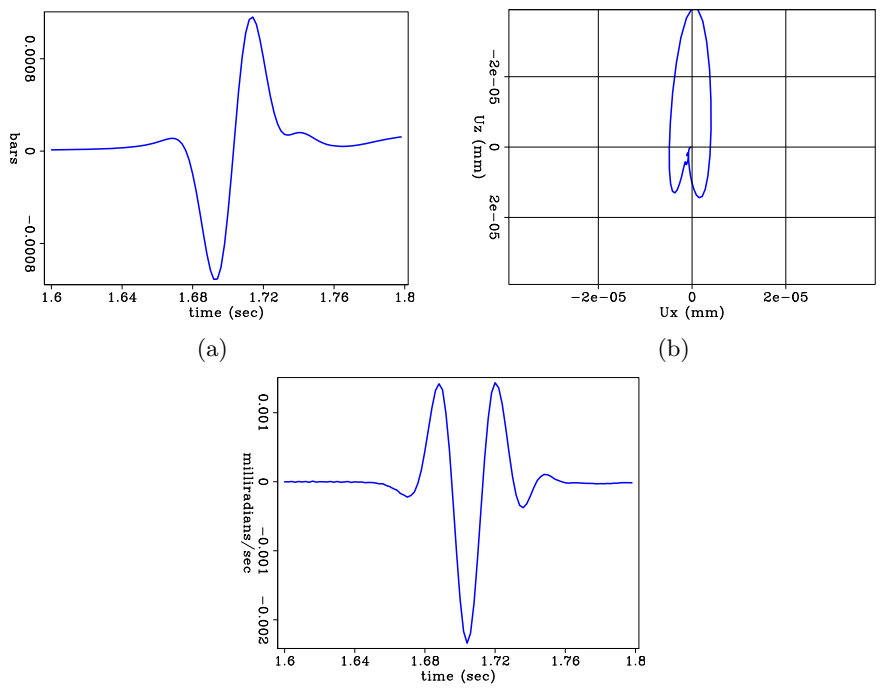

Figure 9: Shear wave arrival at the ocean-bottom receiver at $x = 1000m$, where the scattering was off the anomaly. (a) Pressure of S arrival. (b) Hodogram of displacements of S arrival. (c) Rotation rate of S arrival. [**ER**] ohad2/. 0Pr2-s,0uxzr2-s-hodo,0rotr2-s

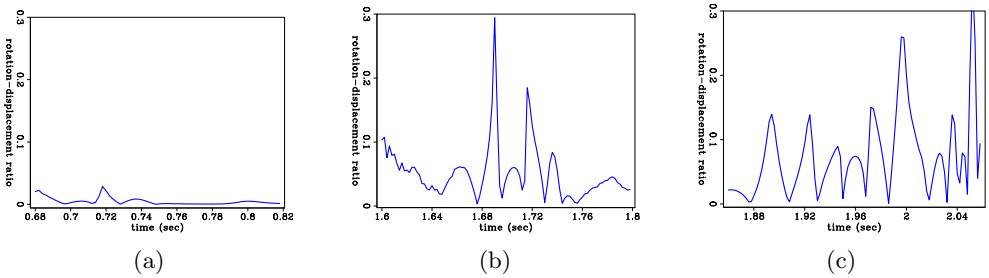

Figure 10: Ratio of rotation rate to absolute value of displacement for P, S and Scholte wave arrivals at the ocean-bottom receiver at $x = 1000$m, where the scattering was off the anomaly. (a) Ratio for P arrival. (b) Ratio for S arrival. (c) Ratio for Scholte wave arrival. Note that the ratio for S and Scholte waves is an order of magnitude greater than for the P wave. [**ER**] ohad2/. 0rotind2-p,0rotind2-s,0rotind2-gr

DISCUSSION AND CONCLUSION

The main conclusion is that rotational sensors can provide us with additional information about the type of waves recorded by ocean-bottom acquisition. The key characteristic for separating between the waves is the ratio between the linear and rotational motions. At the seabed, the P-waves have a mostly linear motion. Scattered S and Scholte waves have a mostly rotational motion.

When designing a new sensor, one of the important questions is its sensitivity. Sensor sensitivity can be parameterized by over-drive level and dynamic range. A sensor that is not sensitive enough will not register weak signal. A sensor that is too sensitive will over-drive too often and will not provide useful information on high amplitude events. Depending on the electronics and the analog instrument impulse response, the time to recover from overdrive may be from a few milliseconds to a second. The dynamic range is of course limited by the analog dynamic range of the sensor and by the number of bits of the digital data (32 bits in modern emerging A/D converters which is usually way above analog dynamic range). In this paper we provide predicted numbers in terms of milliradians/sec of rotation, bars of pressure, and millimeters of displacement.

However, it is important to note that so far our study is based on 2D elastic modeling. In this paper there is circular spreading of body waves and no spreading of surface waves, which is why they do not weaken with offset. The reason we chose the offset $x = 1000$m at which to analyze the displacements was because the different arrivals were sufficiently separated there, and their different characteristics could thus be displayed. In 3D, there is spherical spreading of body waves and circular spreading of surface waves. The relation between the body-wave rotations and surface-wave rotations may be very different in 3D as a result of the added degree of freedom. We plan to extend this study to 3D before providing sensitivity requirements for dynamic range and over-drive levels.

ACKNOWLEDGEMENTS

We thank Tim Owen, Malcolm Lansley and Bob Brune for prompting us to consider rotation sensors.

REFERENCES

Brokesova, J. and J. Malek, 2010: 2nd IWGoRS Workshop in Prague.

Lee, W. H. K., H. Igel, and M. D. Trifunac, 2009, Recent advances in rotational seismology: Seismological Research Letters, **3**, 479–490.

Virieux, J., 1986, P-Sv wave propagation in heterogeneous media: Velocity-stress finite difference method: Geophysics, **51**, 889–901.

Two point raytracing for reflection off a 3D plane

Stewart A. Levin

ABSTRACT

I present a simple, elegant approach to calculating two-point rays reflecting off a 3D dipping plane and investigate extensions to converted wave reflection and offset-vector map demigration.

INTRODUCTION

For SEP-147, I calculated the response of various classic seismic algorithms on a reflection off of a plane in 3D. After wrestling with spatial geometry in old textbooks, I derived the following result from scratch using elegant, coordinate-free vector notation.

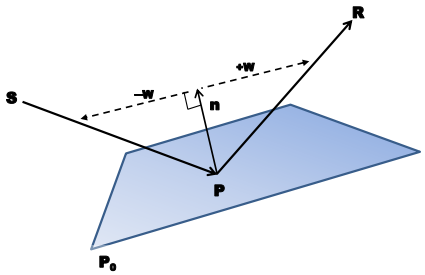

Figure 1: Diagram of planar reflector and the points and vectors I use for calculating the reflected raypath. [**NR**] stew1/. planerayfig

Given a source location S, a receiver location R, and a plane $\mathbf{n} \cdot (P - P_0) = 0$, where $\mathbf{n}$ is a unit normal, to find the reflection point P, drop a perpendicular $\mathbf{w}$ from $\mathbf{n}$ to the line connecting P to R. Snell's Law says that running $\mathbf{w}$ in the other direction connects to the line between P and S. So for some scalars α and β we have

$$\begin{aligned} (R-P) &= \alpha(\mathbf{n}+\mathbf{w}) \\ (S-P) &= \beta(\mathbf{n}-\mathbf{w}) \\ \mathbf{n}\cdot\mathbf{w} &= 0 \\ \mathbf{n}\cdot(P-P_0) &= 0 \end{aligned} \quad .$$

Dotting $\mathbf{n}$ onto the first two equations gives

$$\begin{aligned} \mathbf{n}\cdot(R-P) &= \mathbf{n}\cdot(R-P_0) &= \alpha \\ \mathbf{n}\cdot(S-P) &= \mathbf{n}\cdot(S-P_0) &= \beta \end{aligned} \quad ,$$

and subtracting the first two equations produces

$$(R-S) = (\alpha-\beta)\mathbf{n} + (\alpha+\beta)\mathbf{w},$$

which can be solved directly for $\mathbf{w}$ now that we have α and β. Given this $\mathbf{w}$, the first equation immediately yields

$$P = R - \alpha(\mathbf{n} + \mathbf{w}),$$

the desired reflection point. This can also be described in terms of the midpoint M of the source and receiver as

$$P = M - \tfrac{1}{2}(\alpha + \beta)\mathbf{n} - \tfrac{1}{2}(\alpha - \beta)\mathbf{w} \quad .$$

CONVERTED WAVE REFLECTION

The same approach applies to P-to-S or S-to-P reflection as well with one important difference—the angle of reflection differs from the angle of incidence. Now

$$\begin{array}{rcc} (R-P) & = & \alpha(\mathbf{n}+\mathbf{w}) \\ (S-P) & = & \beta(\mathbf{n}-\zeta\mathbf{w}) \\ \mathbf{n}\cdot\mathbf{w} & = & 0 \\ \mathbf{n}\cdot(P-P_0) & = & 0 \end{array}$$

for some scalar ζ. To determined ζ let v_s and v_r be the velocities of the source and receiver paths respectively and θ_s and θ_r be the corresponding angles of incidence and reflection. Then Snell's Law says

$$\frac{\sin\theta_s}{v_s} = \frac{\sin\theta_r}{v_r} \quad .$$

By our definition of $\mathbf{w}$, we also have the identities

$$\begin{array}{rcc} |\mathbf{w}| & = & \tan\theta_r \\ |\zeta\mathbf{w}| & = & \tan\theta_s \end{array}$$

which, using the identity,

$$\sin\theta = \frac{\tan\theta}{\sqrt{1+\tan^2\theta}} \ ,$$

gives the relation for ζ

$$\frac{1}{\zeta^2} = \left(\frac{v_r}{v_s}\right)^2 + \left(\left(\frac{v_r}{v_s}\right)^2 - 1\right)|\mathbf{w}|^2$$

which, combined with

$$(R-S) = (\alpha-\beta)\mathbf{n} + (\alpha+\zeta\beta)\mathbf{w} \ ,$$

produces a fourth order equation for ζ.

The fourth order equation can be solved directly using algebraic formulas. Lanczos (1956) provides a clean, efficient numerical approximation, reproduced in Appendix A, that is about 10 times faster than using a general purpose numerical root finder. (Appendix B shows how to make it free of floating point divisions.)

An interesting alternative to direct solution is to apply Newton iterations to the shooting method wherein source ray parameters are repeatedly adjusted to return very near to the target receiver. This approach applies to multiple layers and multiple reflections, not just a single interface. In Appendix C, I demonstrate *global* convergence of that method when applied to forward ray tracing through a stack of horizontal layers.

OFFSET-VECTOR MAP DEMIGRATION

Another application of the coordinate neutral approach for 3D reflection point calculation that arose at SEP recently is offset-vector map demigration. For this, the aim is to model where a point, P, on a planar subsurface reflector will appear in a constant-offset, constant-azimuth survey.

For this calculation, there is one fixed coordinate, the depth axis, with the sources and receivers on the surface, described by an arbitrary point Q_0 with (downward) normal $\mathbf{z}$. We are further given the source-to-receiver offset vector $2h\mathbf{x}$ and the reflector inward normal $\mathbf{n}$ from the point P on the reflector.

We know the ellipsoid of specular reflection has its major axis through the source and receiver, and that the inward normal bisects the reflection angle between the source and receiver. Therefore the normal line through the reflection point intersects the source-receiver axis somewhere between the source and receiver. Let Q be the point on the surface where the normal ray would reach. Then we may write

$$Q = P + \gamma \mathbf{n}$$

for some scalar γ. As before we calculate

$$\begin{aligned} \mathbf{z} \cdot (Q - Q_0) &= \mathbf{z} \cdot (P - Q_0) + \gamma \mathbf{z} \cdot \mathbf{n} \\ 0 &= \mathbf{z} \cdot (P - Q_0) + \gamma \mathbf{z} \cdot \mathbf{n} \\ \gamma &= \frac{\mathbf{z} \cdot (Q_0 - P)}{\mathbf{z} \cdot \mathbf{n}} \end{aligned}$$

and the horizontal distance of Q from the vertical plane through P as

$$\mathbf{x} \cdot [(P - \{\mathbf{z} \cdot (P - Q_0)\}\, \mathbf{z}) - (P + \gamma \mathbf{n})] = \gamma\, \mathbf{x} \cdot \mathbf{n}$$

thereby fixing the source-receiver axis and the relative location of Q. What still remains is to ascertain the source-receiver midpoint relative to P. This we can determine by means of tedious algebra, the way I did it, or by a succinct bit of trigonometry provide by Daniel Kane (pers. comm.) of the Stanford Department of Mathematics.

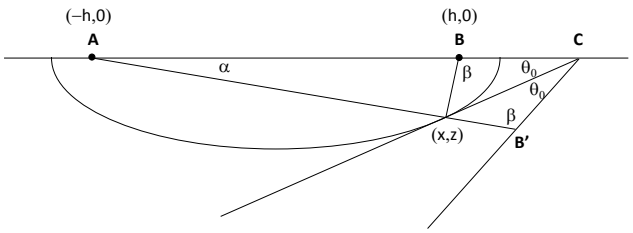

Figure 2: Diagram used to obtaining a quadratic relation for calculating x from z, h, and θ_0. [**NR**] stew1/. KaneProof

Due to symmetry, we may rotate the reflection point around the source-receiver axis until it is directly below that axis. This does not change the unknown distance to the source-receiver midpoint, but does reduce the computation to one on a planar ellipse. Let x_0 and z_0 denote the respective horizontal and vertical distances from the source-receiver midpoint to the reflection point. The dip angle θ_0 is implicitly determined by $\sin\theta_0 = -\mathbf{n} \cdot \mathbf{x}$ and $\cos\theta_0 = \sqrt{1 - \sin^2\theta_0}$. Using this dip angle, z_0 may be written as $\gamma \cos\theta_0$. Referring to Fig. 2, Fermat's principle of extremal traveltime tells us that reflecting a focus of the ellipse

around the tangent produces an image point on the straight line connecting the reflection point and the other focus. Hence we know that $AB'C$ forms a triangle. Denoting the three angles α, β, and θ_0 as illustrated in the figure, we have

$$\alpha + \beta + 2\theta_0 = \pi$$

whence

$$\tan 2\theta_0 = -\frac{\tan\alpha + \tan\beta}{1 - \tan\alpha \tan\beta} \quad .$$

But

$$\tan\alpha = \frac{z_0}{x_0 + h}$$

$$\tan\beta = \frac{z_0}{x_0 - h}$$

hence

$$\tan 2\theta_0 = -\frac{z_0(x_0 - h) + z_0(x_0 + h)}{x_0^2 - h^2 - z_0^2} = \frac{-2x_0 z_0}{x_0^2 - z_0^2 - h^2}$$

and so we have the quadratic relation

$$x_0^2 + 2x_0 z_0 \cot 2\theta_0 - (z_0^2 + h^2) = 0 \quad .$$

Solving the quadratic equation we get

$$\begin{aligned} x_0 &= -z_0 \cot 2\theta_0 + \sqrt{z_0^2 \cot^2 2\theta_0 + z_0^2 + h^2} \\ &= -z_0 \cot 2\theta_0 + \sqrt{z_0^2 \csc^2 2\theta_0 + h^2} \\ &= -\frac{z_0^2(\csc^2 2\theta_0 - \cot^2 2\theta_0) + h^2}{-z_0 \cot 2\theta_0 - \sqrt{z_0^2 \csc^2 2\theta_0 + h^2}} \\ &= \frac{\sin 2\theta_0 (z_0^2 + h^2)}{z_0 \cos 2\theta_0 + \sqrt{z_0^2 + h^2 \sin^2 2\theta_0}} \end{aligned}$$

in a form that does not exhibit a numerical singularity at $\theta_0 = 0$.

The relation $\alpha + \beta + 2\theta_0 = \pi$ is actually a special case of the more general proposition attributed to Bošković (Boscovich) (1754):

From any point H outside an ellipse with foci F and f, with F being no farther from H than f, draw two tangents, touching the ellipse at P and p respectively. Then the interior angle PHp is half the difference of the interior angles PFp and Pfp.

A translation of his original Latin demonstration appears in Appendix D.

So, in summary, only the dot products $\mathbf{z} \cdot \mathbf{n}$ and $\mathbf{x} \cdot \mathbf{n}$ are needed to find the demigration location of point P.

Reflection gradient

If we are interested in map *migration*, the information we have is not the reflector normal, but the normal to the arrival time surface. To calculate this slope, we can conflate distance

and time by choosing an arbitrary temporal unit, say a *glorp* equated to $1/V$ seconds. This makes a traveltime of 1 glorp correspond to 1 meter of travel distance.

I make life simpler by observing that the traveltime gradient has the same azimuth as the reflector's dip azimuth. This must be so because translating the source-receiver pair along strike does not change the reflection arrival time. I note that this does *not* say that the reflection point moves along the dip azimuth when the surface arrival point moves along the dip azimuth.

The next twist is that instead of translating the source-receiver pair along the dip azimuth, I'll translate the reflector plane along its normal direction. This implies that derivatives with respect to the reflector normal direction need to be scaled by the sine of the reflector dip, i.e. $\sin\theta = \sqrt{1-(\mathbf{n}\cdot\mathbf{z})^2}$, as the surface intercept of the reflector moves a distance inversely related to the sine of the dip. Fortunately, even the zero dip case, where the reflector does not intersect the surface, is handled properly because the sine is zero in that case.

If we translate the initial reflection point P by $-\epsilon\mathbf{n}$, where my convention for θ implies $\epsilon \geq 0$ corresponds to a positive time slope, we obtain a point on the displaced reflection plane, though generally not the new reflection point $\hat{P}$. The relation of $\hat{P}$ to P can be ascertained as before by dotting with $\mathbf{n}$:

$$\begin{array}{rcccl} \mathbf{n}\cdot(R-\hat{P}) & = & \mathbf{n}\cdot((R-P)+\epsilon\mathbf{n})) & = & \alpha+\epsilon \\ \mathbf{n}\cdot(S-\hat{P}) & = & \mathbf{n}\cdot((S-P)+\epsilon\mathbf{n})) & = & \beta+\epsilon \end{array} \quad .$$

Continuing as before,

$$\begin{array}{rcccc} R-S & = & (\alpha-\beta)\mathbf{n} & + & (\alpha+\beta)\mathbf{w} \\ R-S & = & ((\alpha+\epsilon)-(\beta+\epsilon))\mathbf{n} & + & ((\alpha+\epsilon)+(\beta+\epsilon))\hat{\mathbf{w}} \end{array} \quad ,$$

yielding

$$\hat{\mathbf{w}} = \left(1-\frac{2\epsilon}{\alpha+\beta+2\epsilon}\right)\mathbf{w}$$

which says that $\mathbf{w}$ does not rotate.

To compute changes in lengths (traveltimes), we have the relations

$$\begin{array}{rcl} R-P & = & \alpha(\mathbf{n}+\mathbf{w}) \\ R-\hat{P} & = & (\alpha+\epsilon)(\mathbf{n}+\hat{\mathbf{w}}) = -(\alpha+\epsilon)(\mathbf{w}-\hat{\mathbf{w}})+(\alpha+\epsilon)(\mathbf{n}+\mathbf{w}) \end{array}$$

and

$$\begin{array}{rcl} S-P & = & \beta(\mathbf{n}-\mathbf{w}) \\ S-\hat{P} & = & (\beta+\epsilon)(\mathbf{n}-\hat{\mathbf{w}}) = (\beta+\epsilon)(\mathbf{w}-\hat{\mathbf{w}})+(\beta+\epsilon)(\mathbf{n}-\mathbf{w}) \end{array} \quad ,$$

whence

$$\begin{array}{rcl} \hat{P}-P & = & -(\alpha+\epsilon)(\hat{\mathbf{w}}-\mathbf{w})-\epsilon(\mathbf{n}+\mathbf{w}) \\ & = & (\beta+\epsilon)(\hat{\mathbf{w}}-\mathbf{w})-\epsilon(\mathbf{n}-\mathbf{w}) \end{array} \quad .$$

Taking first differences, we have

$$\frac{\hat{\mathbf{w}}-\mathbf{w}}{\epsilon} = -\frac{2}{\alpha+\beta+2\epsilon}\mathbf{w}$$

and

$$\begin{aligned}\frac{\hat{P}-P}{\epsilon} &= -(\alpha+\epsilon)\frac{\hat{\mathbf{w}}-\mathbf{w}}{\epsilon} - (\mathbf{n}+\mathbf{w}) \\ &= (\beta+\epsilon)\frac{\hat{\mathbf{w}}-\mathbf{w}}{\epsilon} - (\mathbf{n}-\mathbf{w})\end{aligned}$$

whence

$$\begin{aligned}\frac{dP}{d\epsilon} &= \left(-1+\frac{2\alpha}{\alpha+\beta}\right)\mathbf{w}-\mathbf{n} \\ &= \left(1-\frac{2\beta}{\alpha+\beta}\right)\mathbf{w}-\mathbf{n}\end{aligned}$$

or, averaging the two,

$$= \frac{\alpha-\beta}{\alpha+\beta}\mathbf{w}-\mathbf{n} \quad .$$

With these in hand, we may differentiate the traveltime

$$T = T_R + T_S = |P-R| + |P-S|$$

to get

$$\begin{aligned}\frac{dT}{d\epsilon} &= \left(\frac{P-R}{|P-R|}+\frac{P-S}{|P-S|}\right)\cdot\frac{dP}{d\epsilon} \\ &= -\left(\frac{\alpha(\mathbf{n}+\mathbf{w})}{T_R}+\frac{\beta(\mathbf{n}-\mathbf{w})}{T_S}\right)\cdot\left(\frac{\alpha-\beta}{\alpha+\beta}\mathbf{w}-\mathbf{n}\right) \\ &= \frac{\alpha}{T_R}\left(\frac{(1-|\mathbf{w}|^2)\alpha+(1+|\mathbf{w}|^2)\beta}{\alpha+\beta}\right)+ \\ &\quad \frac{\beta}{T_S}\left(\frac{(1+|\mathbf{w}|^2)\alpha+(1-|\mathbf{w}|^2)\beta}{\alpha+\beta}\right)\end{aligned}$$

which, as remarked earlier, is then multiplied by $\sin\theta$ to obtain the surface time slope.

This last expression has a simple geometric meaning. As

$$\frac{P-R}{|P-R|} \quad \text{and} \quad \frac{P-S}{|P-S|}$$

are unit vectors pointing towards the reflection point from the receiver and source respectively, their sum is necessarily parallel to their angle bisector, the normal. In particular, they sum to $-2\cos\xi\ \mathbf{n}$ where ξ is the angle of incidence or reflection. Dotting this with $dP/d\epsilon$ and multiplying by $\sin\theta$ we have that the time slope is simply $2\cos\xi\sin\theta$. Changing units from glorps back to seconds, this agrees with the well-known zero-offset result $2\sin\theta/V$.

A Postscript

One of the references I allude to in the introduction was the classic posthumous publication of Slotnick (1959). In that tome, I found the proposition, a consequence of Apollonius'

Theorem (see, e.g., Godfrey and Siddons (1908) pages 20–21), that for a fixed source location and with receivers placed diagonally opposite each other at equal distances from the source, the sum of the squares of the two source to receiver traveltimes is *independent* of source-receiver azimuth. This result, analogous on the face of it to the updip-downdip refraction shooting method, appears to have been used fairly routinely to estimate moveout velocities before the advent of the common midpoint gather but is no longer taught to students or industry professionals. I think it, or some modern recasting of it, may well provide uplift to both academia and industry seismic processing and analysis.

DISCUSSION AND CONCLUSIONS

As we have seen, while not a panacea, the power of vector notation really shines once we leave the Euclidean plane and begin to work in 3D. It can allow us to reduce a problem to its algebraic or geometric essentials and to subsequently cleanly code the solution using any Cartesian coordinate system. In addition, the interests of academic scholarship have brought me new insights into historical thinking about seismic acquisition, processing, and imaging that offer tantalizing hints how more recent approaches may benefit from those "old school" ideas. Stay tuned!

APPENDIX A

Lanczos solutions for cubics and quartics

From Lanczos (1956), pages 6–8, 19–22:

3. Cubic equations. Equations of third and fourth order are still solvable by algebraic formulas. However, the numerical computations required by the formulas are usually so involved and time-absorbing that we prefer less cumbersome methods which give the roots *in approximation* only but still close enough for later refinement.

The solution of a cubic equation (with real coefficients) is particularly convenient since one of the roots must be real. After finding this root, the other two roots follow immediately by solving a quadratic equation.

A general cubic equation can be written in the form

$$f(\xi) = \xi^3 + a\xi^2 + b\xi - c = 0 \quad .$$

The factor of ξ^3 can always be normalized to 1 since we can divide through by the highest coefficient. Moreover, the absolute term can always be made negative because, if it is originally positive, we put $\xi_1 = -\xi$ and operate with ξ_1.

Now it is convenient to introduce a new scale factor which will normalize the absolute term to -1. We put

$$x = \alpha\xi, a_1 = \alpha a, b_1 = \alpha^2 b, c_1 = \alpha^3 c$$

and write the new equation

$$f(x) = x^3 + a_1 x^2 + b_1 x - c_1 = 0$$

If we choose

$$\alpha = 1/\sqrt[3]{c}$$

we obtain

$$c_1 = 1.$$

Now, since $f(0)$ is negative and $f(\infty)$ is positive, we know that there must be at least one root between $x = 0$ and $x = \infty$. We put $x = 1$ and evaluate $f(1)$. If $f(1)$ is positive, the root must be between 0 and 1; if $f(1)$ is negative, the root must be between 1 and ∞. Moreover, since

$$x_1 \cdot x_2 \cdot x_3 = 1$$

we know in advance that we cannot have *three* roots between 0 and 1, or 1 and ∞. Hence if $f(1) > 0$, we know that there must be one and *only one* real root in the interval $[0, 1]$, while if $f(1) < 0$, we know that there must be one and only one real root in the interval $[1, \infty]$. The latter interval can be changed to the interval $[1, 0]$ by the transformation

$$\bar{x} = \frac{1}{x}$$

which simply means that the coefficients of the equation change their sequence:

$$-c_1\bar{x}^3 + b_1\bar{x}^2 + a_1\bar{x} + 1 = 0$$

Hence we have reduced our problem to the new problem: find the real root of a cubic equation in the range $[0, 1]$. We solve this problem in good approximation by taking advantage of the remarkable properties of the Chebyshev polynomials (cf. VII, 9) which enable us to reduce a higher power to lower powers with a small error. In particular, the third Chebyshev polynomial

$$T_3^*(x) = 32x^3 - 48x^2 + 18x - 1$$

normalized to the range $[0, 1]$ gives

$$x^3 = \frac{48x^2 - 18x + 1}{32} = 1.5x^2 - 0.5625x + 0.03125$$

with a maximum error of $\pm\frac{1}{32}$. The original cubic is thus reducible to a quadratic with an error not exceeding 3%.

We now solve this quadratic, retaining only the root between 0 and 1.

$\vdots$

11. Equations of fourth order. Algebraic equations of fourth order with generally complex roots occur frequently in the stability analysis of airplanes and in problems involving servomechanisms. The historical method of solving algebraic equations of fourth order (also called biquadratic or quartic equations) involves the following steps. By a transformation of the form $x + \alpha$ the coefficient of the cubic term is annihilated. Then an auxiliary cubic equation is solved. The roots of the original equation are constructed with the help of the three roots of the auxiliary cubic. Numerically this method is lengthy and cumbersome. The following modification of the traditional procedure yields the four roots of an arbitrary

quartic equation with real coefficients on the basis of a quick and numerically convenient scheme.

Every equation of the form

$$x^4 + c_1x^3 + c_2x^2 + c_3x + c_4 = 0$$

can be rewritten as follows:

$$(x^2 + \alpha x + \beta)^2 = (ax + b)^2 \quad .$$

If the original c_i are real, the new coefficients are also real. Hence the original equation becomes solvable in the form of the quadratic equation

$$x^2 + \alpha x + \beta \pm (ax + b) = 0$$

which has four (generally complex) roots, obtainable by the standard formula. The new coefficients can be determined as follows. We evaluate in succession the following numerical constants:

$$\alpha = \frac{c_1}{2}, A = c_2 - \alpha^2, B = c_3 - \alpha A$$

and form the cubic equation

$$\xi^3 + (2A - \alpha^2)\xi^2 + (A^2 + 2B\alpha - 4c_4)\xi - B^2 = 0$$

Since the left side is negative at $\xi = 0$, a positive real root must exist. We determine this root according to the method of § 3. In order to avoid later corrections, it is advisable to add at this point Newton's correction (cf. § 5), obtaining ξ with great accuracy. The coefficients of the reduced equation are then determined as follows:

$$\begin{aligned} \alpha &= \tfrac{1}{2}c_1, \quad \beta = \tfrac{1}{2}(A + \xi) \\ a &= \sqrt{\xi}, \quad b = \frac{a}{2}\left(\alpha - \frac{B}{\xi}\right) \end{aligned} \quad .$$

APPENDIX B

Division-free reciprocal cube roots

Sometime back in the '90s, square roots started to be implemented as $z \times z^{-1/2}$ where the reciprocal square root was implemented using one or two iterations of Newton's method. As the Newton formula for the reciprocal square root could be written with only multiplications and additions, this was several times faster than computer division. Indeed, division was often replaced by squaring the reciprocal square root.

For the Lanczos root-finding methods in the previous appendix, a reciprocal *cube* root is needed. Fortunately, this, too, can be obtained using Newton's method in a division-free manner as follows:

Let

$$f(x) = \frac{1}{x^3} - z$$

be the function whose root we want to find. Taking its derivative,

$$f'(x) = \frac{-3}{x^4} \quad ,$$

produces the Newton step

$$x_{n+1} = x_n - \frac{f(x_n)}{f'(x_n)} = x_n(\tfrac{4}{3} - \tfrac{1}{3} z\, x_n^3) \quad .$$

The remaining issue is choosing an appropriate first guess, x_0, of the root in order to start the iteration. For this I again look to the fast reciprocal square root for guidance. McEniry (2007) reproduces a classic code (without the profane comment) containing a "magic number" from which half the integer representation of the floating point input is subtracted to produce an integer representation of the initial guess. This starting point was good enough that a single Newton iteration resulted in a worst case relative error of less than 0.175%. Mimicing McEniry's development yields the following code for a reciprocal cube root:

```
float InvCubeRoot ( float x ) {
   const float onethird = 0.333333333333;
   const float fourthirds = 1.333333333333;
   float thirdx = x * onethird;
   union {
     int ix;
     float fx;
   } z;

   z.fx = x;
   z.ix = 0x54a21d2a - z.ix/3; /* magic */
   x = z.fx;
   x = x * ( fourthirds - thirdx * x*x*x ); /* max relerr < 2.34E-3 */
   x = x * ( fourthirds - thirdx * x*x*x ); /* max relerr < 1.09E-5 */
   return x;
}
```

There is still one hitch—the "magic" line is not division free. Fortunately, the hacker and compiler community has worked out division-free integer division. For division by 3, this is accomplished by multiplying the numerator by the binary expansion 0.010101010101... of $\frac{1}{3}$ in fixed point arithmetic just like we were all taught in elementary school. For 32 bit numerators, we multiply by the hexadecimal constant 55555556 and shift the (64 bit) result down by 32 binary places. Therefore the "magic" line of code becomes

```
   z.ix = 0x54a21d2a -
          (int) ((z.ix * (int64_t) 0x55555556)>>32); /* magic */
```

where the tail end 6 instead of 5 in the multiplier handles the cases where the integer is not an exact multiple of 3.

Performing timing tests in C with random numbers, this algorithm ran 20 times faster than calling *powf*(*x*,-1.0*f*/3.0*f*) from the C math runtime library and about 10 times faster than my best previous effort to calculate a fast reciprocal cube root.

APPENDIX C

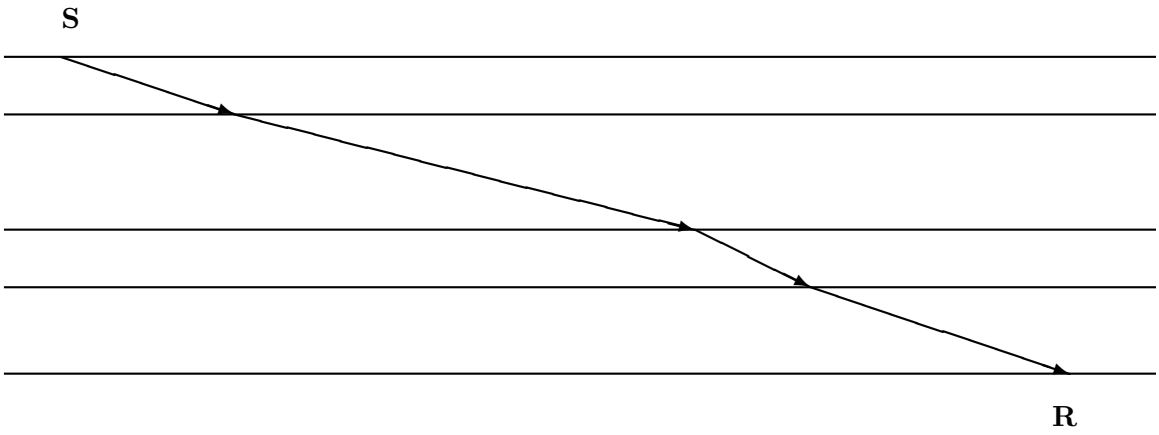

Globally convergent Newton's method for ray shooting

Quite some time ago, Bob Keyes at Mobil mentioned that Newton's method applied to shooting rays to solve the two-point problem in horizontally layered media is globally convergent, assuming, of course, that there is a solution. Specifically, there must be a solution if an initial guess at the ray parameter overshoots the target.

Formally, let the ray parameter p be in the open interval $(0, 1/v_{max})$. Starting from the origin, Snell's law $pv = \sin\theta$ says that

$$x = \int_0^z \tan\theta \, dz = \int_0^z \frac{pv}{(1-p^2v^2)^{1/2}} \, dz$$

gives the horizontal displacement of the ray from the origin when it reaches depth z. Taking two derivatives of this formula with respect to p, we have

$$\frac{dx}{dp} = \int_0^z \frac{v}{(1-p^2v^2)^{3/2}} \, dz \ , \quad \frac{d^2x}{dp^2} = \int_0^z \frac{3pv^3}{(1-p^2v^2)^{5/2}} \, dz \ .$$

At a glance one sees that the second derivative is a quantity guaranteed to be positive in $(0, 1/v_{max})$. By Thorlund-Petersen (2004), Newton's method applied to finding the p for a ray that reaches a given x at given depth z is therefore globally convergent. (Technically, we do need to ensure that the Newton update doesn't overshoot the range $(0, 1/v_{max})$.)

APPENDIX D

Translation of the geometric proof in Bošković (Boscovich) (1754).

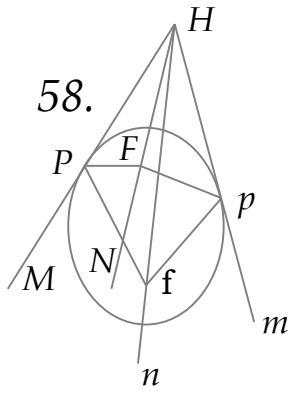

186. At Ellipsi in fig. 58 ductis HFN, Hfn, bini FPH, FpH æquales erunt binis fPM, fpm, sive quatuor internis, & oppofitis PfH, PHf, pfH, pHf, nimirum toti PHp, & toti Pfp. Angulus autem PFp æqualis binis PFN, pFN, sive quatuor internis FPH, FHP, FpH, FHp, vel binis illis FPH, FpH cum angulo PHp, adeoque angulo PHp bis, & toti Pfp semel. Quare angulo Pfp dempto a PFp, remanet angulus PHp bis.

186. In the ellipse in fig. 58, draw HFN and Hfn. Then FPH and FpH are equal to fPM and fpm respectively and so the four internal opposite angles PfH, PHf, pFH, and pfH evidently sum to PHp with Pfp.[†] Now angle PFp is the sum of PFN and pFN and so the sum of internal angles FPH, FHP, FpH, and FHp, hence [the sum of] FPH, FpH and angle PHp. [From above,] this is precisely equal to PHp twice combined with Pfp once. Therefore subtracting Pfp from PFp leaves twice the angle PHp.

[†]The external angle is the sum of the two opposite internal angles in a triangle.

REFERENCES

Bošković (Boscovich), R. J., 1754, Elementorum universæ matheseos 3, Continens sectionum conicarum elementa nova quadam methodo concinnata et dissertationem de transformatione locorum geometricorum ubi de continuitatis legem ac de quibusdam infiniti mysteriis: Amideus.

Godfrey, C. and A. W. Siddons, 1908, Modern geometry: Cambridge University Press.

Lanczos, C., 1956, Applied analysis: Prentice Hall.

McEniry, C., 2007, The mathematics behind the fast inverse square root function code.

Slotnick, M. M., 1959, Lessons in seismic computing, a memorial to the author: Society of Exploration Geophysicists.

Thorlund-Petersen, L., 2004, Global convergence of Newton's method: Mathematical Methods of Operations Research, **59**, 91–110.

Interactive processing: Geometry manipulation

Robert G. Clapp

ABSTRACT

Header manipulation for regularization, registration and quality control is often a time-consuming task with 3-D datasets. These manipulation tasks are often performed multiple times before achieving the desired result, each requiring a large amount of data to be read in with very few operations performed on each byte read. The problem can be made more tractable by reading in a random subset of the headers. Operations such as rotating, windowing, and gridding can then be performed interactively. With each processing step a record is created. These records can then be used to process the entire dataset, requiring only a single read and write of the volume.

INTRODUCTION

SEP has a long history of writing interactive viewers for regularly sampled multi-dimensional volumes (Ottolini, 1982; Biondi and van Trier, 1993; Clapp et al., 2008; Clapp, 2010). It has also dabbled in interactive processing using a range of platforms from Sunview (Claerbout, 1991) to Xtpanel (Cole and Nichols, 1992, 1993) to AVS (Clapp and Biondi, 1994). These attempts have met with limited success because they often did not provide a significant advantage over batch processing in terms of efficiency or ease of use.

The last 15 years have seen a significant change in the relative speeds of disk, memory, and compute power, with the former lagging far behind. In addition the size of seismic data volumes has grown by at least an order of magnitude. This brings into question the paradigm of running a batch program, QC'ing with a viewer a small percentage of the volume, then repeating with new parameters or proceeding to the next step. A different paradigm is to put the viewer as the central player, minimizing the amount of disk IO in exchange for redoing computations. This paradigm can be particularly effective in manipulating headers, which generally involve a low number of operations for each byte read accessed.

In this paper I introduce a new tool, `qthead`, for interactive header manipulation. The application allows the user to perform all of the basic header key functions in SEP3D (Biondi et al., 1996). The user works on a random subset of the headers, rotating, windowing, and gridding until a satisfactory result is achieved. The application stores all of the commands. These commands can then be applied to the entire volume, greatly reducing the required I/O.

DESIGN

In this section I will begin by describing the SEP3D tools that `qthead` replaces. I will then move into a brief description of the various classes in `qthead` and their functionality.

SEP3D tools

There are several SEP3D header manipulation applications in SEPlb that `qthead` attempts to replace. `Headermath` allows the creation of keys based on mathematical expressions using constants and other key values. This includes the ability to rotate the coordinate system by entering a rotation matrix based on `x` and `y` values. `Window_key` subsamples the dataset based on ranges of values for different keys. `Sort3d` allows the user to overlay a regular grid on irregular key locations. Finally, the programs `Stack3d` and `Infill3d` create a regular dataset from an irregular volume using the grid created in `Sort3d`.

FUNCTIONALITY

There are three windows in `qthead`. The main window gives a graphical display of one or more headers. The desired header can be selected from a pull down menu at the top of the display (see Figure 1). In this display the user can window a range of headers by drawing a box using the left mouse button. The right mouse button can be used to draw a line which will be used to rotate the data. After rotation the selected line will be horizontal in the display.

The second window (see Figure 2) displays all of the actions that have been performed on the data such as rotating and windowing. The user can undo an action by selecting the action above it in the list using the left mouse button. The application will then rerun all of the processing steps above and including the selected action. The bottom portion of the window is the gridding parameters that the user has selected for the dataset. These can be set in the final window.

The first two rows of the final window (see Figure 3) allow the user to specify exact windowing parameters for the data and an exact rotation angle (instead of using the mouse approach used in the main window). In addition, the user can create new headers keys by entering the new key name and its formula using constants and other key values. The final row allows the user to add a gridding axis to the dataset. The minimum and maximum of each key are provided by the program, the user adds the sampling then uses the `go` button to create the axis. Once an axis has been created the user has the option of choosing to change the main window display from a cross plot to a multi-dimensional histogram (see Figure 4).

The main window panel provides additional functionality using drop-down menus. The user can store all of the commands in the history buffer to a file. A history buffer can also be read from disk, and the actions in it performed automatically. The user also has several different output options. The user can output all of the SEP3D commands that will produce a SEP3D dataset equivalent to the current display. The user can also directly create the volume using the `Create regular volume` or `Create irregular volume`. The difference between these two options is whether to create a regular cube (requires that gridding axes have been created) or an irregular volume.

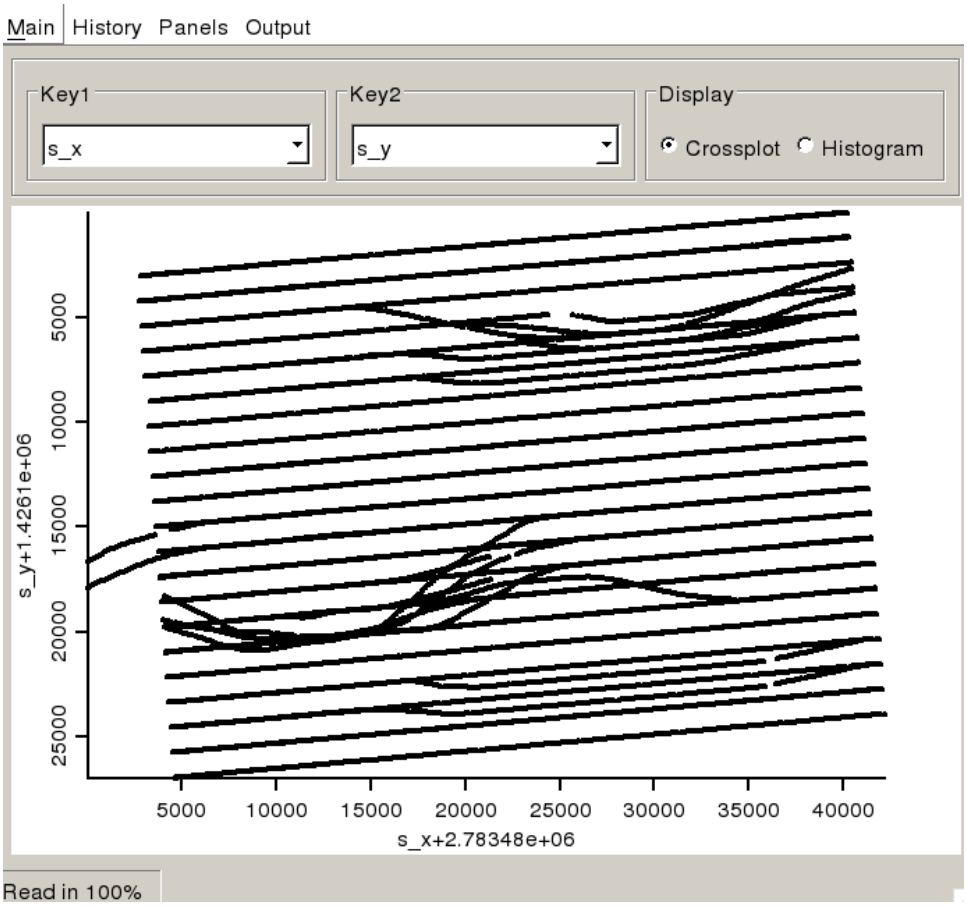

Figure 1: An example of the cross-plot view. In this case we see the source locations displayed. Note the ability to select the headers to be displayed at the top of the figure along with the ability to switch between a cross-plot and histogram view. bob1/. cross-plot

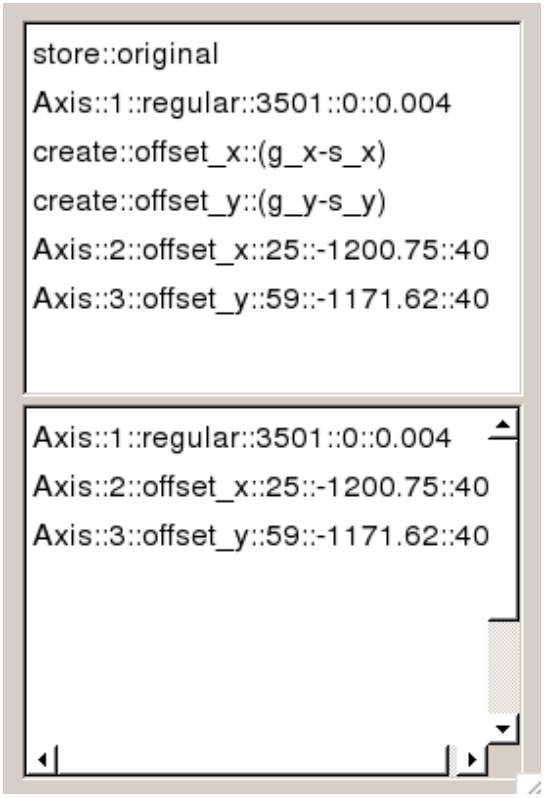

Figure 2: A view of the history panel. Each command can be clicked on, erasing all future processing steps. The display is then recreated by running all commands before and including the selected command. bob1/. history

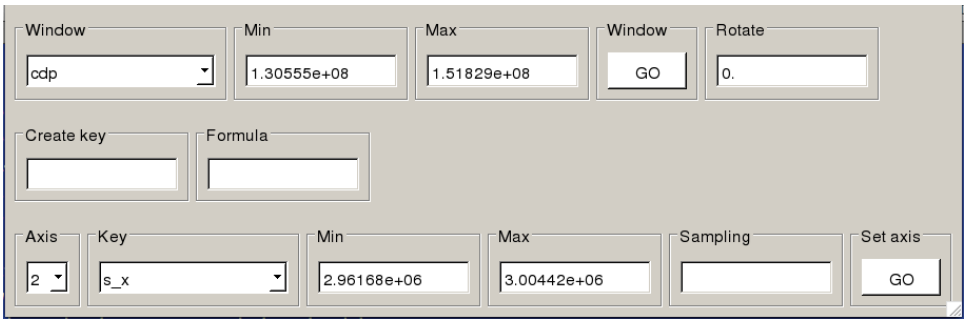

Figure 3: The header manipulation panel. From this panel keys can be windowed and rotated using the keyboard inputs. In addition new keys can be created by entering a formula based on constants and other keys. The bottom row allows gridded axes to be created from a selected key. bob1/. head-manip

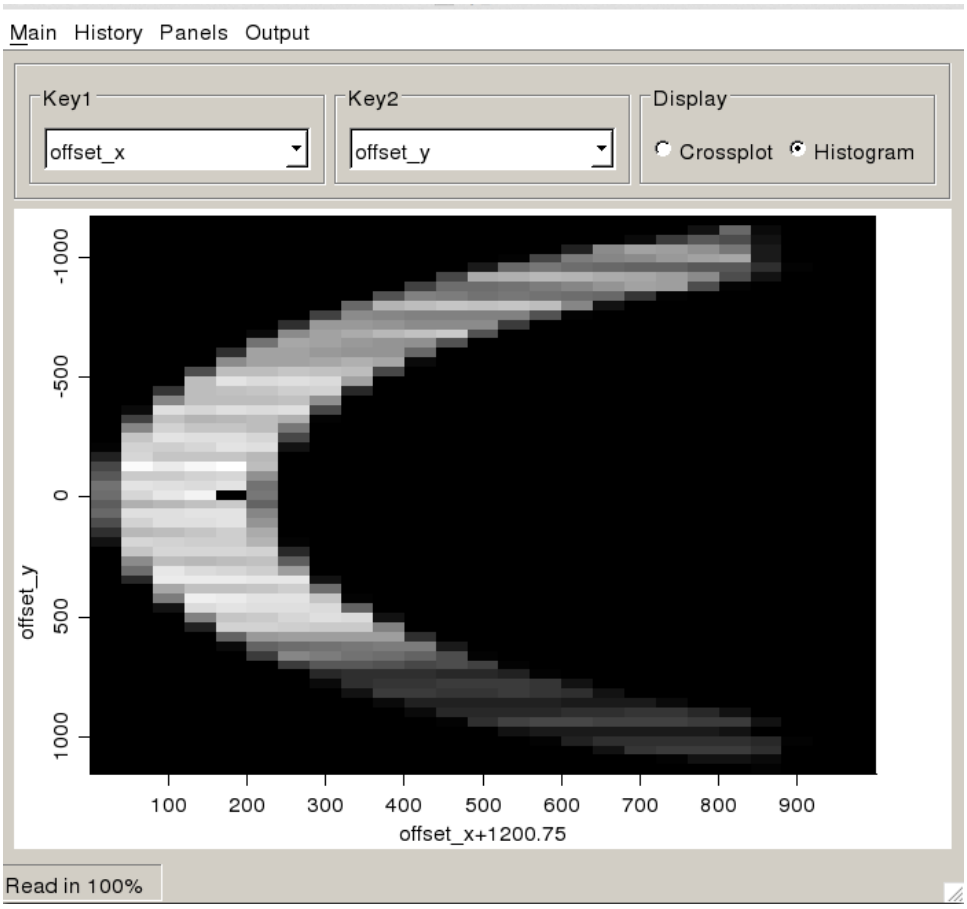

Figure 4: An example of the histogram view. In this case two offset keys have been created and the data binned at 40m. Darker colors indicate more traces falling into a bin. bob1/. histogram

Classes

The application, `qthead` is written in C++ using the QT[1] toolkit. The most basic building block for the application is the `headers` class. The `headers` is the basic storage mechanism for the headers. It has the ability to return an array of floats, doubles, or integers for all the headers currently stored in memory. The `io` class is the interface to read and write header values to disk. Currently only the ability to read/write SEP3D volumes is implemented but expansion to support SEG-Y, SU, etc. would require minimal effort. The `my_data` replicates most of the functionality of `Headermath` and `Window_key` such as creating keys, rotating, and windowing. It is the basic interface to the headers for all of the other components.

The fact that the entire header volume can not be assumed to fit into main memory resulted into several design decisions. Reading in a random subset of the data to interactively manipulate is an effective visualization strategy but is not sufficient to create an output volume to use for further processing. The need to rerun all of the commands on the entire dataset led to the creation of the `action` generic class. This class includes virtual functions (that result in calls to the `my_data` class) to perform desired actions.

The `history` class operates as the control unit for `qthead`. It keeps track of all the actions that user has performed. It has the ability to run a series of actions on a given `my_data` object which is useful both for when the user wants to remove a processing step and when the final output volume needs to be created. This ability to run a series of processing steps on an arbitrary header volume allows the `history` class to replace the functionality of `Sort3d, Stack3d,` and `Infill3d`. It can loop through a given dataset, reading manageable subsets and performing a series of actions before writing out the final dataset.

The most sophisticated class is the `io_thread` class. This class, a separate thread created when the application is started, is responsible for reading in random subsets of the headers. It starts by reading random subsets of the headers in chunks of several MB. After each chunk is read it applies all of the current actions using the functionality of the `history` class. Once all of the allotted header memory is used it stays dormant until one of two conditions is met. If the user requests that an action is undone. This results in the current data volume is abandoned, random subsections are reread, and the remaining processing steps run on it. The second reason for the thread to be awoken is when a windowing option is performed. After a windowing operation the thread will read in more of the headers, applying all of the current actions, until either the entire volume has been read or the maximum allotted space is again reached. Disk I/O can be a significant bottleneck, particularly given the random read approach used by `qthead`. To get around this problem we use Ecoram (Clapp, 2009), a type of solid state memory with a read rate of around 2GB/s, which seems sufficient for this application.

FUTURE WORK

A similar interactive approach can be used for many of the pre- and post-imaging steps now done at SEP using batch processes. Instead of reading in and processing an entire volume, only the portions of the dataset needed for the current view need reside in memory. This

[1]http://www.qt-proj.org

is a subtle but important difference. Processes such as NMO operate on a single trace, but doing a velocity scan requires all of the traces at a given CMP location. As a result each routine must have an awareness of what range of data is required to display a given subsection. As the number of processes increases the application must be able to keep track of a potentially expanding tree of data required to read into main memory to produce a given view.

CONCLUSIONS

I present an interactive 3-D geometry manipulation application, `qthead`. The application allows the user to rotate, window, and grid 3-D data interactively. The user builds a processing flow that is performed on a randomly subsampled portion of the data stored in memory. This processing flow can then be performed on the entire dataset to produce a final output volume or additional random subsets as more memory becomes available. This approach cuts down substantially on 3-D geometry processing costs and is applicable to other low-op pre- and post-imaging steps.

REFERENCES

Biondi, B., R. Clapp, and S. Crawley, 1996, Seplib90: Seplib for 3-D prestack data: SEP-Report, **92**, 343–364.

Biondi, B. and J. van Trier, 1993, Visualization of multi-dimensional seismic datasets with CM-AVS: SEP-Report, **79**, 1–12.

Claerbout, J. F., 1991, Interactive one dimensional seismology program ed1D: SEP-Report, **71**, 293–294.

Clapp, R. G., 2009, Visualization and data reordering using ecoram: SEP-Report, **138**, 297–304.

———, 2010, Hypercube viewer update: SEP-Report, **140**, 229–232.

Clapp, R. G. and B. Biondi, 1994, Iterative velocity model building for 3-D depth migration by integrating GOCAD and AVS: SEP-Report, **80**, 635–643.

Clapp, R. G., D. M. Chen, and S. Luo, 2008, Hypercube viewer: SEP-Report, **134**, 179–192.

Cole, S. and D. Nichols, 1992, Xtpanel: An interactive panel builder: SEP-Report, **75**, 497–520.

———, 1993, Xtpanel update: Interactivity from within existing batch programs: SEP-Report, **77**, 409–414.

Ottolini, R., 1982, Interactive movie machine user's documentation: SEP-Report, **32**, 183–195.

I DON'T ALWAYS CALCULATE GREEN'S FUNCTIONS.
BUT WHEN I DO, I MAKE SURE TO USE THE ONE-WAY WAVE EQUATION IN FREQUENCY-WAVENUMBER DOMAIN.

Aligning microseismic reflections for imaging

Noha S. Farghal and Stewart A. Levin

ABSTRACT

Microseismic data are not created ready for imaging. They can be extremely noisy and it is not a straightforward task identifying reflections. In a previous work, we were able to use multiplets or events of the same waveform to identify some reflections. However, realizing that reflections were weaker on the stack than they are on the individual seismograms, we inferred we had a misalignment issue between the different seismograms. In this work, we use fractional shifts and receiver-by-receiver shifting to align seismograms more effectively. We also investigate some aspects of multiplets and how they are related to each other in space and time, as well test the use of cross correlations of P-direct arrivals with whole seismograms to identify the unfound P-reflections.

INTRODUCTION

The ultimate goal of our research is to use reflections of hydraulically induced microseisms in the Bonner sand of the Bossier play to image the subsurface. In our previous work (Farghal and Levin, 2012), we successfully utilized a method adapted from earthquake seismology to find events originating from closely related sources which produced almost identical seismograms. This method involved cross-correlation of a particular event waveform (called a master) consisting of a P and S direct arrival with the whole dataset to find replicas of this waveform (the collection of which is known as a *multiplet*). Upon identification of similar waveforms (sources), we aligned and stacked their seismograms together to decrease the data size and increase the S/N ratio. Since we were only able to identify S reflections, we were also hoping that by stacking similar seismograms we will boost companion P reflections as well. However, for reasons discussed later in this report, this first attempt was not fruitful.

In SEP–147, we noticed that reflections are weaker on the stack than they are on the individual seismograms. We proposed that this was due to misalignment of the reflections after we aligned the direct arrivals. We attributed this to misalignment of the reflections that may differ by a small amount due to small source location differences in cases of similar rather than identical/coincidental sources. We have since realized that the fracturing and pressure changes could have affected propagation velocities even if the source locations happen to be the same.

In this report, we will show how we successfully address the misalignment problems and enhance the stacked amplitude of reflections. Moreover, we attempt to find P-reflections by cross-correlating P direct arrivals with the whole seismogram in which it lies. The faintest P reflection may well be useful when we come to the migration stage.

Finally, in preparation for imaging, we apply the previously mentioned concepts (of cross-correlations, alignment and stacking) to the whole Bonner dataset.

WARPING OR RECEIVER-BY-RECEIVER VARIABLE SHIFTING

In a previous report, we used the general locations of "stacked" cross-correlation peaks of the microseismic events to find a bulk shift to apply to the whole seismogram (Farghal and Levin, 2012). In Figure 1, we show the stack of two aligned seismograms. Extracting the reflection wavelet on the 30th channel, we can see that the highest positive magnitude is around 0.03, as shown in Figure 3 (a).

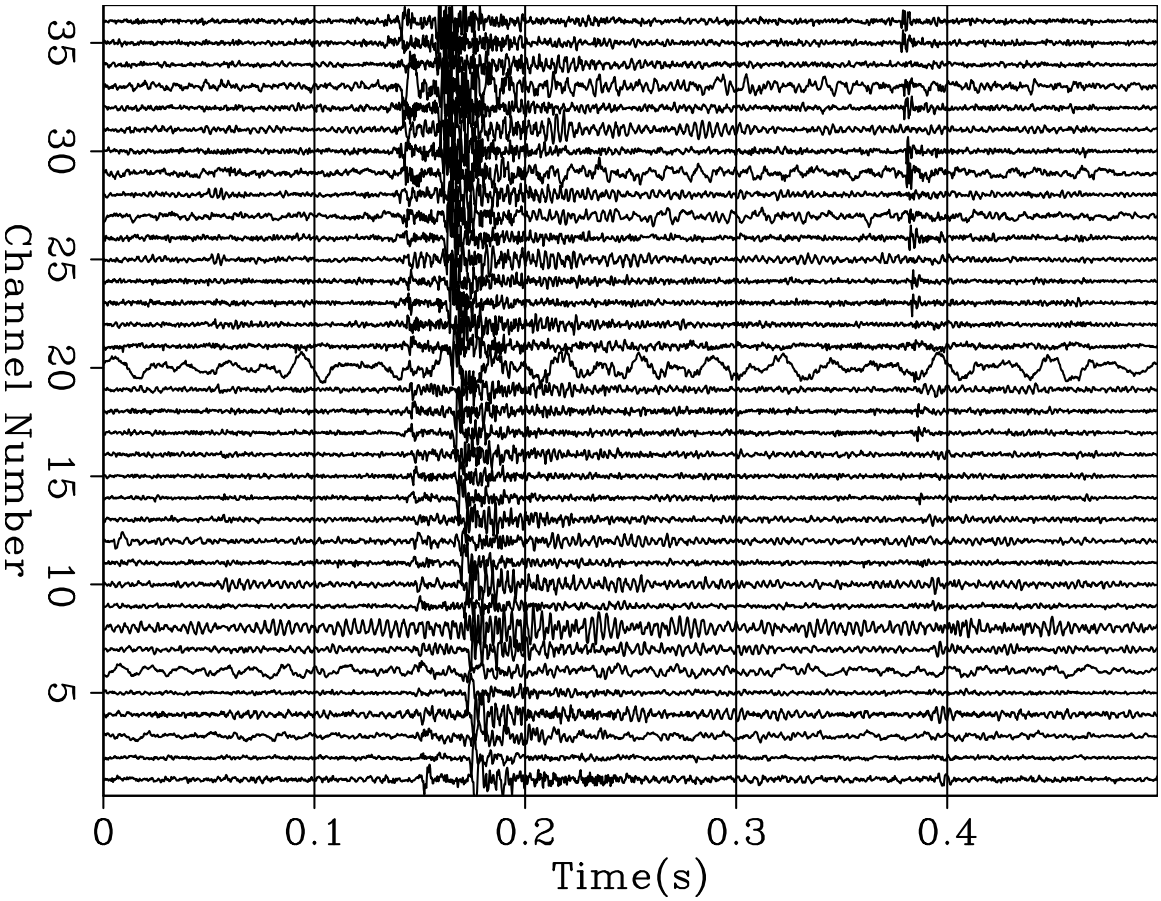

Figure 1: Stack of two seismograms aligned by bulk shifting. [**ER**] nfarghal/. stack209-before

We will now introduce receiver-by-receiver variable shifting, a limited form of warping, to align seismogram reflections within a multiplet. Figure 2 shows the stack of two aligned seismograms using this warping rather than bulk shifting. Figure 3(b) shows a closeup on the 30th channel reflection wavelet, with almost three-fold improvement in peak magnitude, confirming our better alignment of the individual seismogram reflections.

IN SEARCH OF P-REFLECTIONS

The reader will, of course, have observed that we have only shown a shear reflection in the above. Looking at the direct arrivals, we can see that the direct P waves are weaker than

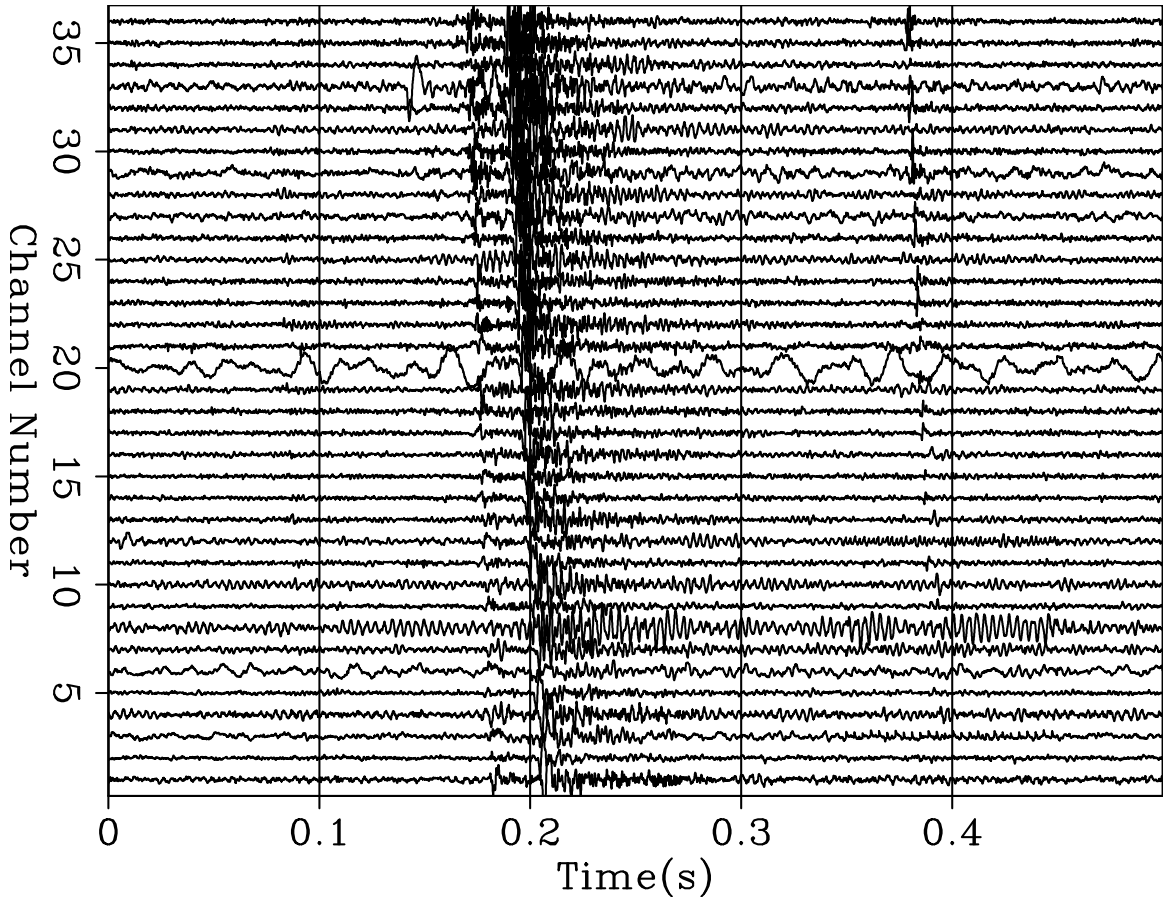

Figure 2: Stack of two seismograms aligned by warping. [**ER**] nfarghal/. stack209-after

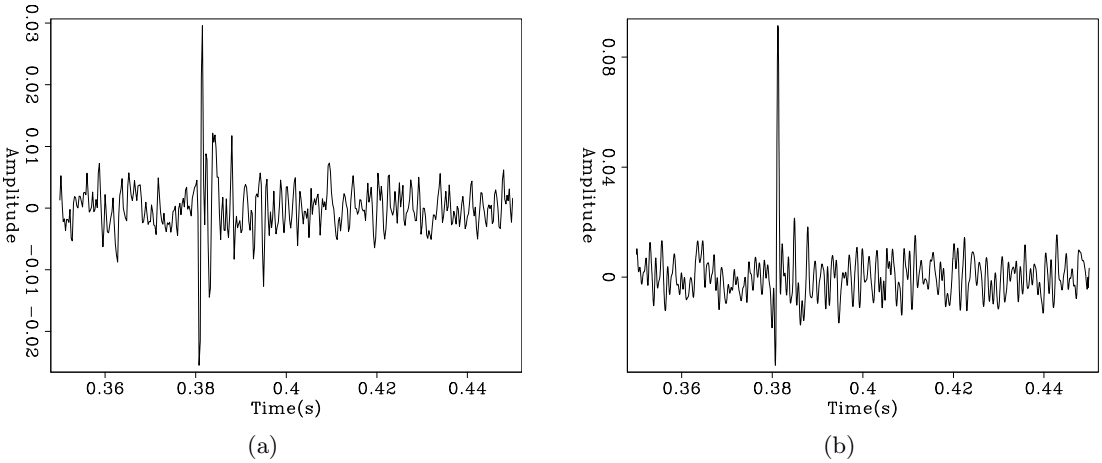

(a) (b)

Figure 3: a) Selected reflection (30th channel) in a stack of 2 seismograms aligned by bulk shifting. b) Close up on the reflection (30th channel) in a stack of 2 seismograms aligned by receiver-by-receiver shifting (warping). Observe the increased peak amplitude after warping. [**ER**] nfarghal/. waveletbulk,waveletwarp

the direct S waves, so it should not be surprising that the reflected P waves may be quite weak.

We used our running window cross-correlation program to cross-correlate direct P arrivals with whole seismograms with the hope of finding P-reflections. Results of such an approach can be seen on Figure 4(b). We can see in this figure that on the original seismogram, the P reflection seen at around 2.2s was not apparent and was actually brought up by the cross-correlation of the direct P with the whole seismogram. It turns out that the stronger the P arrival we use in cross correlations, the more likely we are to find an arrival that can be a P-reflection.

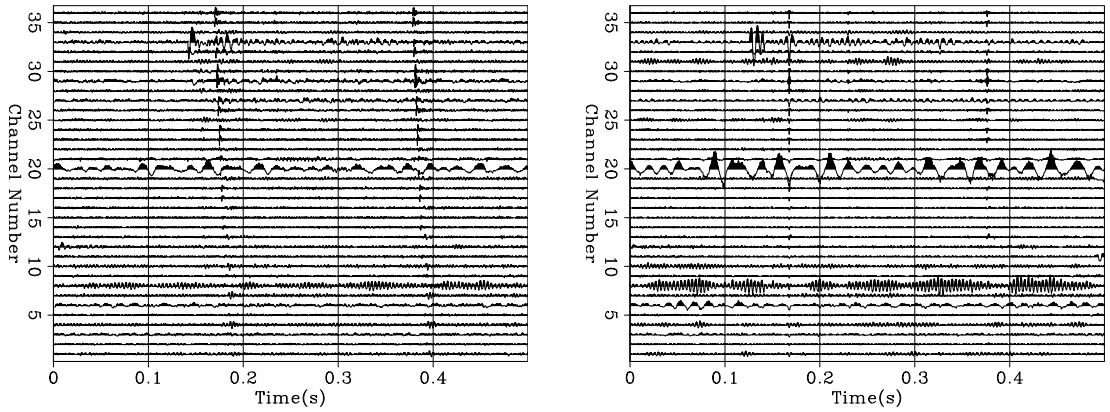

(a) (b)

Figure 4: a) seismogram with P-reflection not strong enough to be seen b) cross-correlation result with direct P-wave, with a possible reflection appearing at about 0.23s. [**ER**] nfarghal/. Bonner0209,B0209-p

AN OBSERVATION ON "POPULAR" WAVEFORMS

Most microseismic sources in the Bonner sand are along the hydraulic fracture (Sharma et al., 2008). Many of them are expected to be very close in location and to have the same waveform (from the same fracking mechanism), while others further apart on the hydraulic fracture have rather different waveforms. This is reflected in the tight clustering of source locations of waveforms having high correlation with the master waveform. However, the clustering of locations does not necessarily imply any fixed distribution of event times. What we observe is a long-tailed distribution, with most appearing at the early stages of the treatment. This we attributed to such events being due mostly to the initial opening of the fracture, with some later slippage as pressures vary during later stages of the treatment.

Due to the high correlation values obtained in most cross-correlations, deciding what the threshold for what constituted a match/multiplet was not possible without visual inspection. We conservatively opted to only include in a given multiplet those records with nearly perfect correlation to the multiplet master.

DISCUSSION AND CONCLUSIONS

From our results, we see that receiver-by-receiver shifting is better than bulk shifting as it produces larger signal amplitude and overlap as demonstrated by the higher amplitudes of the stacked reflections. We note that fractional shifting did not help much to improve alignment in these examples, that is, whole samples were sufficient, but we will continue to use this method in order to develop and mature it for general application to microseismic data that may well need fractional shifting for sufficient alignment.

Finally, although shear reflections are sufficient for imaging, that fact that we were able to identify later P-arrivals that encourages us to not abandon our search for P-reflections.

ACKNOWLEDGMENTS

We thank Pinnacle, a Halliburton company, and the United States Department of Energy for providing the dataset.

APPENDIX A

FRACTIONAL SHIFTS

By first taking the seismograms to the Fourier domain, padding with zeros with a certain factor (interleaving), we obtain fractional shifting. This is because the sampling interval is reduced by that factor, which we call super-sampling of data. Then, we apply the receiver-by-receiver alignment program to align all multiplets with the master seismogram reflection, as will be discussed in the coming section. Fractional shifting does not change a seismogram visually, but it multiplies its sampling density.

APPENDIX B

TRAVEL TIMES AND GRADIENTS

Referring to Figure B-1, the direct arrival time, T_D, is given by

$$T_D = \frac{\sqrt{x^2 + (z_s - z_r)^2}}{V}$$

and the reflected arrival time, T_R, is similarly

$$T_R = \frac{\sqrt{x^2 + (z_s + z_r)^2}}{V} \quad .$$

To calculate the relative effect of small shifts in source or receiver location on these arrival times, we compute the gradients ∇T_D and ∇T_R with respect to changes in source

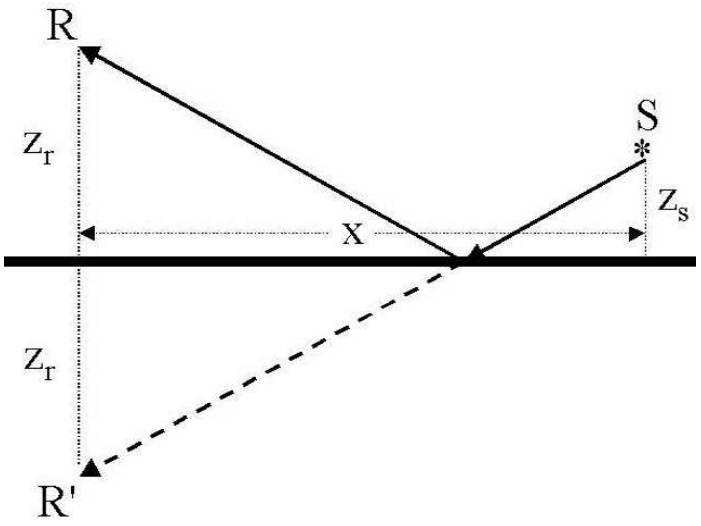

Figure B-1: Diagram showing source-receiver relative locations with respect to the reflector. [**NR**] nfarghal/. useisfigurestew

location:

$$
\begin{aligned}
V\frac{\partial T_D}{\partial x} &= \frac{x}{\sqrt{x^2+(z_s-z_r)^2}} \\
V\frac{\partial T_D}{\partial z_s} &= \frac{z_s-z_r}{\sqrt{x^2+(z_s-z_r)^2}} \\
V\frac{\partial T_R}{\partial x} &= \frac{x}{\sqrt{x^2+(z_s+z_r)^2}} \\
V\frac{\partial T_R}{\partial z_s} &= \frac{z_s+z_r}{\sqrt{x^2+(z_s+z_r)^2}}
\end{aligned}
$$

and with respect to changes in receiver location:

$$
\begin{aligned}
V\frac{\partial T_D}{\partial z_r} &= \frac{z_r-z_s}{\sqrt{x^2+(z_s-z_r)^2}} \\
V\frac{\partial T_R}{\partial z_r} &= \frac{z_s+z_r}{\sqrt{x^2+(z_s+z_r)^2}}
\end{aligned}
$$

With these gradients in hand, let $\mathbf{f}$ be a unit vector aligned with the fracture and $\mathbf{g}$ be a unit vector aligned with the receiver array. Then the directional derivatives $\nabla T_D \cdot \mathbf{f}$ and $\nabla T_R \cdot \mathbf{f}$ give the relative sensitivities of the direct and reflected arrival times to source displacement along the fault that gave rise to some set of multiplets. Similarly, the directional derivatives $\nabla T_D \cdot \mathbf{g}$ and $\nabla T_R \cdot \mathbf{g}$ provide the arrival slopes of the direct and reflected arrivals respectively.

With the above, not only can we estimate where to look for weak reflections behind a direct arrival (or, conversely, how far from the microseismic source a clear reflection

arose), but we can also begin to understand how much or little reflections within multiplets misalign when their associated direct arrivals are aligned. For example, the limiting case of the receiver just above the reflector has the reflected and direct arrivals arriving at the same time and changing at the same rate as the source is displaced whereas if $z_s = z_r = x/2$ the reflected arrival displaces $\sqrt{2}$ times further than the direct arrival. Both of these cases are serendipitous in the sense that aligning the direct arrival across channels also aligns the reflected arrival.

Let us apply these formulas to analyze the shear reflection we spotted in our Bonner multiplet example.

In the example of Figure 1, the receivers are at about 12,800 ft depth and the microseismic source was computed to be at about 13,100 ft depth and an offset of about 300 ft from the monitor well. The dipole sonic log shows a compressional velocity of about 13,750 ft/sec and a shear velocity of about 8,000 ft per second in that depth range. The difference between the direct P and the direct S arrivals would be 22 msec, in good agreement with the actual record. The delay of about 220 msec to the later shear arrival corresponds to a reflector depth of about 13,800, i.e., a thousand feet below the receivers and, sigh, well below the reservoir depth.

REFERENCES

Farghal, N. S. and S. A. Levin, 2012, Hunting for microseismic reflections using multiplets: SEP Report, **147**, 223–236.

Sharma, M. M., P. B. Gadde, R. Sullivan, R. Sigal, R. Fielder, D. Copeland, L. Griffin, and L. Weijers, 2008, Slick water and hybrid fracs in the Bossier: Some lessons learnt: SPE Annual Technical Conference and Exhibition, Houston, TX, USA, 89876–MS.


STANFORD

Earthquake extraction and correlation energy at Long Beach, California seismic survey

Jason P. Chang and Sjoerd de Ridder

ABSTRACT

Seismic interferometry of passive data offers a potential solution to creating reservoir-scale images in urban environments. A four-month, high station density passive seismic dataset collected in Long Beach, California is ideal for testing this hypothesis. Preliminary work on these data is promising. We clearly capture waveforms from earthquakes near (less than 15 km) and far (greater than 250 km). We successfully construct virtual sources through cross-correlation of low-frequency energy (0.175 to 1.75 Hz). The correlated energy is quite noisy and appears to be directed toward the northeast, suggesting that longer correlation times are needed for land data and that the Pacific Ocean is likely producing strong directed energy, respectively. Furthermore, the quality of correlation results differ depending on the time window. We argue that these differences are attributed to weather conditions, with records during stormier periods producing cleaner Green's functions than records during calmer periods.

INTRODUCTION

The Long Beach oil field is a productive oil field located below the city of Long Beach. Due to the urban environment, traditional techniques for collecting data for seismic imaging and velocity analysis are disruptive and difficult to perform. One alternative is using passive seismic data for this type of subsurface analysis. The effectiveness of such data for these purposes at the reservoir scale and in the urban environment is relatively unknown, but the recently deployed Long Beach seismic array provides a great opportunity to investigate their potential. The array is unique given its station density, recording period, and location. These parameters make this survey ideal for testing passive seismic imaging and tomography techniques from earthquake and exploration seismology.

Earthquakes oftentimes have source location depths on the order of kilometers, thereby producing waves that travel deep through the Earth's interior prior to reaching the surface. Depending on the amount of energy that a given event releases, the signal can be recorded by seismometers around the world. These two characteristics make data recorded from earthquakes ideal for resolving structures and velocities at the crustal/mantle scale, whether using body waves (Aki et al., 1977; Kissling, 1988; Romanowicz, 2008; Schmandt and Humphreys, 2010) or very low-frequency (less than 0.025 Hz) surface waves that can sample these depths (Yang and Ritzwoller, 2007; Tanimoto and Sheldrake, 2002). When dealing with these scales, what is considered dense station spacing can seem relatively sparse. For instance, USArray is a transportable array of 400 broad-band seismometers spaced 'densely' at approximately 500 km (Meltzer et al., 1999). With this denser Long Beach array, earthquake signal might be able to resolve structures and velocities at the reservoir scale.

A common drawback with using earthquake events for surface wave tomography is that surface wave dispersion is difficult to measure at frequencies higher than 0.05 Hz (Yang et al., 2008). Seismic interferometry with ambient noise can handle dispersion at these frequencies. By cross-correlating recordings of ambient seismic noise at two receivers, the traveltime between them can be recovered. This traveltime information can then be used for purposes such as velocity modeling, particularly when using low-frequency signal. Shapiro et al. (2005) and Lin et al. (2008) have been able to create velocity maps at the crustal scale by performing ambient noise cross-correlations on data recorded by USArray. At the reservoir scale, de Ridder and Dellinger (2011) showed that virtual low-frequency (0.35-1.75 Hz), omnidirectional Scholte waves along the ocean floor could be generated from ambient seismic noise. They were able to use the Scholte-wave traveltime information for tomographic imaging of structures in the near-surface (0-150 m).

In this report, we will show data that have been extracted from the Long Beach dataset. First, we will present snapshots of interpolated waveforms generated by earthquakes near and far. Second, we will present cross-correlation results for the same station location at various times of the survey. Both these results are viewed with an eye toward determining the capability of such an array for continuous reservoir monitoring in an urban environment using passive seismic data.

DATA

The Long Beach 3D seismic array was deployed by Nodal Seismic, Inc. for recording both passive and active seismic surveys. The array consists of about 2400 vertical-component geophones covering a region approximately 8.5 km north-south by 4 km east-west (Figure 1). Average station spacing is 330 m, both inline and crossline. While battery life limitations means stations are swapped out approximately every 8 days, station locations stay consistent throughout the survey. Data were being continuously recorded (24 hours/day) over a span of four months starting in January 2012, with a sampling rate of 500 Hz. This has provided us with approximately 48 TB of data. While the data have been low-cut at 3 Hz, there is still energy found in the suppressed lower frequencies.

EARTHQUAKE RECORDINGS

With the San Andreas Fault running through California, the Long Beach survey picks up many events, both big and small. We present waveforms from a nearby (approximately 15 km east of the survey) M2.4 event in Yorba Linda, California, and a further away (approximately 250 km southeast of the survey) M4.9 event in Mexicali, Mexico. Given the spatial dimensions and duration of the Long Beach array, both events could potentially be used for resolving structures and velocities at the reservoir scale.

Interpolation

To create these snapshots, we implemented a normalized inverse distance weighting interpolation scheme. First, we normalized the amplitudes of the recordings because we did not want anomalously high amplitudes to dominate the interpolation results. Second, we

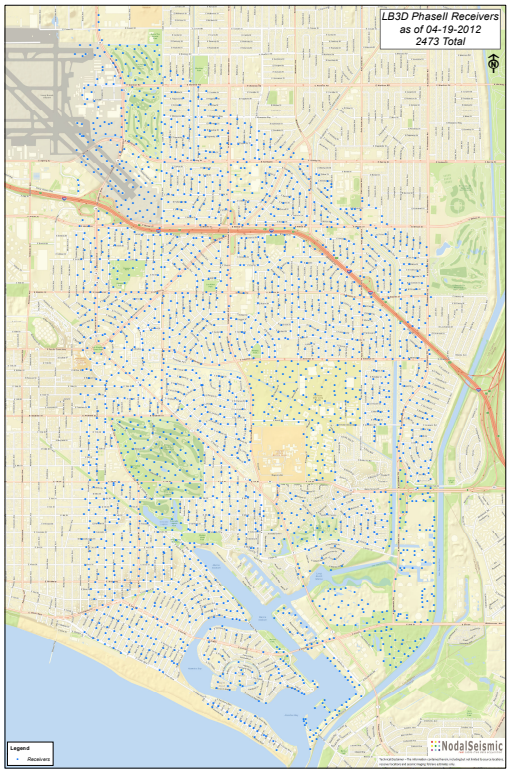

Figure 1: Map of receivers comprising the Long Beach 3D seismic array. [**NR**] jasonpc1/. lbmap

created a 40 by 80 grid of rectangular cells that overlapped with the 8.5 km north-south by 4 km east-west region containing the array. To determine which stations would be used for interpolating the response at a given cell, we implemented nearest-neighbor binning.

Rather than average the recordings from each station for a given cell, we apply a weight to the relevant recordings for a given cell and then sum the recordings. The weight is the normalized inverse of the distance between the location of the recording and the center of the cell, having the form

$$\mathbf{u}(\mathbf{x}) = \sum_{i=1}^{N} \frac{w_i(\mathbf{x})\mathbf{u}_i}{\sum_{i=1}^{N} w_i(\mathbf{x})}, \tag{1}$$

where

$$w_i(\mathbf{x}) = \frac{1}{d_i(\mathbf{x}, \mathbf{x}_i)}. \tag{2}$$

$\mathbf{u}(\mathbf{x})$ is the interpolated recording at cell $\mathbf{x}$, $w_i(\mathbf{x})$ is the weight applied to station i when interpolating for cell $\mathbf{x}$, $\mathbf{u}_i$ is the recording at station i, and $d_i(\mathbf{x}, \mathbf{x}_i)$ is the distance between the center of the cell $\mathbf{x}$ and the relevant station at location $\mathbf{x}_i$. This interpolation scheme weights recordings that are closer to the center of the cell more so than those recordings that are closer to the edges of the cell. The normalization of the weights by the sum of the weights ensures that the amplitudes from cell to cell are relatively similar, particularly because the amplitudes at each station were first normalized.

Earthquake Snapshots

Figure 2 displays an unfiltered snapshot from the relatively nearby Yorba Linda event, while Figure 3 displays the same snapshot after we applied a 8 Hz low-pass filter.

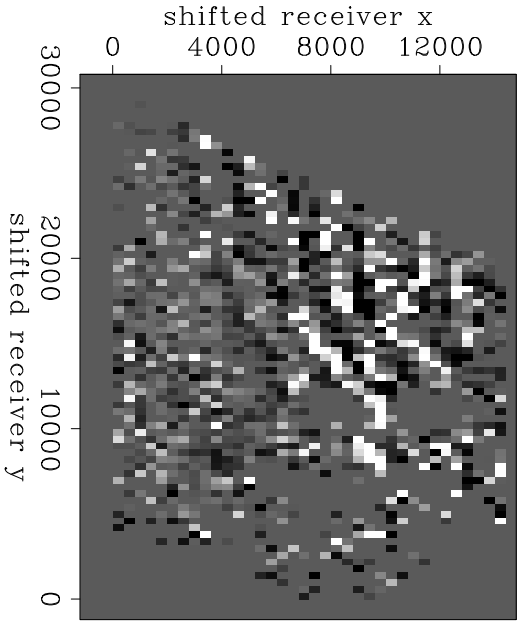

Figure 2: Snapshot of the interpolated waveform generated from the M2.4 Yorba Linda, CA event, roughly 15 km east of the Long Beach survey. [**CR**] jasonpc1/. yorbalinda-snap

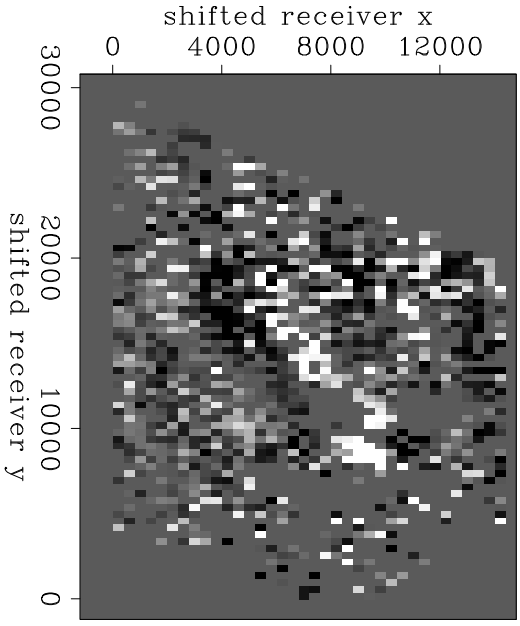

Figure 3: Same snapshot as Figure 2 but after applying a 8 Hz low-cut filter. [**CR**] jasonpc1/. yorbalinda-snap-bp

Figure 4 shows an unfiltered snapshot from the relatively far Mexicali event, while Figure 5 shows the same snapshot after we applied a 6 Hz low-pass filter.

In both unfiltered snapshots (Figures 2 and 4), the incoming waveforms are distinguishable. However, when low-pass filtered (Figures 3 and 5) these waveforms are even easier to identify. This suggests that we are seeing surface waves (and perhaps S-waves), which are more prevalent at lower frequencies, rather than P-waves. Research by Yang and Ritzwoller

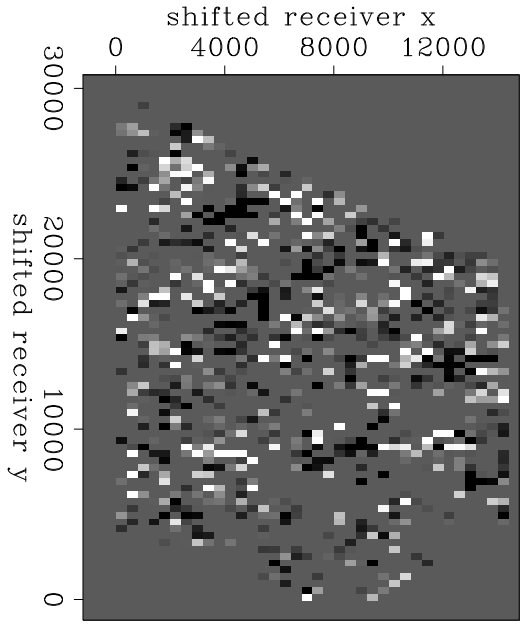

Figure 4: Snapshot of the interpolated waveform generated from the M4.9 Mexicali, Mexico event, roughly 250 km southeast of the survey. [**CR**] jasonpc1/. mexicali2-snap

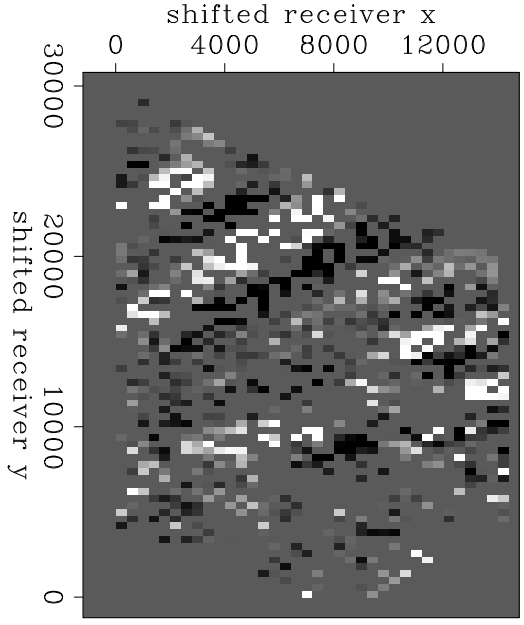

Figure 5: Same snapshot as Figure 4 but after applying a 6 Hz low-cut filter. [**CR**] jasonpc1/. mexicali2-snap-bp

(2007) and Tanimoto and Sheldrake (2002) have shown that surface waves can be used for resolving velocity structure at the crustal scale. With the denser station spacing of the Long Beach array, nearby and teleseismic events can potentially be useful for resolving structures and velocities at the reservoir scale.

SEISMIC INTERFEROMETRY AT LONG BEACH

Theory

In passive seismic interferometry, receivers record data from passive sources such as ambient seismic noise. Cross-correlating the two receiver recordings essentially turns the receivers into a source-receiver pair, thereby synthesizing new seismic responses. Specifically, cross-correlation recovers the Green's function, or the impulse response, and its time-reversed version between the two receivers, convolved with the autocorrelation of a source function such as noise (Wapenaar et al., 2010). In equation form

$$[G(x_B, x_A, t) + G(x_B, x_A, -t)] * S_N(t) = \langle u(x_B, t) * u(x_A, -t) \rangle \quad , \tag{3}$$

where G is the Green's function between two receiver locations (x_A, x_B), $S_N(t)$ is the autocorrelation of the source function (here it is noise), and u is the observed wavefield at a given receiver location. The result of cross-correlation is the traveltime difference of the recorded waves between the two given receivers.

A single cross-correlation of two recordings from two stations will likely produce noisy results. To improve signal-to-noise ratio, cross-correlations between multiple simultaneous recordings from two stations are stacked (or averaged) in the time-lag space (Curtis et al., 2006). This allows stationary signal phases to emerge, since these signals stack coherently and non-stationary phases stack incoherently. Therefore, stacking a month's worth of correlations should produce a better result than stacking a day's worth of correlations.

The method of passive seismic interferometry is effective only under certain conditions. The most important is that the principle of energy equipartition is satisfied. This means that noise must arrive at a receiver from all azimuths with the same amount of energy. If this is not satisfied, then correlation results may be far from ideal.

The station density and recording length of the array at Long Beach makes this dataset ideal for testing the limits of passive seismic interferometry in an urban environment. Higher station density provides more high-frequency information and should therefore provide better subsurface resolution. Longer recording times provide days to months of stacked correlations, as opposed to hours of stacked correlations. With longer stacked correlations, the convergence of the Green's function will improve and perhaps overcome the negative effects of cultural noise that is typically problematic in land data.

Method

Prior to performing any cross-correlations, we searched for time windows that were clear of significant seismic events. This is because one of the primary conditions for seismic interferometry to be effective is that the ambient seismic field satisfies the principle of

equipartition. Because earthquakes produce high amounts of directed energy, they would potentially compromise our correlation results.

Once clear of major seismic events, we formed our time windows. We chose three windows spanning from 1: 30 pm, January 21 to 2: 00 am, January 22 (12.5 hours); 5: 00 pm, February 20 to 5: 00 am, February 21 (12 hours); and 2: 00 pm, February 27 to 4: 00 am, February 28 (14 hours). We received each data file as a time series for a single station, which meant that we had to re-sort our data according to recording time. We chose to synthesize 32.5-minute patches with 2.5-minute tapers at both ends, leading to a 2.5-minute overlap from one window in time to the next.

Prior to cross-correlating, we bandpass all the traces. de Ridder and Dellinger (2011) have had success generating virtual low-frequency (0.35-1.75 Hz), omnidirectional Scholte waves along the ocean floor, so we examine signals that have been similarly bandpassed between 0.175 Hz and 1.75 Hz. Because we want to compare correlation results over time, for each time window we cross-correlate all stations with the same station location. Finally, we stack each time patch within each time window to improve the signal-to-noise ratio of the correlations.

Results

All figures show correlation results with the same virtual source location and at the same acausal and causal time lags (-4 seconds and 4 seconds, respectively). Figure 6 and Figure 7 show the acausal and causal Green's functions from the 12.5 hours of correlations from January 21 to January 22. Figure 8 and Figure 9 show the acausal and causal Green's functions from the 12 hours of correlations from February 20 to February 21. Figure 10 and Figure 11 show the acausal and acausal Green's functions from the 14 hours of correlations from February 27 to February 28. Gaps in the array overlap with parts of the CSU Long Beach campus.

Discussion

A common observation is that the correlation energy is strongest in the southwest portion of the array at acausal (negative) time lags and strongest in the northeast portion of the array at causal (positive) time lags. This might be a consequence of the location of the array. Based on results from research utilizing data from ocean-bottom cables, the correlating energy is typically symmetric and circular about the virtual source location at both causal and acausal times. This is because energy typically reaches a given receiver in equal amounts from all azimuths in these deep-water environments, where the primary source of seismic energy is generated from the interaction of ocean currents with the ocean bottom. In other words, the principle of energy equipartition is more or less satisfied in deep-water environments. However, these results from Long Beach suggest that this principle is not being satisfied. The directionality of the Green's function from southwest to northeast suggests that the Pacific Ocean (which is south-southwest of the array) is a large source of directed, low-frequency energy. This causes the Green's function at causal and acausal times to be asymmetric.

The primary difference between the Green's function from each time window is the qual-

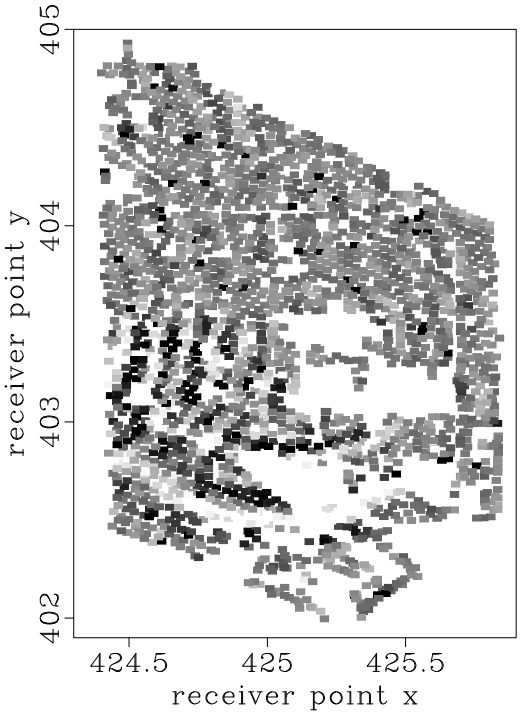

Figure 6: Snapshot of the Green's function at −4 second (acausal) time lag from the 12.5 hours of correlations from January 21 to January 22. [**CR**] jasonpc1/. corr-Jan22-acausal-snap

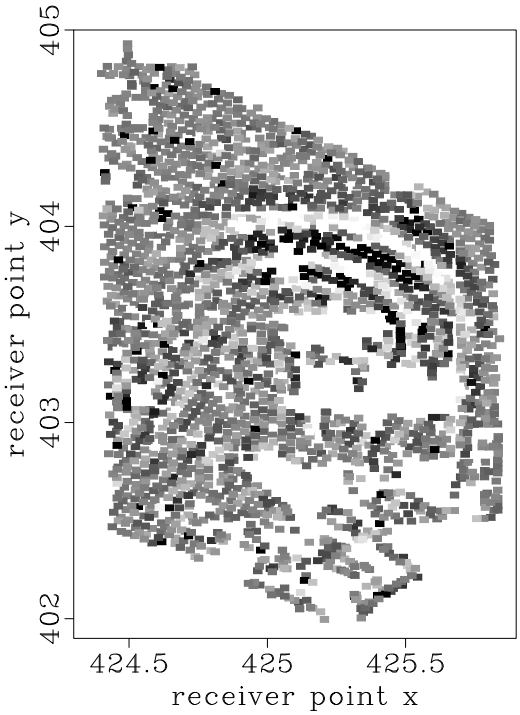

Figure 7: Snapshot of the Green's function at 4 second (causal) time lag from the 12.5 hours of correlations from January 21 to January 22. [**CR**] jasonpc1/. corr-Jan22-causal-snap

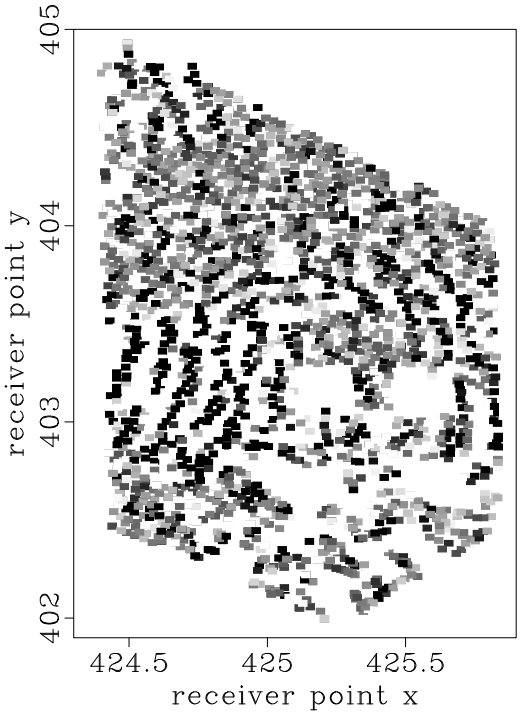

Figure 8: Snapshot of the Green's function at −4 second (acausal) time lag from the 12 hours of correlations from February 20 to February 21. [**CR**] jasonpc1/. corr-Feb21-acausal-snap

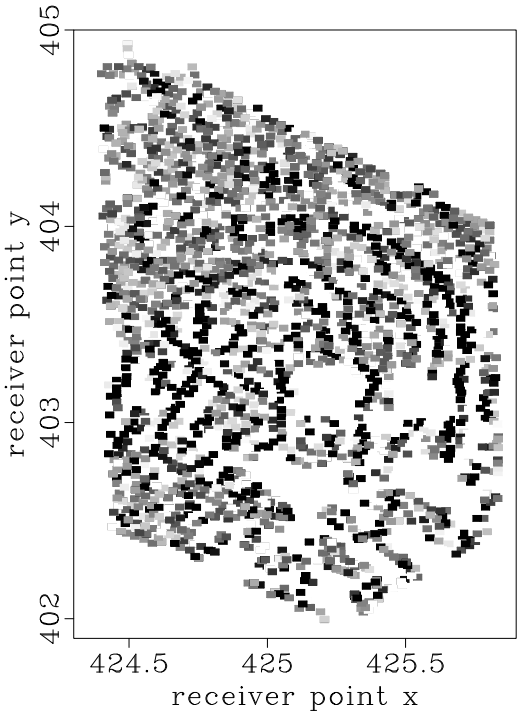

Figure 9: Snapshot of the Green's function at 4 second (causal) time lag from the 12 hours of correlations from February 20 to February 21. [**CR**] jasonpc1/. corr-Feb21-causal-snap

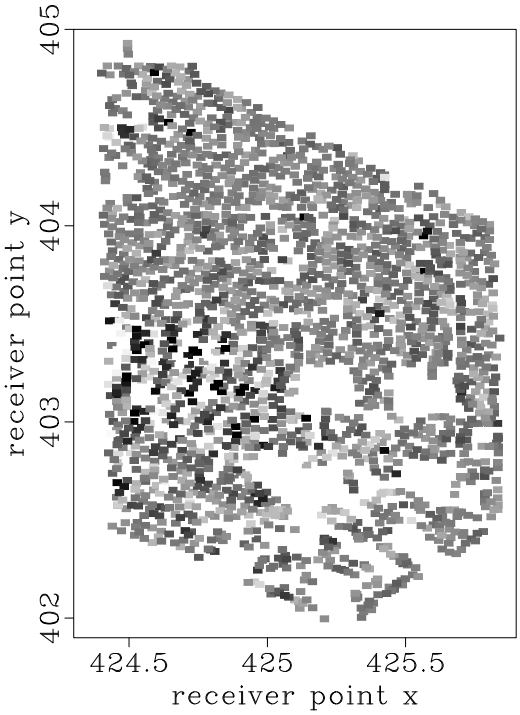

Figure 10: Snapshot of the Green's function at −4 second (acausal) time lag from the 14 hours of correlations from February 27 to February 28. [**ER**] jasonpc1/. corr-Feb28-acausal-snap

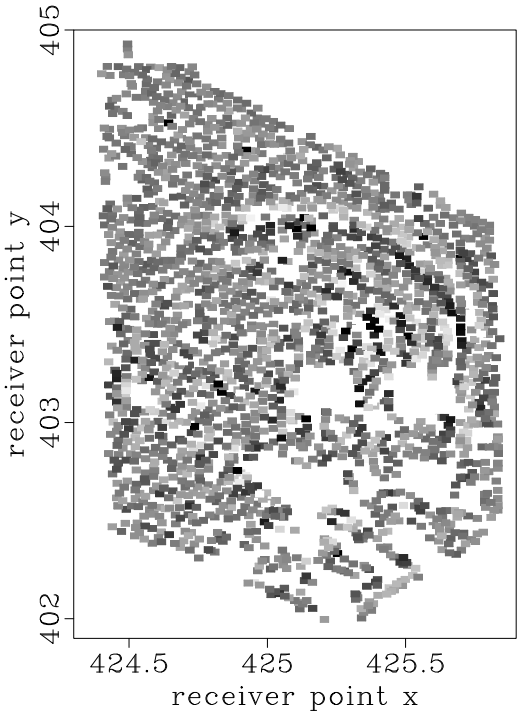

Figure 11: Snapshot of the Green's function at 4 second (causal) time lag from the 14 hours of correlations from February 27 to February 28. [**ER**] jasonpc1/. corr-Feb28-causal-snap

ity. The correlation energy from the January window is by far the most distinct, followed by the result from late-February and the result from mid-February. A look at the weather conditions in southern California may explain these results. At the time of the January time window, there was a large rainstorm that hit the region (http://www.wrh.noaa.gov/). During the late-February window, conditions were somewhat windy. In mid-February, conditions were pretty mild. Therefore, it appears that correlation results are best during stormy conditions, which happens to also be the case with seismic interferometry results from ocean-bottom cable data (de Ridder and Dellinger, 2011). These conditions may be best because during a storm the energy generated by the Pacific Ocean is much higher relative to any other noise source. Because the ocean is likely the dominant source of the directed, low-frequency energy that we see, then the more relative energy it has, the cleaner the resulting Green's function will be. With more correlation time, the results from February may be able to match the result from January.

FUTURE WORK

Earthquake waveforms and cross-correlation results are promising enough that the next step is to perform surface wave tomography for various time windows. For reservoir monitoring, using surface waves generated by passive seismic interferometry appears to be a better option than using surface waves generated by earthquakes. We are interested in the relatively higher frequencies, which seismic interferometry and ambient noise tomography is better equipped to handle. Passive seismic interferometry is also better for reservoir monitoring because signal is continuously available and is not dependent on random events like earthquakes. Therefore, time-lapse images at the reservoir scale may be possible with passive seismic interferometry.

CONCLUSION

Because it is an urban environment, the city of Long Beach is a suitable location to investigate the use of passive seismic data for subsurface imaging and velocity analysis at the reservoir scale. The dense, continuously recording Long Beach array is ideal for time-lapse analysis. We captured a variety of earthquake waveforms, generated both near to and far from the array, that could be used for tomographic imaging. We have also captured correlating energy at low frequencies using seismic interferometry techniques, which can also be used for tomographic imaging. Therefore, there are indications that seismic land data from an urban environment has the potential to be used for subsurface monitoring.

ACKNOWLEDGMENTS

We gratefully acknowledge Signal Hill Petroleum, Inc. for access to this dataset and permission to publish. We would particularly like to thank Dan Hollis for both his effort in helping us acquire this dataset and his enthusiasm in sharing these data with us.

REFERENCES

Aki, K., A. Christoffersson, and E. Husebye, 1977, Determination of the three-dimensional seismic structure of the lithosphere: Journal of Geophysical Research, **82**, 277–296.

Curtis, A., P. Gerstoft, H. Sato, R. Snieder, and K. Wapenaar, 2006, Seismic interferometry - turning noise into signal: The Leading Edge, **25**.

de Ridder, S. and J. Dellinger, 2011, Ambient seismic noise eikonal tomography for near-surface imaging at Valhall: The Leading Edge, **30**, 506–512.

Kissling, E., 1988, Geotomography with local earthquake data: **26**, 659–698.

Lin, F., M. Moschetti, and M. Ritzwoller, 2008, Surface wave tomography of the western United States from ambient seismic noise: Rayleigh and Love wave phase velocity maps: Geophysical Journal International, **173**, 281–298.

Meltzer, A., R. Rudnick, P. Zeitler, A. Levander, G. Humphreys, K. Karlstrom, G. Ekstrom, R. Carlson, T. Dixon, M. Gurnis, P. Shearer, and R. van der Hilst, 1999, USArray initiative: Geological Society of America TODAY, **9**, 8–10.

Romanowicz, B., 2008, Using seismic waves to image Earth's internal structure: Nature, **451**, 266–268.

Schmandt, B. and E. Humphreys, 2010, Complex subduction and small-scale convection revealed by body-wave tomography of the western United States upper mantle: Earth and Planetary Science Letters, **297**, 435–445.

Shapiro, N., M. Campillo, S. L., and M. Ritzwoller, 2005, High-resolution surface-wave tomography from ambient seismic noise: Science, **307**, 1615–1618.

Tanimoto, T. and K. Sheldrake, 2002, Three-dimensional S-wave velocity structure in southern California: Geophysical Research Letters, **29(8)**.

Wapenaar, K., D. Draganov, R. Snieder, X. Campman, and A. Verdel, 2010, Tutorial on seismic interferometry: Part 1—Basic principles and applications: Geophysics, **75**, 75A195–75A209.

Yang, Y. and M. Ritzwoller, 2007, Teleseismic surface wave tomography in the western U.S. using the transportable array component of usarray: Geophysical Research Letters, **35**, 1–5.

Yang, Y., M. Ritzwoller, F. Lin, M. Moschetti, and N. Shapiro, 2008, Structure of the crust in uppermost mantle beneath the western United States revealed by amibent noise and earthquake tomography: Journal of Geophysical Research, **113**, 1–9.

SEP PHONE DIRECTORY

Name	Phone	Login Name
Almomin, Ali	723-0463	ali
Barak, Ohad	723-9282	ohad
Biondi, Biondo	723-1319	biondo
Chang, Jason	724-2974	jason
Claerbout, Jon	723-3717	jon
Clapp, Bob	725-1334	bob
Dahlke, Taylor	723-3187	taylor
de Ridder, Sjoerd	723-1250	sjoerd
Farghal, Noha	723-1250	nfarghal
Halpert, Adam	723-6006	adam
Lau, Diane	723-1703	diane
Leader, Chris	723-0463	chrisl
Levin, Stewart	726-1959	stew
Li, Elita	723-9282	myfusan
Maharramov, Musa	723-1250	musa
Shen, Xukai	723-0463	xukai
Shen, Yi	723-6006	yishen
Wong, Mandy	723-9282	mandyman
Zhang, Yang	723-6006	yang

Dept fax number: (650) 725-7344

E-MAIL

Our Internet address is "*sep.stanford.edu*"; i.e., send Jon electronic mail with the address "*jon@sep.stanford.edu*".

WORLD-WIDE WEB SERVER INFORMATION

Sponsors who have provided us with their domain names are not prompted for a password when they access from work. If you are a sponsor, and would like to access our restricted area away from work, visit our website and attempt to download the material. You will then fill out a form, and we will send the username/password to your e-mail address at a sponsor company.

STEERING COMMITTEE MEMBERS, 2012-2013

Name	Company	Tel #	E-Mail
Raymond Abma	BP	(281)366-4604	abmar1@bp.com
Francois Audebert (Co-chair, 1st year)	TOTAL	–	francois.audebert@total.com
Biondo Biondi	SEP	(650)723-1319	biondo@sep.stanford.edu
Robert Bloor	ION/GX Technology	(281)781-1141	robert.bloor@iongeo.com
Jon Claerbout	SEP	(650)723-3717	jon@sep.stanford.edu
Thomas Dickens	ExxonMobil	(713)431-6011	tom.a.dickens@exxonmobil.com
Yi Luo	Saudi Aramco	–	yi.luo@aramco.com
Alejandro Valenciano (Co-chair, 2nd year)	PGS	–	alejandro.valenciano@pgs.com

Research Personnel

Ali Almomin graduated from Texas A&M University in 2007 with a BS in Geophysics. Then, he joined Saudi Aramco and worked in several exploration and research departments with a focus on 3D seismic processing and near surface imaging. He joined Stanford Exploration Project in 2009 to pursue a PhD in Geophysics and is currently working on seismic tomography. He is a member of SEG, EAGE, and SPE.

Ohad Barak received a B.Sc. (2006) and an M.Sc. (2009) in Geophysics from Tel-Aviv University. In 2008 he joined the R&D team of Paradigm Geophysical, maintaining and developing the production codes. He joined SEP in 2009 and is currently pursuing a Ph.D. in geophysics at Stanford University, and a longer biography. His current research is on P/S separation of ocean-bottom seismic data.

Biondo L. Biondi is professor of Geophysics at Stanford University. Biondo graduated from Politecnico di Milano in 1984 and received an M.S. (1988) and a Ph.D. (1990) in geophysics from Stanford. He is co-director of the Stanford Exploration Project and of the Stanford Center for Computational Earth and Environmental Science. In 2004 the Society of Exploration Geophysicists (SEG) has honored Biondo with the Reginald Fessenden Award. Biondo recently published a book, 3-D Seismic Imaging, that is the first text book to introduce the theory of seismic imaging from the 3-D perspective. The book is published by SEG in the Investigations in Geophysics series. During 2007 gave a one-day short course in 28 cities around the world as the SEG/EAGE Distinguished Short Course Instructor (DISC) . He is a member of AGU, EAGE, SEG and SIAM.

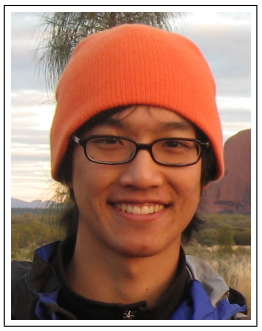

Jason Chang received his B.A. in geophysics from the University of California, Berkeley, in 2010. He joined SEP in autumn of 2011 and is currently working toward a Ph.D. in geophysics. He is a student member of SEG and AGU.

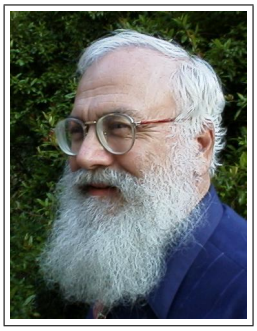

Jon F. Claerbout (M.I.T., B.S. physics, 1960; M.S. 1963; Ph.D. geophysics, 1967), professor at Stanford University, 1967. Emeritus 2008. Best Presentation Award from the Society of Exploration Geophysicists (SEG) for his paper, *Extrapolation of Wave Fields.* Honorary member and SEG Fessenden Award "in recognition of his outstanding and original pioneering work in seismic wave analysis." Founded the Stanford Exploration Project (SEP) in 1973. Elected Fellow of the American Geophysical Union. Authored three published books and five internet books. Elected to the National Academy of Engineering. Maurice Ewing Medal, SEG's highest award. Honorary Member of the European Assn. of Geoscientists & Engineers (EAGE). EAGE's highest recognition, the Erasmus Award.

Robert Clapp received his B.Sc. (Hons.) in Geophysical Engineering from Colorado School of Mines in May 1993. He joined SEP in September 1993, received his Masters in June 1995, and his Ph.D. in December 2000. He is a member of the SEG and AGU.

Noha Farghal Noha received her MS in Physics from the American University in Cairo (AUC), Egypt, in collaboration with the Interuniversity MicroElectronics Center (IMEC) in Leuven, Belgium, with scholarship from the Katholieke Universiteit Leuven. Her MS thesis involved Pulsed Laser Deposition of thin Gold-Nickel alloy films for RF MEMS microswitch contacts. As an undergraduate, she studied Physics at the AUC and served as the Vice President of AUC's Chapter of the Society of Physics Students and Editor-in-Chief of the society's magazine The Kaleidoscope of Physics until she graduated with highest honors (Summa Cum Laude). Her thesis was related to geophysical monitoring of nuclear test explosions and supervised by Dr. Rashad Kebeasy, former director of the International Data Center in Vienna. Noha was the first Egyptian to receive the Gates Cambridge Scholarship from the University of Cambridge, UK. Noha joined SEP in 2011 and is working on subsurface imaging using microseismic reflections.

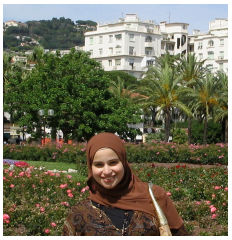

Antoine Guitton received a M.Sc. in geophysics from Université de Strasbourg in 1996. He also received a M.Sc. and Ph.D in geophysics from Stanford University in 1998 and 2005. He is a recipient of the EAGE Arie van Weelden Award in 2004 and SEG J. Clarence Karcher Award in 2007. He received the Best Paper Presented by a Student at the Annual Meeting Award in 1999 for his work on robust norms. Antoine is currently working for Geoimaging Solutions Inc. as a senior research geophysicist working on imaging and velocity estimation. He is also a consulting professor in geophysics at Stanford University. He is a member of the EAGE, SEG and AGU.

Stewart A. Levin was acting director of the Stanford Exploration Project during Jon Claerbout's 1993-4 sabbatical year. After a distinguished career in industry at Mobil and Halliburton, he has returned to Stanford as a consulting professor in the Department of Geophysics.

Musa Maharramov received his diploma c.l. in Mathematics from Baku State University in 1993. In 1995, he received a Ph.D. in Mathematics (Differential Equations) from the Azerbaijan Institute of Mathematics for his thesis "Asymptotic Solutions of Quasilinear Parabolic Equations". In 1995-2001, he worked as an IT& Comms consultant, later IT manager, at Fluor Corporation in Baku. In 2001, he joined BP Azerbaijan, and in 2006 he started his work at BP High Performance Computing as a Computational Scientist. In that role he worked with the BP Imaging Team on mathematical, algorithmic and computational aspects of seismic migration and inversion. Musa joined SEP in the fall of 2011 and is pursuing his second Ph.D., in Geophysics. He is currently working on regularization of seismic inversion problems through the application of Geological/Geomechanical constraints and advanced optimisation techniques. Musa is a member of the SEG, EAGE and SIAM.

Sjoerd de Ridder received his B.Sc. (Dec. 2004) in Earth Sciences from Utrecht University in the Netherlands. After an exchange year at Colorado School of Mines he attended Delft University of Technology. In August of 2007, he obtained an M.Sc. in Applied Earth Sciences with specialization in applied geophysics from Delft University of Technology for his thesis: 'Simulation of interferometric seismoelectric Greens function recovery'. He joined SEP in the fall of 2007 and is pursuing a Ph.D. in Geophysics. He received the 'Jon F. Claerbout - Chevron Fellowship' in 2009-2010. During the summer of 2010 he did an internship at China University of Petroleum in Beijing. Currently he is working on exploration seismology with low-frequency ambient seismic noise. In his free time he likes to run, bike and hike while traveling and discussing philosophy, politics and history.

Shuki Ronen is a geophysicist with Geco-Prakla working on various aspects of seismic data processing and acquisition. Previously he worked with GeoQuest on seismic data interpretation; with Schlumberger on reservoir characterization; with the Institute of Petroleum Research and Geophysics on seismic data processing and acquisition; with the Colorado School of Mines as a visiting professor; and with Saxpy Computer company as an engineer. He has a Ph.D. from Stanford in Geophysics, and a B.Sc. in Physics and Geology from Hebrew University. (Photo: December 1985, Geophysics, p. 2919)

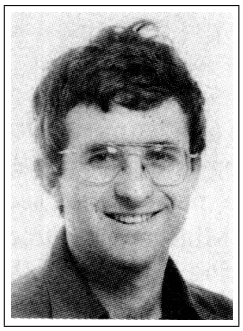

SEP ARTICLES PUBLISHED OR IN PRESS

Almomin, A., 2011, Correlation-based wave-equation migration velocity analysis. SEG Technical Program Expanded Abstracts, **30**, 3887–3891.

Almomin, A., and Biondi, B., 2012, Tomographic full waveform inversion: Practical and computationally feasible approach. SEG Technical Program Expanded Abstracts (Submitted).

Ayeni, G., Tang, Y., and Biondi, B., 2010, Efficient seismic monitoring of hydrocarbon reservoirs using multiple shooting vessels: In Proceedings of the 2010 Offshore Technology Conference.

Ayeni, G., and Biondi, B., 2010, Continuous reservoir monitoring with asynchronous simultaneous-source seismic data: 72nd Conference & Technical Exbition, EAGE, Extended Abstracts.

Ayeni G., and Biondi, B., 2010, Target-oriented joint least-squares migration/inversion of time-lapse seismic data sets: Geophysics, **75**, no. 3, R61–R75.

Ayeni, G., and Biondi, B., 2011, Wave-equation inversion of time-lapse seismic data sets: SEG Technical Program Expanded Abstracts (Submitted).

Ayeni, G., Almomin, A., and Nichols, D., 2011, On the separation of simultaneous-source data by inversion: SEG Technical Program Expanded Abstracts (Submitted).

Guerra, C., and Biondi, B., 2011, Fast 3D velocity updates using the pre-stack exploding reflector model: SEG Technical Program Expanded Abstracts **29**, 4375–4379.

Guerra, C., and Biondi, B., 2010, Fast 3D velocity updates using the pre-stack exploding reflector model: Geophysics (Accepted).

Biondi, B., 2010, Velocity estimation by image focusing analysis: Geophysics, **75**, pp. 49–60.

Biondi, B., 2010, Velocity estimation by image focusing analysis: SEG Technical Program Expanded Abstracts **29**, 4066–4070.

Chang, J., and de Ridder, S., 2012, Correlation energy between surface and borehole stations at Valhall: SEG Technical Program Expanded Abstracts **31** (Submitted).

de Ridder, S., N. Crook, S.S. Haines, and S.T. Ide, 2010, Seismic investigation of underground coal fires: A feasibility study at the Southern Ute Nation Coal Fire site. Symposium on the Application of Geophysics to Engineering and Environmental Problems **23**, 630–638.

de Ridder, S., and B. Biondi, 2010, Low-frequency passive seismic interferometry for land data: SEG Technical Program Expanded Abstracts **29**, 4041–4046.

de Ridder, S., and J. Dellinger, 2011, Imaging of near-surface structures at Valhall using ambient-seismic-noise Eikonal tomography: EAGE Third Passive Seismic Workshop, Athens, Greece, PSP13.

de Ridder, S., and J. Dellinger, 2011, Ambient seismic noise eikonal tomography for near-surface imaging at Valhall. The Leading Edge, **30**, no. 5, pp. 936–942.

de Ridder, S., 2011, Ambient seismic noise tomography at Valhall. SEG Technical Program Expanded Abstracts **30**, 1597–1601.

de Ridder, S., 2011, Ambient seismic noise tomography for exploration seismology at Valhall. Presented at 2011 AGU Fall Meeting, San Francisco, CA, 5-9 December 2011.

Grobbe, N., F.C. Schoemaker, M.D. Schakel, S.A.L. de Ridder, E.C. Slob, and D.M.J. Smeulders, 2012, Electrokinetic fields and waves: Theory, experiments, and numerical modeling. Geophysical Research Abstracts, Vol. **14**, EGU2012–10636.

de Ridder, S., and B. Biondi, 2012, Continuous passive seismic monitoring of CCS projects by correlating seismic noise: A feasibility study. 74th Conference & Technical Exbition,

EAGE, Extended Abstracts (Accepted).
de Ridder, S., and B. Biondi, 2012, Reservoir monitoring by passive seismic interferometry. SEG/SPE/AAPG Joint Workshop, La Jolla, CA, 24-29 June 2012 (Accepted).
de Ridder, S., 2012, Ambient seismic noise correlations for reservoir monitoring. SEG Technical Program Expanded Abstracts **31** (Submitted).
de Ridder, S., and B. Biondi, 2012, Continuous reservoir monitoring by ambient seismic noise tomography. SEG Technical Program Expanded Abstracts **31** (Submitted).
Schoemaker, F.C., N. Grobbe, M.D. Schakel, S.A.L. de Ridder, E.C. Slob, and D.M.J. Smeulders, 2012, Experimental validation of the electrokinetic theory and development of seismoelectric interferometry by cross-correlation: International Journal of Geophysics (Accepted).
Dellinger, J., J. Yu, and S. de Ridder, 2010, Virtual-source interferometry of 4C OBC data at Valhall without a low-cut recording filter: SEG/EAGE Summer Research Workshop, Snowbird, Utah, 15-20 August 2010.
Farghal, M.S., and Levin, S.A., 2012, Hunting for microseismic reflections using multiplets: SEG Technical Program Expanded Abstracts **31** (Submitted).
Guitton, A., Ayeni, G., and Esteban, D.A., 2012, Constrained full-waveform inversion by model reparameterization: Geophysics, 77, No. 2, R117–R127.
Guitton, A., and Esteban, D.A., 2012, Attenuating crosstalk noise with simultaneous source full waveform inversion: Geophysical Prospecting (In Press).
Guitton, A., 2012, Blocky regularization schemes for full waveform inversion: Geophysical Prospecting (In Press).
Halpert, A., Model-building with image segmentation and fast image updates: SEG Technical Program Expanded Abstracts **30**, 4035–4039.
Halpert, A., Clapp, R.G., and B. Biondo, 2010, Speeding up seismic image segmentation: SEG Technical Program Expanded Abstracts **29**, 1276–1280.
Halpert, A., Clapp, R.G., and B. Biondo, 2011, Interpreter guidance for automated seismic image segmentation: 73rd Conference & Exhibition, EAGE, Extended Abstracts.
Leader, C., Shen, X., and R. Clapp, 2011, Memory efficient reverse time migration in 3D: Proceedings of Nvidia GPU Technology Conference 2011/2012 (Accepted).
Leader, C., and R. Clapp, 2012, Least squares reverse time migration on GPUs - balacing IO and computation: 74th Conference & Technical Exbition, EAGE, Extended Abstracts (Accepted).
Leader, C., and A. Almomin, 2012, How incoherent can we be? Phase encoded linearised inversion with random boundaries: SEG Technical Program Expanded Abstract **31** (Submitted).
Li, Y., Y. Zhang, and J. Claerbout, 2010, Geophysical applications of a novel and robust L1 solver: SEG Technical Program Expanded Abstracts **29**, 3519–3523.
Li, Y., and B. Biondi, 2011, Migration velocity analysis for anisotropic models: SEG Technical Program Expanded Abstracts **30**, 201–206.
Li, Y., Nicoles, D., Osypov, K., and Bachrach, R., 2011, Anisotropic tomography with rock physics constraints: 73rd Conference & Technical Exbition, EAGE, Extended Abstracts.
Li, Y., Y. Zhang, and J. Claerbout, 2012, Hyperbolic estimation of sparse models from erratic data: Geophysics **77**, 1–9.
Li, Y., P. Shen, and C. Perkins, 2012, VTI migration velocity analysis using RTM: SEG Technical Program Expanded Abstract **31** (Submitted).
Maharramov, M., 2011, Random boundary condition for low-frequency wave propagation: SEG Technical Program Expanded Abstracts **30**, 2962.

Maharramov, M., and B. Nolte, 2011, Efficient one-way wave-equation migration in tilted transversally isotropic media: 73rd Conference & Technical Exbition, EAGE, Extended Abstracts.

Shen, X., 2010, Near-surface velocity estimation by weighted early-arrival waveform inversion: SEG Technical Program Expanded Abstracts **29**, 1975–1979.

Shen, X., and R. Clapp, 2011, Random boundary condition for low-frequency wave propagation: SEG Technical Program Expanded Abstracts (Submitted).

Tang, Y., and B. Biondi, 2010, Target-oriented wavefield tomography using demigrated Born data: SEG Technical Program Expanded Abstracts **29**, 4280–4285.

Tang, Y., and B. Biondi, 2011, Target-oriented wavefield tomography using synthesized Born data: Geophysics (Accepted).

Tang, Y., and B. Biondi, 2011, Subsalt velocity analysis by target-oriented wavefield tomography: A 3-D field-data example: SEG Technical Program Expanded Abstracts (Submitted).

Wong, M., Biondi, B.L., and Ronen, S., 2010, Joint inversion of up- and down-going signal for ocean bottom data: SEG Technical Program Expanded Abstracts **29**, 2752–2756.

Wong, M., and Ronen, S., and Biondi, B.L., 2011, Least-squares reverse-time migration/inversion for ocean bottom data: A case study. SEG Technical Program Expanded Abstracts **30**, 2369–2373.

Wong, M., and Ronen, S., and Biondi, B.L., 2012, Joint imaging with streamer and ocean bottom data. SEG Technical Program Expanded Abstracts **31** (Submitted).

Wong, M., and Ronen, S., and Biondi, B.L., 2012, Imaging with multiples using linearized full-wave inversion. SEG Technical Program Expanded Abstracts **31** (Submitted).

Zhang, Y., Claerbout, J., Guitton, A., 2011, A new bidirectional deconvolution that overcomes the minimum phase assumption. 73rd Conference & Technical Exbition, EAGE, Extended Abstracts.

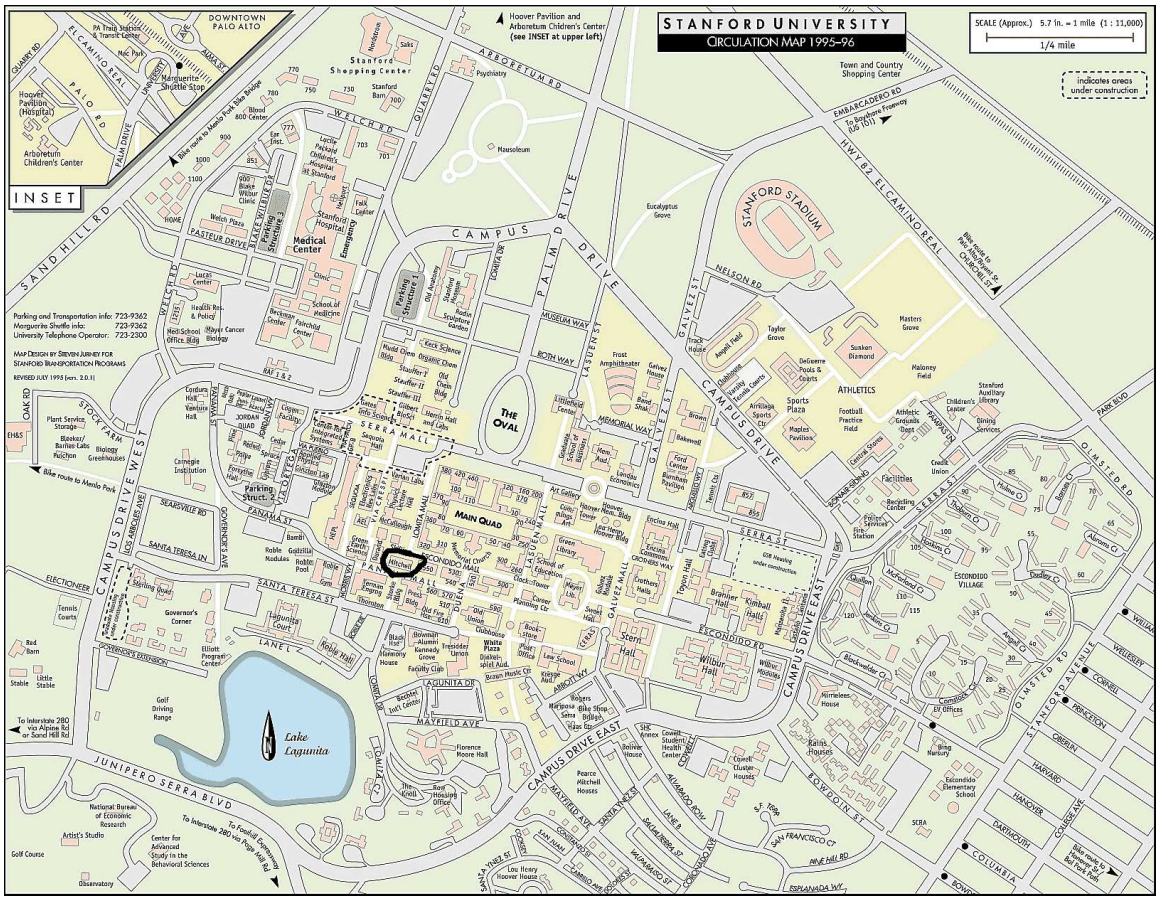
STANFORD UNIVERSITY
CIRCULATION MAP 1995–96
SCALE (Approx.) 5.7 in. = 1 mile (1 : 11,000)
1/4 mile
indicates areas under construction
INSET
Hoover Pavilion and Arboretum Children's Center (see INSET at upper left)
DOWNTOWN PALO ALTO
Stanford Shopping Center
Town and Country Shopping Center
Medical Center
Stanford Hospital
Emergency
Mausoleum
Eucalyptus Grove
STANFORD STADIUM
ATHLETICS
Sports Plaza
Football Practice Field
Maloney Field
Masters Grove
Taylor Grove
Angell Field
Frost Amphitheater
THE OVAL
MAIN QUAD
Lake Lagunita
Golf Driving Range
Golf Course
Observatory
Tennis Courts
Governor's Corner
Lagunita Court
Stern Hall
Wilbur Hall
Florence Moore Hall
Escondido Village
Escondido Elementary School
Parking Structure 1
Parking Structure 2
Parking Struct. 3
Parking Struct. 4
Parking Struct. 5
Parking Struct. 6
Parking Struct. 7
Parking Struct. 8
Parking Struct. 9
Parking and Transportation info: 723-9362
Marguerite Shuttle info: 723-9362
University Telephone Operator: 723-2300
MAP DESIGN BY STEVEN JURNEY FOR STANFORD TRANSPORTATION PROGRAMS
REVISED JULY 1995 (ver. 2.0.1)
Bike route to Menlo Park
Bike route to Palo Alto
Bike route to Alpine Rd. and Portola Valley
Bike route to Bol Park Path
To Interstate 280 via Alpine Rd or Sand Hill Rd
To Interstate 280 via Page Mill Rd
To Foothill Expressway
To Bayshore Freeway (US 101)
SAND HILL RD
CAMPUS DRIVE WEST
CAMPUS DRIVE EAST
PALM DRIVE
ARBORETUM RD
EMBARCADERO RD
HWY 82 - EL CAMINO REAL
QUARRY RD
WELCH RD
CAMPUS DR
MUSEUM WAY
BOTH WAY
LASUEN ST
GALVEZ ST
NELSON RD
MEMORIAL WAY
SERRA MALL
SERRA ST
PANAMA ST
SANTA TERESA ST
SANTA TERESA IN
SEARSVILLE RD
ELECTIONEER
LANE L
LAGUNITA DR
MAYFIELD AVE
JUNIPERO SERRA BLVD
ESCONDIDO RD
OLMSTED RD
PARK BLVD
OAK RD
STOCK FARM
LOMITA DR
ALVARADO ROW
PALOMA AVE
SAN FRANCISCO CT
ESPLANADA WY
Hoover Pavilion (Hospital)
Arboretum Children's Center
Marguerite Shuttle Stop
PA Train Station & Transit Center
Bldg 420 Center
Lucas Center
Health Res. & Policy
Med School Office Bldg
Hoover Cancer Biology
Beckman Center
Fairchild Center
School of Medicine
Clark Center
Organic Chem
Mudd Chem Bldg
Stauffer I
Stauffer II
Stauffer III
Old Chem Bldg
Gates Comp. Sci.
Gilbert Biol.
Herrin Hall and Labs
Jordan Hall
Cubberley Education
Cemex Facility
Cypress Facility
Redwood Facility
Pine Facility
Fir Facility
Yew Facility
Peter Low Barn Bldg
Peter Low Residence
Plant Service Storage
Blankley/Barker Labs
Biology Greenhouses
Carnegie Institution
Condron Hall
Varian Physics
Varian Lab
Physics Lab
Physics Annex
Physics Temp
Physics Bldg
Math Corner
Math Annex
Math Temp
Math Bldg
Encina Hall
Encina Hall West
Encina Hall Central
Encina Hall East
Encina Commons
Cypress Way
Redwood Way
Sequoia Hall
Sequoia Way
Cedro
Alder
Ayrshire Farm
Lou Henry Hoover House
Hoover Inst. Bldg
Hoover Tower
Lou Henry Hoover Bldg
Art Gallery
Cubberley Education
Mem. Aud.
Lasuen Economics
Ford Center
Bernard Berelson Pavilion
Tresidder Union
Bookstore
Post Office
Clubhouse
Faculty Club
Bowman Alumni House
Kennedy Grove
Lou Henry Hoover House
Law School
Crothers Halls
Town Hall
Braun Music Ctr
Braun Music Center
Bldg 550
Bldg 560
Bldg 570
Bldg 580
Bldg 590
Bldg 600
Bldg 610
Bldg 620
Bldg 630
Bldg 640
Bldg 650
Bldg 660
Bldg 670
Bldg 680
Bldg 690
Bldg 700
Bldg 710
Bldg 720
Bldg 730
Bldg 740
Bldg 750
Bldg 760
Bldg 770
Bldg 780
Bldg 790
Bldg 800
Bldg 810
Bldg 820
Bldg 830
Bldg 840
Bldg 850
Bldg 860
Bldg 870
Bldg 880
Bldg 890
Bldg 900
Bldg 910
Bldg 920
Bldg 930
Bldg 940
Bldg 950
Bldg 960
Bldg 970
Bldg 980
Bldg 990
Bldg 1000
Bldg 1100
Bldg 1200
Bldg 1300
Bldg 1400
Bldg 1500
Bldg 1600
Bldg 1700
Bldg 1800
Bldg 1900
Bldg 2000
Bldg 2100
Bldg 2200
Bldg 2300
Bldg 2400
Bldg 2500
Bldg 2600
Bldg 2700
Bldg 2800
Bldg 2900
Bldg 3000
Bldg 3100
Bldg 3200
Bldg 3300
Bldg 3400
Bldg 3500
Bldg 3600
Bldg 3700
Bldg 3800
Bldg 3900
Bldg 4000
Bldg 4100
Bldg 4200
Bldg 4300
Bldg 4400
Bldg 4500
Bldg 4600
Bldg 4700
Bldg 4800
Bldg 4900
Bldg 5000
Bldg 5100
Bldg 5200
Bldg 5300
Bldg 5400
Bldg 5500
Bldg 5600
Bldg 5700
Bldg 5800
Bldg 5900
Bldg 6000
Bldg 6100
Bldg 6200
Bldg 6300
Bldg 6400
Bldg 6500
Bldg 6600
Bldg 6700
Bldg 6800
Bldg 6900
Bldg 7000
Bldg 7100
Bldg 7200
Bldg 7300
Bldg 7400
Bldg 7500
Bldg 7600
Bldg 7700
Bldg 7800
Bldg 7900
Bldg 8000
Bldg 8100
Bldg 8200
Bldg 8300
Bldg 8400
Bldg 8500
Bldg 8600
Bldg 8700
Bldg 8800
Bldg 8900
Bldg 9000
Bldg 9100
Bldg 9200
Bldg 9300
Bldg 9400
Bldg 9500
Bldg 9600
Bldg 9700
Bldg 9800
Bldg 9900
Bldg 10000
Bldg 10100
Bldg 10200
Bldg 10300
Bldg 10400
Bldg 10500
Bldg 10600
Bldg 10700
Bldg 10800
Bldg 10900
Bldg 11000
Bldg 11100
Bldg 11200
Bldg 11300
Bldg 11400
Bldg 11500
Bldg 11600
Bldg 11700
Bldg 11800
Bldg 11900
Bldg 12000
Bldg 12100
Bldg 12200
Bldg 12300
Bldg 12400
Bldg 12500
Bldg 12600
Bldg 12700
Bldg 12800
Bldg 12900
Bldg 13000
Bldg 13100
Bldg 13200
Bldg 13300
Bldg 13400
Bldg 13500
Bldg 13600
Bldg 13700
Bldg 13800
Bldg 13900
Bldg 14000
Bldg 14100
Bldg 14200
Bldg 14300
Bldg 14400
Bldg 14500
Bldg 14600
Bldg 14700
Bldg 14800
Bldg 14900
Bldg 15000
Bldg 15100
Bldg 15200
Bldg 15300
Bldg 15400
Bldg 15500
Bldg 15600
Bldg 15700
Bldg 15800
Bldg 15900
Bldg 16000
Bldg 16100
Bldg 16200
Bldg 16300
Bldg 16400
Bldg 16500
Bldg 16600
Bldg 16700
Bldg 16800
Bldg 16900
Bldg 17000
Bldg 17100
Bldg 17200
Bldg 17300
Bldg 17400
Bldg 17500
Bldg 17600
Bldg 17700
Bldg 17800
Bldg 17900
Bldg 18000
Bldg 18100
Bldg 18200
Bldg 18300
Bldg 18400
Bldg 18500
Bldg 18600
Bldg 18700
Bldg 18800
Bldg 18900
Bldg 19000
Bldg 19100
Bldg 19200
Bldg 19300
Bldg 19400
Bldg 19500
Bldg 19600
Bldg 19700
Bldg 19800
Bldg 19900
Bldg 20000
Bldg 20100
Bldg 20200
Bldg 20300
Bldg 20400
Bldg 20500
Bldg 20600
Bldg 20700
Bldg 20800
Bldg 20900
Bldg 21000
Bldg 21100
Bldg 21200
Bldg 21300
Bldg 21400
Bldg 21500
Bldg 21600
Bldg 21700
Bldg 21800
Bldg 21900
Bldg 22000
Bldg 22100
Bldg 22200
Bldg 22300
Bldg 22400
Bldg 22500
Bldg 22600
Bldg 22700
Bldg 22800
Bldg 22900
Bldg 23000
Bldg 23100
Bldg 23200
Bldg 23300
Bldg 23400
Bldg 23500
Bldg 23600
Bldg 23700
Bldg 23800
Bldg 23900
Bldg 24000
Bldg 24100
Bldg 24200
Bldg 24300
Bldg 24400
Bldg 24500
Bldg 24600
Bldg 24700
Bldg 24800
Bldg 24900
Bldg 25000
Bldg 25100
Bldg 25200
Bldg 25300
Bldg 25400
Bldg 25500
Bldg 25600
Bldg 25700
Bldg 25800
Bldg 25900
Bldg 26000
Bldg 26100
Bldg 26200
Bldg 26300
Bldg 26400
Bldg 26500
Bldg 26600
Bldg 26700
Bldg 26800
Bldg 26900
Bldg 27000
Bldg 27100
Bldg 27200
Bldg 27300
Bldg 27400
Bldg 27500
Bldg 27600
Bldg 27700
Bldg 27800
Bldg 27900
Bldg 28000
Bldg 28100
Bldg 28200
Bldg 28300
Bldg 28400
Bldg 28500
Bldg 28600
Bldg 28700
Bldg 28800
Bldg 28900
Bldg 29000
Bldg 29100
Bldg 29200
Bldg 29300
Bldg 29400
Bldg 29500
Bldg 29600
Bldg 29700
Bldg 29800
Bldg 29900
Bldg 30000
Bldg 30100
Bldg 30200
Bldg 30300
Bldg 30400
Bldg 30500
Bldg 30600
Bldg 30700
Bldg 30800
Bldg 30900
Bldg 31000
Bldg 31100
Bldg 31200
Bldg 31300
Bldg 31400
Bldg 31500
Bldg 31600
Bldg 31700
Bldg 31800
Bldg 31900
Bldg 32000
Bldg 32100
Bldg 32200
Bldg 32300
Bldg 32400
Bldg 32500
Bldg 32600
Bldg 32700
Bldg 32800
Bldg 32900
Bldg 33000
Bldg 33100
Bldg 33200
Bldg 33300
Bldg 33400
Bldg 33500
Bldg 33600
Bldg 33700
Bldg 33800
Bldg 33900
Bldg 34000
Bldg 34100
Bldg 34200
Bldg 34300
Bldg 34400
Bldg 34500
Bldg 34600
Bldg 34700
Bldg 34800
Bldg 34900
Bldg 35000
Bldg 35100
Bldg 35200
Bldg 35300
Bldg 35400
Bldg 35500
Bldg 35600
Bldg 35700
Bldg 35800
Bldg 35900
Bldg 36000
Bldg 36100
Bldg 36200
Bldg 36300
Bldg 36400
Bldg 36500
Bldg 36600
Bldg 36700
Bldg 36800
Bldg 36900
Bldg 37000
Bldg 37100
Bldg 37200
Bldg 37300
Bldg 37400
Bldg 37500
Bldg 37600
Bldg 37700
Bldg 37800
Bldg 37900
Bldg 38000
Bldg 38100
Bldg 38200
Bldg 38300
Bldg 38400
Bldg 38500
Bldg 38600
Bldg 38700
Bldg 38800
Bldg 38900
Bldg 39000
Bldg 39100
Bldg 39200
Bldg 39300
Bldg 39400
Bldg 39500
Bldg 39600
Bldg 39700
Bldg 39800
Bldg 39900
Bldg 40000
Bldg 40100
Bldg 40200
Bldg 40300
Bldg 40400
Bldg 40500
Bldg 40600
Bldg 40700
Bldg 40800
Bldg 40900
Bldg 41000
Bldg 41100
Bldg 41200
Bldg 41300
Bldg 41400
Bldg 41500
Bldg 41600
Bldg 41700
Bldg 41800
Bldg 41900
Bldg 42000
Bldg 42100
Bldg 42200
Bldg 42300
Bldg 42400
Bldg 42500
Bldg 42600
Bldg 42700
Bldg 42800
Bldg 42900
Bldg 43000
Bldg 43100
Bldg 43200
Bldg 43300
Bldg 43400
Bldg 43500
Bldg 43600
Bldg 43700
Bldg 43800
Bldg 43900
Bldg 44000
Bldg 44100
Bldg 44200
Bldg 44300
Bldg 44400
Bldg 44500
Bldg 44600
Bldg 44700
Bldg 44800
Bldg 44900
Bldg 45000
Bldg 45100
Bldg 45200
Bldg 45300
Bldg 45400
Bldg 45500
Bldg 45600
Bldg 45700
Bldg 45800
Bldg 45900
Bldg 46000
Bldg 46100
Bldg 46200
Bldg 46300
Bldg 46400
Bldg 46500
Bldg 46600
Bldg 46700
Bldg 46800
Bldg 46900
Bldg 47000
Bldg 47100
Bldg 47200
Bldg 47300
Bldg 47400
Bldg 47500
Bldg 47600
Bldg 47700
Bldg 47800
Bldg 47900
Bldg 48000
Bldg 48100
Bldg 48200
Bldg 48300
Bldg 48400
Bldg 48500
Bldg 48600
Bldg 48700
Bldg 48800
Bldg 48900
Bldg 49000
Bldg 49100
Bldg 49200
Bldg 49300
Bldg 49400
Bldg 49500
Bldg 49600
Bldg 49700
Bldg 49800
Bldg 49900
Bldg 50000
Bldg 50100
Bldg 50200
Bldg 50300
Bldg 50400
Bldg 50500
Bldg 50600
Bldg 50700
Bldg 50800
Bldg 50900
Bldg 51000
Bldg 51100
Bldg 51200
Bldg 51300
Bldg 51400
Bldg 51500
Bldg 51600
Bldg 51700
Bldg 51800
Bldg 51900
Bldg 52000
Bldg 52100
Bldg 52200
Bldg 52300
Bldg 52400
Bldg 52500
Bldg 52600
Bldg 52700
Bldg 52800
Bldg 52900
Bldg 53000
Bldg 53100
Bldg 53200
Bldg 53300
Bldg 53400
Bldg 53500
Bldg 53600
Bldg 53700
Bldg 53800
Bldg 53900
Bldg 54000
Bldg 54100
Bldg 54200
Bldg 54300
Bldg 54400
Bldg 54500
Bldg 54600
Bldg 54700
Bldg 54800
Bldg 54900
Bldg 55000
Bldg 55100
Bldg 55200
Bldg 55300
Bldg 55400
Bldg 55500
Bldg 55600
Bldg 55700
Bldg 55800
Bldg 55900
Bldg 56000
Bldg 56100
Bldg 56200
Bldg 56300
Bldg 56400
Bldg 56500
Bldg 56600
Bldg 56700
Bldg 56800
Bldg 56900
Bldg 57000
Bldg 57100
Bldg 57200
Bldg 57300
Bldg 57400
Bldg 57500
Bldg 57600
Bldg 57700
Bldg 57800
Bldg 57900
Bldg 58000
Bldg 58100
Bldg 58200
Bldg 58300
Bldg 58400
Bldg 58500
Bldg 58600
Bldg 58700
Bldg 58800
Bldg 58900
Bldg 59000
Bldg 59100
Bldg 59200
Bldg 59300
Bldg 59400
Bldg 59500
Bldg 59600
Bldg 59700
Bldg 59800
Bldg 59900
Bldg 60000
Bldg 60100
Bldg 60200
Bldg 60300
Bldg 60400
Bldg 60500
Bldg 60600
Bldg 60700
Bldg 60800
Bldg 60900
Bldg 61000
Bldg 61100
Bldg 61200
Bldg 61300
Bldg 61400
Bldg 61500
Bldg 61600
Bldg 61700
Bldg 61800
Bldg 61900
Bldg 62000
Bldg 62100
Bldg 62200
Bldg 62300
Bldg 62400
Bldg 62500
Bldg 62600
Bldg 62700
Bldg 62800
Bldg 62900
Bldg 63000
Bldg 63100
Bldg 63200
Bldg 63300
Bldg 63400
Bldg 63500
Bldg 63600
Bldg 63700
Bldg 63800
Bldg 63900
Bldg 64000
Bldg 64100
Bldg 64200
Bldg 64300
Bldg 64400
Bldg 64500
Bldg 64600
Bldg 64700
Bldg 64800
Bldg 64900
Bldg 65000
Bldg 65100
Bldg 65200
Bldg 65300
Bldg 65400
Bldg 65500
Bldg 65600
Bldg 65700
Bldg 65800
Bldg 65900
Bldg 66000
Bldg 66100
Bldg 66200
Bldg 66300
Bldg 66400
Bldg 66500
Bldg 66600
Bldg 66700
Bldg 66800
Bldg 66900
Bldg 67000
Bldg 67100
Bldg 67200
Bldg 67300
Bldg 67400
Bldg 67500
Bldg 67600
Bldg 67700
Bldg 67800
Bldg 67900
Bldg 68000
Bldg 68100
Bldg 68200
Bldg 68300
Bldg 68400
Bldg 68500
Bldg 68600
Bldg 68700
Bldg 68800
Bldg 68900
Bldg 69000
Bldg 69100
Bldg 69200
Bldg 69300
Bldg 69400
Bldg 69500
Bldg 69600
Bldg 69700
Bldg 69800
Bldg 69900
Bldg 70000
Bldg 70100
Bldg 70200
Bldg 70300
Bldg 70400
Bldg 70500
Bldg 70600
Bldg 70700
Bldg 70800
Bldg 70900
Bldg 71000
Bldg 71100
Bldg 71200
Bldg 71300
Bldg 71400
Bldg 71500
Bldg 71600
Bldg 71700
Bldg 71800
Bldg 71900
Bldg 72000
Bldg 72100
Bldg 72200
Bldg 72300
Bldg 72400
Bldg 72500
Bldg 72600
Bldg 72700
Bldg 72800
Bldg 72900
Bldg 73000
Bldg 73100
Bldg 73200
Bldg 73300
Bldg 73400
Bldg 73500
Bldg 73600
Bldg 73700
Bldg 73800
Bldg 73900
Bldg 74000
Bldg 74100
Bldg 74200
Bldg 74300
Bldg 74400
Bldg 74500
Bldg 74600
Bldg 74700
Bldg 74800
Bldg 74900
Bldg 75000
Bldg 75100
Bldg 75200
Bldg 75300
Bldg 75400
Bldg 75500
Bldg 75600
Bldg 75700
Bldg 75800
Bldg 75900
Bldg 76000
Bldg 76100
Bldg 76200
Bldg 76300
Bldg 76400
Bldg 76500
Bldg 76600
Bldg 76700
Bldg 76800
Bldg 76900
Bldg 77000
Bldg 77100
Bldg 77200
Bldg 77300
Bldg 77400
Bldg 77500
Bldg 77600
Bldg 77700
Bldg 77800
Bldg 77900
Bldg 78000
Bldg 78100
Bldg 78200
Bldg 78300
Bldg 78400
Bldg 78500
Bldg 78600
Bldg 78700
Bldg 78800
Bldg 78900
Bldg 79000
Bldg 79100
Bldg 79200
Bldg 79300
Bldg 79400
Bldg 79500
Bldg 79600
Bldg 79700
Bldg 79800
Bldg 79900
Bldg 80000
Bldg 80100
Bldg 80200
Bldg 80300
Bldg 80400
Bldg 80500
Bldg 80600
Bldg 80700
Bldg 80800
Bldg 80900
Bldg 81000
Bldg 81100
Bldg 81200
Bldg 81300
Bldg 81400
Bldg 81500
Bldg 81600
Bldg 81700
Bldg 81800
Bldg 81900
Bldg 82000
Bldg 82100
Bldg 82200
Bldg 82300
Bldg 82400
Bldg 82500
Bldg 82600
Bldg 82700
Bldg 82800
Bldg 82900
Bldg 83000
Bldg 83100
Bldg 83200
Bldg 83300
Bldg 83400
Bldg 83500
Bldg 83600
Bldg 83700
Bldg 83800
Bldg 83900
Bldg 84000
Bldg 84100
Bldg 84200
Bldg 84300
Bldg 84400
Bldg 84500
Bldg 84600
Bldg 84700
Bldg 84800
Bldg 84900
Bldg 85000
Bldg 85100
Bldg 85200
Bldg 85300
Bldg 85400
Bldg 85500
Bldg 85600
Bldg 85700
Bldg 85800
Bldg 85900
Bldg 86000
Bldg 86100
Bldg 86200
Bldg 86300
Bldg 86400
Bldg 86500
Bldg 86600
Bldg 86700
Bldg 86800
Bldg 86900
Bldg 87000
Bldg 87100
Bldg 87200
Bldg 87300
Bldg 87400
Bldg 87500
Bldg 87600
Bldg 87700
Bldg 87800
Bldg 87900
Bldg 88000
Bldg 88100
Bldg 88200
Bldg 88300
Bldg 88400
Bldg 88500
Bldg 88600
Bldg 88700
Bldg 88800
Bldg 88900
Bldg 89000
Bldg 89100
Bldg 89200
Bldg 89300
Bldg 89400
Bldg 89500
Bldg 89600
Bldg 89700
Bldg 89800
Bldg 89900
Bldg 90000
Bldg 90100
Bldg 90200
Bldg 90300
Bldg 90400
Bldg 90500
Bldg 90600
Bldg 90700
Bldg 90800
Bldg 90900
Bldg 91000
Bldg 91100
Bldg 91200
Bldg 91300
Bldg 91400
Bldg 91500
Bldg 91600
Bldg 91700
Bldg 91800
Bldg 91900
Bldg 92000
Bldg 92100
Bldg 92200
Bldg 92300
Bldg 92400
Bldg 92500
Bldg 92600
Bldg 92700
Bldg 92800
Bldg 92900
Bldg 93000
Bldg 93100
Bldg 93200
Bldg 93300
Bldg 93400
Bldg 93500
Bldg 93600
Bldg 93700
Bldg 93800
Bldg 93900
Bldg 94000
Bldg 94100
Bldg 94200
Bldg 94300
Bldg 94400
Bldg 94500
Bldg 94600
Bldg 94700
Bldg 94800
Bldg 94900
Bldg 95000
Bldg 95100
Bldg 95200
Bldg 95300
Bldg 95400
Bldg 95500
Bldg 95600
Bldg 95700
Bldg 95800
Bldg 95900
Bldg 96000
Bldg 96100
Bldg 96200
Bldg 96300
Bldg 96400
Bldg 96500
Bldg 96600
Bldg 96700
Bldg 96800
Bldg 96900
Bldg 97000
Bldg 97100
Bldg 97200
Bldg 97300
Bldg 97400
Bldg 97500
Bldg 97600
Bldg 97700
Bldg 97800
Bldg 97900
Bldg 98000
Bldg 98100
Bldg 98200
Bldg 98300
Bldg 98400
Bldg 98500
Bldg 98600
Bldg 98700
Bldg 98800
Bldg 98900
Bldg 99000
Bldg 99100
Bldg 99200
Bldg 99300
Bldg 99400
Bldg 99500
Bldg 99600
Bldg 99700
Bldg 99800
Bldg 99900
Bldg 100000